# Precision Measurement of the Proton Structure Function $F_2$ at Low $Q^2$ and Very Low $x$ at HERA

by

Ulrich Fricke

# Precision Measurement of the Proton Structure Function $F_2$ at Low $Q^2$ and Very Low $x$ at HERA

**DISSERTATION**

zur Erlangung des Doktorgrades
des Fachbereichs Physik
der Universität Hamburg

vorgelegt von

**Ulrich Fricke**
aus Hamburg

Hamburg
November 1999

| | |
|---|---|
| Gutachter der Dissertation: | Prof. Dr. R. Klanner |
| | Prof. Dr. F.-W. Büßer |
| Gutachter der Disputation: | Prof. Dr. E. Lohrmann |
| | Prof. Dr. J. Meyer |
| Datum der Disputation: | 15.12.1999 |
| Dekan des Fachbereichs Physik und Vorsitzender des Promotionsausschusses: | Prof. Dr. F.-W. Büßer |

## Abstract

The kinematic region covered by the two HERA experiments H1 and ZEUS in the measurement of the total virtual photon-proton ($\gamma^* p$) cross section $\sigma_{\rm tot}^{\gamma^* p}$ and the proton structure function $F_2$ has been significantly extended since the start of data taking in 1992. In 1995 the two experiments extended their kinematic acceptance to probe the transition region between the regime of perturbative QCD (pQCD, $Q^2 \geq 1.5$ GeV$^2$) and the photoproduction region ($Q^2 \approx 0$ GeV$^2$). By shifting the interaction point in both experiments the lower limit in $Q^2$ was extended down to 0.6 GeV$^2$. To access even lower values of $Q^2$ (0.11–0.65 GeV$^2$), the ZEUS Beam Pipe Calorimeter (BPC) was installed in 1995. To further extend the kinematic acceptance of the BPC and decrease the systematic uncertainties, a new detector, the Beam Pipe Tracker (BPT), was installed in front of the BPC in 1997. It consists of two silicon microstrip detectors and is located between the BPC and the interaction point. By making use of the BPT, the main systematic uncertainties related to the BPC (energy calibration and alignment), to photoproduction background, and to the uncertainty of the interaction point position, were reduced significantly. The total systematic error was reduced by roughly a factor of two to three. The kinematic region was extended towards lower values of $Q^2$ and towards lower and higher values of $x$. At very low values of $Q^2$ and very low values of $x$ the measurement was extended into previously unexplored areas, while the new data at high $x$ allows for the first time a comparison with the data from the fixed-target experiment E665. $\sigma_{\rm tot}^{\gamma^* p}$ and $F_2$ have been measured in inelastic neutral current scattering, $e^+ p \to e^+ X$, using the ZEUS detector at HERA. The analysis covers the kinematic region for $0.045 \leq Q^2 \leq 0.80$ GeV$^2$ and $3 \cdot 10^{-7} \leq x \leq 10^{-3}$. This corresponds to a range in the $\gamma^* p$ center-of-mass energy of $25 \leq W \leq 281$ GeV. The data is compared to various models for the low $x$ and low $Q^2$ region. It can be well described by a phenomenological model based on Regge theory and the Generalized Vector Dominance Model. Deviations of the data from this model and the comparison to predictions from other models indicate that the effects of perturbative QCD are already present at $Q^2$ as low as 0.5 GeV$^2$.



## Zusammenfassung

Der Meßbereich der beiden HERA-Experimente, H1 und ZEUS, zur Bestimmung des totalen Wirkungsquerschnitts $\sigma_{\rm tot}^{\gamma^* p}$ und der Proton-Strukturfunktion $F_2$ konnte seit dem Anfang der Datennahme deutlich vergrößert werden. Beide Experimente dehnten ihren Meßbereich zu kleinen Werten von $Q^2$ aus, um die Übergangsregion zwischen dem Wirkungsbereich der perturbativen QCD (pQCD, $Q^2 \geq 1.5$ GeV$^2$) und dem Photoproduktionsbereich ($Q^2 \approx 0$ GeV$^2$) zu untersuchen. Durch Verschiebung des Wechselwirkungspunktes konnte die untere Grenze in $Q^2$ bis zu 0.6 GeV$^2$ ausgedehnt werden. Um auch den Bereich von $0.11 \leq Q^2 \leq 0.65$ GeV$^2$ zu untersuchen, wurde 1995 das ZEUS-Strahlrohrkalorimeter (BPC) installiert. Zur weiteren Ausdehnung des Meßbereiches und zur Verbesserung der Meßgenauigkeit wurde 1997 ein weiterer Detektor, der Beam Pipe Tracker (BPT), vor dem BPC installiert. Dieser aus zwei Siliziumstreifendetektoren bestehende Detektor wurde zwischen dem BPC und dem Wechselwirkungspunkt eingebaut. Durch seine Verwendung konnten die dominierenden Unsicherheiten der Messung, gegeben durch das BPC (Energiekalibration und Positionierung), die Abschätzung des Photoproduktionsuntergrundes und die Bestimmung des Wechselwirkungspunktes um einen Faktor zwei bis drei verringert werden. Der Meßbereich konnte zu kleineren Werten von $Q^2$, sowie zu kleineren und größeren Werten von $x$, ausgedehnt werden. Während die ersten beiden Erweiterungen in unerschlossene Bereiche gehen, erlaubt die letztere einen Vergleich mit Daten des Experiments E665. $\sigma_{\rm tot}^{\gamma^* p}$ and $F_2$ wurden in der Reaktion $e^+ p \to e^+ X$ mit dem ZEUS-Detektor bei HERA gemessen. Die hier beschriebene Analyse wurde im Bereich $0.045 \leq Q^2 \leq 0.80$ GeV$^2$ und $3 \cdot 10^{-7} \leq x \leq 10^{-3}$ durchgeführt. Dies entspricht einem Bereich der $\gamma^* p$-Schwerpunktsenergie von $25 \leq W \leq 281$ GeV. Die Ergebnisse wurden mit Vorhersagen für den Bereich von kleinen $x$ und $Q^2$ verglichen. Die Daten konnten durch ein phänomenologisches Modell gut beschrieben werden. Abweichungen von den Vorhersagen dieses sowie anderer Modelle lassen vermuten, daß der Einfluß der perturbativen QCD bereits bei 0.5 GeV$^2$ vorhanden ist.

To

Michaela

and

Edith

# Contents


**1 Introduction** **1**

**2 Theoretical background** **3**
2.1 A brief history of lepton-nucleon scattering . . . 3
2.2 The low $Q^2$ and very low $x$ region . . . 4
2.3 Definition of the kinematic variables . . . 5
2.4 Structure functions . . . 7
2.5 Virtual photon-proton scattering . . . 8
2.6 The Quark Parton Model (QPM) . . . 10
2.7 The Quantum Chromodynamics (QCD) . . . 11
2.7.1 Factorization . . . 13
2.7.2 The DGLAP equations . . . 13
2.7.3 The BFKL equation . . . 15
2.7.4 The CCFM equation . . . 16
2.7.5 Saturation . . . 16
2.8 The transition region . . . 16
2.8.1 Vector Dominance Model . . . 17
2.8.2 Regge theory . . . 19

**3 HERA and DIS experiments** **21**
3.1 Deep Inelastic Scattering (DIS) . . . 21
3.2 HERA design and experiments . . . 23
3.3 Structure function measurements at HERA . . . 24
3.4 Reconstruction of kinematic variables at HERA . . . 24

**4 The ZEUS detector at HERA** **31**
4.1 The main detector . . . 32
4.1.1 The Central Tracking Detector . . . 33
4.1.2 The uranium calorimeter . . . 34
4.2 Proton and neutron detectors . . . 36
4.3 The luminosity detector and electron taggers . . . 36
4.4 The ZEUS trigger and data acquisition system . . . 37
4.5 Event reconstruction and analysis . . . 38

**5 The Beam Pipe Calorimeter and Beam Pipe Tracker** **41**
5.1 BPC design . . . 41
5.2 BPC readout and trigger . . . 44
5.3 BPT design . . . 46





5.4 BPT readout and trigger . . . 47
5.5 Commissioning of the BPT . . . 48
5.6 BPT data quality monitoring . . . 50
5.7 MC simulation of BPC and BPT . . . 51

**6 Detector studies** **53**
6.1 Introduction . . . 53
6.2 BPC position reconstruction . . . 53
6.3 BPC time and shower width reconstruction . . . 55
6.4 Preliminary alignment of the BPC . . . 56
6.5 BPT track reconstruction . . . 59
6.6 BPT vertex reconstruction . . . 59
6.7 Alignment of the BPT . . . 61
6.8 BPT efficiency . . . 63
6.9 BPT position and angular resolution . . . 66
6.10 BPC energy reconstruction and calibration . . . 68
6.10.1 Energy reconstruction . . . 68
6.10.2 Energy calibration . . . 69
6.10.3 Estimation of the BPC energy non-linearity . . . 72
6.11 BPC fiducial area . . . 76

**7 MC generation** **79**
7.1 Signal events . . . 79
7.2 Modifications to RAPGAP . . . 82
7.3 Mixing of DJANGOH and RAPGAP events . . . 82
7.4 Background MC events . . . 85

**8 Efficiency and data quality studies** **87**
8.1 Introduction . . . 87
8.2 Vertex and beam tilt . . . 87
8.3 BPC timing . . . 91
8.4 BPT efficiency . . . 92
8.5 BPC trigger efficicency . . . 92

**9 Event selection** **97**
9.1 Trigger selection . . . 97
9.2 Reconstruction . . . 99
9.2.1 Reconstruction of BPC and BPT quantities . . . 99
9.2.2 Reconstruction of the hadronic final state . . . 99
9.2.3 Reconstruction of kinematic variables . . . 99
9.3 Background reduction . . . 100
9.4 Analysis cuts . . . 101
9.5 Effects of the selection cuts . . . 112
9.6 Comparison of data and MC . . . 112
9.7 Background estimation . . . 114

**10 Extraction of $\sigma_{tot}^{\gamma^* p}(W^2, Q^2)$ and $F_2(x, Q^2)$** **121**
10.1 Introduction . . . 121
10.2 Binning of the data . . . 121
10.3 Determination of $\sigma_{tot}^{\gamma^* p}$ and $F_2$ . . . 127
10.3.1 Treatment of BPC and BPT efficiency . . . 129
10.3.2 Treatment of $\epsilon$ ($F_L$) . . . 130
10.3.3 Treatment of the radiative correction . . . 130
10.3.4 Unfolding of $\sigma_{tot}^{\gamma^* p}$ and $F_2$ . . . 134
10.4 Evaluation of the systematic uncertainties . . . 136
10.4.1 Systematic errors related to the positron identification . . . 136
10.4.2 Systematic errors related to the main ZEUS detector . . . 137
10.4.3 Systematic errors related to the MC event simulation . . . 138
10.4.4 Other sources of systematic uncertainties . . . 138
10.5 Results on $\sigma_{tot}^{\gamma^* p}$ and $F_2$ . . . 140

**11 Results** **147**
11.1 Introduction . . . 147
11.2 The functional form of $\sigma_{tot}^{\gamma^* p}$ used in the unfolding . . . 147
11.2.1 The $Q^2$-dependence of $\sigma_{tot}^{\gamma^* p}$ . . . 148
11.2.2 The $W$-dependence of $\sigma_{tot}^{\gamma^* p}$ . . . 153
11.3 Models for $\sigma_{tot}^{\gamma^* p}$ and $F_2$ and in the low $Q^2$ and very low $x$ region . . . 154
11.3.1 Abramowicz, Levin, Levy, Maor (ALLM, ALLM97) . . . 154
11.3.2 Adel, Barreiro, Ynduráin (ABY) . . . 154
11.3.3 Badelek, Kwiecinski (BK) . . . 155
11.3.4 Capella, Kaidalov, Merino, Tran-Than-Van (CKMT, CKMT98) . . . 155
11.3.5 D'Alesio, Metz, Pirner (DMP) . . . 155
11.3.6 Desgrolard, Lengyel, Martynov (DLM) . . . 156
11.3.7 Donnachie, Landshoff (DL, DL98) . . . 156
11.3.8 Golec-Biernat, Wüsthoff (GBW) . . . 157
11.3.9 Haidt (HAIDT) . . . 157
11.3.10 Martin, Ryskin, Stasto (MRS) . . . 157
11.3.11 Schildknecht, Spiesberger (SCSP) . . . 158
11.4 Comparison of $F_2$ to various models . . . 158
11.5 Slope of $F_2$ . . . 161

**12 Conclusions** **165**

**A Bin definitions** **169**

**B BPC trigger cuts** **172**



# List of Figures

2.1 Lowest order Feynman diagram describing unpolarized $ep$ scattering . . . 5
2.2 Resolution of the proton substructure . . . 7
2.3 Expected behaviour of $F_2$ for a certain substructure of the proton . . . 12
2.4 Range of validity for various evolution equations in the $(x - Q^2)$-plane . . . 14

3.1 Kinematic coverage in the $(x - Q^2)$-plane of fixed-target and HERA experiments . . . 21
3.2 Aerial view of the DESY laboratory . . . 22
3.3 The HERA accelerator complex . . . 23
3.4 Isolines of the primary measured variables . . . 25
3.5 Schematics of the final state in neutral current $ep$ scattering . . . 26

4.1 The main ZEUS detector along the beam direction . . . 31
4.2 The main ZEUS detector perpendicular to the beam direction . . . 32
4.3 Layout of a CTD octant . . . 33
4.4 Layout of a FCAL module . . . 34
4.5 Location of ZEUS detectors in positive Z-direction . . . 35
4.6 Location of ZEUS detectors in negative Z-direction . . . 36
4.7 Schematic diagram of the ZEUS trigger, data acquisition system, and software . . . 38

5.1 BPC modules and modified beam pipe . . . 41
5.2 CAD drawing of the BPC modules . . . 42
5.3 BPC trigger configuration in 1997 . . . 44
5.4 The BPT in 1997 . . . 46
5.5 Determination of BPT delay time . . . 49
5.6 Determination of BPT threshold . . . 51

6.1 Resolution and bias of the BPC position reconstruction . . . 55
6.2 BPC alignment using elastic QED Compton events . . . 57
6.3 BPT strip clustering . . . 58
6.4 Comparison of MC and data: Reconstructed Z-vertex . . . 60
6.5 BPT vertex resolution . . . 61
6.6 BPT efficiency . . . 64
6.7 BPT efficiency correction vs $\Delta_{XCUT}$ and $X_{BPC}$ . . . 65
6.8 BPT noise . . . 66
6.9 Angular resolution of BPT and BPC . . . 67
6.10 BPC energy uniformity . . . 70
6.11 BPC energy scale . . . 71
6.12 BPC radiation dose profile and accumulated dose . . . 73
6.13 Schematics of $^{60}$Co scans of the BPC . . . 74
6.14 Comparison of measured and simulated attenuation curves . . . 75

6.15 Estimation of the non-linearity of the reconstructed BPC energy . . . . . 76
6.16 Determination of the BPC fiducial area . . . . . 77

7.1 Diffractive and non-diffractive event pictures . . . . . 79
7.2 Generated $x$, $y$, and $Q^2$ distributions for both MC samples . . . . . 81
7.3 $\eta_{\max}$ distributions for data and MC . . . . . 83
7.4 Parametrization of the diffractive fraction . . . . . 84

8.1 Mean X-, Y-, and Z-vertex in the data as a function of the run number . . . . . 88
8.2 Determination of the positron beam tilt . . . . . 89
8.3 Positron beam tilt as a function of the run number . . . . . 90
8.4 BPC timing . . . . . 91
8.5 BPT efficiency as a function of the run number . . . . . 93
8.6 FLT and SLT efficiency . . . . . 94
8.7 TLT efficiency in the low $y$ region . . . . . 95

9.1 BPC trigger configuration used for the analysis . . . . . 98
9.2 Comparison of MC and data: Low $y$ region (part one) . . . . . 102
9.3 Comparison of MC and data: Low $y$ region (part two) . . . . . 103
9.4 Comparison of MC and data: Medium $y$ region (part one) . . . . . 104
9.5 Comparison of MC and data: Medium $y$ region (part two) . . . . . 105
9.6 Comparison of MC and data: High $y$ region (part one) . . . . . 106
9.7 Comparison of MC and data: High $y$ region (part two) . . . . . 107
9.8 Comparison of MC and data: Low $y$ (prescaled) region (part one) . . . . . 108
9.9 Comparison of MC and data: Low $y$ (prescaled) region (part two) . . . . . 109
9.10 Comparison of MC and data: ISR region (part one) . . . . . 110
9.11 Comparison of MC and data: ISR region (part two) . . . . . 111
9.12 Reduction of beam-related background by the BPT . . . . . 114
9.13 Reduction of photoproduction background by the BPT . . . . . 115
9.14 Estimation of the photoproduction background . . . . . 116
9.15 Background estimation using the BPT hit multiplicity . . . . . 118
9.16 Background distribution in the $(x - Q^2)$-plane. . . . . 119

10.1 Resolution in $y$ and $Q^2$ . . . . . 122
10.2 Selected $(y - Q^2)$-bins . . . . . 123
10.3 Fractional $y$ and $Q^2$ resolution per $(y - Q^2)$-bin . . . . . 124
10.4 Migration of $y$ and $Q^2$ in the $(x - Q^2)$-plane . . . . . 125
10.5 Bin quality factors for each $(y - Q^2)$-bin . . . . . 126
10.6 BPC trigger efficiency per $(y - Q^2)$-bin . . . . . 129
10.7 Angular distribution of ISR and FSR photons . . . . . 131
10.8 Migration of events due to ISR . . . . . 132
10.9 $F_2$ as determined in the ISR bins . . . . . 133
10.10 Individual systematic errors of $F_2$ for all bins (part one) . . . . . 139
10.11 Individual systematic errors of $F_2$ for all bins (part two) . . . . . 140
10.12 $\sigma_{\text{tot}}^{\gamma^* p}$ as a function of $Q^2$ for fixed values of $W$ . . . . . 141
10.13 $\sigma_{\text{tot}}^{\gamma^* p}$ as a function of $W^2$ for fixed values of $Q^2$ . . . . . 142
10.14 $F_2(x, Q^2)$ as a function of $x$ for fixed values of $Q^2$ ($Q^2 > 0.20$ GeV$^2$) . . . . . 143
10.15 $F_2(x, Q^2)$ as a function of $x$ for fixed values of $Q^2$ ($Q^2 \leq 0.20$ GeV$^2$) . . . . . 144

11.1 Extrapolation of $\sigma_{\text{tot}}^{\gamma^* p}$ to $Q^2 = 0$ GeV$^2$ . . . . . 149



11.2 Comparison of $\sigma_0^{\gamma p}$ to direct measurements at $Q^2 = 0$ GeV$^2$ and results of fits to the $W$-dependence of $\sigma_0^{\gamma p}$. . . . . 150
11.3 $R = \sigma_L^{\gamma^* p} / \sigma_T^{\gamma^* p}$ as a function of $Q^2$ . . . . . 152
11.4 Comparison of $F_2$ to several models . . . . . 159
11.5 Comparison of $F_2$ in terms of $\chi^2$/bin to various models . . . . . 160
11.6 $\lambda_{\text{eff}}$ as a function of $Q^2$ . . . . . 163

# List of Tables


3.1 HERA parameters . . . . . 24

5.1 BPC performance specifications . . . . . 43
5.2 Specifications of the BPT silicon microstrip detectors . . . . . 48

6.1 Parameters used in the BPC position reconstruction for data and MC . . . . . 54
6.2 BPC alignment in 1997 . . . . . 56
6.3 BPC and BPT alignment in 1997 . . . . . 62
6.4 Masked dead and noisy BPT strips . . . . . 63

9.1 Effects of the selection cuts for data . . . . . 112
9.2 Effects of the selection cuts for MC . . . . . 113

10.1 Summary of bin quantities . . . . . 126
10.2 Results on the estimation of $F_2$ in the ISR region . . . . . 134
10.3 Results on the measurement of $F_2$ and $\sigma_{\mathrm{tot}}^{\gamma^* p}$ (part one, $Q^2 > 0.25$ GeV$^2$) . . . . . 145
10.4 Results on the measurement of $F_2$ and $\sigma_{\mathrm{tot}}^{\gamma^* p}$ (part two, $Q^2 \leq 0.25$ GeV$^2$) . . . . . 146

11.1 Parameters of the functional form of $\sigma_{\mathrm{tot}}^{\gamma^* p}$ used in the unfolding . . . . . 148
11.2 Extrapolated cross section at $Q^2 = 0$ GeV$^2$. . . . . 151
11.3 $W$-dependence of $\sigma_{\mathrm{tot}}^{\gamma^* p}$ extrapolated to $Q^2 = 0$ GeV$^2$ . . . . . 153
11.4 Comparison of $F_2$ to various models . . . . . 161
11.5 $\lambda_{\mathrm{eff}}$ as obtained from a fit to the BPT and E665 data . . . . . 162

A.1 Bins of the ISR region in the $(y - Q^2)$-plane used to estimate the uncertainty due to radiative corrections . . . . . 169
A.2 Bins in the $(y - Q^2)$-plane used to extract $F_2$ and $\sigma_{\mathrm{tot}}^{\gamma^* p}$ (part one, $Q^2 > 0.25$ GeV$^2$) 170
A.3 Bins in the $(y - Q^2)$-plane used to extract $F_2$ and $\sigma_{\mathrm{tot}}^{\gamma^* p}$ (part two, $Q^2 \leq 0.25$ GeV$^2$) 171

B.1 1997 BPC FLT and SLT trigger cuts . . . . . 172
B.2 1997 BPC TLT trigger cuts . . . . . 173

# Chapter 1

# Introduction

What is the structure of matter? This is one of the oldest questions asked by men. Starting in the 18th century great progress has been made to answer this question. Deeper understanding in the behaviour of chemical elements lead to the introduction of the periodic table of elements by Dmitri Mendelejew in 1869. In 1897 the electron was discovered by Thompson. Experiments by Rutherford together with Geiger and Marsden (1909–1911) revealed that the atoms consist of a tiny positively charged nucleus of less than 20 fm diameter made out of protons and neutrons and electrons circulating around it. With the discovery of the neutron by James Chadwick in 1932 all constituents of the atom were discovered. However, analysis of cosmic rays and the data from the first particle accelerators lead to the discovery of several hundreds of hadrons by the 1960s. The substructure of the hadrons first proposed by Gell-Mann and Zweig in 1964 [Ge64, Zw64] and later by Feynman [Fe69] was experimentally confirmed by the first inelastic electron-proton scattering experiments at the **S**tanford **L**inear **A**ccelerator **C**enter (SLAC) and later by several fixed-target experiments. In the *Standard Model* of particle physics as we know it today, all matter is composed of the fermions, *leptons* and *quarks*, which interact through *gauge fields* with each other via the exchange of *gauge bosons*. The predictions of the Standard Model are in good agreement with experimental results. Several open questions remain about the structure of matter. The existence (or non-existence) of the Higgs boson which is postulated by the Higgs mechanism is one of these questions as is the existence of supersymmetric particles. Furthermore, there is still the open question if there is a substructure of leptons and quarks. Future accelerators like the **L**arge **H**adron **C**ollider (LHC) proton-proton collider currently being built at **C**onseil **E**uropéen pour la **R**echerche **N**ucléaire (CERN) or the proposed linear accelerators like TESLA will increase the experimentally accessible area to address these and other questions.

The **H**adron-**E**lectron-**R**ing-**A**nlage (HERA) is the first electron-proton collider. It is located at the DESY laboratory (**D**eutsches **E**lektronen-**S**ynchrotron) in Hamburg, Germany. It follows the tradition of electron-proton scattering experiments at SLAC and several fixed-target experiments, which have contributed substantially to the experimental confirmation of the Standard model. With a center-of-mass energy of 300 GeV, the HERA collider was able to access a new kinematic region to explore the structure of the proton. The kinematic region covered by the two HERA experiments, H1 and ZEUS, in the measurement of the total virtual photon-proton ($\gamma^* p$) cross section $\sigma_{\mathrm{tot}}^{\gamma^* p}$ and the proton structure function $F_2$ has been significantly extended since the start of data taking in 1992. One of the surprising results from HERA was the continuing rise of the total virtual photon-proton ($\gamma^* p$) cross section $\sigma_{\mathrm{tot}}^{\gamma^* p}$ with increasing square of the $\gamma^* p$ center-of-mass energy $W^2$ for $Q^2 \geq 1.5$ GeV$^2$, which is well described by perturbative QCD (pQCD). In contrast to these results, the rise of total cross section for real photon-proton scattering $\sigma_{\mathrm{tot}}^{\gamma p}$ ($Q^2 \approx 0$ GeV$^2$) as a function of $W^2$ is less strong. This is not well described by pQCD, but shows good agreement with models within the framework of non-perturbative QCD such as Regge theory and the Generalized Vector Dominance Model.





In 1995 the two experiments extended their kinematic coverage to probe the transition region between the regime of perturbative QCD (pQCD, $Q^2 \geq 1.5$ GeV$^2$) and the photoproduction region ($Q^2 \approx 0$ GeV$^2$). By shifting the interaction point in both experiments the lower limit in $Q^2$ was extended down to 0.6 GeV$^2$. To access even lower values of $Q^2$ (0.11–0.65 GeV$^2$), the ZEUS Beam Pipe Calorimeter (BPC) was installed in 1995. From the analysis of the shifted vertex and the ZEUS BPC data it was concluded that the data is well described by pQCD down to $Q^2 \geq 1.0$ GeV$^2$. At lower values of $Q^2$ the data is in good agreement with a description based on Regge theory and the Generalized Vector Dominance Model. The transition between both regimes was found to be smooth.

To further extend the kinematic region covered by the BPC and decrease the systematic uncertainties, a new detector, the Beam Pipe Tracker (BPT), was installed in front of the BPC in 1997. It consists of two silicon microstrip detectors and is located between the BPC and the interaction point. Making use of the BPT, the main systematic uncertainties related to the BPC (energy calibration and alignment), the amount of photoproduction background, and the determination of the interaction point were reduced by roughly a factor of two to three. The kinematic acceptance was extended towards lower values of $Q^2$ and towards lower and higher values of $x$. The two former extensions go into previously unexplored areas, while the latter one results in overlap with data from the fixed-target experiment E665. The analysis presented here is based on $3.9\,\mathrm{pb}^{-1}$ of data taken during 1.5 months from the 1997 HERA run. Presented are the measurements of the proton structure function $F_2$ and the total virtual photon-proton ($\gamma^* p$) cross section $\sigma_{\mathrm{tot}}^{\gamma^* p}$ in the transition region from deep inelastic scattering to the photoproduction regime. The data is from $e^+ p$ scattering at a center-of-mass energy of 300 GeV using the ZEUS BPC and BPT. The kinematic region covered in terms of the momentum transfer $Q^2$ ranges from 0.045 to 0.80 GeV$^2$. Bjœrken x ranges between $3 \cdot 10^{-7}$ and $10^{-3}$. This corresponds to a range in the $\gamma^* p$ center-of-mass energy of $25 \leq W \leq 281$ GeV.

The first part of this thesis covers the theory describing inelastic lepton-proton scattering especially at low values of $Q^2$ and Bjœrken $x$ (chapter 2). This includes a discussion on various aspects of the physics related to the transition region such as a brief introduction into the Vector Dominance Model and Regge theory. Chapter 3 describes design and performance of the electron-proton collider HERA. Several methods to reconstruct the relevant kinematic quantities from the data are discussed and compared in terms of resolution. This is followed by a description of the ZEUS detector in chapter 4, which concentrates on the components used in this analysis. BPC and BPT will be described in more detail in chapter 5 as these are the two main ZEUS components used.

Data selection, the generation of simulated events, and systematic checks are described in the second part of this thesis. Several detector studies like reconstruction, alignment, calibration, and the estimation of the BPC and BPT efficiency are described in chapter 6. The next chapter details the generation of signal and background (MC) events used for these studies and the extraction of $F_2$ and $\sigma_{\mathrm{tot}}^{\gamma^* p}$. Several time-dependent quantities like the position of the interaction point and the electron beam tilt, which influence the data selection, are discussed in chapter 8. The event selection including background rejection and an estimation of the amount of background in the final data sample is described in chapter 9.

The third part of this thesis covers the extraction of the total virtual photon-proton cross section $\sigma_{\mathrm{tot}}^{\gamma^* p}$ and the proton structure function $F_2$ (chapter 10) and a discussion on the interpretation of the obtained results (chapter 11). Chapter 10 gives a detailed discussion on the determination of systematic uncertainties. The results on $\sigma_{\mathrm{tot}}^{\gamma^* p}$ and $F_2$ are compared to various models (chapter 11). A summary of the analysis and the resulting conclusions are given in the last chapter.

# Chapter 2

# Theoretical background

## 2.1 A brief history of lepton-nucleon scattering

Scattering experiments played a pivotal part in the development of the Standard Model of particle physics as we know it today. They can be divided into two categories, fixed-target experiments, in which a high energy particle is scattered on a stationary target, and colliding beam experiments, where both the projectile and the target particle are moving. In order to probe the structure of matter, electrons or muons have often been used as projectile particles, with targets of hydrogen, deuterium or bare protons. Information about the structure of the target particle can be derived from the measured angular and energy distribution of the scattered and (or) the target particle or of particles produced in the interaction. The square of the center-of-mass energy in a fixed-target experiment is proportional to the beam energy of the projectile particles. In a colliding beam experiment significantly larger values of the center-of-mass energy are possible since the square of the center-of-mass energy is directly proportional to the product of the projectile and target beam energies. The first mathematical description of the angular distribution of the scattered projectile particle was made by Rutherford in order to describe the results of the scattering of $\alpha$-particles on a thin sheet of gold foil. His ansatz was valid for non-relativistic spin-less point-like projectiles and (heavy) targets. In order to properly describe later scattering experiments it had to be modified. Mott extended the description to include relativistic particles with spin $\frac{1}{2}$ [Mo29]. However, since neither an extended structure nor the anomalous magnetic moment of the target was incorporated, his ansatz still failed to describe the scattering of electrons off protons. Finally in 1950, Rosenbluth included the spin $\frac{1}{2}$ of the target and projectile particles and the finite size and the anomalous magnetic moment of the target in his calculation of the cross section of elastic electron-proton scattering [Ro50]. The Rutherford [Cl86] experiment (1909–1911) led to the conclusion that atoms are made out of a tiny positive charged nucleus of less than 20 fm diameter, which is surrounded by electrons. In the early 1950s Hofstadter conducted scattering experiments of electrons off protons [Ho53, Ho55, Ho57], which revealed for the first time evidence of an extended structure of the proton. In the 1960s, electron-proton scattering experiments at SLAC confirmed the earlier results [Pa68, Bl69] and found that the two structure functions $W_1$ and $W_2$ [Dr64], which describe deep inelastic electron-proton scattering, only depend on the Bjœrken scaling variable $x$ (*scaling*). This implied that the electrons are scattered on free point-like charges. Two models were developed to describe the structure of the proton and other hadrons. The *Quark Model* was developed independently by Gell-Mann and Zweig [Ge64, Zw64] to explain Gell-Mann's and Ne'eman's proposed classification of observed hadrons known as the *Eightfold Way*. Feynman's *parton model* [Fe69] was motivated by the new data from the electron-proton





scattering experiments at SLAC. In 1969 Bjœrken and Paschos suggested, that the elementary spin-$\frac{1}{2}$ particles that made up the proton in both models, *quarks* and *partons* are identical. In order to resolve the inconsistency of the Quark Model with the Pauli exclusion principle, it was suggested that quarks carry an additional quantum number called *colour* [Gr64], which was experimentally confirmed. Since no evidence for the *colour*-charged hadrons had been found, it was concluded that observed hadrons are colour singlets. The gauge theory *Quantum Chromodynamics* (QCD) of the strong interactions in general [Fr73, Gr73, We73] was able to explain the experimental result, that no experiment has found free quarks (*quark confinement*). The QCD is a non-Abelian gauge theory, which requires the interactions among its gauge bosons, the gluons. At short distances, the quarks are quasi-free (*asymptotic freedom*), but at large distances the interaction becomes stronger due to the interactions among the gluons, which prevents the observation of free quarks. The resulting prediction from QCD, that the scaling behaviour of the deep-inelastic structure functions $W_1$ and $W_2$ is logarithmically broken, was experimentally observed at the **F**ermi **N**ational **A**ccelerator **L**aboratory (FNAL) in 1974 [Fo74]. A number of fixed-target experiments have been carried out at CERN, DESY, FNAL, and SLAC in order to obtain more information about the substructure of the nucleons. The HERA accelerator at DESY is the first colliding beam experiment using electron and proton beams. With a center-of-mass energy of 300 GeV, the kinematic region covered by the two HERA experiments H1 and ZEUS extends several orders of magnitude beyond that of fixed-target experiments in terms of larger values in $Q^2$ and much lower values in the Bjœrken scaling variable $x$. The analysis of the data at medium and high $Q^2$ [Ai96, De96], together with the study of the total virtual photon-proton ($\gamma^* p$) cross section $\sigma_{\rm tot}^{\gamma^* p}$ and the proton structure function $F_2$ at low $Q^2$ and very low $x$ [Br97] have resulted in fascinating and encouraging results.

## 2.2 The low $Q^2$ and very low $x$ region

A surprising early observation at HERA was the rapid rise of the proton structure function $F_2$ with decreasing $x$ for fixed value of $Q^2$ even for $Q^2$ as low as 1.5 GeV$^2$ [Ai96], [De96]. This translates to a strong rise of the total virtual photon-proton cross section $\sigma_{\rm tot}^{\gamma^* p}$ with the $\gamma^* p$ center-of-mass energy $W$. Since the total cross section for real photon-proton scattering $\sigma_{\rm tot}^{\gamma^* p}$ was measured to have a much slower rise with $W$, the question arose where and how the transition between the two regions takes place. In 1995 the kinematic region covered by the two HERA experiments H1 and ZEUS was extended in order to probe the transition region between the regime of perturbative QCD (pQCD, $Q^2 \geq 1.5$ GeV$^2$) and the photoproduction region ($Q^2 \approx 0$ GeV$^2$). By shifting the interaction point in both experiments, the lower limit in $Q^2$ was extended down to 0.6 GeV$^2$. To access even lower values of $Q^2$ (0.11 to 0.65 GeV$^2$), the ZEUS Beam Pipe Calorimeter (BPC) was installed in 1995. The results from 1995 ([Br97], [Br98a]) confirmed the earlier measurements. It was found that the data was well described by perturbative QCD (pQCD) down to $Q^2 = 1$ GeV$^2$. At lower values of $Q^2$ the data was best described by a model based on Regge theory (see section 2.8.2) and the Generalized Vector Dominance Model (see section 2.8.1). The data suggest that there is a transition region between the two domains, which extends up to approximately $Q^2 = 1$ GeV$^2$, and that the transition is smooth. Several questions remain about how the transition towards $Q^2 = 0$ GeV$^2$ takes place and how to describe the data. The rise of $F_2$ with decreasing $x$ is expected to stop at a certain $Q^2$ as $F_2(x \to 0, Q^2 \to 0)$ should be zero. Even for the lowest value of $Q^2 = 0.11$ GeV$^2$, $F_2$ was still found to be increasing towards lower values of $x$. The $\gamma^* p$ cross section as measured from the BPC in 1995 were extrapolated to $Q^2 = 0$ GeV$^2$ using the Regge and GVDM motivated ansatz which describes the low $Q^2$ data. It was found that there is a discrepancy between

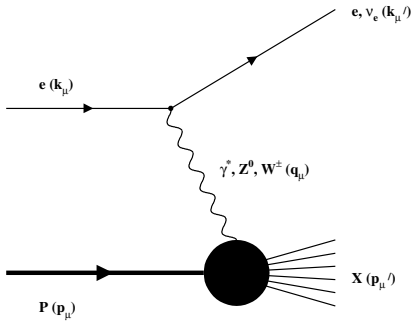


Figure 2.1: Feynman diagram describing unpolarized $ep$ scattering to lowest order in perturbation theory [Su98]. In the case of NC events, the exchanged gauge boson is either a virtual photon $\gamma^*$ or a $Z^0$ boson and the final state lepton is an electron. For CC events the final state lepton is a neutrino due to the exchange of a $W^+$ or $W^-$ boson.

extrapolated cross sections at $Q^2 = 0$ GeV$^2$ and the H1 and ZEUS measurements of the $\gamma p$ cross section. More precise data is needed to investigate the problems described above and to compare the data to new or updated models for this kinematic region. A further extension of the kinematic acceptance at low $Q^2$ and very low $x$ is desirable towards lower values of $Q^2$ and higher values of $x$. The former one will allow the study of the behaviour of $\sigma_{tot}^{\gamma^* p}$ and $F_2$ closer to the photoproduction regime, while the latter one results in an overlap with the region covered by the fixed-target experiment E665. An extension upwards from $Q^2 = 0.65$ GeV$^2$ together with a reduction of the systematic uncertainties is also desirable for a detailed study of the transition towards the region of pQCD. The motivation of the analysis presented here was to address the problems described above.

## 2.3 Definition of the kinematic variables

This section gives a short introduction to the kinematic variables used to describe the scattering of unpolarized electrons on unpolarized protons. The natural system of units is used throughout this thesis, i.e. $\hbar = 1$ and $c = 1$. Furthermore, the term 'electron' will be used as a synonym for both electrons and positrons unless explicitly stated otherwise.
The Feynman diagram to first order in perturbation theory for the scattering of unpolarized electrons on unpolarized protons is shown in figure 2.1. Electrons and protons with initial four-momentum $k = (E_e; \vec{k_e})$ and $p = (E_P; \vec{P})$ respectively interact via the exchange of a Standard Model electroweak gauge boson:

$$e(k) + P(p) \rightarrow l(k') + X(p') \tag{2.1}$$

Ignoring initial and final state radiation from the lepton, the final state consists of the scattered lepton $l$ ($k' = (E_l'; \vec{k_l'})$) and the hadronic final state system $X$ ($p' = (E_X; \vec{p_X})$). In the case of a neutral current (NC) event, the exchanged gauge boson is either a virtual photon $\gamma^*$ or a $Z^0$



boson and the final state lepton is an electron. For charged current (CC) events the final state lepton is a neutrino due to the exchange of a $W^+$ or $W^-$ boson. The HERA collider experiments, H1 and ZEUS, cannot detect the neutrino directly, but are able to measure directly the energy and direction of both the scattered lepton (in the case of NC events only) and the hadronic final state system. For fixed beam energies, as in the case of the HERA collider, two independent variables are sufficient to define the unpolarized inelastic $ep$ event kinematics. Depending on the kinematic region covered, the detectors used, and whether NC or CC events are analyzed, one of several options of how to reconstruct these variables is chosen. These will be discussed in more detail in section 3.4. The following variables provide a relativistic-invariant formulation of the unpolarized inelastic $ep$ event kinematics:

$$s = (k+p)^2 \simeq 4E_e E_P \tag{2.2}$$

$$Q^2 = -(k-k')^2 = -(p-p')^2 = -q^2 \quad Q^2 \leq s \tag{2.3}$$

$$x = \frac{Q^2}{2(p \cdot q)} \qquad 0 \leq x \leq 1 \tag{2.4}$$

$$y = \frac{p \cdot q}{p \cdot k} \qquad 0 \leq y \leq 1 \tag{2.5}$$

$$W^2 = (p+q)^2 = (p')^2 = m_p^2 + \frac{Q^2}{x}(1-x) \quad W \geq m_p \tag{2.6}$$

$$t = (p-p')^2 \tag{2.7}$$

For the 1997 HERA running period a positron beam of $E_e = 27.5$ GeV and a proton beam of $E_P = 820$ GeV were used. The resulting center-of-mass energy $\sqrt{s}$ is 300 GeV neglecting the electron and proton masses. $Q^2$ is the negative square of the momentum transfer $q$ and denotes the virtuality of the exchanged gauge boson, i.e. $Q^2 = 0$ corresponds to real photon-proton scattering. $x$ is the Bjœrken scaling variable interpreted in the Quark Parton Model as the fraction of the proton momentum carried by the struck parton. $y$ is the fraction of energy w.r.t. the initial electron energy transferred between the lepton and hadronic system in the proton rest frame. $W^2$ is the square of the invariant mass of the proton gauge boson system. $t$ is the four-momentum transfer at the proton vertex. Ignoring the electron and proton masses, $x$, $y$, $Q^2$, and $s$ are related through the following relation:

$$Q^2 \simeq s \cdot x \cdot y \tag{2.8}$$

The momentum transfer $q = \sqrt{-Q^2}$ can be related to the wavelength $\lambda$ of the virtual boson through Heisenberg's uncertainty principle:

$$\lambda = \frac{1}{|\vec{q}|} \approx \frac{2m_p x}{Q^2} \tag{2.9}$$

In order to resolve objects of size $\Delta$, $\lambda$ has to be smaller than $\Delta$. At low $Q^2$ the resolution is small and the substructure of the proton is 'visible' (see figure 2.2). At higher $Q^2$ the resolution increases, and quark-antiquark pairs originating from gluons can be resolved, and processes like QCD Compton events or Boson-Gluon-Fusion (BGF) become 'visible'. The cross section

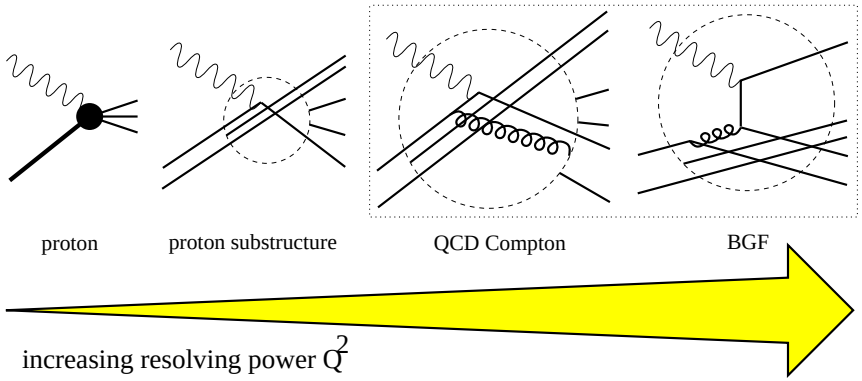


Figure 2.2: Resolution of the proton substructure as a function of $Q^2$ [Qu96].

for the reaction above can be described in terms of proton structure functions and in terms of the scattering of virtual photons off protons. The following sections give an overview of both approaches. Compared to the single photon exchange, the exchange of the heavy $Z^0$ ($m_{Z^0} = 91.2\,\mathrm{GeV}$) and $W^{\pm}$ ($m_{W^{\pm}} = 80.2$ GeV) bosons is kinematically suppressed by a term $Q^4/(Q^2+M^2_{Z^0,W^{\pm}})^2$ [In87]. Since the contribution from $(\gamma^* - Z^0)$-interference is also suppressed by a factor $Q^2/(Q^2+M^2_{Z^0})$ [In87], the single $\gamma^*$ exchange is dominant at low $Q^2$. Since only NC events at low $Q^2$ were used in this analysis, the following discussion will be restricted to the case of NC scattering through a virtual photon as the exchanged gauge boson, to lowest order in perturbation theory.

## 2.4 Structure functions

The concept of structure functions is one of the main tools to explore the structure of the nucleus in general [Ha84]. In the single boson exchange approximation the cross section can be factorized into a leptonic tensor $L_{\mu\nu}$ and a hadronic tensor $W^{\mu\nu}$

$$d\sigma \approx L_{\mu\nu} W^{\mu\nu} \tag{2.10}$$

Neglecting the electron mass the leptonic tensor has been calculated from Quantum Electrodynamics (QED) to be

$$L_{\mu\nu} = \frac{1}{2} Tr(\not{k}' \gamma_\mu \not{k} \gamma_\nu) = 2(k'_\mu k_\nu + k_\mu k'_\nu + \frac{q^2}{2} g_{\mu\nu}) \tag{2.11}$$

where $g_{\mu\nu}$ is the metric tensor. It is symmetric in $\mu$ and $\nu$. The detail of the interaction at the hadronic vertex and hence the substructure of the proton which takes part in the interaction are parametrized by the hadronic tensor $W^{\mu\nu}$. The most general form of $W^{\mu\nu}$, taking into account Lorentz-invariance and the symmetry of $L_{\mu\nu}$ in $\mu$ and $\nu$, is [Ha84]

$$W^{\mu\nu} = -W_1 g^{\mu\nu} + \frac{W_2}{m_p^2} p^\mu p^\nu + \frac{W_4}{m_p^2} q^\mu q^\nu + \frac{W_5}{m_p^2}(p^\mu q^\nu + q^\mu p^\nu) \tag{2.12}$$



The scalars $W_i$ depend on $q^2$ and $p \cdot q$. Four-current conservation can be used to reduce the number of independent scalars $W_i$. Usually, $W_4$ and $W_5$ are chosen to be replaced by:

$$W_4 = (\frac{p\cdot q}{q^2})^2 \cdot W_2 + \frac{m_p^2}{q^2} \cdot W_1 \qquad W_5 = \frac{p\cdot q}{q^2} \cdot W_2 \tag{2.13}$$

The functions $W_{i,i=1,3}$ depend on two Lorentz-invariant variables, which in this case are chosen to be $\nu = \frac{p\cdot q}{m_p}$ and $Q^2$. The behaviour of these functions as a function of $\nu$ and $Q^2$ reflect the dynamics of the strong interaction. Usually the three functions are transformed into *proton structure functions* $F_{i,i=1,3}$:

$$F_1(x,Q^2) = m_p \cdot W_1(\nu, Q^2) \tag{2.14}$$

$$F_2(x,Q^2) = \nu \cdot W_2(\nu, Q^2) \tag{2.15}$$

$$F_3(x,Q^2) = \nu \cdot W_3(\nu, Q^2) \tag{2.16}$$

Using the proton structure function convention, the double-differential deep-inelastic NC Born $e^{\pm}p \to e^{\pm}X$ cross section can be written as

$$\left(\frac{\mathrm{d}^2\sigma^{\mathrm{NC}}(e^{\pm}p)}{\mathrm{d}x\,\mathrm{d}Q^2}\right)_{\mathrm{Born}} = \frac{2\pi\alpha^2}{xQ^4}[Y_+ F_2(x,Q^2) - y^2 F_L \mp Y_- x F_3(x,Q^2)] \tag{2.17}$$

$$F_L = F_2 - 2xF_1$$

$$Y_\pm = 1 \pm (1-y)^2$$

$F_3(x,Q^2)$ describes the parity violation contribution due to $(\gamma^* - Z^0)$-interference and is small in the low and medium $Q^2$ range. Neglecting the contribution from $F_3(x,Q^2)$ one obtains the following expression for the Born cross section in terms of $y$ and $Q^2$:

$$\left(\frac{\mathrm{d}^2\sigma^{\mathrm{NC}}(e^{\pm}p)}{\mathrm{d}y\,\mathrm{d}Q^2}\right)_{\mathrm{Born}} = \frac{2\pi\alpha^2 Y_+}{yQ^4}\left(F_2 - \frac{y^2}{Y_+}F_L\right) \tag{2.18}$$

The three proton structure functions are defined with respect to the Born cross section. As also higher order QED corrections contribute to the measured cross section, a correction has to be applied in the extraction of $F_2$ from the data. This is usually parametrized by a QED radiative correction factor $\delta_r(y,Q^2)$ to the Born cross section:

$$\left(\frac{\mathrm{d}^2\sigma^{\mathrm{NC}}(e^{\pm}p)}{\mathrm{d}y\,\mathrm{d}Q^2}\right)_{\mathrm{Meas}} = \left(\frac{\mathrm{d}^2\sigma^{\mathrm{NC}}(e^{\pm}p)}{\mathrm{d}y\,\mathrm{d}Q^2}\right)_{\mathrm{Born}} \cdot [1 + \delta_r(y,Q^2)] \tag{2.19}$$

## 2.5 Virtual photon-proton scattering

The deep inelastic scattering of electrons off protons by the exchange of a virtual photon can be viewed as the scattering of virtual photons off the proton. If the lifetime of the virtual photons is large compared to the interaction time [Io69] the differential $ep$ cross section may be interpreted as the product of two factors: the flux of virtual photons and the total cross

section $\sigma_{\text{tot}}^{\gamma^* p}$ for the scattering of virtual photons off protons [Dr64, Ha63, Gi72]. This leads to the following requirement:

$$x \ll \frac{\sqrt{1+\frac{4m_p^2x^2}{Q^2}}}{2r_p m_p} \tag{2.20}$$

where $r_p \approx 5\,\text{GeV}^{-1}$ is the radius of the proton. Since virtual photons may be both longitudinally and transversely polarized, the total virtual photon-proton cross section is defined as

$$\sigma_{\text{tot}}^{\gamma^* p} \equiv \sigma_T^{\gamma^* p} + \sigma_L^{\gamma^* p} \tag{2.21}$$

where $\sigma_T^{\gamma^* p}$ and $\sigma_L^{\gamma^* p}$ are the cross section for the scattering of transverse and longitudinal polarized virtual photons off a proton respectively. Using the proton structure functions $F_1$ and $F_2$ and Hand's convention [Ha63] for the definition of the flux factor K of the virtual photons, the two cross sections are given by:

$$\sigma_T^{\gamma^* p} = \frac{4\pi^2\alpha}{m_p K_{\text{Hand}}} \cdot F_1 \tag{2.22}$$

$$\sigma_L^{\gamma^* p} = \frac{4\pi^2\alpha}{K_{\text{Hand}}}\left[\left(1+\frac{Q^2}{4x^2m_p^2}\right)\cdot\left(\frac{2xm_p}{Q^2}\right)\cdot F_2 - \frac{F_1}{m_p}\right] \tag{2.23}$$

$$\approx \frac{4\pi^2\alpha}{m_p K_{\text{Hand}}}\cdot\left(\frac{F_2}{2x}-F_1\right) = \frac{4\pi^2\alpha}{m_p K_{\text{Hand}}}\cdot\left(\frac{F_L}{2x}\right) \tag{2.24}$$

$$K_{\text{Hand}} = \nu - \frac{Q^2}{2m_p} = \frac{Q^2}{2m_p}\left(\frac{1-x}{x}\right)$$

Equation 2.24 is only valid if $Q^2/4x^2m_p^2$ is significantly larger than 1. $F_L$ is referred to as the longitudinal structure function because of the relationship to the longitudinal cross section $\sigma_L$ in equation 2.24. Since both $\sigma_L^{\gamma^* p}$ and $\sigma_T^{\gamma^* p}$ are required to be greater or equal to 0, $F_L$ is bound to be in the range of $0 \le F_L \le F_2$. The total virtual photon-proton cross section from equation 2.21 can be written as

$$\sigma_{\text{tot}}^{\gamma^* p} \equiv \sigma_T^{\gamma^* p} + \sigma_L^{\gamma^* p} = \frac{4\pi^2\alpha}{Q^2(1-x)}\cdot\left(1+\frac{1}{\frac{Q^2}{4m_p^2x^2}}\right)\cdot F_2(x,Q^2) \tag{2.25}$$

In the case of HERA equation 2.24 is valid, and in this analysis $x$ is much smaller than 1. Therefore, equation 2.25 can be simplified to

$$\sigma_{\text{tot}}^{\gamma^* p} \approx \frac{4\pi^2\alpha}{Q^2}F_2(x,Q^2) \tag{2.26}$$

Rewriting the Born cross section from equation 2.18 in terms of $\sigma_T$ and $\sigma_L$ yields

$$\frac{\mathrm{d}^2\sigma^{\text{NC}}(e^\pm p)}{\mathrm{d}y\mathrm{d}Q^2} = \Gamma\cdot(\sigma_T^{\gamma^* p}+\epsilon\sigma_L^{\gamma^* p}) = \Gamma\cdot(\sigma_{\text{tot}}^{\gamma^* p})_{\text{eff}} \tag{2.27}$$

$$\epsilon(y) = 2(1-y)/(1+(1-y)^2) \quad \text{Photon Polarization}$$

$$\Gamma(y,Q^2) = \alpha(1+(1-y)^2)/(2\pi Q^2 y) \quad \text{Photon Flux}$$



where $(\sigma_{\text{tot}}^{\gamma^* p})_{\text{eff}} = \sigma_T^{\gamma^* p} + \epsilon\sigma_L^{\gamma^* p}$ is called the effective $\gamma^* p$ cross section. For the BPC and BPT data $\epsilon(y)$ has a value of (0.31–0.99) depending on $y$. Because the center-of-mass energy at HERA is fixed, $\epsilon(y)$ cannot be varied independently of $x$ and $Q^2$. The measured quantity is the effective cross section $\sigma_T^{\gamma^* p} + \epsilon\sigma_L^{\gamma^* p}$. For the extraction of $(\sigma_{\text{tot}}^{\gamma^* p})$ $[F_2]$ one needs to assume the value of $\epsilon(y)$ $[F_L]$ for each bin. This is done by rewriting equation 2.27 using the ratio $R$ of the longitudinal and transverse cross section $R = \sigma_L^{\gamma^* p}/\sigma_T^{\gamma^* p} = F_L/2xF_1$ and assuming a certain model for the behaviour of $R$.

$$\frac{\mathrm{d}^2\sigma^{\text{NC}}(e^\pm p)}{\mathrm{d}y\mathrm{d}Q^2} = \Gamma\cdot\sigma_T^{\gamma^* p}(1+\epsilon R) \tag{2.28}$$

The contribution of $F_L$ to the differential $ep$ cross section increases for $y \to 1$. In the case of HERA it can be determined if $\mathrm{d}^2\sigma/\mathrm{d}x\mathrm{d}Q^2$ is measured at fixed values of $x$ and $Q^2$, but at different center-of-mass energies $s$. This can be done by either varying the energies of the electron and/or the proton beam or by using radiative events at reduced center-of-mass energies due to initial state radiation [Bo99e] [Ke98].

## 2.6 The Quark Parton Model (QPM)

Two models were developed to describe the structure of the proton and other hadrons, Feynman's *parton model* [Fe69] and the *Quark Model*. The latter one was developed independently by Gell-Mann and Zweig [Ge64, Zw64] to explain the classification of observed hadrons known as the *Eightfold Way*, which had been proposed by Gell-Mann and Ne'eman. In the parton model the proton consists of quasi-free point-like objects. Each so-called parton $i$ carries a fraction $\xi_i p$ of the proton momentum $p$ $(0 \le \xi_i \le 1)$. The inelastic $ep$ cross section is given by the incoherent sum of quasi-elastic electron parton scattering. If the partons were indeed point-like, one would expect that even with increasing momentum transfer $Q^2$ no new details would be visible. In 1968 Bjœrken predicted the behaviour of the structure functions for the high energy limit of $Q^2 \to \infty$, $\nu \to \infty$, but $x = \frac{Q^2}{2m_p\nu}$ finite. His prediction that the structure functions would depend only on a dimensionless scaling variable $x$ was confirmed by SLAC experiments.

$$F_1(x,Q^2) \to F_1(x) \tag{2.29}$$

$$F_2(x,Q^2) \to F_2(x) \tag{2.30}$$

In the infinite momentum frame of the proton, the scaling variable $x$ can be interpreted as the fractional momentum $\xi_i$ of the struck quark. Neglecting the parton mass $m_x$ and the proton mass, four-momentum conservation implies for this fraction:

$$m_p^2 = (\xi p+q)^2 = \xi^2 p^2 - Q^2 + 2\xi pq = m_x^2 - Q^2 + 2\xi pq$$

$$\to \xi = \frac{1}{2pq}\cdot(m_p^2 - m_x^2 + Q^2) \approx \frac{Q^2}{2pq} \tag{2.31}$$

In 1969 Bjœrken and Paschos suggested that the elementary point-like spin-$\frac{1}{2}$ particles that made up the proton in both models, *quarks* and *partons* were identical, thus the name *Quark Parton Model (QPM)*. The lifetime of a given state of partons in the proton is significantly larger in the center-of-mass system than in the rest frame of the proton due to Lorentz contraction

and time dilation. The parton distribution during the $ep$ collision is effectively frozen [St95], so that only one parton takes part in the interaction. The probability that an additional parton takes part in the interaction is suppressed by the geometrical factor $1/(\pi r_p^2 Q^2)$, where $r_p$ is the radius of the proton. The QPM relates the structure functions $F_1$ and $F_2$ to the sum of the parton distribution functions $x f_i(x)$ weighted by the square of their electric charge $e_i$ in units of the proton charge $e$.

$$F_2(x) = \frac{1}{2}\sum_i e_i^2 f_i(x) \tag{2.32}$$

$$F_1(x) = \frac{1}{2x}F_2(x) \tag{2.33}$$

Equation 2.33 is known as the Callan-Cross relation [Ca69] and was approximately confirmed by SLAC experiments. It implies that $F_L$ or, in terms of virtual photon-proton scattering $\sigma_L^{\gamma^* p}$ is 0. The predicted fractional charge of the quarks was confirmed using neutrino and electron nucleon scattering data and the postulated number of three valence quarks in the proton (uud) and neutron (ddu) using the Llewellyn-Smith sum rule [De75]. Although the QPM was very successful in explaining some of the early $ep$ results, some problems of this model became apparent. One prediction from the QPM model was that the sum of the respective integrated distribution functions $x \cdot f_i(x)$ should be equal to unity:

$$\int_0^1 dx\ x \sum_i f_i(x) = 1 \tag{2.34}$$

The experimental value of the sum in equation 2.34 was approximately 0.5. The conclusion was that about half of the momentum of the proton is carried by neutral particles [Ab83]. Also the fact that no free quarks were observed (quark confinement) could not be explained. Both problems were solved by the formulation of a field theory of the strong interaction, the Quantum Chromodynamics (QCD), which in the asymptotic limit $Q^2 \to \infty$ reproduces the QPM.

## 2.7 The Quantum Chromodynamics (QCD)

The Quantum Chromodynamics (QCD) is the gauge theory of the strong interaction. It was developed at the beginning of the 1970s. The additional quantum number colour of the quarks, introduced to solve the inconsistency of the Quark Model with the Pauli exclusion principle [Gr64], was found to be the colour charge of QCD. Three colour states were needed: 'red' (r), 'green' (g), and 'blue' (b). The three coloured quarks of one flavour form a triplet. The gauge bosons of QCD are the eight gluons, which carry a combination of colour and anti-colour. In 1979 they were experimentally observed through three-jet events at the PETRA collider at DESY [Wu84]. In contrast to the QED, QCD is a non-Abelian gauge theory, which is based on a SU(3) gauge group. Therefore, the gluons are able to interact with each other, which is a fundamental difference between QCD and QED. In the case of QED, the effective coupling, i.e. the effective charge decreases for small momentum transfers (large distances), while for QCD it is the other way around. This allows the description of two rather different experimental results, the absence of free quarks in nature (quark *confinement* in hadrons) and their quasi-free behaviour at large momentum transfers (small distances) (*asymptotic freedom*). The



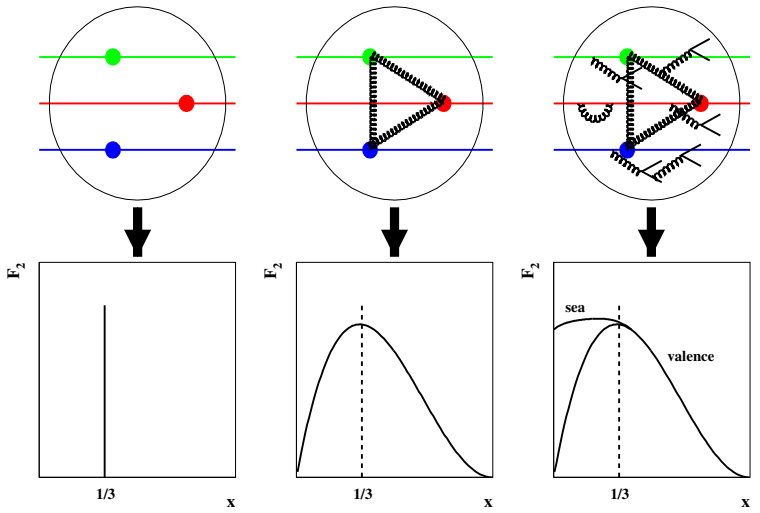


Figure 2.3: Expected behaviour of $F_2$ for a certain substructure of the proton [Su98]. In the case of only three valence quarks (left), $F_2$ would have a single peak at 1/3. For three bound valence quarks (middle) the distribution is smeared. If also QCD dynamics is taken into account, the different contributions to $F_2$ from sea and valence quarks have to be separated.

QCD coupling constant $\alpha_s(Q^2)$ depends on the number of quark flavours $n_f$ and a free scale parameter $\Lambda$ and is given in the leading order approximation by the following formula:

$$\alpha_s(Q^2) = \frac{4\pi}{(11 - 2n_f/3)\ln(\frac{Q^2}{\Lambda^2})} \tag{2.35}$$

$\Lambda$ has been measured to be $(100 - 300)$ MeV [Ba96]. For large $Q^2$, $\alpha_s$ is small and the quarks are quasi-free and can be described by perturbative calculations. In the case of low $Q^2$, $\alpha_s$ becomes large and it is expected that perturbative calculations are not valid beyond a certain minimum $Q^2$. The dynamics of the parton distributions inside the proton are given by three reactions: gluon splitting ($g \to gg$), quark-gluon radiation ($q \to qg$), and pair production of so-called *sea quarks* ($g \to q\overline{q}$). The expected qualitative behaviour of $F_2$ as a function of $x$ for different parton compositions of the proton is pictured in figure 2.3. In the case of only three valence quarks without Fermi motion one would expect the proton momentum to be equally divided between them, i.e. $F_2$ would have a single peak at 1/3 and equation 2.34 would be valid. For valence quarks bound by gluon exchange a somewhat smeared distribution is expected. If the whole QCD dynamics are included, $F_2$ is expected to rise at low $x$. This is because the low $x$ region is populated by gluons and sea quarks and the quark density is large. Because the resolution increases with $Q^2$, more quark-antiquark pairs originating from gluons can be resolved at higher $Q^2$. Therefore, the rise of $F_2$ at low $x$ for fixed $Q^2$ is expected to increase with $Q^2$. The large $x$ region is dominated by the valence quarks. With increasing $Q^2$, $F_2$

decreases due to gluon radiation. The resulting logarithmic dependence of $F_2$ on $Q^2$ at fixed $x$ is referred to as *scaling violation*. Both the scaling violation and rapid rise of $F_2$ at small $x$ have been measured by the HERA experiments H1 and ZEUS ( [De93], [Ab93]). Another effect of the quark-antiquark pair-production via gluons is that, contrary to the QPM, quarks can have transverse momentum. Therefore, they can couple to longitudinally polarized virtual photons and the Callan-Gross relation 2.33 is no longer valid.

### 2.7.1 Factorization

In the framework of QCD, hadron-hadron and lepton-hadron scattering are described in terms of interactions between the quarks and gluons of one hadron with those from the other hadron, or the lepton respectively. Two ingredients are needed to calculate for example the $ep$ cross section. The interaction between the virtual photon and a quark with a given momentum fraction in the proton is a short-range process and can be calculated using perturbative calculations. The probability to find a particular quark having a momentum fraction between $x$ and $(x + dx)$ is a long-range process. It cannot be calculated in perturbative QCD (pQCD). The separation of the scattering processes in short-range and long-range physics is called *factorization*. An additional scale, the factorization scale $\mu_F$, has to be introduced. In pQCD the calculation of self-energy diagrams such as gluon splitting into a quark-antiquark pair or the recombination of the pair into a gluon yields divergent integrals. By introducing the renormalization scale $\mu_R$ the divergence is absorbed into the definition of the long-range parton distribution functions. Only momenta less than $\mu_R$ are integrated over. Several renormalization schemes are used, for example the *minimal subtraction scheme* ($\overline{\text{MS}}$) or the *deep inelastic scattering* (DIS) scheme. For the latter one, the structure function $F_2(x, Q^2)$ is given as

$$F_2(x, Q^2) = \sum_i^{n_f} e_i^2 \left[ x q_i(x, Q^2) + x \overline{q}_i(x, Q^2) \right] \tag{2.36}$$

where $n_f$ is the number of quark flavours and $q_i$ and $\overline{q}_i$ are the quark and anti-quark distribution functions of the hadron respectively. They are process independent. The quark and anti-quark distributions and the gluon distribution function $g_i(x, Q^2)$ must be determined experimentally. However, if they are known at one particular value of $Q^2$ they can under certain conditions be calculated for other regions. This is done using the DGLAP, BFKL or CCFM equations. The DGLAP equations allow one to determine the parton distributions for fixed $x$ at any value of $Q^2$ if they are known at a particular value $Q_0^2$. The BFKL equations can be used to do it the other way around. Attempts have been made to achieve a unified BFKL/DGLAP description [Kw97]. The CCFM equations [Ca90] were derived in order to be able to evolve the parton distribution in both $x$ and $Q^2$. Figure 2.4 shows the domains of the DGLAP, BFKL, and CCFM evolution equations. The three sets of equations are discussed in the following sections.

### 2.7.2 The DGLAP equations

The Dokshitzer-Gribov-Lipatov-Altarelli-Parisi (DGLAP) equations [Al77, Gr72] are a set of $(2n_f + 1)$ coupled integro-differential equations. They can be used to determine the quark and gluon distribution functions for any value of $Q^2$ if they are known at one particular value $Q_0^2$ within the range of applicability of pQCD. The DGLAP equations are derived by requiring that both $F_1$ and $F_2$ as measurable quantities, should not depend on the choice of the factorization scale $\mu_F$. Starting from the requirement $\mu_F^2(dF_i(x, Q^2)/d\mu_F^2) = 0$ $(i = 1, 2)$, the DGLAP equations were derived in the *leading logarithmic approximation (LLA)*. The terms which give



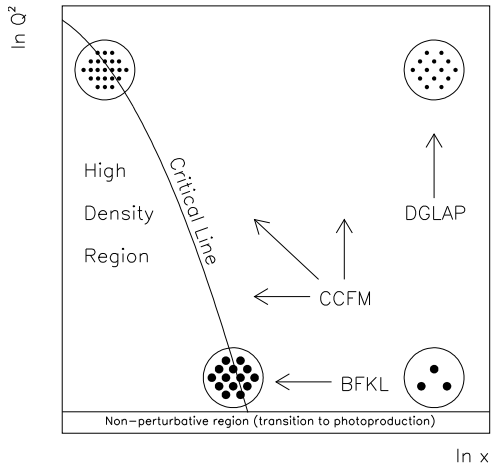


Figure 2.4: Range of validity for the various evolution equations. The circles indicate the parton density 'visible' at a certain $x$ and $Q^2$. Increasing $Q^2$ leads to a better spatial resolution. Smaller values in $x$ yield an increase in the parton density driven by the gluon density. At high parton density saturation is expected to diminish the rise of $F_2$ with decreasing $x$. The 'critical' line indicates the transition region into the region of high parton density where saturation and shadowing is expected to dominate. The DGLAP equation allows the evolution in $Q^2$ for fixed $x$, the BFKL equation the evolution in $x$ for fixed $Q^2$. The CCFM equations describe an evolution in both $x$ and $Q^2$.

the dominant contribution at large $x$ and large $Q^2$ were summed to all orders and all others neglected. The remaining terms have the form $\alpha_s^n \cdot (\ln Q^2)^n$. Therefore, the DGLAP equations are only valid as long as the impact of the neglected terms is small, which is expected for

$$\alpha_s(Q^2) \ln (Q^2) \sim \mathcal{O}(1) \qquad \alpha_s(Q^2) \ln \frac{1}{x} \ll 1 \tag{2.37}$$

The DGLAP equations for the quark, anti-quark, and gluon distributions are given by:

$$\frac{\mathrm{d}q_i(x, Q^2)}{\mathrm{d}\ln Q^2} = \frac{\alpha_s(Q^2)}{2\pi} \int_x^1 \frac{\mathrm{d}z}{z} \left[ q_i(z, Q^2) P_{qq}\left(\frac{x}{z}\right) + g(z, Q^2) P_{qg}\left(\frac{x}{z}\right) \right] \tag{2.38}$$

$$\frac{\mathrm{d}\overline{q}_i(x, Q^2)}{\mathrm{d}\ln Q^2} = \frac{\alpha_s(Q^2)}{2\pi} \int_x^1 \frac{\mathrm{d}z}{z} \left[ \overline{q}_i(z, Q^2) P_{qq}\left(\frac{x}{z}\right) + g(z, Q^2) P_{qg}\left(\frac{x}{z}\right) \right] \tag{2.39}$$

$$\frac{\mathrm{d}g(x, Q^2)}{\mathrm{d}\ln Q^2} = \frac{\alpha_s(Q^2)}{2\pi} \int_x^1 \frac{\mathrm{d}z}{z} \left[ \sum_{i=1}^{n_f} (q_i(x, Q^2) + \overline{q}_i(x, Q^2)) P_{gq}\left(\frac{x}{z}\right) + g(z, Q^2) P_{gg}\left(\frac{x}{z}\right) \right] \tag{2.40}$$

$P_{ij}(x/z)$ are QCD splitting functions, which describe the probability to find a parton of type $i$ with momentum fraction $x$ originating from a parton of type $j$ having a momentum fraction $z$ when the scale changed from $Q^2/\mathrm{GeV}^2$ to $Q^2/\mathrm{GeV}^2 + \mathrm{d}\ln(Q^2/\mathrm{GeV}^2)$. Up to now they are calculated up to next-to-leading order (NLO) and can be found in [Gu80, Fu82]. If the quark, anti-quark, and gluon distributions are known at a starting scale $Q_0^2$ they can be evolved using the equations (2.38–2.40). Under the assumption that the contributions from quarks are negligible at low $x$ it is possible to extract the gluon density directly from a measurement of $F_2$. Using the method proposed by Prytz in leading order [Pr93] and the DGLAP equations the following relation between $F_2$ and $g(x,Q^2)$ is derived:

$$\frac{\mathrm{d}F_2(x,Q^2)}{\mathrm{d}\ln\,Q^2} \approx \frac{5\alpha_s(Q^2)}{9\pi}\frac{2}{3}xg(2x,Q^2) \tag{2.41}$$

The *Double Logarithmic Approximation (DLLA)* can also be used to estimate the gluon distribution at low values of $x$, where the LLA approximation used to derive the DGLAP equations is not valid. Leading terms in $(\ln\frac{1}{x})$ accompanied by leading terms in $(\ln\,Q^2)$ are included, which results in the gluon distribution below, which is numerically compatible with $x^{-0.4}$ [Le97].

$$\begin{aligned} xg(x,Q^2) &\sim \exp\sqrt{\left[\frac{48}{11-\frac{2}{3}n_f}\ln\left(\frac{\ln\frac{Q^2}{\Lambda^2}}{\ln\frac{Q_0^2}{\Lambda^2}}\right)\ln\frac{1}{x}\right]} \\ \alpha_s(Q^2)\cdot\ln\,Q^2 &\ll 1, \quad \alpha_s(Q^2)\cdot\ln\frac{1}{x}\ll 1, \quad \alpha_s(Q^2)\cdot\ln\,Q^2\,\ln\frac{1}{x}\sim\mathcal{O}(1) \end{aligned} \tag{2.42}$$

Equation 2.42 violates unitarity in the limit $x \to 0$, which is also true for the solution of the BFKL equation 2.43 discussed in the next section. The model of saturation in which the growth of the gluon and sea quark density at low $x$ is compensated by quark-antiquark annihilation and gluon recombination is discussed briefly in section 2.7.5.

### 2.7.3 The BFKL equation

Work done by Balitzky, Fadin, Kuraev, and Lipatov resulted in the BFKL evolution equation. This equation provides an evolution in $x$ for fixed values of $Q^2$ [Ba78] for the unintegrated gluon distribution $f_g(x,k_T^2)$. $k_T^2$ is the square of the transverse momentum of the gluons. In contrast to the DLLA approximation the BFKL evolution scheme provides a way to sum up all leading terms in $\ln\frac{1}{x}$. The BFKL equation according to [As94]and the relationship of the unintegrated to integrated gluon distribution are given in equation 2.43 and 2.44 respectively.

$$\begin{aligned} -x\frac{\partial\, f_g(x,k_T^2)}{\partial\, x} &= \frac{3\alpha_s}{\pi}k_T^2\int_0^\infty\frac{\mathrm{d}k_T'^2}{k_T'^2}\left[\frac{f_g(x,k_T'^2)-f_g(x,k_T^2)}{|k_T'^2-k_T^2|}+\frac{f_g(x,k_T^2)}{\sqrt{4k_T'^4+k_T^4}}\right] \\ &\equiv K\otimes f_g \\ \alpha_s\ln(Q^2) &\ll 1, \quad \alpha_s\ln\frac{1}{x}=\mathcal{O}(1) \end{aligned} \tag{2.43}$$

$$xg(x,Q^2) = \int_o^{Q^2}(\mathrm{d}k_T^2/k_T^2)f_g(x,k_T^2) \tag{2.44}$$

$K$ is the BFKL kernel. The solution of 2.43 is dominated by the largest eigenvalue $\lambda$ of the kernel $K$ resulting in the following $x$ and $Q^2$ dependence for $F_2$ [As94a]:

$$F_2(x,Q^2) \sim (Q^2)^{1/2}x^{-\lambda}, \qquad \lambda=\frac{3\alpha_s}{\pi}4\ln 2 \tag{2.45}$$



Equation 2.45 violates unitarity in the limit of $x \to 0$. An upper limit of the rise of $F_2$ is given by the Froissart bound [Fr61] because $F_2$ is related to the total cross section of virtual photon-proton scattering $\sigma_{\mathrm{tot}}^{\gamma^* p}$ by equation 2.25:

$$\sigma_{\mathrm{tot}}^{\gamma^* p} = \frac{4\pi^2\alpha}{Q^2}\cdot F_2 \;\le\; \frac{\pi}{m_\pi^2}(\ln\,\frac{s}{s_0})^2 \tag{2.46}$$

$m_\pi$ is the mass of the charged pion and $s_0$ a scale factor, which has to be determined experimentally. Because of the limit given by equation 2.46 there must exist some mechanism which dampens the rise of $F_2$ at low $x$. Two models of such a mechanism are briefly discussed in section 2.7.5. A modified version of the BFKL equations takes into account the recombination of gluons ($gg \to g$) as one mechanism to dampen the rise of $F_2$. The ansatz proposed by Gribov, Levin, and Ryskin includes non-linear terms into equation 2.43:

$$-x\frac{\partial\, f_g(x,k_T^2)}{\partial\, x} = K\otimes f_g - \frac{81\alpha_s^2(k_T^2)}{16R^2k_T^2}[xg(x,k_T^2)]^2 \tag{2.47}$$

### 2.7.4 The CCFM equation

The equation proposed by Catani, Ciafaloni, Fiorani, and Marchesini (CCFM) is based on the coherent radiation of gluons. In the limit of low $x \to 0$ the CCFM equation is equivalent to the BFKL equation, while for $x \to 1$ it reproduces the DGLAP equations. CCFM based MC generators did archieve a reasonably good description of the $F_2$ data from HERA, but until recently failed to describe the production of forward jets at HERA, which is believed to be a good signature for parton dynamics at low $x$. In [Ju99] the results of a modified version of the MC generator based on CCFM were found to be in good agreement with $F_2$ data for $5\cdot10^{-6} < x < 0.05$ and $3.5 < Q^2 < 90$ GeV$^2$ and cross section for forward jet production. Whether this improved model is able to provide a good description of the $F_2$ data for lower and higher values of $Q^2$ remains to be seen.

### 2.7.5 Saturation

It is expected that the rise of the quark and gluon density at low $x$ stops at a a certain $x_{\mathrm{min}}(Q^2)$, because of quark-antiquark annihilation and recombination of gluons. $x_{\mathrm{min}}$ is expected to depend on $Q^2$, because at low $Q^2$ the resolving power of the virtual photon is low compared to higher $Q^2$ and less partons can be seen. This is indicated by the 'critical line' in figure 2.4. It has been estimated in [Le97] that recombination of gluons result in saturation if

$$xg(x,Q^2) \sim \frac{r_p^2}{r_g^2(Q^2)} \sim \frac{5\ \mathrm{GeV}^{-1}}{\frac{2}{Q^2}} \sim 6\ Q^2 \tag{2.48}$$

$r_p$ is the radius of the proton ($\sim 1$ fm) and $r_g(Q^2) = 2/Q$ the gluon radius at a certain value of $Q^2$. So far the gluon densities derived from HERA have been well below this limit and no signs of saturation have been observed. In a model proposed by Mueller [Mu90], the saturation starts in small localized areas of the proton, the *hot spots*. This would result in saturation at lower overall gluon densities.

## 2.8 The transition region

The main motivation for the measurement presented in this thesis was to further expand the kinematic region at low $x$ and low $Q^2$ and reduce the systematic uncertainties of the previous

measurement [Br97]. This is done to study the transition from the region of pQCD at $Q^2 \geq 1.0$ GeV$^2$ to the photoproduction limit ($Q^2 \approx 0$ GeV$^2$). For $Q^2 \to 0$ GeV$^2$ the virtual photon-proton cross section $\sigma_{\rm tot}^{\gamma^* p}$ approaches the cross section for real photon-proton scattering $\sigma_{\rm tot}^{\gamma p}$. As real photons can only be transversely polarized, $\sigma_{\rm L}^{\gamma^* p}$ has to vanish at $Q^2 = 0$.

$$\sigma_{\rm tot}^{\gamma p} = \lim_{Q^2 \to 0} \left[\sigma_{\rm T}^{\gamma^* p}\right] = \lim_{Q^2 \to 0} \left[\frac{4\pi^2\alpha}{Q^2} F_2(x, Q^2)\right] \tag{2.49}$$

Two constraints for the structure functions $F_2$ and $F_L$ in the limit of $Q^2 \to 0$ GeV$^2$ can be derived from the $ep$ cross section in terms of structure functions. The hadronic tensor $W^{\mu\nu}$ from equation 2.12 rewritten in terms of $F_1$ and $F_2$ neglecting the contribution of $F_3$ at low $Q^2$ exhibits two singularities. Since both $F_1$ and $F_2$ are physical quantities, the singularities have to be canceled by imposing the following conditions on $F_1$ and $F_2$:

$$F_2 = \mathcal{O}(Q^2) \qquad F_L = F_2 - 2xF_1 = \mathcal{O}(Q^4) \tag{2.50}$$

As expected from the behaviour of the strong coupling constant (equation 2.37), pQCD is not able to describe the data down to $Q^2 \approx 0$ GeV$^2$. As pQCD was found only to work above $Q^2 = 1$ GeV$^2$ [Br97], non-perturbative concepts have to be used to describe $\sigma_{\rm tot}^{\gamma^* p}$ and $F_2$ in the region of low $Q^2$. Most of the phenomenological models used to describe the transition region are based on the concepts of the *Vector Dominance Model (VDM)* [Sa60] and/or *Regge theory* [Co70]. These concepts will be discussed in the next section. A description of the various models and parametrizations, which are compared to the results of this analysis is given in section 11.

### 2.8.1 Vector Dominance Model

The Vector Dominance Model (VDM) is based on the phenomenological observation that photon-hadron interactions exhibit striking similarities to hadron-hadron interactions. In the VDM the photon is a superposition of the bare photon $|\gamma\rangle_{\rm bare}$ and a hadronic component $|\gamma\rangle_{\rm hadronic}$. The latter one is given by a fluctuation of the photon into a quark-antiquark pair with the same quantum numbers ($J^{PC} = 1^{--}$, $Q = B = S = 0$):

$$|\gamma\rangle = |\gamma\rangle_{\rm bare} + |\gamma\rangle_{\rm hadronic} \tag{2.51}$$

The VDM makes the assumption that the photon-hadron interaction is given by the interaction of the hadronic components of the photon. Furthermore, it assumes that the photon only fluctuates into the three lightest vector mesons ($\rho^0$, $\omega$, and $\phi$), which all have the same quantum numbers as the bare photon. The VDM ansatz is only valid if the fluctuation time $\tau_f$, which can be estimated using the uncertainty principle, is large compared to the interaction time [Le97]. $\tau_f$ can be estimated from the energy difference $\Delta E$ between the mass of the vector meson $m_V$ and the momentum of the bare photon and is given by:

$$\tau_f \approx \frac{2\nu}{m_V^2 + Q^2} \quad (Q^2 \geq 0) \tag{2.52}$$

Note that equation 2.52 is valid for both virtual and real ($Q^2 = 0$ GeV$^2$) photons. In fact [Ab95] in the limit of $x \to 0$, even virtual photons at high $Q^2$ can fluctuate into $q\bar{q}$ pairs and $\tau_f$ is given by:

$$\tau_f \approx \frac{1}{(2m_p x)} \tag{2.53}$$



From equation 2.53 it is clear that at low $x$ the fluctuation time is large and the VDM ansatz valid. $|\gamma\rangle_{\rm hadronic}$ is then given by:

$$|\gamma\rangle_{\rm hadronic} \propto \sum_{V=\rho^0,\omega,\phi} \left(\frac{4\pi\alpha \cdot r_V}{(1+Q^2/m_V^2)}\right) |V\rangle \tag{2.54}$$

The sum extends over the three lightest vector mesons. In the framework of the VDM the cross sections for transversely and longitudinally polarized photons, $\sigma_T^{\gamma^* p}(W, Q^2)$ and $\sigma_L^{\gamma^* p}(W, Q^2)$ from equation 2.21, are related to the total cross sections of transversely and longitudinally polarized vector mesons scattering off protons at $Q^2 = 0$ GeV$^2$:

$$\sigma_T^{\gamma^* p}(W, Q^2) = \left(\sum_{V=\rho^0,\omega,\phi} \frac{4\pi\alpha \cdot r_V}{(1+Q^2/m_V^2)^2} + \sigma_{T,C}^{\gamma^* p}\right) \cdot \sigma_T^{Vp}(W) \tag{2.55}$$

$$\sigma_L^{\gamma^* p}(W, Q^2) = \left(\sum_{V=\rho^0,\omega,\phi} \frac{4\pi\alpha \cdot r_V}{(1+Q^2/m_V^2)^2} \cdot \xi_V \cdot \frac{Q^2}{m_V^2} + \sigma_{L,C}^{\gamma^* p}\right) \cdot \sigma_T^{Vp}(W) \tag{2.56}$$

$W$ is the center-of-mass energy of the $(\gamma - p)$-system as defined in equation 2.6. The possible difference in $\sigma_T^{Vp}$ and $\sigma_L^{Vp}$ at $Q^2 = 0$ is taken into account by the factors $\xi_V$, which are expected to be within $0 \leq \xi_V \leq 1$ [Ba92]. $\sigma_{T,C}^{\gamma^* p}$ and $\sigma_{L,C}^{\gamma^* p}$ were not included in the original VDM, but are added to account for higher mass states than the three used vector mesons in the extension of this model discussed below. The coupling constants $r_V$ have been determined experimentally in $\gamma\, p$ and $e^+e^-$ reactions [Ba92]. The measurements confirm that the VDM ansatz is valid. However, several experimental results from inelastic $ep$ scattering were not reproduced by the VDM model as discussed above. It was found that the three lightest vector mesons only contribute at approximately 78 % of the total cross section ($r_{\rho^0} = 0.65$, $r_\omega = 0.08$, $r_\phi = 0.05$). The *generalized vector dominance model* (GVDM) [Sa72] is an extension of the VDM. It includes not only the three lightest vector mesons but all higher mass states [Sa72]. A simple extension of the VDM is to include the additional term $\sigma_{T,C}^{\gamma^* p}$ ($\sigma_{L,C}^{\gamma^* p}$) to equation 2.55 (2.56) to take into account the contribution from higher mass states. A simple ansatz of these terms [Sa72] is also used in the analysis presented here (see chapter 11):

$$\sigma_{T,C}^{\gamma^* p} = \frac{4\pi\alpha \cdot r_C}{(1+Q^2/m_0^2)} \tag{2.57}$$

$$\sigma_{L,C}^{\gamma^* p} = 4\pi\alpha \cdot r_C \cdot \xi_C \cdot \left[\frac{m_0^2}{Q^2} \cdot \ln\left(1 + \frac{Q^2}{m_0^2}\right) - \frac{1}{(1+Q^2/m_0^2)}\right] \tag{2.58}$$

In the most general form of the GVDM, the equations 2.55 and 2.56 are modified by taking into account the diagonal approximation of the transverse photon absorption cross section:

$$\sigma_T^{\gamma^* p}(W^2, Q^2) = \int_{m_0^2} {\rm d}m^2 \frac{\rho_T(W^2, m^2)}{(1+Q^2/m^2)^2} \tag{2.59}$$

$$\sigma_L^{\gamma^* p}(W^2, Q^2) = \int_{m_0^2} {\rm d}m^2 \frac{\rho_T(W^2, m^2)}{(1+Q^2/m^2)^2} \cdot \xi \cdot \frac{Q^2}{m^2} \tag{2.60}$$

$$\rho_T(W^2, m^2) = (1/4\pi^2\alpha)\sigma_{e^+e^-}(m^2)\sigma_{\rm hadr}(W^2, m^2) \tag{2.61}$$

The spectral weight-function $\rho_T$ is proportional to the cross sections $e^+e^- \to m_V$ and $m_V p \to m_{V'} p$, where $m_V$ and $m_{V'}$ are vector meson states with different masses. The VDM is included in the GVDM as the special cases of $\rho_T(W^2, m^2) = \sum_V (4\pi\alpha \cdot r_V)\delta(m^2 - m_V^2) \cdot \sigma_{Vp}^T(W)$.

### 2.8.2 Regge theory

In the context of this thesis only a short summary of Regge theory is given. Several detailed introductions are available, for example [Co70].
Regge theory was first formulated to describe hadron-hadron scattering cross sections by the exchange of several particles. It turned out that lepton-hadron interactions could also under certain conditions be described by this ansatz, for example the interaction of photons with hadrons due to the possible fluctuations of the photons in hadrons as discussed in the last section. Regge theory is expected to be valid in the high energy limit $s \gg Q^2$, which is true for the kinematic region covered in this thesis ($\sqrt{s} \approx 300$ GeV$^2$, $Q^2 < 1$ GeV$^2$). Note that in the following discussion the same notation as in [Co70] is used. $s$ is the square of the center-of-mass energy of the relevant process. In $\gamma^* p$ collisions $s \equiv W^2_{\gamma^* p}$. $t$ is the negative squared momentum transfer at the proton vertex ($t = -(p - p')^2$).
The behaviour of the cross section as predicted by Regge theory was found to solve one problem of the simple ansatz of one particle exchange. For the exchange of one particle with spin $j$ the cross section was found to be proportional to $s^{2(j-1)}$. For exchanged particles with spin $j > 1$ the cross section increases with $s$. This was violating the Froissart bound and unitarity. The cross section as predicted by Regge theory was found to be decreasing with the center-of-mass energy $s$. It was found that all possible exchange particles and resonances of a given isospin and strangeness were connected by a line in the Chew-Frautschi plot of spin $l$ versus the $m_l^2$, where $m_l$ is the mass of a given particle or resonance with spin $l$. These lines were called *Regge trajectories* or *Reggeon* and of the simple form $\alpha(t) = \alpha(t = 0) + \alpha' t$. $\alpha(t = 0)$ is called the intercept of the trajectory. In the Regge limit of $s \gg Q^2$ the scattering amplitude $A(s, t)$ is given by

$$\mathcal{A}(s, t) = \beta(t) \cdot \left(\frac{s}{s_0}\right)^{\alpha(t)} \tag{2.62}$$

where $s_0$ is a constant. Using the optical theorem, which connects the total cross section $\sigma_{\text{tot}}$ to the imaginary part of the scattering amplitude

$$\sigma_{\text{tot}} = \frac{1}{s}\text{Im}\,\mathcal{A}(s, t = 0) \tag{2.63}$$

the s-dependence of $\sigma_{\text{tot}}$ is predicted as

$$\sigma_{\text{tot}} \propto s^{\alpha(t=0)-1} \tag{2.64}$$

which for $\alpha(t = 0) < 1.0$ falls with increasing center-of-mass energy $s$ and conserves unitarity. For $W < 10$ GeV the measured cross sections for hadron-hadron interactions were found to be in good agreement with the prediction from Regge theory, but measurements at higher $W$ have revealed a slow rise of the cross section with $W$. This resulted in an extension of the Regge theory. In order to describe the rise, an additional trajectory, the *Pomeranchuk trajectory* or in short the *Pomeron* with $\alpha(t = 0) > 1.0$ was introduced. The Pomeron was not an observed or predicted particle, but a mathematical construct to account for the observed rise of the total cross section. It was required to have the quantum number of the vacuum $J^{PC} = 0^{++}$ and to be colourless. With the discovery of events with a large rapidity gap at HERA, which were explained by the exchange of a colourless object, some models assume the Pomeron to be composed of two gluons [Ab96], but this remains to be proven. In the context of this analysis only the $\gamma\, p$ and $\gamma^*\, p$ cross sections are discussed. The former one was found to be well described by a Pomeron trajectory with $\alpha_P^{(\text{soft})}(t) = (1.08 + 0.25t)$ [Do92], which leads to $\sigma_{\text{tot}}^{\gamma p} \propto (W^2)^{\alpha_P(t=0)-1} = (W^2)^{0.08}$. This Pomeron is usually referred to as *soft*



or *non-perturbative*. One of the surprising results from HERA was, that for virtual photon-proton scattering the Pomeron intercept $\alpha_p(t = 0)$ was found to increase with $Q^2$ and to be significantly larger than 1.08 [De96, Ai96] (*hard* or *perturbative* Pomeron) for $Q^2 > 1.0$ GeV$^2$, but to be approximately constant at 0.16 for $0.11 < Q^2 < 0.65$ GeV$^2$ [Su98]. One of the motivations for the analysis presented here is to further examine the transition from the hard to the soft Pomeron in the region of $Q^2$ below 1.0 GeV$^2$.

# Chapter 3

# HERA and DIS experiments

## 3.1 Deep Inelastic Scattering (DIS)

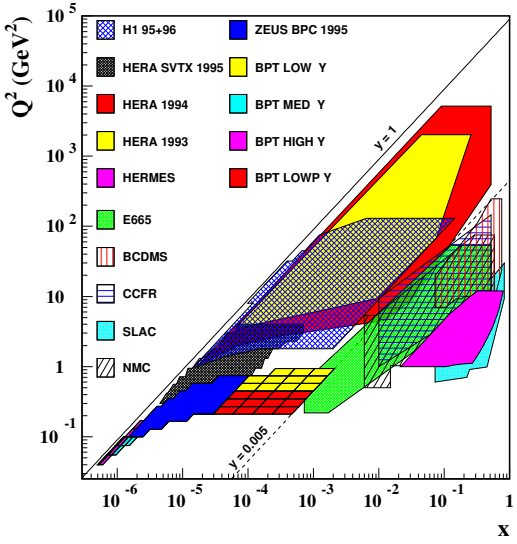


Figure 3.1: Kinematic coverage in the $(x - Q^2)$-plane for various fixed-target experiments and the HERA collider experiments H1 and ZEUS as of 1997 including the measurements presented here ('BPT').

Several experiments have contributed to the measurements of the proton and neutron structure functions in *Deep Inelastic Scattering* (DIS) of leptons off nucleons. With the start of data taking with the two experiments H1 and ZEUS at HERA, the kinematic region covered was





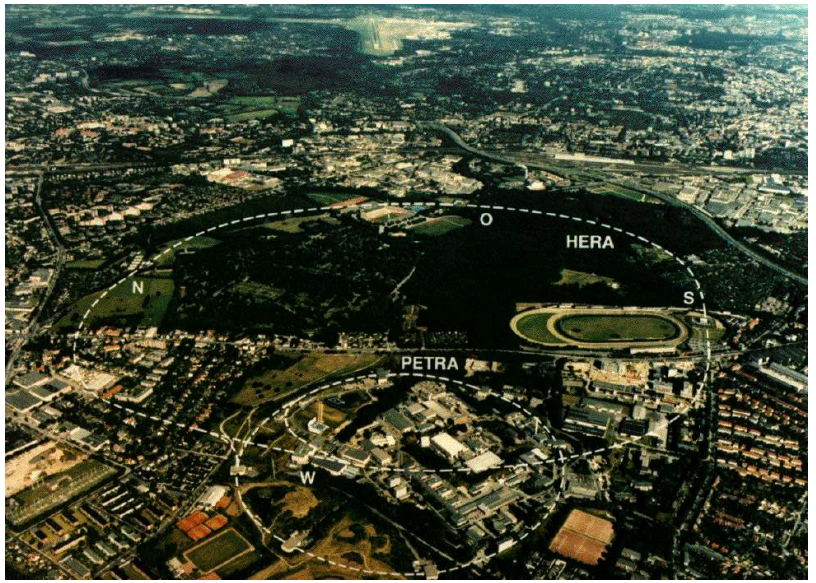


Figure 3.2: Aerial view of DESY and the surrounding area in Hamburg, Germany. The location of the accelerators PETRA (enclosing the DESY site) and HERA are highlighted.

significantly increased. Figure 3.1 shows the kinematic coverage of various experiments in the $(x - Q^2)$-plane up to 1997. The fixed-target experiments (BCDMS, CCFR, E665, NMC, SLAC) were conducted at CERN, FNAL, and SLAC. The SLAC experiments concentrated on structure function measurements using an electron beam of $(2.65 - 20.0)$ GeV on hydrogen and deuterium targets. BCDMS (Bologna, CERN, Dubna, Munich, Saclay) and NMC (New Muon Collaboration) used muon beams of $(90 - 280)$ GeV on liquid hydrogen targets. E665 at FNAL used $(400 - 500)$ GeV muons and liquid hydrogen and deuterium targets and CCFR scattered a neutrino beam of $30 < E_\nu < 600$ GeV on an iron target. The HERA experiments H1 and ZEUS were able to extend the accessible kinematic region by more than two orders of magnitude towards lower values of $x$ and higher values of $Q^2$. It was possible due to the higher center-of-mass energy at HERA ($\approx 300$ GeV$^2$). A further extension towards lower values in $Q^2$ and even lower values in $x$ was possible in 1995. This was done by shifting the interaction point in both experiments by about 70 cm. Measurements in the region of $Q^2$ below 1 GeV$^2$ were possible after the installation of a new component of the ZEUS detector, the BPC ('ZEUS BPC 1995' in figure 3.1). In the analysis presented here the kinematic acceptance of the BPC in 1995 was extended towards lower values of $Q^2$ and lower and higher values of $x$. It includes the 'ZEUS BPC 1995' region and the area labeled 'BPT 1997'. The extension was possible after the installation of another new component, the ZEUS BPT in 1997. Both the BPC and BPT are described in section 5.

Figure 3.3: The HERA accelerator complex. The left figure shows the layout of HERA. Four experiments are located in the experimental halls ('Experimentierhalle') South (ZEUS), West (HERA-B), North (H1), and East (HERMES). The right figure displays the system of DESY pre-accelerators used for HERA.

## 3.2 HERA design and experiments

The HERA collider is located at DESY in Hamburg, Germany. It offers unique opportunities to explore the structure of the proton as it is the only $ep$ collider in the world. Figure 3.2 shows an aerial view of DESY and the surrounding area including the location of the two largest accelerators HERA and PETRA. HERA was approved in 1984 and first collisions were observed in 1991. Operations for physics started in 1992. HERA consists of one storage ring for protons and one for electrons. The design energy is 30 GeV for electrons and 820 GeV for protons. Each storage ring consists of four 90° arcs connected by 360 m long straight sections and is located (10–25) m below ground. Superconducting magnets are used for the proton storage ring. Four experimental halls (North, South, East, West) are situated in the middle of the straight sections. The two collider experiments , H1 and ZEUS, are located in the southern and northern experimental halls respectively. In both interaction regions electrons and protons collide head-on at zero crossing angle. Two fixed-target experiments, HERMES and HERA-B, have been installed in the eastern and western experimental halls respectively. They make use of only the HERA electron (HERMES) and proton (HERA-B) beams respectively. HERMES [HE93] is investigating the spin structure of the nucleon and HERA-B [HB94] aims to study the $\mathcal{CP}$-violation in the $B^0\overline{B^0}$-system. Figure 3.3 (left) shows the layout of the HERA collider. The system of pre-accelerators used at DESY is shown in figure 3.3 (right). In the first step electrons and protons are accelerated using linear accelerators ('Electronen-Linac', 'Positronen-Linac', 'H$^-$-Linac'). A small storage ring PIA (Positron-Intensity-Accumulator) is used in between the linear accelerator and DESY II to accumulate electrons until sufficient intensity is reached. In the next step the particles are injected into DESY II (electrons) and DESY III (protons). After injection into PETRA and further acceleration electrons and protons are injected into HERA.
From 1995 to 1997 positrons were used instead of electrons because severe lifetime problems of the electron beam were observed. The reason is most likely the capturing of positively charged dust which originates from ion getter pumps from the HERA electron vacuum system by the electron beam [DESY94]. With the installation of new pumps in the winter shutdown 1997/1998 the problem has been significantly reduced and HERA switched back to electrons



| HERA parameters | Design Values | | Values of 1997 | |
|---|---|---|---|---|
| | $e^{\pm}$ | p | $e^+$ | p |
| Circumference (m) | 6336 | | | |
| Energy (GeV) | 30 | 820 | 27.6 | 821.2 |
| Center-of-mass energy (GeV) | 314 | | 301 | |
| Injection energy (GeV) | 14 | 40 | 12 | 40 |
| Energy loss per turn (MeV) | 127 | $1.4 \cdot 10^{-10}$ | 127 | $1.4 \cdot 10^{-10}$ |
| Current (mA) | 58 | 160 | 36 | 78 |
| Magnetic field (T) | 0.165 | 4.65 | 0.165 | 4.65 |
| Number of bunches | 210 | 210 | 174+15 | 174+6 |
| Bunch crossing time (ns) | 96 | | | |
| Horizontal beam size (mm) | 0.301 | 0.276 | 0.200 | 0.200 |
| Vertical beam size (mm) | 0.067 | 0.087 | 0.054 | 0.054 |
| Longitudinal beam size (mm) | 0.8 | 11 | 0.8 | 11 |
| Specific luminosity ($cm^{-2}s^{-1}mA^{-2}$) | $3.6 \cdot 10^{29}$ | | $5.0 \cdot 10^{29}$ | |
| Instantaneous luminosity ($cm^{-2}s^{-1}$) | $1.6 \cdot 10^{31}$ | | $1.45 \cdot 10^{31}$ | |
| Integrated luminosity per year ($pb^{-1}/a$) | 35 | | 36.5 | |

Table 3.1: HERA parameters. In 1997 HERA operated with 174 colliding bunches, 15 positron-pilot bunches and 6 proton-pilot bunches.

in 1998. Several HERA parameters from 1997 and the corresponding design values are given in table 3.1.

## 3.3 Structure function measurements at HERA

The measurements of the proton structure function $F_2$ at HERA cover a huge area in the $(x - Q^2)$-plane ranging from very low values of $Q^2$ in the order of $10^{-1}$ GeV$^2$ to very high values of $Q^2$ in the order of $10^4$ GeV$^2$. The specific region in the kinematic plane covered by a certain measurement determines which detector components and/or reconstruction methods have to be used. Figure 3.4 displays isolines for various primary measured quantities in the kinematic plane of HERA. The kinematic region of HERA is limited by the center-of-mass energy $s$ and the maximal possible value of $y = 1$. From equation 2.8 $Q^2$ and $x$ are in the case of $y = 1$ related by $Q^2 = sx$. For the low $Q^2$ region ($Q^2 \leq 1.0$ GeV$^2$, $x \leq E_e/E_P$) the energy of the scattered electron is below the electron beam energy and the scattering angle greater than 177°. In this region the lines of constant $y$ values are essentially parallel to lines of constant energy of the scattered electron. For $x = E_e/E_P$ the energy of the scattered electron is the same as the electron beam energy. This is referred to as the kinematic peak. The isolines of constant electron energy are closer together near the kinematic peak. Therefore, small errors in the energy measurements in this region can result in large errors in the reconstructed kinematic variables. The energy of the current jet is found to be smaller than the electron beam energy as well, but the angle of the current jet covers almost the whole range from 0 to 180 degrees.

## 3.4 Reconstruction of kinematic variables at HERA

In order to conduct any accurate measurement at HERA, a precise measurement of the Lorentz-invariant variables describing the kinematics is required. This section gives a description of

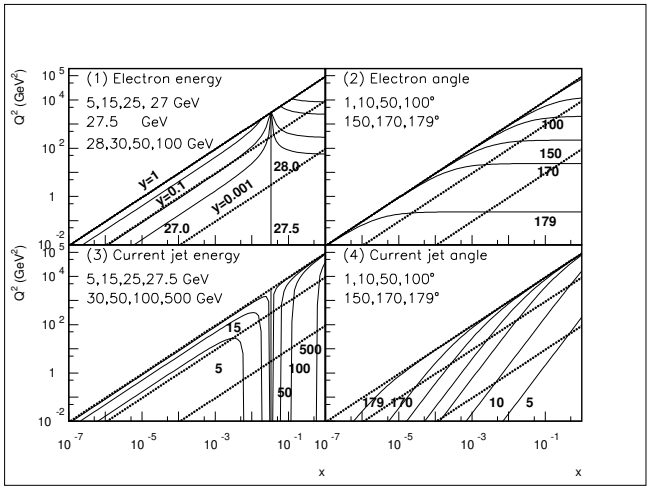


Figure 3.4: Isolines of the primary measured variables. The dashed lines represent lines of constant $y$ values (1, 0.1, 0.01). The electron beam energy amounts to 27.5 GeV whereas the proton beam energy is 820 GeV. Isolines of constant electron energy (1), electron scattering angle (2), current jet energies (3), and current jet angles (4) are displayed.

various reconstruction methods used in the measurement of $\sigma_{\rm tot}^{\gamma^* p}$ and $F_2$ at HERA. It concentrates on NC events and the region of low $Q^2$ covered by this analysis. The final state in first order for NC $ep$ scattering is shown in figure 3.5. It consists of the final state electron scattered under a polar angle $\theta_e^{'}$ with an energy $E_e^{'}$ and the hadronic final state system $X$. The latter one consists of two jets, the current jet under the angle $\gamma$, and the proton remnant jet close to the initial direction of the proton. In the QPM the current jet is associated to the fragmentation of the quark in the proton which took part in the interaction. The proton remnant jet originates from the fragmentation of the other partons. For the measurement of $\sigma_{\rm tot}^{\gamma^* p}$ and $F_2$ the relevant kinematic quantities are $x$, $y$, and $Q^2$. The hadronic system or the electron alone or any combination of them can be used to reconstruct the event kinematics. Each method has its own advantages and disadvantages depending on the position in the kinematic plane and the resolution of the experimental detectors used. A detailed analysis of the different reconstruction methods used at HERA is given in [Ba97a]. The coordinate system used by the ZEUS collaboration is a right-handed Cartesian one. It is discussed in section 4. In this coordinate system the four-vectors of the initial and final state of the process $e(k) + P(p) \rightarrow e(k^{'}) + X(p^{'})$ are given as follows:

$$k = \begin{pmatrix} E_e \\ 0 \\ 0 \\ -E_e \end{pmatrix} \quad k^{'} = \begin{pmatrix} E_e^{'} \\ E_e^{'} \sin\theta_e^{'} \cos\phi_e^{'} \\ E_e^{'} \sin\theta_e^{'} \sin\phi_e^{'} \\ E_e^{'} \cos\theta_e^{'} \end{pmatrix} \quad p = \begin{pmatrix} E_P \\ 0 \\ 0 \\ E_P \end{pmatrix} \quad p^{'} = \begin{pmatrix} \sum_h E_h \\ \sum_h p_{X,h} \\ \sum_h p_{Y,h} \\ \sum_h p_{Z,h} \end{pmatrix} \tag{3.1}$$



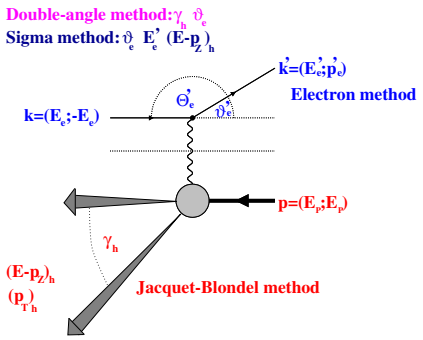


Figure 3.5: Schematics of the final state in neutral current $ep$ scattering. The final state consists of the scattered electron and the hadronic final state, which in first order is divided into the current and the proton remnant jet.

$E_e$, respectively $E_P$, is the energy of the initial state electron, respectively proton. $E_e^{'}$, $\theta_e^{'}$, and $\phi_e^{'}$ are the energy, polar angle, and azimuthal angle of the scattered electron. The hadronic final state system $X$ is described by the sum over all energy deposits in the final state as measured in the detector excluding the scattered electron. $\sum_h E_h$ and $(\sum_h p_{X,h}, \sum_h p_{Y,h}, \sum_h p_{Z,h})$ are the energy and momentum of the hadronic final state. The sum runs over all final state particles $h$ excluding the scattered electron. In the next sections several reconstruction methods are compared in terms of resolution of the kinematic quantities $x$, $y$, and $Q^2$.

### Electron method

The electron method uses only the final state electron to reconstruct the kinematics. It is applicable to NC events only. Using the four-vectors $k$ and $k^{'}$ of the initial and final state electron the kinematic variables $x$, $y$, and $Q^2$ in terms of $E_e^{'}$ and $\theta_e^{'}$ can be calculated as follows:

$$x_e = \frac{E_e^{'} \cos^2 \frac{\theta_e^{'}}{2}}{E_p(1 - \frac{E_e^{'}}{E_e} \sin^2 \frac{\theta_e^{'}}{2})} \tag{3.2}$$

$$y_e = 1 - \frac{E_e^{'}}{2E_e}(1 - \cos\theta_e^{'}) \tag{3.3}$$

$$Q_e^2 = 2E_e E_e^{'}(1 + \cos\theta_e^{'}) \tag{3.4}$$

The relative errors $\delta x_e$, $\delta y_e$, and $\delta Q_e^2$ of the kinematic variables are related to the errors $\delta E_e^{'}$ and $\delta\theta_e^{'}$ of the measured energy and polar angle of the final state electron:

$$\left(\frac{\delta x_e}{x_e}\right) = \left(\frac{1}{y_e}\right) \frac{\delta E_e^{'}}{E_e^{'}} \oplus \left[\frac{x_e}{E_e/E_P} - 1\right] \tan\left(\frac{\theta_e^{'}}{2}\right) \delta\theta_e^{'} \tag{3.5}$$

$$\left(\frac{\delta y_e}{y_e}\right) = \left(1 - \frac{1}{y_e}\right) \frac{\delta E_e^{'}}{E_e^{'}} \oplus \left(\frac{1}{y_e} - 1\right) \cot\left(\frac{\theta_e^{'}}{2}\right) \delta\theta_e^{'} \tag{3.6}$$

$$\left(\frac{\delta Q_e^2}{Q_e^2}\right) = \frac{\delta E_e^{'}}{E_e^{'}} \oplus \tan\left(\frac{\theta_e^{'}}{2}\right) \delta\theta_e^{'} \tag{3.7}$$

The resolution in $x_e$ and $y_e$ diverges for $y_e \to 0$. For high values of $y_e$ $\delta x_e$ and $\delta y_e$ are dominated by the relative error of the energy measurement $\delta E_e^{'}$. For a given detector with energy resolution $\delta E_e^{'}$ this leads to a lower bound in $y_e$ for the use of the electron method. The resolution in $Q_e^2$ at low $Q_e^2$ is dominated by $\delta\theta_e^{'}$. It diverges for $\theta_e^{'} \to 180°$. The use of the electron method to reconstruct $x$, $y$, and $Q^2$ at low $Q^2$ requires a precise energy and angular measurement. It cannot be used in the region of low $y$ as the resolution in $x_e$ and $y_e$ diverges for $y_e \to 0$.

### Jacquet-Blondel method

A method to reconstruct the kinematics using only the hadronic final state is the Jacquet-Blondel method [Ja79]. The transverse momentum $p_{T,h}^2 = (\sum_h p_{X,h})^2 + (\sum_h p_{Y,h})^2$ and the difference of the energy and the longitudinal momentum of the hadronic final state $\delta_h = (E - P_Z)_h = \sum_h (E_h - p_{Z,h})$ are used to reconstruct $x$, $y$, and $Q^2$. The method is insensitive to the loss of final state particles in the direction of the initial proton as these particles contribute essentially nothing to $\delta_h$ and the transverse momentum of the final state. It is also insensitive to the final state fragmentation process. Using the four-vectors $p$ and $p^{'}$ of the hadronic system from equation 3.1 the following expressions for the kinematic variables are obtained:

$$y_{\mathrm{JB}} = \frac{\delta_h}{2E_e} \tag{3.8}$$

$$Q^2_{\mathrm{JB}} = \frac{p_{T,h}^2}{1 - y_{\mathrm{JB}}} \tag{3.9}$$

$$x_{\mathrm{JB}} = \frac{Q^2_{\mathrm{JB}}}{s y_{\mathrm{JB}}} \tag{3.10}$$

The kinematics of the hadronic final state can be described by a massless object with energy $F$ and the polar angle $\gamma$ [Be91]. In QPM $F$ and $\gamma$ are associated with the energy and scattering angle of the struck quark in the proton and therefore to the energy and angle of the current jet.

$$F = \frac{p_{T,h}^2 + \delta_h^2}{2\delta_h} \tag{3.11}$$

$$\gamma = \arccos\left(\frac{p_{T,h}^2 - \delta_h^2}{p_{T,h}^2 + \delta_h^2}\right) \tag{3.12}$$

Equations 3.8 to 3.10 can be rewritten in terms of $F$ and $\gamma$ to determine the dependencies of the kinematic variables on the measured quantities $F$ and $\gamma$. The relative errors of $x$, $y$, and $Q^2$ are given as follows:

$$\left(\frac{\delta x_{\mathrm{JB}}}{x_{\mathrm{JB}}}\right) = \left(\frac{1}{1 - y_{\mathrm{JB}}}\right)\frac{\delta F}{F} \oplus \left[2\cot\gamma + \left(\frac{2y_{\mathrm{JB}} - 1}{1 - y_{\mathrm{JB}}}\right)\cot\left(\frac{\gamma}{2}\right)\right]\delta\gamma \tag{3.13}$$

$$\left(\frac{\delta y_{\mathrm{JB}}}{y_{\mathrm{JB}}}\right) = \frac{\delta F}{F} \oplus \cot\left(\frac{\gamma}{2}\right)\delta\gamma \tag{3.14}$$

$$\left(\frac{\delta Q^2_{\mathrm{JB}}}{Q^2_{\mathrm{JB}}}\right) = \left(\frac{2 - y_{\mathrm{JB}}}{1 - y_{\mathrm{JB}}}\right)\frac{\delta F}{F} \oplus \left[2\cot\gamma + \left(\frac{y_{\mathrm{JB}}}{1 - y_{\mathrm{JB}}}\right)\cot\left(\frac{\gamma}{2}\right)\right]\delta\gamma \tag{3.15}$$

For $\gamma \to 0°$ and $\gamma \to 180°$ the resolution of all three variables is dominated by the angular resolution. Therefore, a precise angular measurement of the hadronic final state at low $Q^2$ is necessary. At low values of $y$ the Jacquet-Blondel method is superior to the electron method as it is not divergent in $x$ or $y$ for $y \to 0$. It can therefore be used at lower values of $y$ if the angular resolution is sufficient. The resolution in $x_{\mathrm{JB}}$ and $Q^2_{\mathrm{JB}}$ diverges for $y_{\mathrm{JB}} \to 1$.



### Double Angle method

The Double Angle method reconstructs the kinematic variables using the angles $\theta_e^{'}$ and $\gamma$. The use of this method is restricted by the limited acceptance of a particular detector for $\theta_e^{'}(\gamma) \to 0°$ and $\theta_e^{'}(\gamma) \to 180°$.

$$y_{\mathrm{DA}} = \frac{\sin(\theta_e^{'})(1 - \cos(\gamma))}{\sin(\gamma) + \sin(\theta_e^{'}) - \sin(\gamma + \theta_e^{'})} \tag{3.16}$$

$$Q^2_{\mathrm{DA}} = 4E_e\frac{\sin(\gamma)(1 + \cos(\gamma))}{\sin(\gamma) + \sin(\theta_e^{'}) - \sin(\gamma + \theta_e^{'})} \tag{3.17}$$

$$x_{\mathrm{DA}} = \frac{E_e}{E_p}\frac{\sin(\gamma) + \sin(\theta_e^{'}) + \sin(\gamma + \theta_e^{'})}{\sin(\gamma) + \sin(\theta_e^{'}) - \sin(\gamma + \theta_e^{'})} \tag{3.18}$$

The relative errors of the kinematic variables are given by:

$$\left(\frac{\delta y_{\mathrm{DA}}}{y_{\mathrm{DA}}}\right) = -\left(\frac{1 - y_{\mathrm{DA}}}{\sin(\gamma)}\right)\delta\gamma \oplus \left(-\frac{1 - y_{\mathrm{DA}}}{\sin(\theta_e^{'})}\right)\delta\theta_e^{'} \tag{3.19}$$

$$\left(\frac{\delta Q^2_{\mathrm{DA}}}{Q^2_{\mathrm{DA}}}\right) = \left(\frac{-y_{\mathrm{DA}}}{\sin(\gamma)}\right)\delta\gamma \oplus \left(-\frac{1}{\sin(\theta_e^{'})} + \frac{y_{\mathrm{DA}}}{2\cos^2(\frac{\theta_e^{'}}{2})\tan(\frac{\gamma}{2})}\right)\delta\theta_e^{'} \tag{3.20}$$

$$\left(\frac{\delta x_{\mathrm{DA}}}{x_{\mathrm{DA}}}\right) = \left(-\frac{1}{\sin(\gamma)}\right)\delta\gamma \oplus \left(-\frac{y_{\mathrm{DA}}}{\sin(\theta_e^{'})} + \frac{y_{\mathrm{DA}}}{2\cos^2(\frac{\theta_e^{'}}{2})\tan(\frac{\gamma}{2})}\right)\delta\theta_e^{'} \tag{3.21}$$

The resolution of the Double Angle method for all variables degrades for very large and very small angles of $\theta_e^{'}$ and $\gamma$. At low $Q^2$, a good angular resolution is therefore necessary.

### $\Sigma$ and $e\Sigma$ method

The $\Sigma$ method uses the energy and angular information of the scattered electron and $\Sigma = \delta_h$ from the hadronic final state.

$$y_\Sigma = \frac{\Sigma}{\Sigma + E_e^{'}(1 - \cos\theta_e^{'})} \tag{3.22}$$

$$Q^2_\Sigma = \frac{(E_e^{'}\sin\theta_e^{'})^2}{1 - y_\Sigma} \tag{3.23}$$

$$x_\Sigma = \frac{Q^2_\Sigma}{s y_\Sigma} \tag{3.24}$$

$$\Sigma = \sum_h (E_h - P_{Z,h})$$

The error on the reconstructed kinematic variables in terms of $\delta E_e^{'}$, $\delta\theta_e^{'}$, and due to errors from the hadronic variables $\delta\Sigma$ is given by:

$$\left(\frac{\delta y_\Sigma}{y_\Sigma}\right) = (y_\Sigma - 1)\frac{\delta E_e^{'}}{E_e^{'}} \oplus \left(\frac{y_\Sigma - 1}{\tan(\frac{\theta_e^{'}}{2})}\right)\frac{\delta\theta_e^{'}}{\theta_e^{'}} \oplus (1 - y_\Sigma)\frac{\delta\Sigma}{\Sigma} \tag{3.25}$$

$$\left(\frac{\delta Q^2_\Sigma}{Q^2_\Sigma}\right) = (2 - y_\Sigma)\frac{\delta E_e^{'}}{E_e^{'}} \oplus \left(-\tan(\frac{\theta_e^{'}}{2}) + \frac{1 - y_\Sigma}{\tan(\frac{\theta_e^{'}}{2})}\right)\frac{\delta\theta_e^{'}}{\theta_e^{'}} \oplus y_\Sigma\frac{\delta\Sigma}{\Sigma} \tag{3.26}$$

$$\left(\frac{\delta x_\Sigma}{x_\Sigma}\right) = (3 - 2y_\Sigma)\frac{\delta E_e^{'}}{E_e^{'}} \oplus \left(-\tan(\frac{\theta_e^{'}}{2}) + \frac{2(1 - y_\Sigma)}{\tan(\frac{\theta_e^{'}}{2})}\right)\frac{\delta\theta_e^{'}}{\theta_e^{'}} \oplus (2y_\Sigma - 1)\frac{\delta\Sigma}{\Sigma} \tag{3.27}$$

Neither a divergence in $y$ for $y \to 0$ as in the electron method nor the one for $y \to 1$ as in the Jacquet-Blondel method are present. $\delta\theta'_e$ dominates the resolution in both $x$ and $Q^2$ for $\theta'_e \to 180°$. A modification of the $\Sigma$ method is to reconstruct $y$ using this method, but to reconstructed $Q^2$ from the electron method. $x$ can then be calculated using the relation between $x$, $y$, $Q^2$, and $s$ (equation 2.8). This is known as the $e\Sigma$ method. The advantages are that the divergence in $x$ and $y$ for $y \to 0$ are no longer present and that the good resolution in $Q^2$ from the electron method is used.

# Chapter 4

# The ZEUS detector at HERA

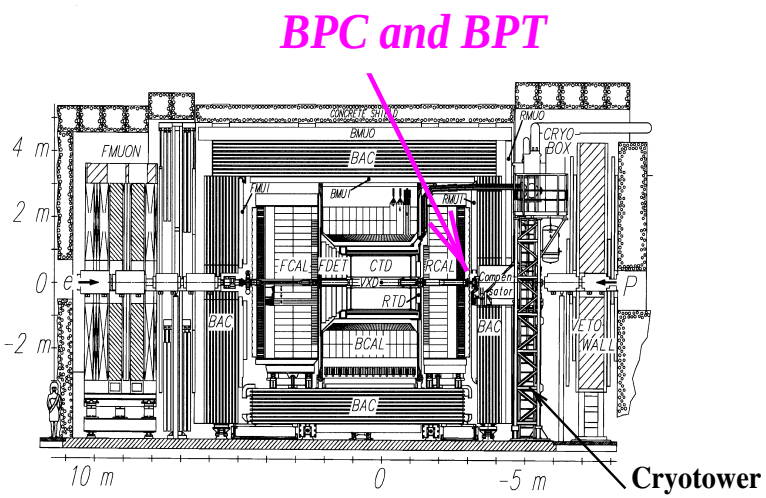


Figure 4.1: The main ZEUS detector along the beam direction. See text for a description of the components. BPC and BPT are described in the next chapter.

The chapter provides a brief overview of the ZEUS detector at HERA concentrating on the components used for the analysis presented in this thesis. The two components used for electron identification are discussed in the next chapter.
The ZEUS detector is a general purpose magnetic detector designed to study various aspects of electron-proton scattering. It has been in operation since 1992 [Ho93] and consists of various sub-components to measure the hadrons and leptons in the final-state and therefore characterize the $ep$ final-state in terms of energy, direction, and type of the produced particles.
The coordinate system of the ZEUS detector is a Cartesian right-handed coordinate system with its axis defined by the central tracking detector described below. The origin ($(X,Y,Z) = (0,0,0)$) is located at the nominal interaction point. The Z-axis points in the proton beam





Figure 4.2: The main ZEUS detector perpendicular to the beam direction. See text for a description of the components.

direction, the Y-axis upwards, and the X-axis horizontally towards the center of HERA. The polar (azimuthal) angle $\theta$ ($\phi$) is determined relative to the positive Z-axis (X-axis). With this definition the polar angle of the incoming electron beam is 180°, the one of the incoming proton beam 0°. The +Z-direction is defined as the *forward*, the –Z-direction as the *backward* direction. The ZEUS detector consists of the main detector located around the nominal interaction point and several small detectors positioned along the beam line in both positive and negative Z-direction, which are discussed in section 4.2 and 4.3. The main detector is shown in figure 4.1 and 4.2 along and perpendicular to the beam direction, respectively. The design is asymmetric with respect to the Z-axis because of the large forward-backward asymmetry of the $ep$ final-state system. The difference in the energy of the electron beam (27.5 GeV) and proton beam (820 GeV) results in a center-of-mass system which is moving in the direction of the proton beam relative to the lab-frame system.

## 4.1 The main detector

The inner part of the main detector consists of the tracking system enclosed by a superconducting solenoid which produces an axial magnetic field of 1.43 T. A vertex detector (VXD) was installed until 1995 directly around the beam pipe. Around the VXD, the CTD, a cylindrical drift chamber, surrounds the beam pipe at the interaction point. In order to provide additional means of track reconstruction in the forward (backward) direction, the CTD was supplemented by the FTD (RTD). The FTD consists of three sets of planar drift chambers with transition radiation detectors (TRD) in between. The RTD is one planar drift chamber with three layers.

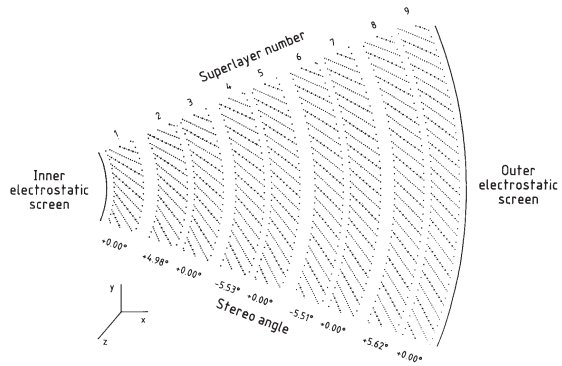


Figure 4.3: Layout of a CTD octant. Each octant has nine superlayers with the even numbered ones declined with respect to the beam axis ('Stereo angle').

The transfer line for the liquid helium used to cool the superconducting solenoid extends from the cryobox on top of the cryotower into the detector.
The high resolution uranium calorimeter (UCAL) encloses the tracking detectors. It is subdivided into the forward (FCAL), the barrel (BCAL), and the rear calorimeter (RCAL).
The UCAL in turn is surrounded by an iron yoke made of 7.3 cm thick iron plates. The yoke serves two purposes: it provides a return path for the solenoid magnetic field flux and is in addition instrumented with proportional chambers. The latter design feature makes it possible to measure energy leakage out of the UCAL. The yoke is therefore referred to as the backing calorimeter (BAC). As the yoke is magnetized to 1.6 T by copper coils it is used to deflect muons. In order to measure the momentum of the muons, limited streamer tubes are mounted inside and outside of the barrel (BMUI, BMUO) and the rear (RMUI, RMUO) iron yoke. As the particle density and the muon momentum in the forward direction is higher than in the barrel and rear direction due to the energy difference of the electron and proton beam, the muon chambers in the forward direction are designed differently. Limited streamer tubes mounted on the inside of the iron yoke (FMUI) and drift chambers and limited streamer tubes (FMUO) mounted outside the iron yoke are used for this purpose. Two iron toroids provide a toroidal magnetic field of 1.7 T. In the backward direction at Z = −7.3 m, a veto wall outside the detector composed of iron and scintillator strips is used to reject background events dominated by proton-beamgas reactions.
The BPC, a small electromagnetic sampling calorimeter, was installed in 1995 close to the beam pipe at Z = −2.94 m between RCAL and the compensator magnet. In 1997 it was supplemented by the BPT, which consists of two silicon microstrip detectors. These two components were used for the analysis presented in this thesis to detect electrons at small scattering angles which correspond to low values of $x$ and $Q^2$ and are described in more detail in chapter 5.

### 4.1.1 The Central Tracking Detector

The Central-Tracking Detector (CTD) [Fo93] is a cylindrical drift chamber. It provides a high-precision measurement of the direction and transverse momentum of charged particles and of



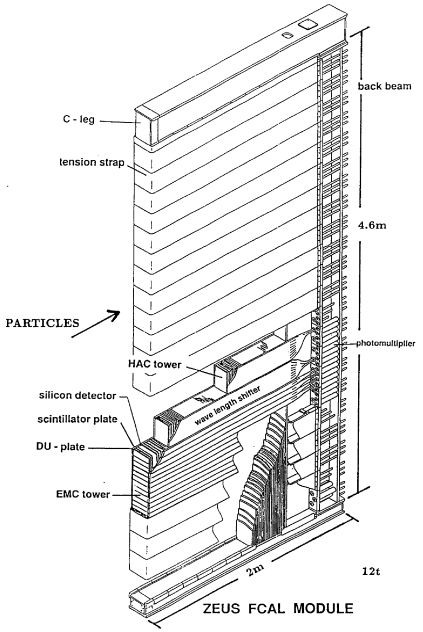


Figure 4.4: Layout of a FCAL module. The UCAL modules are subdivided into EMC and HAC sections, which in turn are divided into cells. A cell is read out on two opposite sides by one wavelength shifter each.

the event vertex. The position resolution in $r-\phi$ is about 230 $\mu$m and the transverse momentum resolution is $\frac{\sigma(p_t)}{p_t} = 0.005 \cdot p_p/(\mathrm{GeV/c}) \oplus 0.0016$. The position of the interaction point in X and Y is measured with a resolution of 0.1 cm and in Z with a resolution of 0.4 cm.
The CTD is filled with a mixture of argon, $CO_2$, and ethane. Particle identification is possible by measurements of the mean energy loss dE/dx of charged particles within the CTD. The CTD covers a polar angle of $15° < \theta < 164°$ and the full range of the azimuthal angle $\phi$. Its active volume has a length of 205 cm, an inner radius of 18.2 cm, and an outer radius of 79.4 cm. The CTD is designed as a multi-cell stereo superlayer chamber and subdivided into eight sections and nine superlayers. One octant is shown in figure 4.3. The CTD consists of 576 cells with each cell being equipped with eight sense wires. 24192 field wires are installed. The number of cells increases from 32 in the innermost superlayer to 96 cells for the outermost superlayer. Every other superlayer has its sense wires rotated by a certain angle with respect to the beam axis. The angles for each superlayer are given in figure 4.3.

### 4.1.2 The uranium calorimeter

The ZEUS calorimeter (UCAL) is a sampling calorimeter ($e/h = 1.00 \pm 0.02$). It is divided into three parts, which cover different polar angles [An91, De91, Be93]. All parts of the calorimeter,

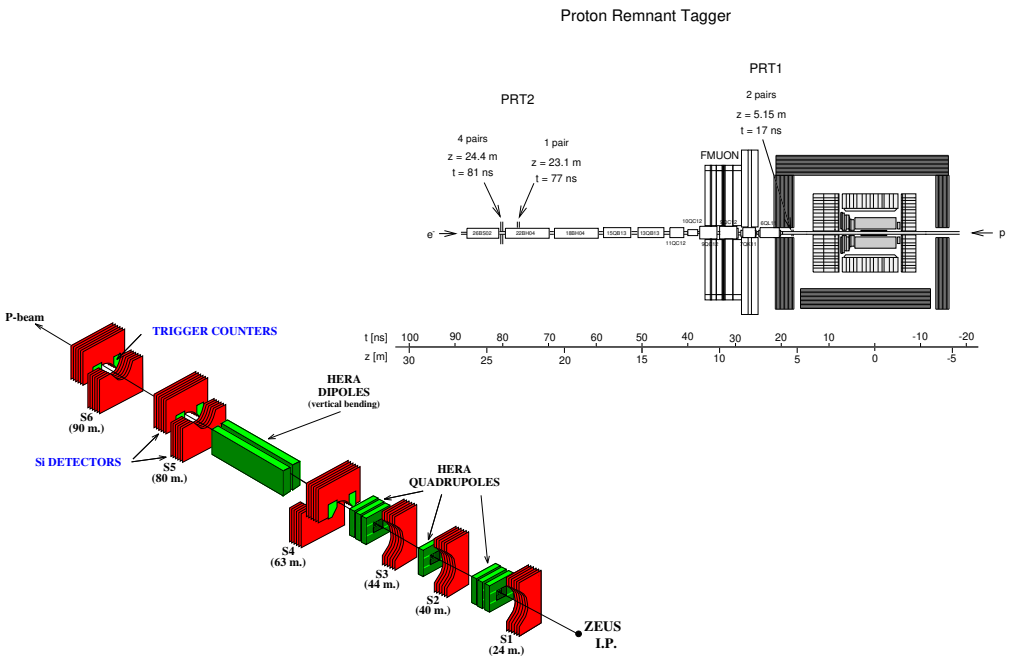


Figure 4.5: Location of ZEUS detectors in positive Z-direction. Shown are the different detectors from the PRT (upper plot) and LPS (lower plot). The FNC, located at Z = 105.6 m, is not shown.

FCAL ($2.2° < \theta < 39.9°$), BCAL ($36.7° < \theta < 128.1°$), and RCAL ($128.1° < \theta < 176.5°$) are built of alternating layers of 3.3 mm thick depleted uranium and 2.6 mm thick plastic scintillator plates (SCSN38). The natural radioactivity of $^{238}$U is used as a reference signal to calibrate the readout channels to a precision of $< 0.2\%$. The three calorimeter parts are subdivided into single modules. The modules are transversally separated into towers and the towers in turn longitudinally into electromagnetic (EMC) and hadronic sections (HAC1). The design of an FCAL module is shown in figure 4.4. FCAL and RCAL are planar and perpendicular with respect to the beam axis (see figure 4.1), while the BCAL modules are wedge-shaped and projective in the polar angle. The calorimeter modules are further segmented into cells. The design of the three calorimeter parts takes into account the different particle densities and energies due to the asymmetric electron and proton beam energies. Each EMC section is segmented transversally into four cells (two in RCAL), while the HAC sections are not divided transversally. They are instead longitudinally subdivided into two (one in RCAL) hadronic cells (HAC1, HAC2). Each cell is read out on two opposite sides. This is done on each side by a wavelength shifter coupled to one photomultiplier tube. The information of both photomultiplier tubes is used to provide a limited reconstruction of the position of the measured particle and to check the uniformity of the readout. The energy resolution for hadrons (electrons) was determined in testbeam experiments to be $\sigma_E/E = 0.35/\sqrt{E/\mathrm{GeV}}$



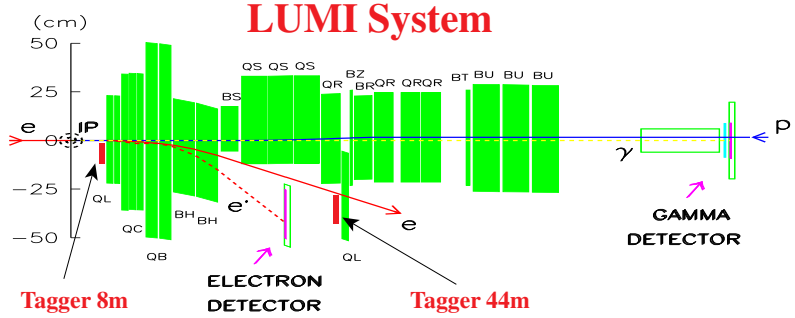


Figure 4.6: Location of ZEUS detectors in negative Z-direction. Shown are the gamma (LUMIG) and electron detectors (LUMIE) used for the ZEUS luminosity measurement together with the electron taggers at Z = −44 m and Z = −8 m.

($\sigma_E/E = 0.18/\sqrt{E/\mathrm{GeV}}$)

## 4.2 Proton and neutron detectors

In the forward (+Z)-direction, several detectors have been installed close to the beam pipe to obtain information about the hadronic final state as shown in figure 4.5. The proton remnant tagger (PRT) and the leading proton spectrometer (LPS) are used to examine the final state proton in the extreme forward direction. The PRT consists of three groups of lead/scintillator counters located at Z = 5.15 m, Z = 23.1 m, and Z = 24.4 m. The LPS is located very close to the beam at $Z = (24 - 90)$ m and consists of six stations of silicon strip detectors. Neutrons produced in the very forward direction are detected by the forward neutron calorimeter (FNC). This lead/scintillator sandwich calorimeter is installed at $Z = 105.6$ m.

## 4.3 The luminosity detector and electron taggers

Figure 4.6 shows the layout of the HERA magnet system and the ZEUS luminosity detectors and electron taggers in the backward (–Z)-direction. A precise determination of the luminosity is essential for any cross section measurement in a high energy physics experiment. The luminosity of $ep$-collisions at HERA is measured by observing the rate of hard bremsstrahlung photons from the Bethe-Heitler process $ep \to e\gamma p$ [Be34]. As the theoretical cross section is known to an accuracy of 0.5% from QED, a precise measurement of the photon rate permits a precise determination of the $ep$-luminosity at HERA. In the case of ZEUS this is done by two lead/scintillator electromagnetic calorimeters at Z = −34 m (LUMIE) and Z = −107 m (LUMIG). Photons with $\theta_\gamma < 0.5$ mrad originating from the Bethe-Heitler process $ep \to e\gamma p$ are detected by the LUMIG detector [An92, Pi93]. A Cu-Be window was installed in the beam pipe at Z = −92 m in order to limit the amount of inactive material. The energy resolution of the LUMIG detector was measured under test-beam conditions to be $18\%/\sqrt{E}$. It was also determined that the carbon/lead filter placed in front of the detector to shield it against

synchrotron radiation reduces the resolution to $23\%/\sqrt{E}$. The impact position of incoming photons can be determined with a resolution of 0.2 cm in $X$ and $Y$, because at a depth of $7X_0$ 1 cm wide scintillator strips are installed within the LUMIG detector. The LUMIG detector is also used to determine the electron beam tilt (see section 8.2) and to measure photons from initial-state-radiation (see section 10.3.3).
The LUMIE calorimeter [An92, Pi93] at Z = −35 m detects electrons in the limited energy range from 7 to 20 GeV, which are produced under polar angles less than 5 mrad with respect to the electron beam direction. These electrons are deflected by the HERA magnet system and leave the beam pipe at Z = −27 m through an exit window similar to the one in front of the LUMIG detector. The LUMIE detector has an energy resolution of $18\%/\sqrt{E}$ under test-beam conditions. It was initially designed to measure the electrons of the Bethe-Heitler process $ep \to e\gamma p$ at the same time as the photons of this process are measured in the LUMIG detector. It was found that this was not necessary to have a precise measurement of the luminosity. In the analysis presented here it is used to tag events in a limited kinematic range of $0.2 < y < 0.6$ and $Q^2 < 0.01\,\mathrm{GeV}^2$ (photoproduction events) by measuring the scattered electron (see section 9.7). Taggers at Z = −8 m and Z = −44 m have been installed to identify electrons scattered at small angles.

## 4.4 The ZEUS trigger and data acquisition system

The three-level trigger system used by ZEUS was designed to separate the $ep$ physics events from background and to reduce the event rate to an acceptable level. The background is dominated by interactions of the proton beam with the residual gas in the beam pipe with a rate on the order of $(10-100)$ kHz. Other background sources include beam halo interactions, electron beam gas interactions, and cosmic ray events. The separation of background and signal events cannot be completed within the HERA bunch spacing time of 96 ns. A schematic of the ZEUS trigger system is shown in the left plot in figure 4.7. Each ZEUS component has its own first (FLT) and second level trigger (SLT). At the third level trigger (TLT) the combined information of all subcomponents is available. The input rate is reduced to below 1 kHz after the FLT, 100 Hz after the SLT, and to a few Hz after the TLT. The component readout and FLT systems are pipelined using 10.4 MHz pipelines to avoid dead time. The component FLT each analyze a particular event within 25 clock cycles and the result is transferred to the Global-First-Level-Trigger (GFLT). Logical combinations among its input are used to determine the GFLT decision, which takes about 20 bunch crossings. If an event is accepted by the GFLT, the data stored in the pipeline is transferred to the components SLT, where it is stored in memory buffers. The component SLTs are based on a network of programmable transputers. More sophisticated algorithms than those used in the FLT identify and reject background events. The result of the local SLTs are combined in the global second level trigger (GSLT) [Ui92] to execute a final decision. If the event is also accepted by the GSLT, the information from all components is transferred to the EVENTBUILDER, which combines all the data to be accessible by the third level trigger (TLT), which consists of a processor farm of Silicon Graphics CPUs. The data is formatted in the ADAMO format [Gr89] which is used at the TLT and in the offline reconstruction and analysis.
The HERA beam conditions directly influence the event rate of the different triggers. High luminosity results in a high trigger rate. The trigger rate can also increase due to high background. Each different trigger slot is affected differently. The total trigger rate has to be limited because the amount of events that can be written to tape in each HERA running period is limited, and to avoid deadtime. To have control of the rate for each FLT, SLT, and TLT trigger



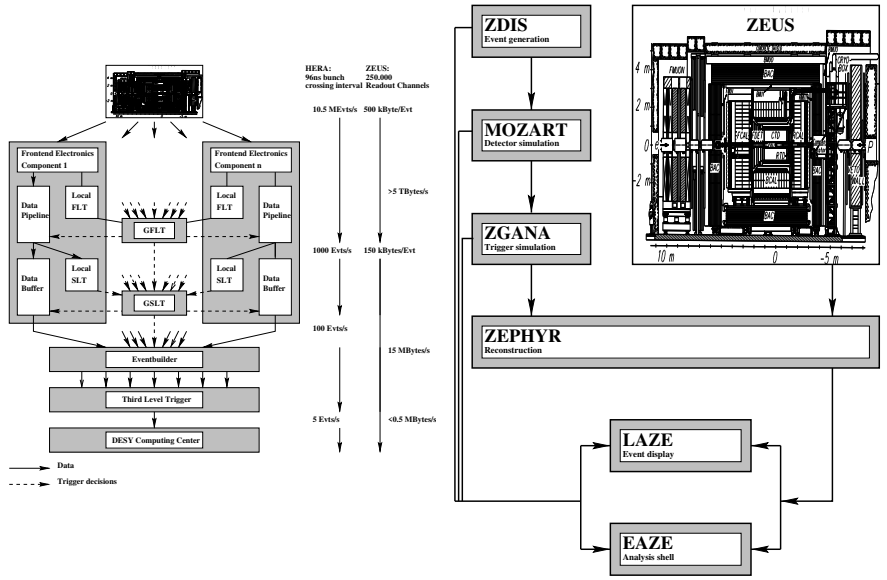


Figure 4.7: Schematic diagram of the ZEUS trigger and data acquisition system (left) and interrelationship of the ZEUS offline and Monte Carlo (MC) programs (right).

slot $j$, a prescale factor $p_j$ is assigned to the slot. Only each $p_j$th event accepted by the trigger slot $j$ is used. Typical values for $p_j$ are in the range between 1 and 9999, where a value of 1 corresponds to no rate reduction for the trigger slot. A value of 9999 corresponds to the trigger being turned off. Typically several sets of trigger versions with prescale factors for all trigger slots are available. Depending on the HERA beam conditions one of these sets is chosen for data taking. In 1997 two sets were used for low and high luminosity. From time to time single trigger slots and prescale factors are changed to collect specific data sets for example for calibration or commissioning of ZEUS components (see section 5.5). After the TLT, the amount of data to be stored is less than 0.5 MBytes/s. The ZEUS data taking is divided into different runs, where each run corresponds to a certain trigger configuration and status of the ZEUS subcomponents. The number of events varies from a few hundred to several hundred thousand per run. A typical run contains thirty to eighty thousand events.

## 4.5 Event reconstruction and analysis

The scheme of the ZEUS offline and Monte Carlo (MC) programs is shown in the right plot in figure 4.7. Events from the real detector or simulated MC events are reconstructed by the program ZEPHYR. The user has access to the raw and reconstructed quantities via the program

EAZE. In the framework of EAZE, the user writes his own analysis program in either Fortran or C. It is used to reconstruct relevant quantities and perform selection cuts. Subsets of the data or MC events can be saved for further analysis. The program LAZE is an event display program which allows one to view graphically various aspects of an event including e.g. the tracks of charged particles in the CTD, energy depositions in the CAL, and other component-related quantities. To allow fast access to specific types of events during reconstruction each event is checked whether it meets one of the conditions designed by the ZEUS analysis groups. If a specific condition is met, a flag called a DSTBIT is set. Before analyzing detailed component information in the user's EAZE program, the events can be preselected by requiring certain DSTBITS. This allows a faster loop over the whole data sets since only those events are processed further. In most cases the DSTBITs correspond to certain TLT slots.
MC events are generated using the program ZDIS which contains a shell environment to steer a number of MC generator programs. The output data is stored in the same (ADAMO) format as the data from the real detector and passed to the ZEUS detector simulation program MOZART. MOZART is based on the CERN GEANT program [Br89]. A simulation of the ZEUS trigger chain is done by the program ZGANA. Interfaces between the programs used for MC generation and the programs EAZE and LAZE provide specific MC information such as generated kinematic quantities, vertices, and particles to the user. An overview of the physics analysis environment of the ZEUS experiment can be found in [Ba95].

# Chapter 5

# The Beam Pipe Calorimeter and Beam Pipe Tracker

The Beam Pipe Calorimeter (BPC) and the Beam Pipe Tracker (BPT) were installed in the main ZEUS detector in 1995 and 1997 respectively. They are located close to the beam pipe at approximately Z = −2.5 m to Z = −3.2 m between the RCAL and the compensator as shown in figure 4.1. They are used to detect electrons at very small scattering angles, which correspond to the low $Q^2$ and very low $x$ region in the kinematic plane at $x$ smaller than $10^{-3}$ and $Q^2$ smaller than 1 GeV$^2$. This chapter provides an overview of the design of both detectors.

## 5.1 BPC design

The BPC consists of two modules, located at Z = −293.7 cm on the right and left side of the beam pipe. Both modules are segmented tungsten-scintillator calorimeters. They are designed

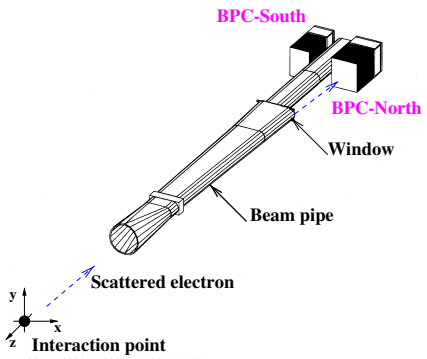


Figure 5.1: Location of the two BPC modules with respect to the beam pipe and the interaction point.





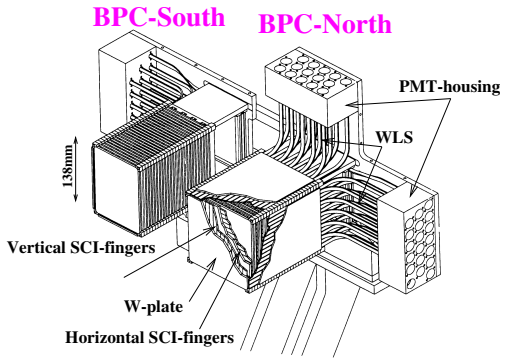


Figure 5.2: CAD drawing of the two BPC modules including the wavelength shifters (WLS) and the housings for the photomultipliers (PMT).

to detect electrons scattered at angles of less than 40 mrad with respect to the initial direction of the electron beam. The two modules are labeled **BPC North** and **BPC South**. The names refer to their location relative to the beam pipe. Figure 5.1 shows the location of the two modules with respect to the beam pipe and the interaction point. The beam pipe was modified to include two exit windows at Z = −249.8 cm. The exit windows are made of 1.5 mm thick aluminium which corresponds 0.016 $X_0$. This allows electrons to exit the beam pipe with minimal interference. The outer edges in X and the dimensions of the exit windows in Y are restricted by the surrounding RCAL modules. The positions of the inner edges in X were chosen to prevent direct or backscattered synchrotron radiation to hit the beam pipe. The transverse sizes of the exit windows determine the actual fiducial volume for the BPC modules which is substantially smaller in the case of the BPC South module.
The dimensions of the two BPC modules are restricted by the surrounding RCAL modules. This results in both modules having the same dimensions in Y (13.0 cm) and Z (16.0 cm) but different sizes in X (BPC South 9.8 cm, BPC North 13.8 cm). Each module is mounted on a support structure located below the compensator magnet. The two modules are connected by two metal spacer bars below and two spacer bars above the beam pipe. The distance between the two modules is fixed to be 12.31 cm by the length of the spacers which were manufactured with a precision of 0.1 mm. The design of the two modules is shown in figure 5.2. The modules consist of alternating layers of tungsten alloy plates and scintillator layers. The layers are labeled A, B, .., X, Y, Z starting from the first scintillator layer which faces the interaction point. The 26 passive layers are made of 3.5 mm tungsten alloy plates (DENSIMET D18K) [Pl94] with a density of 18 gcm$^{-3}$ and a radiation length of 3.87 mm. The total radiation length of the passive layers amounts to 24 $X_0$. This provides sufficient longitudinal shower containment for electrons up to the expected maximum energy of 27.5 GeV. Each of the 26 active layers consist of 2.6 mm thick scintillator (SCSN38) [Ka83] of the same material used for the ZEUS UCAL [Ho93]. The scintillator layers are subdivided into 7.9 mm wide scintillator fingers. The orientation of the fingers alternates from layer to layer between the X- and Y-direction as shown in figure 5.2. The chosen width of 7.9 mm represents a compromise between optimizing the position resolution and

| BPC specification | BPC performance |
|---|---|
| Depth | $\simeq 24\,X_0$ (1) |
| Molière radius | $\simeq 13\,$mm (1) |
| Energy resolution | $17\%/\sqrt{E}$ (stochastic term)(2) |
| Energy scale calibration | $\pm 0.3\%$ (3) |
| Energy uniformity | $\pm 0.3\%$ (3) |
| Linearity | $\leq 1\%$ (2)<br>$\leq 1.25\%$ at 3 GeV (3) |
| Position resolution | $\approx 0.22\,\mathrm{cm}/\sqrt{E/\mathrm{GeV}}$ (3) |
| Intrinsic position bias | $< 0.3\,$mm (3) |
| Alignment accuracy | $\pm 0.2\,$mm (3) |
| Time resolution | $< 1\,$ns (1) |
| (1) as determined from design<br>(2) as determined from test beam measurements<br>(3) as determined from 1997 BPC and BPT data | |

Table 5.1: BPC performance specifications.

limitations due to the size of various readout elements. Vertically-oriented scintillators allow reconstruction of the impact position in X, horizontally-oriented ones in Y. Each scintillator finger is optically decoupled from its neighbours and is read out from one side by a 7 mm wide and 2 mm thick wavelength shifting (WLS) bars of 30 ppm Y7 in PMMA. The other side of each scintillator finger is aluminized to provide an efficient end reflector. Scintillator fingers which are oriented behind each other in longitudinal direction are read out together by a WLS bar representing one readout channel (see figure 5.2). Therefore, no longitudinal measurement of the shower profile is possible. The readout channels are labeled as follows: The first letter indicates the BPC module (**N**orth or **S**outh) and the second one the orientation of the finger either horizontal (**Y**) or vertical (**X**). The X (vertical) readout channels are counted in the direction away from the beam pipe and the Y (horizontal) ones from bottom to top. BPC South has only 11 X channels due to its smaller dimension in X.

$$NX1(\text{closest to beam pipe}) \ldots NX15 \quad \text{and} \quad NY1(\text{bottom}) \ldots NY16(\text{top}) \tag{5.1}$$

$$SX1(\text{closest to beam pipe}) \ldots SX11 \quad \text{and} \quad SY1(\text{bottom}) \ldots SY16(\text{top}) \tag{5.2}$$

Miniature Hamamatsu R5600-03 photomultipliers (PMTs) [Ha94] are used. They are placed inside a PMT housing made of ARMCO magnetic iron block ($\mu \approx 1000$ for $B = 800\,G$) [Ar95] to provide in addition an effective magnetic shielding. It was chosen to move the PMTs farther away from the beam pipe because both the magnetic field and the radiation background were found to be increasing towards the beam pipe. In order to do so, all WLS bars were bent by $90^0$ with a radius of 30 mm away from the calorimeter as can be seen in figure 5.2. Each of the two BPC modules has a single scintillator tile ('backtile') installed between the tungsten layer Z and the back plate. These 5 mm thick tiles are surrounded by 2 mm thick lead plates and are read out from two sides by WLS bars which in turn are read out using the same PMTs as the other BPC channels. The scintillator tiles are designed to be used to reject hadrons showering in the BPC and background from proton beam gas interactions outside the detector. A list of BPC specifications and performance parameters as determined from the design, test beam data, and the analysis presented here is given in table 5.1. Detailed information about the



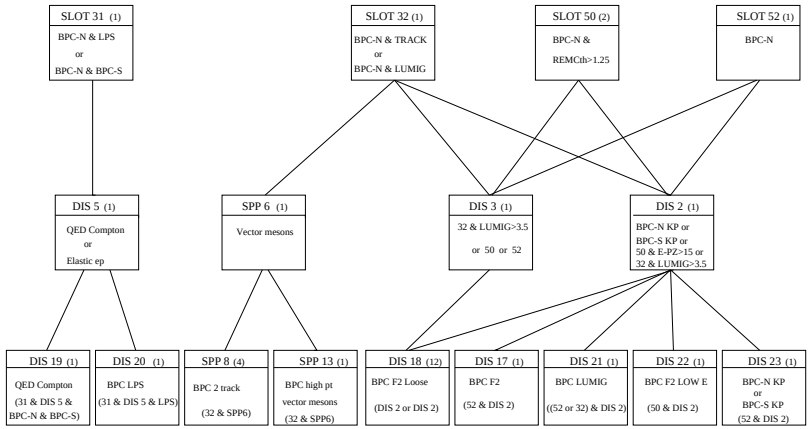


Figure 5.3: BPC trigger configuration in 1997. The FLT trigger slots are shown at the top, the SLT slots in the middle, and the TLT slots at the bottom. Several triggers not used in this analysis have been omitted. The lines indicate the relationship between the different trigger slots. The number in parenthesis after the slot name indicates the prescale factor used for most of the 1997 HERA running period. For the TLT slots a short description of the requirements is given in parenthesis.

design, assembly, and test beam measurements of the BPC is given in [Mo98] and [Su98]. Since the BPC modules are located very close to the beam pipe, they are exposed to radiation from synchrotron radiation and electron beam dumps. Radiation damage of the scintillator fingers is expected to increase the non-linearity and non-uniformity of the BPC energy and to change the energy scale of the BPC with time. To monitor the radiation dose, tubes filled with TLD (Thermo-luminescence dosimetry) crystals (Harshaw TLD-700) were placed on the face of the BPC modules facing the interaction point. The crystals were exchanged on a regular basis and analyzed by measuring the glow curve of exposed TLD crystals. These measurements were used to estimate the non-linearity of the BPC in 1995 [Bo96] and also of the BPC in 1997 (see section 6). Monitoring of the dark current of silicon diodes located at approximately the same position as the TLDs has lead to the conclusion that the main contribution to the radiation dose results from electron beam dumps and losses of the electron beam [Su98].

## 5.2 BPC readout and trigger

The BPC has been incorporated in the ZEUS trigger and readout chain as described in section 4.4 as a subcomponent of the main calorimeter (UCAL). The BPC front-end electronics is mounted inside the ZEUS cryotower [Ho93]. Pulses from the BPC PMTs are sent on 5 m coaxial cables to the trigger summing cards which split off a charge of approximately 10% for each of the BPC PMT pulses to be used for the BPC first-level trigger. The remaining charge is sent to the BPC analog cards, where one card integrates and shapes up to twelve PMT signals, samples the shaped signal at a rate of 96 ns, and stores the samples in a 5 $\mu$s deep analog pipeline. Following a positive trigger decision from the GFLT, the samples for the event are

transferred to a one-event buffer which stores up to eight samples from a pipeline. The samples are then multiplexed to the digital cards. For each PMS signal eight samples are available to reconstruct energy and time for the particular BPC channel. This is done by **D**igital **S**ignal **P**rocessors (DSPs) on the digital cards as described in [An91].
The reconstructed energy response is converted into GeV by means of a conversion factor. The factor was found to be 1660.0 ADC units per GeV in 1995 and 1875.0 ADC units per GeV from 1996 onwards after a change in the DSP code. The factor is fixed for all readout channels and during the whole data taking. The resulting reconstructed energy can be considered only a first approximation of the true energy since changes in the readout chain effect the output of the ADC stage. Possible reasons for these changes are for example radiation damage of scintillators or changes of the gain of PMTs. A final calibration of the BPC energy is therefore required as discussed in section 6.10.2. The analog and digital cards of the BPC are identical to those used for the ZEUS UCAL [Ca93].
The stability of the readout is checked by daily test triggers. LED and laser light injected into the PMTs are used to monitor their stability. Pedestal test triggers and charge injection into the analog cards provide additional means to check the readout chain. A full electronic calibration is done once a week. The stability of the readout electronics was found to be within 0.1% [Ho93].
The BPC triggers were designed to select events with $ep$ collisions and a final state electron detected by the BPC. Since the BPC is located very close to the beam pipe the background is significantly higher than for other triggers and has to be reduced at an early stage of the trigger chain. Several triggers are used to select different classes of events and to have more flexibility to control the rate as the cross section for inelastic $ep$ scattering increases significantly with $Q^2 \to 0$.
The BPC first-level trigger uses energy and timing information based on sums of BPC readout channels. The analog sums are formed among the BPC readout channels and are a first approximation of the fiducial area of the BPC modules due to the restricted size of the beam pipe windows (see section 6.11). The following analog sum signals are provided for the North (South) module:

- Vertical sum: $NV = \sum_{i=1}^{10} NX_i$
  (BPC South: $SV = \sum_{i=1}^{6} SX_i$)
- Horizontal sum: $NH = \sum_{i=3}^{14} NY_i$
  (BPC South: $SH = \sum_{i=3}^{14} SY_i$)
- Outer sum: $NO = \sum_{i=11}^{15} NX_i + NY_1 + NY_2 + NY_{15} + NY_{16}$
  (BPC South: $SO = \sum_{i=7}^{11} SX_i + SY_1 + SY_2 + SY_{15} + SY_{16}$)
- Inner sum: $NI = NX_1$
  (BPC South: $SI = SX_1$)
- Backtile sum: $NB = \sum_{i=1}^{2} NB_i$
  (BPC South: $SB = \sum_{i=1}^{2} SB_i$)

In the case of the BPC North module, the energy information for the GFLT is derived using a 4-bit FADC (**F**lash **A**nalog-to-**D**igital **C**onverter) which allows four analog input signals to be digitized into a 4-bit digital word at a frequency of up to 100 MHz and a sampling time as short as 4 ns. The fast conversion process is necessary to be able to use the BPC at the ZEUS first-level trigger. Since the BPC South module is not explicitly used for any physics



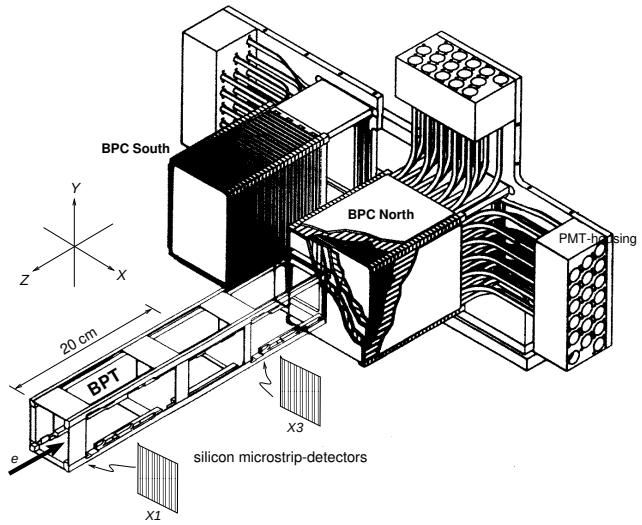


Figure 5.4: BPT attached to the BPC North module. Shown is the BPT as used in 1997 with two planes of silicon microstrip detectors (X1 and X3) [Mo98a].

analysis, only lower and upper thresholds are needed for the BPC energy information at the first-level trigger. Therefore, a discriminator is used to check the BPC South sum signals and the BPC North and South backtile sum signals. All digitized signals are sent to the GFLT to be used in various FLT applications. The timing information for both BPC modules are derived using conventional LeCroy discriminators whose respective logic output signals are fed into 4-bit TDCs (**T**ime-to-**D**igital **C**onverter) with a 5 ns step at the GFLT.
Several second and third-level trigger slots include BPC information. At these trigger levels, a modified version of the BPC reconstruction code provides more detailed information than is available at the first-level trigger. This includes the reconstructed energy, position, and shower size for both BPC modules. Figure 5.3 shows the BPC trigger configuration for 1997. A more detailed description of the trigger slots used in this analysis is given in section 9.

## 5.3 BPT design

The Beam Pipe Tracker (BPT) was designed to supplement the BPC which was described in the last two sections or a new BPC composed of a matrix of lead tungstate ($PbWO_4$) crystals [Ca96] [Me99] [Ge99]. As a tracking system independent from the ZEUS central tracking chambers, it is designed to provide an independent Z-vertex reconstruction, reduce photoproduction background, and increase the position resolution compared to that of the BPC. The

BPT is designed to include five silicon microstrip detectors mounted orthogonal to the Z-axis between BPC North and the corresponding beam pipe exit window. Each detector adds 0.32% of a radiation length $X_0$ of inactive material between interaction point and BPC. The three (two) detectors are oriented in such a way as to determine the X-(Y-)coordinates of the tracks intersecting them. The support structure has dimensions of $X \times Y \times Z = 6.3 \times 7.0 \times 41.0$ cm$^3$ and is covered in metal and plastic foils in order to isolate it optically and electromagnetically. In July 1997 the first two microstrip detectors were mounted inside a carbon-fibre structure, which in turn was attached via a special flange to the front face of the BPC as depicted in figure 5.4. Carbon-fibre is used because it is robust and adds little inactive material in front of the BPC. By construction, the relative alignment of the silicon detectors is known within 50 $\mu$m. The two detectors have strips oriented along the Y-axis and are used to reconstruct the X-coordinate of intersecting tracks. Due to the location of the BPC the resolution in $\theta$ is dominated by the resolution in X. The BPT as installed in 1997 was expected to increase the resolution in $\theta$ and therefore in $Q^2$. After a few weeks of commissioning (see section 5.5) data taking started in early September 1997.
The BPT microstrip detectors are single-sided and consist of N-type silicon. Each detector has an active area of 5.76 $\times$ 5.76 cm$^2$ and is (300$\pm$15) $\mu$m thick. The active area consists of 576 implanted $p^+$ strips with a pitch of p = 100 $\mu$m. The expected spatial resolution is given by $\sigma = p/\sqrt{12} \approx 30$ $\mu$m. The strips are numbered from 0 to 575 starting from the strip closest to the beam pipe in the case of the vertical strips and from the one at the bottom in the case of horizontal strips. The strips are AC-coupled to the readout electronics to suppress signal shifts due to the dark current, which increases if the detectors are exposed to radiation. This is done by a layer of silicon oxide between the $p^+$ implantation and the aluminium readout strips. A guard ring is used to bias the detector through the punch-through effect.
The front-end electronics is rotated by 90° with respect to the silicon detectors. It is mounted inside the carbon-fibre support structure on multi-layer Printed Circuit Board (PCB), which serve as mechanical support and distribute power and signal lines. Cooling is provided by a copper pipe of 1 mm$^2$ circulating water of 20 °C. 50 $\mu$m thick fanout cables of upilex substrate are used to connect the front-end electronics to the detector strips. Electroplated copper strips covered by a thin layer of gold are used to provide good electrical contact. An overview of the BPT specifications is given in table 5.2.
It was necessary to remove the metal tube including the TLDs and the silicon diodes in front of the BPC North, in order to connect the BPT support structure to this BPC module: both devices have been moved inside the carbon-fibre structure.

## 5.4 BPT readout and trigger

The BPT readout is of the binary type. If the pulse height of a given readout channel exceeds the threshold, this channel is marked as hit. The strip and detector identifiers of each hit channel are stored. The front-end electronics and readout of the BPT is identical to that used by the ZEUS LPS [La93] [Co96], which was briefly described in section 4.2. The BPT has been included in the readout and calibration scheme of the LPS [Mo98a]. 64 BPT channels are read out by the same chain of two readout chips. Due to space constraints, only eight pairs of chips could be mounted for each detector. The 128 silicon strips of each detector far away from the beam pipe were connected to a pair of chips in groups of two, which reduces the number of readout channels to 512. The readout channels are numbered from 0 to 511 for each plane. The analog amplifier and comparator chip (TEKZ) is connected to the silicon strips. For each channel a charge amplifier is followed by a comparator, whose threshold can be set externally. A



| Topic | Specification |
|---|---|
| Size (Height $\times$ Width $\times$ Depth) | (6 $\times$ 6 $\times$ 0.03) cm$^3$ |
| Bulk material | N type high purity silicon |
| Resistivity | (8–10) kOhm$\times$cm |
| Thickness | (300 $\pm$15) $\mu$m |
| Full depletion (FD) voltage | 30 V typically |
| Active area | (58 $\times$ 58) mm |
| N. of channels | 576 |
| Element pitch | 100 $\mu$m |
| Element width | 80 $\mu$m |
| Readout | AC |
| Guard ring | included |
| Metalization (Al) | (8000 $\pm$ 1000) A° |
| Oxide edge width | 1125 $\mu$m between last guard ring and edge |
| Operational voltage | 1,5 $\times$ FD |
| Element capacitance | 35 pF/cm$^2$ |
| Total leakage current (FD) | typ. 100 nA max 500 nA |
| Dynamic biasing resistor | $>$ 100 MOhm |
| Radiation hardness | $>$ 200 krad (Co$^{60}$) |

Table 5.2: Specifications of the BPT silicon microstrip detectors.

shaping time of 32 ns ensures that each event is assigned to the correct HERA bunch crossing. The digital output of the TEKZ is transferred to the Digital Time Slice Chip (DTSC), which stores the data until a GFLT decision has been made. The BPT information was not used in the ZEUS trigger selection.

## 5.5 Commissioning of the BPT

The average energy loss for minimum ionizing particles (MIPs) in silicon is about 39 keV/100 $\mu$m [Le87]. For the silicon microstrip detectors used in the BPT an energy deposition of 120 keV is expected. Since the average energy required to create an electron-hole pair in silicon at 20 °C is 3.6 eV, for a MIP approximately 30,000 electron-hole pairs are created in one BPT detector, which corresponds to a charge of 4.8 fC. From the design of the BPT readout, simulations, and test measurements before installation, the thresholds of the detectors for data taking were estimated to be of the order of 1.5 fC. After installation of the BPT it was found that thresholds below 1.6 fC resulted in artificial noise in a large number of channels [Pe99].
Before the BPT was used in the data taking, its time delay w.r.t. the ZEUS readout and the thresholds for both detectors had to be determined. The procedures used in both cases are described below. The readout of the LPS detectors is synchronized to the HERA clock. In order to make sure that signals from the BPT are assigned to the correct HERA bunch crossing, the time delay between the LPS detectors and the BPT readout was determined. Special runs were taken in August 1997 to determine the correct time delay, which compensates for the different cable lengths of the BPT compared to the LPS detectors. In the absence of noise and background the expected mean number of hits in each silicon detector for events with a

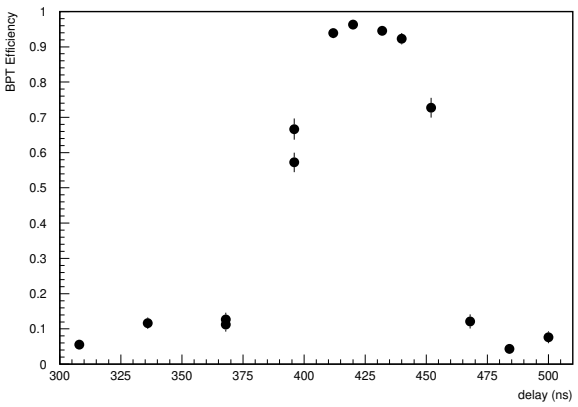


Figure 5.5: BPT efficiency as a function of the delay time w.r.t. the GFLT. The efficiency is defined as the fraction of events with hits in both BPT planes from a sample of well-measured BPC positrons. The delay time selected for data taking was 420 ns.

highly energetic positron in the BPC is slightly above 1. In most cases the particle trajectory only intersects one strip, but in a small fraction of events it might hit the area between two readout strips and thus cause a signal in both strips. Noise and background are expected to increase this value. Special runs were taken in August 1997 to determine the correct time delay. A modified BPC trigger (FLT 52, SLT DIS 2, TLT DIS 18, see section 9) was used to select events triggered by energy deposition in the BPC. The data was taken in the high luminosity trigger mode with the modification being that the prescale factors for FLT 52 and TLT DIS 18 were changed from 64 to 8 and 9999 to 1 respectively. In order to use a well-measured positron sample with a low number of background events, only events with a positron energy above 20 GeV measured in the BPC were selected. This corresponds to the kinematic region of low $y$ (see section 3.4), where photoproduction background is small and the current jet is far away from the BPC. The thresholds for both BPT detectors were set to 2.4 fC to minimize the amount of noise in the measurement. The efficiency $\epsilon_{\mathrm{BPT}}$ was defined as the fraction of events $\mathrm{N_{BPC}}$ with at least one hit in the BPT $\mathrm{N_{BPC+BPT}}$:

$$\epsilon_{\mathrm{BPT}} = \frac{\mathrm{N_{BPC+BPT}}}{\mathrm{N_{BPC}}} \tag{5.3}$$

Figure 5.5 shows the efficiency as a function of time delay. The optimal value for the data taking was determined to be 420 ns.
The same BPC trigger used above was used to determine the threshold for both detectors for data taking. The thresholds are required to be low enough so that few signal events are rejected and thus the detectors are as efficient as possible. On the other hand if the thresholds are too low the noise will increase which might lead to additional reconstructed tracks. Using the time delay of 420 ns, additional runs were taken with the thresholds for both planes varied between



1.3 fC and 2.4 fC. Based on the analysis of 1995 data the following cuts were applied to select positrons in the BPC:

- Energy : $15 < E_{\mathrm{BPC}} < 30$ GeV
- X-position: $5.2 < X_{\mathrm{BPC}} < 8.0$ cm
- Y-position: $-2.5 < Y_{\mathrm{BPC}} < 2.5$ cm
- Shower size: $\sigma_X < 0.7$ cm, $\sigma_Y < 0.7$ cm
- Z-vertex : $-50 < Z_{\mathrm{VTX}} < 50$ cm

The Z-vertex was taken from the CTD and the BPC quantities were reconstructed using the algorithms developed in the context of the 1995 analysis [Su98], [Mo98]. In addition, several noisy channels in the BPT were masked (1, 189, 190, 197 in plane X1, 0, 1, 386, 392-402, 485-511 in plane X3) and the total number of hits in both planes were required to be less than 200. The efficiency for one plane to detect a positron is defined in two steps. First the reconstructed vertex and the position of the detected positron in the BPC are used to estimate the hit position in both BPT planes. The particle trajectory is assumed to be a straight line between the event vertex and the BPC. The effect of the magnetic field is ignored. If the closest hit in one plane is less than 0.2 cm from the extrapolated line, then this hit is used further. This hit and the vertex position are used to get a better estimate of the hit position in the other plane, since the BPT resolution is better than that of the BPC. Again the particle trajectory is assumed to be a straight line between the two points. The $\mathrm{N_{Extrapolation,J}}$ events with a prediction for a hit in plane J are used to determine the efficiency $\epsilon_{\mathrm{BPT,J}}$ of this plane. $\epsilon_{\mathrm{BPT,J}}$ is defined as

$$\epsilon_{\mathrm{BPT,J}} = \frac{\mathrm{N_{Found,J}}}{\mathrm{N_{Extrapolation,J}}} \tag{5.4}$$

$\mathrm{N_{Found,J}}$ are the events with the closest hit in plane J being less than 0.2 cm away from the prediction. Figure 5.6 shows $\epsilon_{\mathrm{BPT,J}}$ and the number of hits $\mathrm{N_{Hits,J}}$ per plane J per bunch-crossing for both BPT planes as a function of the threshold set in DAC units. From calibration measurements the conversion of the threshold in DAC units into fC was determined to be given, to good approximation, by [Pe99]:

$$\text{threshold (fC)} \simeq \frac{A_1\,(\mathrm{mV}) \cdot \text{ threshold (DAC)}}{A_2(\mathrm{mV/fC})} \tag{5.5}$$

The parameters $A_1$ and $A_2$ were determined for each detector. The mean values found were $A_1 = 140$ mV and $A_2 = 185$ mV/fC. The different amount of noise in the two planes required a higher threshold for plane X3 of 3.5 DAC units (2.6 fC) than for plane X1 with 3.1 DAC units (2.4 fC).

## 5.6 BPT data quality monitoring

The BPT is included in the ZEUS data quality monitoring (DQM). In the online DQM, bias voltage, temperature, and strip occupancy of the detectors are monitored. This allows the shift crew to identify dead or noisy readout channels. The offline DQM consists of an analysis program in the framework of the ZEUS analysis package EAZE (see section 9.2). During data taking a fraction of the events is copied to disk. For a typical run several tens of thousands of

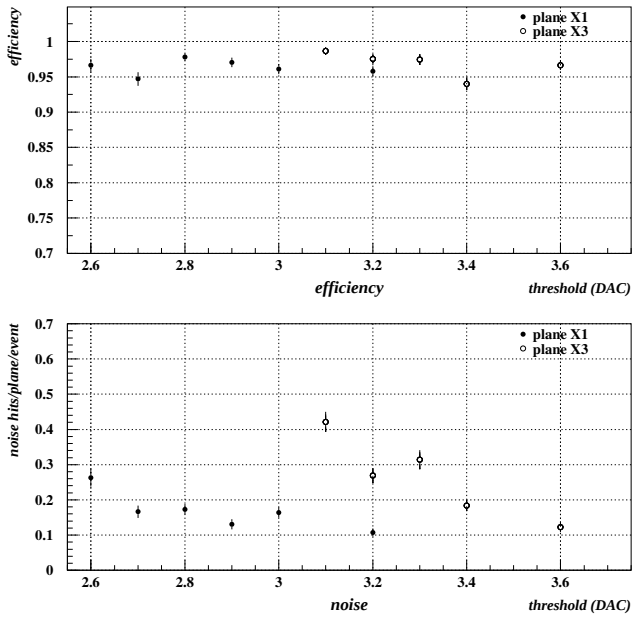


Figure 5.6: Determination of BPT threshold [Am99b]. Shown is the efficiency (upper plot) and mean number of noise hits (lower plot) in the two BPT silicon detectors as a function of threshold. The threshold values selected for data taking were 3.1 DAC units (2.4 fC) for plane X1 and 3.5 DAC units (2.6 fC) for plane X3.

events are available. In the BPT offline DQM more detailed information is provided compared to the online DQM. In the offline DQM the BPT track and vertex reconstruction and the BPC reconstruction are run (see chapter 6). In addition to occupancy plots for all silicon strips, similar to those generated in the online DQM, the reconstructed vertices and tracks from the BPT are used to check the alignment of the BPC w.r.t. the BPC and the CTD.

## 5.7 MC simulation of BPC and BPT

All ZEUS detector components have been included in the detector simulation program MOZART. Since both BPC and BPT were installed several years after the start of the ZEUS data taking, it was necessary to modify MOZART to include these two components. The BPC was included in 1995 and the simulation was tuned according to the knowledge gained from the BPC test-beam measurements and the analysis of 1995 data [Ti97]. The implementation of the BPT was done in 1997. The main parts of the support structure and the hybrids are implemented as partly overlapping volumes of carbon, copper, and epoxy. The silicon detectors are modeled as boxes of silicon, subdivided into 576 sub-volumes to represent the single strips. The inactive



area around the edges of the detectors is simulated by additional volumes of silicon. If the energy deposit in a certain sub-volume representing one silicon strip is above the threshold, a hit is assigned to the strip. The threshold is set to 30 keV, which roughly corresponds to 8300 created electron-hole pairs and a charge of 1.5 fC originally foreseen for the threshold of the real BPT.

# Chapter 6

# Detector studies

## 6.1 Introduction

In order to extract reliable physics results from BPC and BPT, a number of detector studies were required. These included alignment of the detectors with respect to each other and to the ZEUS coordinate system. The BPC position reconstruction and energy calibration and the BPT track reconstruction were optimized. Additionally, the BPC trigger efficiency and the BPT tracking efficiency had to be determined. All these topics required detailed studies and were interrelated. For example it was not possible to calibrate the BPC without a proper alignment and a functioning position reconstruction. Therefore, the studies detailed in the following sections were performed on an iterative basis. It was found that only a few iterations were necessary to obtain stable results. The different studies were not conducted in the same order as presented here.
In this analysis, the BPT is used to reconstruct the event vertex in Z, the X-position of the scattered positron, and its scattering angle. The resolution for these quantities were determined during the detector studies presented in this chapter.

## 6.2 BPC position reconstruction

The reconstruction of the impact position of the scattered positron by the BPC is required for a precise measurement at low $Q^2$. Firstly it is needed for the alignment of BPC and BPT. Secondly, the BPT in its 1997 configuration cannot measure the Y-position at all. Thirdly, the BPC position is used in the BPT track reconstruction to find the best track in the case of multiple candidates and in the track matching (see section 9.4) between BPT and BPC.
The BPC is segmented transversely in X- and Y-fingers as discussed in section 5.1. Since no information of the longitudinal energy deposition in the BPC is available, only the X- and Y-position ($X_{\mathrm{BPC}}$, $Y_{\mathrm{BPC}}$) of particles measured in the BPC can be calculated. This is done at the 'effective depth' $Z_{\mathrm{BPC}}$ given by the electromagnetic shower produced by the initial particle inside the BPC. $Z_{\mathrm{BPC}}$ is assumed to be the position where the number of shower particles is maximal and is parametrized as a function of the reconstructed BPC energy $E_{\mathrm{BPC}}$ and the critical energy $E_{\mathrm{C,BPC}} = 10.6$ MeV:

$$Z_{\mathrm{BPC}} = Z_0 - (\ln(\frac{E_{\mathrm{BPC}}}{E_{\mathrm{C,BPC}}}) - 0.5) \cdot X_{0,\mathrm{BPC}} \tag{6.1}$$

where $X_{0,\mathrm{BPC}} = 0.7$ cm is the radiation length of the BPC and $Z_0$ the Z-position of the BPC front face. $Z_{\mathrm{BPC}}$ is used to extrapolate $X_{\mathrm{BPC}}$ and $Y_{\mathrm{BPC}}$ to the BPC front face.





| | Data | | MC | |
|---|---|---|---|---|
| Parameter | value | error | value | error |
| $p_2$ | –0.0218 | 0.0002 | –0.0244 | 0.0002 |
| $p_3$ | –2.0233 | $< 10^{-4}$ | –2.5182 | 0.0032 |
| $p_4$ | 3.2386 | $< 10^{-4}$ | 4.0752 | 0.0007 |
| $p_5$ | 10.18 | 0.014 | 17.72 | 0.022 |
| $\chi^2/ndf$ | 1.1 | | 1.1 | |

Table 6.1: Parameters used in the BPC position reconstruction for data and MC [Am99a].

In the previous analysis of BPC data, the reconstruction of $X_{\mathrm{BPC}}$ and $Y_{\mathrm{BPC}}$ was performed using a weighted sum of the positions $X_i$ and $Y_i$ of each single scintillator strip ([Su98], [Mo98], [Ma98]). The weight $w_i$ of strip $i$ was defined as:

$$w_i = \begin{cases} W_0 + \ln(\frac{\mathrm{E_i}}{\mathrm{E_{BPC}}}) & \frac{\mathrm{E_i}}{\mathrm{E_{BPC}}} > e^{-W_0} \\ 0 & \frac{\mathrm{E_i}}{\mathrm{E_{BPC}}} < e^{-W_0} \end{cases} \tag{6.2}$$

The value of the parameter $W_0 = 2.8$ was determined from MC studies [Su98]. The resolution $\delta X(\delta Y)$ of the method was reasonably well described by $\delta X(\delta Y) = 0.33\ \mathrm{cm}/\sqrt{E_{\mathrm{BPC}}/\mathrm{GeV}}$.
A new method has been developed for the analysis of 1997 BPC and BPT data and incorporated into the BPC reconstruction software [Fr98]. It uses the imbalance between the strip energies $E_i$ of the most energetic strip and the two neighbouring ones. The imbalances $\mathrm{Imbal_X}$ and $\mathrm{Imbal_Y}$ are defined as follows:

$$\mathrm{Imbal_X} = \frac{(E_{cx+1} - E_{cx-1}) + p_2 \cdot E_{cx}}{p_3 \cdot (E_{cx+1} + E_{cx-1}) + p_4 \cdot E_{cx}} \tag{6.3}$$

$$\mathrm{Imbal_Y} = \frac{(E_{cy+1} - E_{cy-1}) + p_2 \cdot E_{cy}}{p_3 \cdot (E_{cy+1} + E_{cy-1}) + p_4 \cdot E_{cy}} \tag{6.4}$$

$cx$ and $cy$ denote the BPC X- and Y-strips respectively with the most energy. $p_i (i = 2, 3, 4)$ are parameters. $X_{\mathrm{BPC}}$ and $Y_{\mathrm{BPC}}$ are reconstructed using the two imbalances and the position of the most energetic strip:

$$X_{\mathrm{BPC}} = X_0 + cx \cdot d - d/2 + \frac{d}{2\mathrm{atan}(p_5)} \cdot \mathrm{atan}(\mathrm{Imbal_X} \cdot p_5) \tag{6.5}$$

$$Y_{\mathrm{BPC}} = Y_0 + cy \cdot d - d/2 + \frac{d}{2\mathrm{atan}(p_5)} \cdot \mathrm{atan}(\mathrm{Imbal_Y} \cdot p_5) \tag{6.6}$$

$X_0$ ($Y_0$) is the position of the inner (lower) edge of the scintillator strips in the BPC as determined from the alignment studies. $d$ is the width of the BPC scintillators (7.9 mm) and $p_5$ a parameter, which describes the correlation between imbalance and reconstructed position. The values of the four parameters $p_i, i = 2, 3, 4, 5$ were determined by comparing the reconstructed BPC and BPT X-position at the effective depth of the shower $Z_{\mathrm{BPC}}$ in the BPC. The reconstructed BPT track (see section 6.5) was extrapolated to the $Z = Z_{\mathrm{BPC}}$. A comparison of the reconstructed Y-position was not possible, since the BPT in 1997 only allowed a measurement of the X-position. Since the design of the BPC X- and Y-fingers is identical in terms of width,

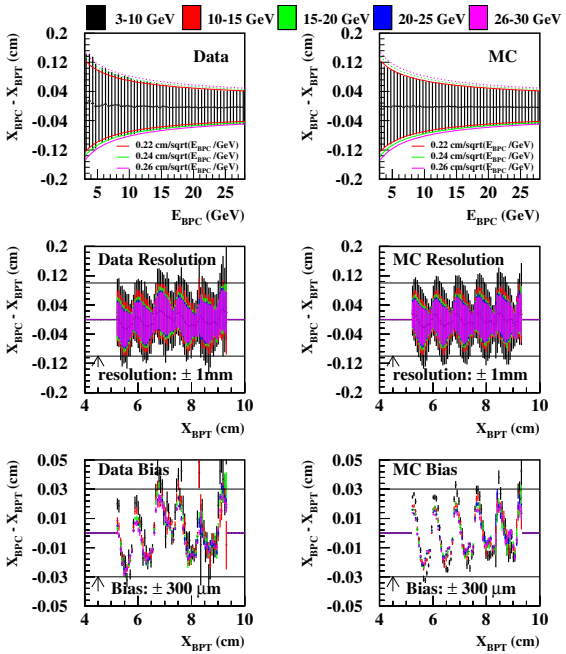


Figure 6.1: Resolution and bias of the BPC position reconstruction.

depth and wrapping, and the variations in the responses of different readout channels are taken care of by the energy calibration (see section 6.10), there is no reason for the parameters $p_i$ to be different for the X- and Y-fingers. The parameters have been determined separately for MC and data by a fit using MINUIT [Ja75]. The $\chi^2$ used in the fit is defined as

$$\chi^2 = \sum_1^N \left( \frac{X_{\mathrm{BPC}} - X_{\mathrm{BPT}}}{0.22 \text{ cm}/\sqrt{E_{\mathrm{BPC}}/\mathrm{GeV}}} \right)^2 \tag{6.7}$$

where the sum runs over all events used. The results are given in table 6.1. Resolution and bias in X are shown in figure 6.1. For both data and MC the resolution $\delta X$ is approximately $\delta X = 0.22 \text{ cm}/\sqrt{E_{\mathrm{BPC}}/\mathrm{GeV}}$. The bias of the reconstruction was found to be less than 0.03 cm, similar to the old reconstruction algorithm described above.

## 6.3 BPC time and shower width reconstruction

The reconstructed time $T_{\mathrm{BPC}}$ and the shower size $\sigma_{\mathrm{BPC}}$ are used to reject background events (see section 9.4). $T_{\mathrm{BPC}}$ is reconstructed for each BPC module from the energy-weighted time



| Method | BPC | $X_0$(cm) | $Y_0$(cm) | $Z_0$(cm) | Error (cm) |
|---|---|---|---|---|---|
| Optical survey | North | 4.33 | –6.38 | –293.7 | 0.05 |
| Optical survey | South | –8.05 | –6.14 | –293.7 | 0.05 |
| QED Compton events | North (Run $<$ 27490) | 4.316 | - | - | 0.075 |
| QED Compton events | North (Run $>$ 27490) | 4.374 | - | - | 0.073 |

Table 6.2: Results of the preliminary BPC alignment in 1997 from the optical survey [We99] and the alignment with QED Compton events [Mo98a].

$t_i$ of the single scintillator strips as calculated from the DSPs (see section 5.2):

$$T_{\mathrm{BPC}} = \frac{\sum_{i=1}^{N_{\mathrm{strips}}} (E_i t_i)}{\sum_{i=1}^{N_{\mathrm{strips}}} (E_i)} \tag{6.8}$$

$N_{\mathrm{strips}}$ is the total number of strips for the module, i.e. 31 for the BPC North module (15 X-strips plus 16 Y-strips) and 27 for the BPC South module (11 X-strips plus 16 Y-strips).
The shower width $\sigma_{\mathrm{BPC}}$ is given by the second moments of the lateral shower distributions in X and Y. Since the new position reconstruction does not use weight factors for single strips, $\sigma_{\mathrm{BPC}}$ is calculated using the logarithmically-weighted strip energies as defined in section 6.2:

$$\sigma_{\mathrm{BPC}} = \left[ \frac{1}{2} \cdot \left( \frac{\sum_{i=1}^{15} w_i (X_{\mathrm{center(i)}} - X_{\mathrm{BPC}})^2}{\sum_{i=1}^{15} w_i} \right)^2 + \frac{1}{2} \cdot \left( \frac{\sum_{j=1}^{16} w_j (Y_{\mathrm{center(j)}} - Y_{\mathrm{BPC}})^2}{\sum_{j=1}^{11} w_j} \right)^2 \right]^{\frac{1}{2}} \tag{6.9}$$

$X_{\mathrm{center(i)}}$ ($Y_{\mathrm{center(j)}}$) is the center of strip $i$ ($j$) in X (Y) and $w_i$ ($w_j$) the weight given by equation 6.2. For the BPC North module the sums run over all 15 X-strips and 16 Y-strips respectively.

## 6.4 Preliminary alignment of the BPC

The alignment of the BPC and BPT was performed in two steps. In the first step the BPC was aligned w.r.t. the ZEUS coordinate system using the results of an optical survey and QED Compton events. This is described in this section. The results are summarized in table 6.2. In the second step the results of the alignment are used as the basis of a more sophisticated procedure used to align both BPC and BPT as described in section 6.7.
After the installation of the BPT an optical survey similar to those made in 1995 [Su98] and 1996 was conducted. The position of both BPC modules with respect to the ZEUS coordinate system was determined with an accuracy of approximately 0.5 mm. After the data taking in 1997 it was possible to use the QED Compton process $ep \to e'p'\gamma$ [Co92] to confirm the results of the optical survey. In this process the exchanged photon is almost real ($Q^2 \approx 0$ GeV$^2$) and a photon is emitted by the initial or final state positron. For $Q^2 \to 0$ GeV$^2$ the final state of this process is, to good approximation, given by a hadronic system X with the same momentum as the initial proton plus an positron and a photon. The positron and photon are coplanar, the sum of their energies is equal to the positron beam energy, and their transverse momenta are balanced.
A detailed description of the procedure and the evaluation of the systematic errors is given in [Mo98a]. A short summary of the procedure is given below.

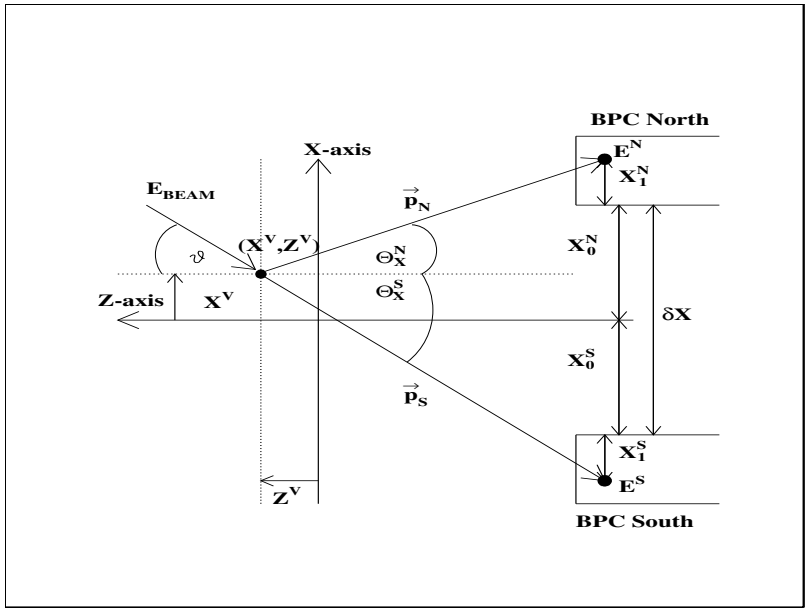


Figure 6.2: BPC alignment using elastic QED Compton events.

The elastic QED Compton events can be used to determine the X-position of one BPC module if the final state positron and photon are detected in the BPC modules. For the following discussion we do not distinguish between positron and photon. One particle with four-momentum $p^N = (E^N, p_X^N, p_Y^N, p_Z^N)$ is measured in the BPC North and the other one with four-momentum $p^S = (E^S, p_X^S, p_Y^S, p_Z^S)$ in the BPC South. Figure 6.2 gives a schematic overview of the measurement. Conservation of the X-momentum results in the following requirement on the momenta of the two particles:

$$p_X^e + p_X^p = p_X^N + p_X^S + p_X^{p'} \quad (6.10)$$

$$\Leftrightarrow p_X^N + p_X^S = p_X^e + \Delta p_X^p \quad (6.11)$$

Here $p_X^e$ is the X-momentum of the initial state positron. $p_X^p$ ($p_X^{p'}$) is the X-momentum of the initial (final) state proton and $\Delta p_X^p = p_X^p - p_X^{p'}$. For a given event with the reconstructed vertex at $(X^V, Y^V, Z^V)$ $p_X^N$ and $p_X^S$ can be calculated from the reconstructed X-positions and energies in the two BPC modules:

$$p_X^N = E^N \sin\theta_X^N = \frac{X_0^N + X_1^N - X_V}{|Z^N - Z^V|} E^N \quad (6.12)$$

$$p_X^S = E^S \sin\theta_X^S = \frac{X_0^S + X_1^S + X_V}{|Z^S - Z^V|} E^S \quad (6.13)$$

$X_0^N$ ($X_0^S$) is the position of the inner edge of the BPC scintillator strips and $X_1^N$ ($X_1^S$) the reconstructed position with respect to this edge. $Z^N$ ($Z^S$) is the Z-position of the center-of-



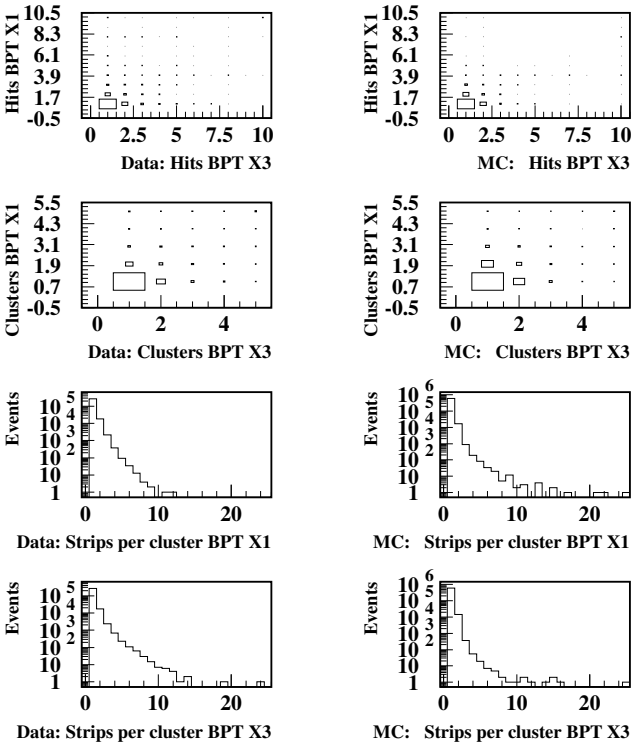


Figure 6.3: Results of the clustering algorithm used before the BPT track reconstruction.

gravity of the shower in the BPC North (South) module calculated using equation 6.1.
The distance of the two BPC modules $\delta X = X_0^N + X_0^S$ is fixed at (12.41±0.05) cm by the length of the connecting metal bars (12.31 cm) and the tungsten shieldings of the BPC modules towards the beam pipe of 0.5 mm each. The X-momentum of the initial state positron is given by $p_X^e = E_{\mathrm{BEAM}} \sin\theta_X^e$, where $\theta_X^e$ is the tilt of the positron beam w.r.t. the ZEUS coordinate system in the X-Z-plane and $E_{\mathrm{BEAM}}$ the positron beam energy. In the case of the QED Compton process, $E^N$ and $E^S$ are related to $E_{\mathrm{BEAM}}$ by:

$$E^N + E^S = E_{\mathrm{BEAM}} - E_{\mathrm{ISR}} \quad (6.14)$$

$E_{\mathrm{ISR}}$ takes into account the reduced positron beam energy in the case of initial state radiation. Using equations 6.12, 6.13, and 6.14, the conservation of X-momentum (equation 6.11) can be

used to obtain a measurement of $X_0^N$ on an event-by-event basis:

$$X_0^N = X^V + \frac{(p_X^e + \Delta p_X^p)|Z^N - Z^V||Z^S - Z^V| - X_1^N E^N |Z^S - Z^V|}{E^N |Z^S - Z^V| + (E_{\rm BEAM} - E^N - E_{\rm ISR})|Z^N - Z^V|} + \frac{(X_1^S + \delta X)(E_{\rm BEAM} - E^N - E_{\rm ISR})|Z^N - Z^V|}{E^N |Z^S - Z^V| + (E_{\rm BEAM} - E^N - E_{\rm ISR})|Z^N - Z^V|} \quad (6.15)$$

It was assumed that $\Delta p_X^p = 0$ and $E_{\rm ISR} = 0$. From the analysis of the 1997 data it was concluded that the CTD was moved in X with respect to the other ZEUS components during the HERA access day after the ZEUS run 27490. Therefore, the data taken with BPC and BPT was divided into two periods, before and after the run 27490. QED Compton events were used to determine the X-position of the BPC North module for both periods. The results are given in table 6.2.

## 6.5 BPT track reconstruction

The BPT reconstruction software BPRECON [Wi98] was designed for the BPT with all five silicon microstrip detectors. For this analysis a simple approach was taken to reconstruct BPT tracks. In the first step a simple clustering algorithm was used to combine adjacent hits in the same BPT detector. Dead and noisy strips are masked for both data and MC and noise is simulated in the case of MC (see section 6.8). Remaining adjacent strips in one plane are combined to a cluster. For a given cluster with strips $n_1$ to $n_2$ ($n_1 \leq n_2$), the center is defined as $n = n_1 + (n_2 - n_1)/2$. For isolated strips ($n_1 = n_2$), the impact position is assumed to be the center of the strip. As shown in figure 6.3 only one cluster is reconstructed for the majority of the events for both data and MC consisting of one strip only. The number of events with two strips per cluster is already reduced by a factor of 10 compared to this. These events were expected due to positrons which hit the BPT detectors between two readout strips. Clusters with more strips are either caused by noise or background events.
For the BPT track reconstruction the particle trajectory is assumed to be a straight line through clusters in the BPT planes. If there are multiple clusters in one or both planes then all possible hit combinations are compared. Taken is the combination of one cluster in each plane, for which the reconstructed track is in best agreement with the reconstructed X-position at the center-of-gravity of the shower in the BPC and the mean X-vertex as measured by the CTD for the particular run. It was checked that the effect of the magnetic field is negligible by tracing the same MC positron sample through the detector simulation with the simulation of the magnetic field turned off [We98].

## 6.6 BPT vertex reconstruction

Once a BPT track is found, it can be extrapolated to the mean X-position of the vertex for the particular run as determined by the CTD. This is used to determine the Z-vertex independently of the CTD. Figure 6.4 displays the Z-vertex as determined by the CTD and the BPT after all analysis cuts (see section 9.4). In the previous analysis of BPC data [Br97], it was found that about 4% of all events have no reconstructed CTD vertex. The same feature was observed in this analysis. This is most pronounced in the case of events at low $y$ or diffractive events, where most of the hadronic final state is produced in the forward direction outside the acceptance



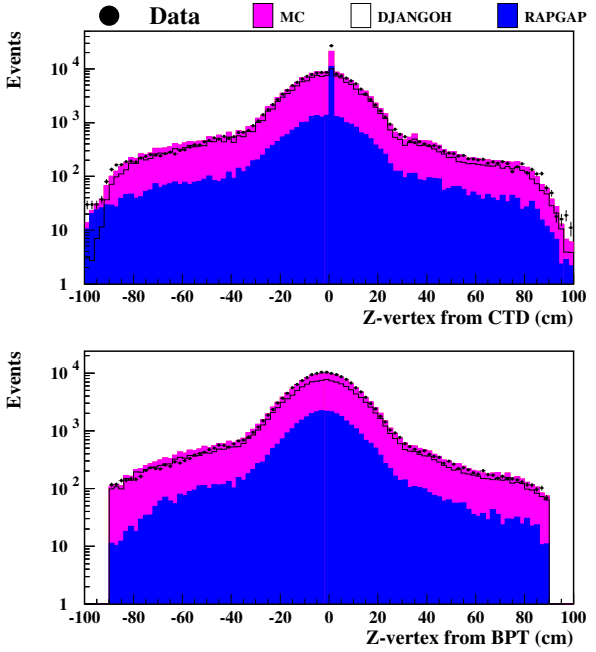


Figure 6.4: Reconstructed Z-vertex for data and MC as obtained from the CTD (upper plot) and by extrapolation of the best BPT track to the mean X-position of the vertex (lower plot). The Z-vertex reconstructed by the BPT was required to be within ± 90 cm for this analysis.

of the CTD. In figure 6.4 these events have been assigned a Z-vertex of 0. The number of events without reconstructed CTD vertex is not well described by the MC as can be seen from the peak in the CTD Z-vertex distribution in figure 6.4. This is not the case for the Z-vertex reconstructed by the BPT. If the final state positron is detected in the BPC, the BPT is fully efficient in the reconstruction of the Z-vertex, and data and MC are in good agreement.
The resolution of the Z-vertex obtained from the BPT was estimated by comparing the reconstructed CTD and BPT Z-vertex on an event-by-event basis. A data sample with a well-defined CTD vertex (at least three tracks and $\chi^2/ndf$ smaller than 3) was used. Only events with one hit in each BPT plane and an positron measured in the BPC with at least 20 GeV were used to minimize the effect of noise in the BPT and the contamination from background events. The resulting distribution is shown in figure 6.5. Since the CTD resolution in Z is much better (0.4 cm) than that of the BPT, the BPT vertex resolution was estimated by a Gaussian fit to the distribution. From this, $\sigma_{\rm VTX}^{\rm BPT}$ was determined to be 3 cm for both data and MC, as shown in figure 6.5.

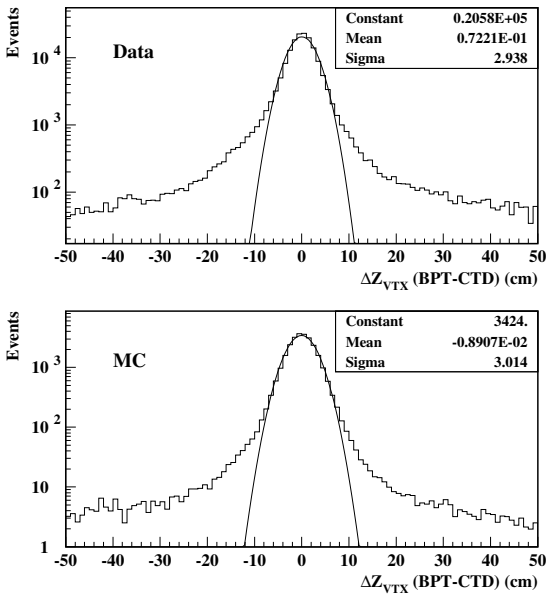


Figure 6.5: Difference of the reconstructed Z-vertex from BPT and CTD for data (upper plot) and MC (lower plot).

## 6.7 Alignment of the BPT

The Z-positions of the BPT planes were determined from bench measurements before the installation. The accuracy of the distance between the two planes is 300 $\mu$m. The MC simulation of the BPT used the design positions for both planes, which resulted in a difference in the Z-position between MC and data for plane X1 (X3) of 1.02 (1.00) cm. This is taken into account in the BPT track reconstruction. Because the two BPT planes installed in 1997 could only measure the X-position, possible shifts in Y could not be determined from the data and the detectors are assumed to be perfectly aligned w.r.t. the BPC. The impact of a misalignment in Y is negligible. This is because the distance between the edges of the fiducial area of the BPC in Y (see section 6.11) and the area covered by the BPT is bigger than a possible misalignment of the BPT planes.
The alignment of the BPT used in this analysis was taken from [Am99]. The applied procedure is based on a method developed in [We98]. The vertex position measured by the CTD, the reconstructed position in the BPC, and the reconstructed BPT track were used to determine the alignment parameters by a fit. The program MINUIT was used with a large number of events. An independent method described in [Mo98a] resulted in compatible results. A short



| Parameter | MC | Data (Run < 27490) | Data (Run > 27490) | Error | Comment |
|---|---|---|---|---|---|
| $X_0$(cm) | 4.3881 | 4.3547 | 4.3807 | 0.02 | |
| $Y_0$(cm) | 0.18 | 0.02 | 0.02 | 0.05 | taken from survey |
| $Z_0$(cm) | –293.70 | –293.70 | –293.70 | 0.05 | (data) or design (MC) |
| $X_{\mathrm{BPT1}}$(cm) | 6.85 | 6.8228 | 6.8488 | 0.02 | |
| $X_{\mathrm{BPT3}}$(cm) | 6.85 | 6.8942 | 6.9202 | 0.02 | |
| $Z_{\mathrm{BPT1}}$(cm) | –251.65 | –252.67 | –252.67 | 0.02 | taken from bench test |
| $Z_{\mathrm{BPT3}}$(cm) | –278.05 | –279.05 | –279.05 | 0.02 | (data) or design (MC) |
| $\Delta\phi_{\mathrm{BPT1}}$(mrad) | 0.0 | –2.02 | –2.02 | 0.150 | |
| $\Delta\phi_{\mathrm{BPT3}} - \Delta\phi_{\mathrm{BPT1}}$ (mrad) | 0.0 | 13.23 | 13.23 | 0.034 | |

Table 6.3: BPC and BPT alignment in 1997 [Am99a]. The total error was calculated by adding the statistical and systematic errors in quadrature.

description of the procedure is given below.
The crucial alignment parameters are: shifts of the BPT planes in X ($\Delta X_{\mathrm{BPT1}}, \Delta X_{\mathrm{BPT3}}$), and rotations around the Z-axis ($\Delta\phi_{\mathrm{BPT1}}, \Delta\phi_{\mathrm{BPT3}}$), and shifts of the BPC North in X ($\Delta X_{\mathrm{BPC}}$). The shift in the CTD position after run 27490 is taken into account by the parameter $\Delta X_{\mathrm{CTD}}$. Because the CTD defines the ZEUS coordinate system, it was chosen to apply $\Delta X_{\mathrm{CTD}}$ as a (virtual) shift of the BPC ($X_0$) and BPT ($X_{\mathrm{BPT1}}, X_{\mathrm{BPT3}}$) X-position. Relative distances and rotations can be determined with higher precision than absolute ones. Therefore, it was not the absolute shift $\Delta X_{\mathrm{BPT3}}$ and rotation $\Delta\phi_{\mathrm{BPT3}}$ of plane X3 which were determined by the fit, but the differences $(\Delta X_{\mathrm{BPT1}} - \Delta X_{\mathrm{BPT3}})$ and $(\Delta\phi_{\mathrm{BPT1}} - \Delta\phi_{\mathrm{BPT3}})$ w.r.t. plane X1.
The events used in the alignment were required to have a well-defined CTD-vertex with at least three tracks and $\chi^2/ndf < 3$. To minimize the effect of noise in the BPT detectors, only events with exactly one hit in each BPT plane were used. All events were required to have a BPC positron with at least 15 GeV in order to reduce the number of background events. For each event $j$ a BPT track is reconstructed as a straight line through the two hits using the functional form:

$$X(Z) = c_j + m_j \cdot Z \tag{6.16}$$

$c_j$ and $m_j$ are the intercept and the slope of the reconstructed BPT track and calculated from the numbers of the hit BPT strips in the two detectors. The alignment parameters discussed above are taken into account in this step. Due to the large spread of the Z-vertex distribution as shown in figure 6.4, the Z-vertex measured by the CTD can be used as a constraint for the alignment. The BPT track is compared to the (X-Z)-position of the event vertex as measured by the CTD and and the reconstructed BPC X-position at the BPC front face at $Z_0 = -293.7$ cm. The $\chi^2$ used in the minimization was defined as the sum over all used $n$ events:

$$\chi^2 = \sum_{j=1}^{n} \chi_j^2 = \sum_{j=1}^{n} \sum_{i=1}^{2} \frac{\delta X_{ji}^2}{\sigma(\delta X_{ji})^2} \tag{6.17}$$

$$\delta X_{ji} = (X_i - c_j + m_j \cdot Z_i) \tag{6.18}$$

The first sum runs over all $n$ selected events. The second one runs over the predicted points $(X_i, Z_i)$ from the CTD ($i = 1$) and BPC ($i = 2$) on the reconstructed BPT track. The

| Plane | Dead strips | Noisy strips |
|---|---|---|
| X1 | 71, 92, 191, 192, 229, 251, 407, 419, 448-511, | 0, 1, 189, 197 |
| X3 | 112, 114, 204, 329, 392–404, 472, 485–511, | 0, 1, 484 |

Table 6.4: Masked dead and noisy BPT strips.

uncertainties $\sigma(\delta X_{ji})$ were calculated from the uncertainties in the reconstructed vertex, the reconstructed BPC X-position, and the alignment parameters. The correlations between the reconstructed X- and Z-vertex and the two track parameters were taken into account. Details are given in [We98] and [Am99].
Several fits were done in order to estimate the uncertainty of the procedure. For data, the runs before and after the shift of the CTD were fitted separately both with and without the $\Delta X_{\rm CTD}$ as a free parameter. In the case of MC, the whole MC sample was used for one fit and equally divided into two halves to test the validity of the statistical errors given by MINUIT, which were found to be reasonable. The total systematic error of the fit was found to be $\pm 200$ $\mu$m and was dominated by the uncertainty of the distance between the two BPT planes in Z. It was decided to use the results of the fit which included the CTD shift as a free parameter for the analysis of the 1997 data. The results for this fit are given in table 6.3.

## 6.8 BPT efficiency

The BPT efficiency is determined by two factors: the number of dead strips and the thresholds of the BPT readout used for noise suppression. For events with a well-measured positron in the BPC, the distribution of hits as a function of the BPT channel number for one detector is expected to be smooth if the detector is fully efficient. Dead strips appear as entries with no or much fewer events than for the neighbouring channels. Noisy strips have a higher hit number than their neighbours. By default the MC has no dead or noisy channels. To have a proper simulation of the data, the dead and noisy channels found in the data are masked both in data and MC before the BPT track reconstruction is used. Strips are masked according to their position relative to the positron beam rather than their strip number, to take into account the difference in the alignment in data and MC. Some dead strips in the data have neighbouring strips with a higher number of hits than expected. It is believed that either capacitative coupling of the strips or crosstalk effects at the bonding are responsible for this effect. This results at least partly in a compensation of the inefficiency due to the dead strip. The dead strips belonging to the category described above are not masked. The masked dead and noisy strips are listed in table 6.4. It is assumed that by masking the dead and noisy strips, all position dependent effects were properly simulated in the MC. Additional global effects are expected to arise, due to the high thresholds.
The overall efficiency of each BPT detector is estimated using the CTD and the BPC. A similar event sample as used to determine the resolution of the reconstructed Z-vertex from the BPT (see section 6.6) is required to have a well-measured vertex and reconstructed positron in the BPC. The mean X- and Y-vertex for each run as measured by the CTD is used. No cut is imposed on the number of hits in each BPT detector.
In the first step the hit position in both BPT detectors $X_{\rm pred,BPTX_i}$ is predicted from a straight line through the vertex position $X_{\rm VTX}$ as measured by the CTD and the reconstructed X-position $X_{\rm BPC}$ in the BPC (equation 6.19). As discussed in section 8.2 the mean X-vertex was



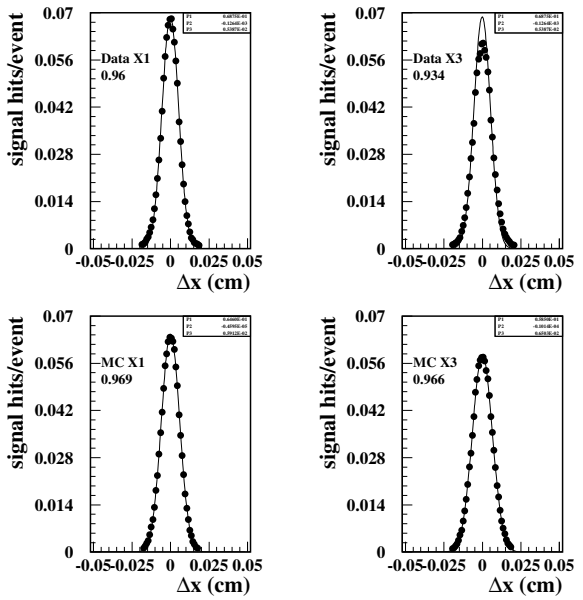


Figure 6.6: Difference of predicted and reconstructed hit position in the two BPT planes for data (upper plots) and MC (lower plots). The efficiency determined with $\Delta_{\rm XCUT} = 500$ $\mu$m is given in the plots.

used because the resolution of the CTD in X is worse than the spread of the HERA beams of about 300 $\mu$m in X. In the second step the hit in each BPT plane closest to the predicted position is determined. If the best found hit in one particular plane is closer than $2\Delta_{\rm XCUT}$ to the prediction, it is used together with the CTD vertex in the next step to get a better prediction of the hit in the other BPT plane (equation 6.20).

$$X_{\rm pred,BPTX_i} = X_{\rm VTX} + \frac{(X_{\rm VTX} - X_{\rm BPC})}{(Z_{\rm VTX} - Z_{\rm BPC})} \cdot (Z_{\rm VTX} - Z_{\rm BPTX_i}) \quad i = 1,3 \tag{6.19}$$

$$X_{\rm pred,BPTX_i} = X_{\rm VTX} + \frac{(X_{\rm VTX} - X_{\rm BPTX_j})}{(Z_{\rm VTX} - Z_{\rm BPTX_j})} \cdot (Z_{\rm VTX} - Z_{\rm BPTX_i}) \quad i = 1,3 \;\; j = 4 - i \tag{6.20}$$

This is done because the position resolution of the BPT is better than that of the BPC. Plane $X_j$ ($j = 1,3$) is counted as efficient if a hit is found within $\Delta_{\rm XCUT}$ of the predicted position and inefficient otherwise. If no prediction from CTD and plane $X_{4-j}$ ($j = 1,3$) is given because the hit there is too far away from the prediction then the event is not used in the determination of the efficiency. This takes into account the fact that neutral particles also occasionally fake an positron signal in the BPC or noise in the BPT which results in additional hits not related to an

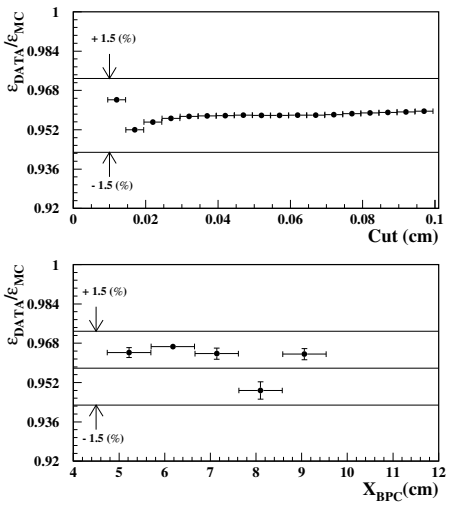


Figure 6.7: BPT efficiency correction as a function of $\Delta_{\mathrm{XCUT}}$ and $X_{\mathrm{BPC}}$.

positron. These kinds of events should not be used in the determination of the BPT efficiency, therefore a hit in one plane is implicitly used as a trigger for expecting a signal in the other one. Figure 6.6 shows the difference between the estimated and reconstructed hit positions for both BPT planes for data and MC for $\Delta_{\mathrm{XCUT}} = 500$ $\mu$m. The efficiencies for each plane for data (MC) $\epsilon_{\mathrm{Data,X1}}$ and $\epsilon_{\mathrm{Data,X3}}$ ($\epsilon_{\mathrm{MC,X1}}$ and $\epsilon_{\mathrm{MC,X3}}$) determined with this cut are given in the plot. Comparing the results for data and MC, the inefficiency of plane $X_3$ is higher than for plane $X_1$. This is consistent with the fact that the threshold for $X_3$ was chosen to be higher than for $X_1$.
As the BPT is used in the selection of the data and MC samples for the measurement of $\sigma_{\mathrm{tot}}^{\gamma^* p}$ and $F_2(x, Q^2)$, the different efficiencies for both samples had to be taken into account. The number of selected data events was corrected by the ratio $\epsilon_{\mathrm{Data}}/\epsilon_{\mathrm{MC}} = (\epsilon_{\mathrm{Data,X1}} \cdot \epsilon_{\mathrm{Data,X3}})/(\epsilon_{\mathrm{MC,X1}} \cdot \epsilon_{\mathrm{MC,X3}})$ of the efficiencies in the data ($\epsilon_{\mathrm{Data}}$) and in the MC ($\epsilon_{\mathrm{MC}}$) to account for the difference. The ratio was found to be 95.8%. It was checked that it was independent of the choice of $\Delta_{\mathrm{XCUT}}$ and of the X-position $X_{\mathrm{BPC}}$ in the BPC. The results are shown in figure 6.7. The correction is stable within $\pm$1.5%. The uncertainty of $\pm$1.5% was taken into account in the determination of the systematic uncertainties in the measurement of $\sigma_{\mathrm{tot}}^{\gamma^* p}$ and $F_2(x, Q^2)$ (see section 10.4).
During the efficiency study the noise in the BPT planes for data was measured. This was done by counting the hits in each plane outside the range of $\Delta_{\mathrm{XCUT}}$ around the prediction from the other plane and the CTD. In order to further improve the simulation of the BPT planes in MC, the amount of noise in the data was simulated in the MC by adding randomly distributed artificial hits according to a Poisson distribution of 0.15 hits per plane and event. The measured number of noise hits per plane and event for MC is in good agreement with this



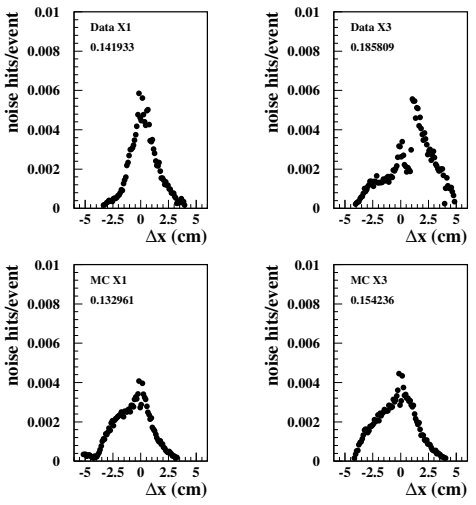


Figure 6.8: Difference of predicted and reconstructed hit position in the two BPT planes for data (upper plots) and MC (lower plots) for noise hits. The mean number of noise hits per plane and event determined with $\Delta_{\mathrm{XCUT}} = 500$ $\mu$m is given in the plots.

number. Figure 6.8 shows the results of the study in terms of noise distribution for data and MC for $\Delta_{\mathrm{XCUT}} = 500$ $\mu$m. Note the different scales in the efficiency and noise plots.

## 6.9 BPT position and angular resolution

The distributions $\Delta X_{\mathrm{BPTXi}}$ in figure 6.6 for plane X1 are centered at –2 $\mu$m (–0.5 $\mu$m) for data (MC) and for plane X3 at 1.4 $\mu$m (0.4 $\mu$m) for data (MC). These values are compatible with 0 $\mu$m. The position resolution of the two BPT planes can be extracted from the width $\delta_{\Delta\mathrm{X,BPTXi}}$ of the distributions. Using equation 6.19 and 6.20, the width $\delta_{\Delta\mathrm{X,BPTXi}}$ of the distribution can be related to the resolution of the Z-vertex $\delta_{Z_{\mathrm{VTX}}} = 0.4$ cm of the CTD and the position resolution of the two BPT detectors $\delta_{\mathrm{X,BPTXi}}$. The vertex resolution in X is negligible, because the mean vertex is used. Using the approximations $Z_{\mathrm{VTX}} - Z_{\mathrm{BPTX1}} = 250$ cm, $Z_{\mathrm{VTX}} - Z_{\mathrm{BPTX3}} = 280$ cm, and $X_{\mathrm{VTX}} - X_{\mathrm{BPTX1}} = X_{\mathrm{VTX}} - X_{\mathrm{BPTX3}} = 6$ cm, the resolution of the two BPT planes are approximately given by:

$$\delta^2_{\Delta\mathrm{X,BPTX_1}} = \left(\frac{180}{280^2}\right)^2 \cdot \delta^2_{Z_{\mathrm{VTX}}} + \delta^2_{\mathrm{X,BPTX1}} + \left(\frac{250}{280}\right)^2 \cdot \delta^2_{\mathrm{X,BPTX3}} \quad (6.21)$$

$$= (8\,\mu\mathrm{m})^2 + 1.8 \cdot \delta^2_{\mathrm{X,BPT}} \quad (6.22)$$

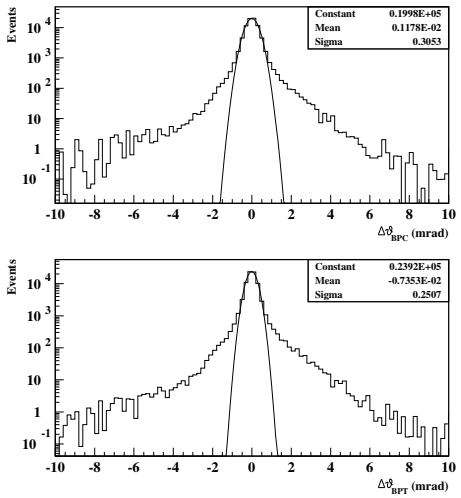


Figure 6.9: Difference between generated and reconstructed positron scattering angle $\vartheta$. $\vartheta$ was reconstructed from the BPC position (upper plot) and the BPT X-position and BPC Y-position (lower plot).

$$\delta^2_{\Delta\mathrm{X,BPTX_3}} = \left(\frac{180}{250^2}\right)^2 \cdot \delta^2_{Z_{\mathrm{VTX}}} + \delta^2_{\mathrm{X,BPTX3}} + \left(\frac{280}{250}\right)^2 \cdot \delta^2_{\mathrm{X,BPTX1}} \quad (6.23)$$

$$= (12\ \mu\mathrm{m})^2 + 2.25 \cdot \delta^2_{\mathrm{X,BPT}} \quad (6.24)$$

Equations 6.22 and 6.24 are only valid under the assumption that the position resolutions of both BPT detectors are equal, i.e. $\delta_{\mathrm{X,BPTX1}} = \delta_{\mathrm{X,BPTX3}} = \delta_{\mathrm{X,BPT}}$. The extracted position resolutions $\delta_{\mathrm{X,BPT}}$ of the two BPT detectors are 41$\mu$m for data and 43$\mu$m for MC. This is slightly worse than the prediction of 100 $\mu$m/$\sqrt{12} \approx 30$ $\mu$m based on the strip pitch of 100 $\mu$m as discussed in section 5.3. Other small contributions to $\delta_{\Delta\mathrm{X,BPTXi}}$ like the uncertainty of the mean X-vertex and the reconstructed BPC X-position have been neglected in the approximation used in equations (6.21–6.24). The extracted position resolution $\delta_{\mathrm{X,BPT}}$ of the two BPT detectors is therefore considered an upper limit.

Only the horizontal scattering angle can be reconstructed with the BPT. The vertical scattering angle has to be reconstructed from the Y-position as measured from the BPC. The resolution of the horizontal scattering angle reconstructed with BPT is about 0.04 mrad given from the BPT resolution in X (40 $\mu$m) and the resolution of the Z-vertex measured by the CTD (0.4 cm). The resolution of the Y-position reconstructed by the BPC $\delta Y$ is given approximately by $\delta Y = 0.22\ \mathrm{cm}/\sqrt{E_{\mathrm{BPC}}/\mathrm{GeV}}$, which is, even for high positron energies, about a factor of 10 higher than the resolution of the BPT detectors of $\delta_{\mathrm{X,BPT}} \approx 40$ $\mu$m. Therefore, the dominating contribution to the resolution in $\vartheta$ is the resolution $\delta Y$ of the Y-position reconstructed by the BPC.



Two methods to reconstruct the positron scattering angle $\vartheta$ were studied using the MC sample. In the first case only the reconstructed X- and Y-position from the BPC were used. The second method used the reconstructed X-position from the BPT and the Y-position from the BPC. The results are shown in figure 6.9. In both cases the generated and reconstructed scattering angles are in good agreement. The resolution increases from 0.31 mrad to 0.25 mrad if the X-position reconstructed from the BPT is used. The dominating contribution to the resolution in $\vartheta$ is the resolution $\delta Y$ of the Y-position reconstructed by the BPC.

## 6.10 BPC energy reconstruction and calibration

The BPC energy calibration is of vital importance for the analysis presented here. The reconstructed BPC energy is used in the calculation of the kinematic variables with the positron method and the e$\Sigma$ method (see section 3.4) and therefore influences the event selection. A different energy scale between data and MC or a non-uniformity or non-linearity of the reconstructed energy may result in event migration in the $(x-Q^2)$-plane and influence the unfolding of $\sigma^{\gamma^* p}_{\mathrm{tot}}$ and $F_2$. The following discussion concentrates on the BPC North module as only this module was used in the physics analysis presented here.

### 6.10.1 Energy reconstruction

The first step in the energy calibration of the BPC is to determine the voltages of the PMTs such that the response of each readout channel for a given energy deposit is approximately equal. The signal response as a function of the voltage of all the PMTs purchased for the BPC was measured as described in [Mo98]. Prior to the installation of the BPC, scans of the whole BPC using a point-like $^{60}$Co source emitting $\gamma$ rays of 1.17 MeV and 1.33 MeV were done as described in section 6.10.3. The $^{60}$Co scans were done with a constant voltage of 700 V for all readout channels. The average output signal of each readout channel is proportional to the energy response of this channel. Using the results of the $^{60}$Co scans together with the measurements of the response functions of the PMTs, the voltage of each PMT for data taking was determined [Mo98]. During data taking the BPC energy for each readout channel is calculated by the DSPs from the sampled signals of the PMTs (see section 5.2). It is only a first approximation of the true energy and has to be corrected for strip-to-strip gain variations, energy leakage out of the calorimeter, light attenuation inside the scintillators, and non-uniformities believed to be caused by the 0.1 mm gap between two adjacent scintillators. In order to correct for the strip-to-strip gain variations, the energy of each BPC X- and Y-channel is corrected by a factor $c_i^{\mathrm{X}}$ or $c_i^{\mathrm{Y}}$ respectively. In the first step of the energy reconstruction, the energy sum of all X- and Y-channels is calculated taking into account the correction factors:

$$E^{\mathrm{X},0}_{\mathrm{BPC}} = \sum_{i=1}^{15} c_i^{\mathrm{X}} E_i^{\mathrm{X}} \quad (6.25)$$

$$E^{\mathrm{Y},0}_{\mathrm{BPC}} = \sum_{i=1}^{16} c_i^{\mathrm{Y}} E_i^{\mathrm{Y}} \quad (6.26)$$

The position dependent correction functions for energy leakage $L^{\mathrm{X}}(X)$ $(L^{\mathrm{Y}}(X))$, light attenuation $A^{\mathrm{X}}(Y)$ $(A^{\mathrm{Y}}(X))$, and non-uniformity $N^{\mathrm{X}}(X-X_0)$ $(N^{\mathrm{Y}}(Y-Y_0))$ are in the next step used

to correct $E^{X,0}_{BPC}$ ($E^{Y,0}_{BPC}$):

$$E^{X,1}_{BPC} = E^{X,0}_{BPC} \cdot \frac{1}{L^X(X)} \cdot \frac{1}{A^X(Y)} \cdot \frac{1}{N^X(X)} \quad (6.27)$$

$$E^{Y,1}_{BPC} = E^{Y,0}_{BPC} \cdot \frac{1}{L^Y(X)} \cdot \frac{1}{A^Y(X)} \cdot \frac{1}{N^Y(Y)} \quad (6.28)$$

Due to the design of the BPC modules and the exit windows in the beam pipe, scattered positrons from the interaction point passing the exit window hit only a limited area in the BPC (see section 6.11). This area is far away from the BPC edges in Y and the edge in X facing away from the beam pipe. Thus the electromagnetic shower originating from the positron is fully contained in these directions. The only energy leakage that has to be corrected for is the leakage towards the beam pipe in the negative X-direction. In the case of the horizontal Y-fingers the attenuation and non-uniformity correction functions only depend on the reconstructed X-position and in the case of the vertical X-fingers only on the reconstructed Y-position.

### 6.10.2 Energy calibration

The calibration procedure developed in 1995 and used again slightly modified in 1996 was carried out in two steps. In the first step the correction functions for attenuation and leakage were determined (no correction for non-uniformity was done). The strip-to-strip calibration factors $c_i$ were set to 1 in this step, based on the assumption that these factors were close to 1 and therefore have less influence on the reconstructed energy than the leakage and attenuation correction functions. These were determined by fitting the distributions $E^{X,0}_{BPC}$ and $E^{Y,0}_{BPC}$ as a function of the reconstructed X- and Y-position. In the next step, the correction factors $c_i$ were determined from the $E^{X,1}_{BPC}$ and $E^{Y,1}_{BPC}$ [Su98] [Mo98].
Two problems were observed with the procedure described above. In 1996 the strip-to-strip variations were found to be considerably bigger than in 1995, and a first estimate of the correction factors $c_i$ had to be used in the determination of the correction functions [Bo99d]. Also the choice of parameters for the correction functions was somewhat arbitrary, because changes in the energy leakage correction could be compensated by a different attenuation correction. In 1997 a different approach was taken. A simultaneous fit of all parameters was done using MINUIT. This was done by Christoph Amelung and is described in detail in [Am99]. The results were checked in the analysis presented here and in [Mo98a]. A short description of the procedure is given below.
The correction functions for the calibration were parametrized in the following way:

$$L^X(X) = \int_{-\infty}^{l_1^X(X-l_2^X)} \frac{1}{\sqrt{2\pi}} e^{-\frac{1}{2}t^2}\,dt \quad (6.29)$$

$$L^Y(X) = \int_{-\infty}^{l_1^Y(X-l_2^Y)} \frac{1}{\sqrt{2\pi}} e^{-\frac{1}{2}t^2}\,dt \quad (6.30)$$

$$A^X(Y) = e^{\frac{Y-Y_R}{\lambda^X}} \quad (6.31)$$

$$A^Y(X) = e^{\frac{X-X_R}{\lambda^Y}} \quad (6.32)$$

$$N^X(X) = 1.0 - |X - X_{edge(n)} - X_{center(n)}| \quad (6.33)$$

$$N^Y(Y) = 1.0 - |Y - Y_{edge(m)} - Y_{center(m)}| \quad (6.34)$$

$Y_R$ ($X_R$) is the position of the edges of the X-fingers (Y-fingers) in Y (X), where these are coupled to the wavelength shifters. n (m) is the number of the X-finger (Y-finger), in which



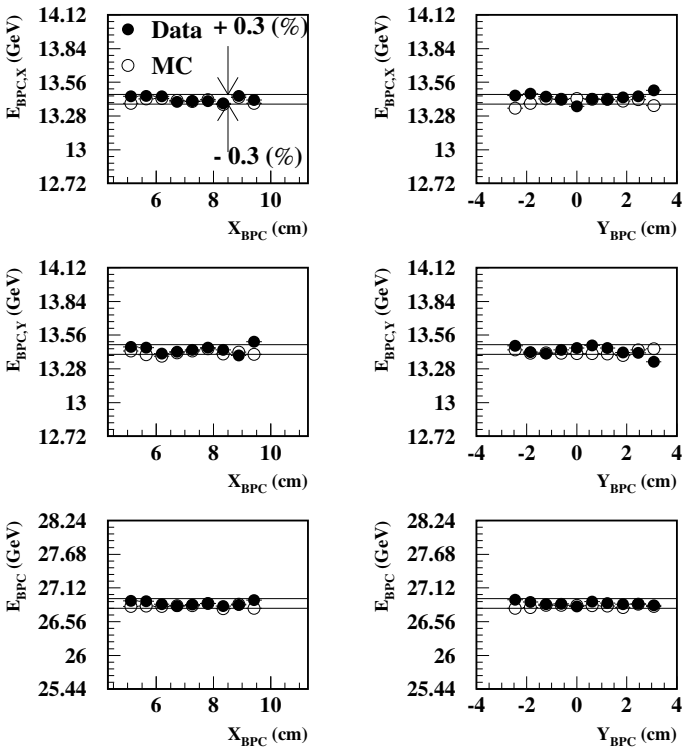


Figure 6.10: Energy reconstructed from the BPC X-fingers (upper plots), the BPC Y-fingers (middle plots), and the total BPC reconstructed energy (lower plots) as a function of the BPC X- and Y-position for data and MC.

the X-position (Y-position) is reconstructed. $X_{center(n)}$ ($Y_{center(m)}$) is the position of the center and $X_{edge(n)}$ ($Y_{edge(m)}$) the position of the left edge of the X-finger (lower edge of the Y-finger) of the same finger. The numbering convention is given by equation 5.1 (5.2). Therefore, $|X - X_{edge(n)} - X_{center(n)}|$ ($|Y - Y_{edge(m)} - Y_{center(m)}|$) is the distance from the center of X-finger n in X (Y-finger m in Y). The leakage correction functions parametrize the energy leakage of the shower with a Gaussian transverse profile for two reasons. The attenuation correction is a simplification of the real behaviour. The light attenuation in the scintillator is wavelength dependent, and is, to good approximation, given by the sum of two exponentials. The light can reach the wavelength shifter either directly or after being reflected on the mirrored end of

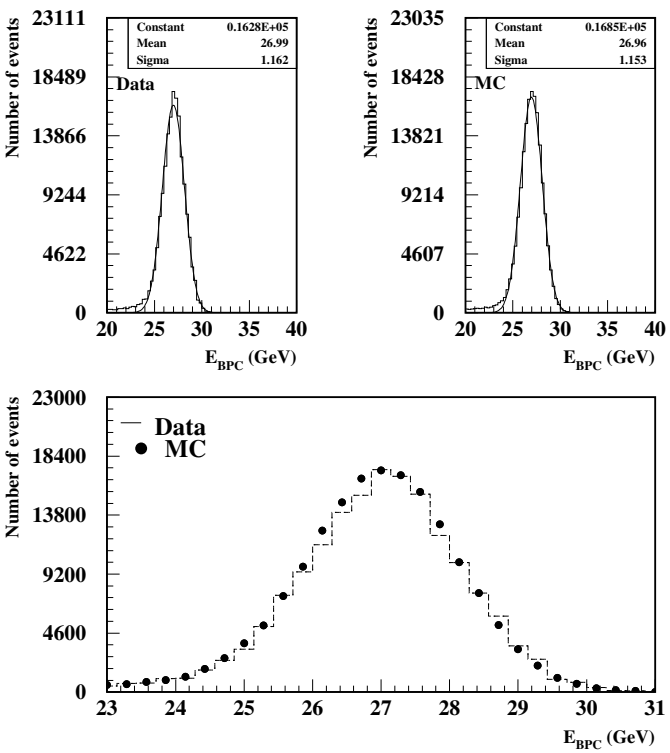


Figure 6.11: Reconstructed BPC energy for a sample of kinematic peak events. The upper plots show the energy distributions for data and MC fitted by a Gaussian. The lower plot shows a magnification of both distributions.

the scintillator. The simple ansatz used here describes the attenuation by one effective attenuation length $\lambda^X$ ($\lambda^Y$) for the X-(Y-)fingers. As expected from the 1995 and 1996 calibration, the leakage correction is flexible enough to absorb any error made by the simple ansatz. The strip-to-strip calibration constants $c_i$ can only be determined for strips inside or close to the fiducial area of the BPC. The others were initially fixed at 1.0 in both data and MC. After the calibration procedure described below is was found that a value of 0.72 in the case of MC resulted in a sightly better uniformity outside of the fiducial area of the BPC. Because the changes inside the fiducial area were negligible, the value was changed to 0.72 in the case of MC. The 25 free parameters ($c_i^X$, i=1,..,8, $c_i^Y$, i=4,..,13, $l_1^X$, $l_2^X$, $l_1^Y$, $l_2^Y$, $\lambda^X$, $\lambda^Y$, $n$) were determined using MINUIT with the following definition of $\chi^2$:



$$\chi^2 = \sum_{j=1}^{N} \left[ \left( \frac{\frac{E^{X,1}_{BPC}}{GeV} - 13.75}{\sqrt{2} \cdot 0.17\sqrt{13.75}} \right)^2 + \left( \frac{\frac{E^{Y,1}_{BPC}}{GeV} - 13.75}{\sqrt{2} \cdot 0.17\sqrt{13.75}} \right)^2 + \left( \frac{\frac{(E^{X,1}_{BPC}+E^{y,1}_{BPC})}{GeV} - 27.5}{0.17\sqrt{27.5}} \right)^2 \right] \quad (6.35)$$

The sum runs over all $N$ selected events. The third term in equation 6.35 was found to slightly increase the BPC energy uniformity based on the results of the fit [Am99b]. The resulting values of the parameters are given in [Am99a].
Kinematic peak events were selected in both data and MC and the procedure described above applied. The X-position from the BPT was used, while the Y-position was taken from the BPC. In data, a decrease of the mean reconstructed energy as function of time (run number) of –160 MeV per month (–0.0015% per run) was observed after the calibration. This is believed to be due to radiation damage in the BPC and corrected for by a linear function of the run number. The energy resolution in data was found to be slightly better than in MC. Given the fact that a modification of the simulation of the BPC in MOZART would have been very time consuming, and that the difference is small, it was decided to smear the reconstructed energy in data using Gaussian-distributed random numbers (center = 1.0, $\sigma$ = 0.0144). The fit by construction forces the mean reconstructed energy of the kinematic peak sample to be at 27.5 GeV. The MC sample was used to determine the difference of the reconstructed and true kinematic peak energy for the applied selection cuts. The reconstructed energy was found to be too high by 2.3% and both data and MC were corrected accordingly.
Figure 6.10 shows the energy reconstructed from the X-fingers ($E_{BPC,X}$), the Y-fingers ($E_{BPC,Y}$), and the total BPC energy ($E_{BPC}$) as a function of the X- and Y-position. Except close to the edges of the fiducial area in Y, $E_{BPC,X}$ and $E_{BPC,Y}$ were found to be stable within ±0.3% over the fiducial area of the BPC for both data and MC. Close to the edges of the fiducial area in Y, the deviations are slightly worse. The total energy $E_{BPC}$ is stable within ±0.3% over the whole fiducial area of the BPC for both data and MC. After the smearing of the reconstructed energy in the data, the absolute energy scale between data and MC was found to differ less than 0.3%. The comparison between the energy of the kinematic peak sample in data and MC is shown in figure 6.11. The agreement of the energy scale between data and MC to 0.3% has been checked with elastic $\rho^0$ events [Mo99].

### 6.10.3 Estimation of the BPC energy non-linearity

The calibration procedure described in 6.10.2 permits the determination of the BPC energy scale and uniformity in the limited energy range at the kinematic peak. Dose profile measurements on the front face of the BPC conducted from 1995 to 1997 have shown that the amount of radiation at the BPC is strongly localized to the area of the BPC close to the beam pipe in X, and around Y = 0 cm. Figure 6.12 shows the results from the dose profile measurements in 1997 (right plot) and the accumulated dose for 1995, 1996, and 1997 as a function of the HERA running time (left plot). In 1995 and 1996 the mean reconstructed energy of the BPC was found to decrease with time. This was believed to be due to radiation damage of the scintillators which causes reduction of primary light yield and a change in the attenuation [Wu94]. It was decided to exchange the affected scintillators. Measurements of single scintillators using $^{60}$Co, $^{106}$Ru, and $^{90}$Sr sources in 1995 confirmed that these fingers suffered from a position-dependent reduction of primary light yield and a change in the attenuation [Bo96].
The amount of radiation was significantly reduced from 1995 to 1997, due to a better understanding of the HERA positron accelerator and a change in the procedure used to dump the

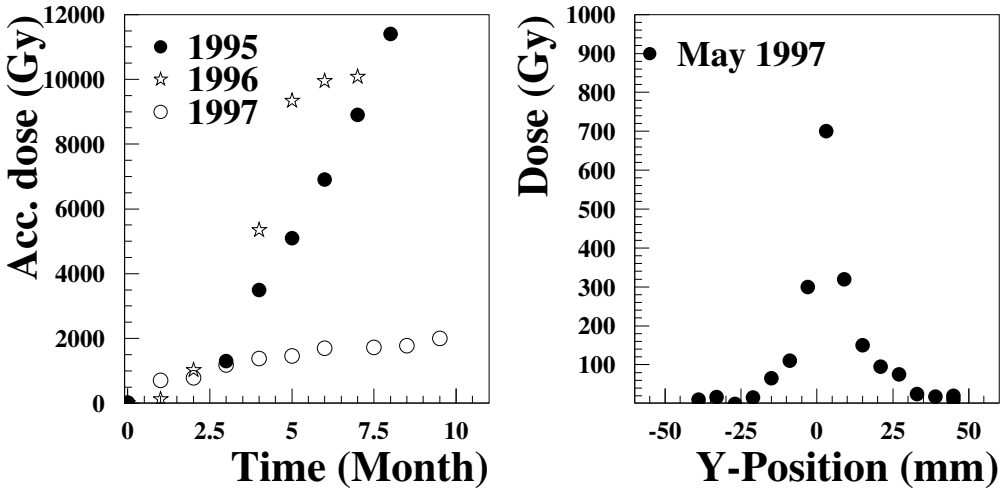


Figure 6.12: BPC accumulated dose from 1995, 1996, and 1997 (left) and dose profile from one TLD measurement in May 1997 (right).

positron beam [Su97]. After the 1997 HERA running period, the measured accumulated radiation dose and first results from calibration studies and $^{60}$Co scans indicated that the radiation damage was significantly lower than in the previous years. Based on these results, it was decided not to exchange the BPC scintillators. The results from [Bo96] were used to estimate the non-linearity of the reconstructed BPC energy in 1995. The estimated non-linearity in turn was included in the evaluation of the systematic uncertainties of the measurements of $F_2$ in 1995 [Su98].

In order to estimate the impact of the radiation damage on the linearity of the BPC in 1997 a study based on the procedure developed in 1995 was conducted [Bo99a] [Bo99b]. Similar to 1995, scans of the whole BPC using a point-like $^{60}$Co source emitting $\gamma$ rays of 1.17 MeV and 1.33 MeV conducted before and after the data taking were used to determine the change of the scintillator response due to radiation damage. As shown in figure 6.13 the $^{60}$Co source is moved parallel to the wavelength shifters. The emitted $\gamma$ rays deposit energy at the edge of the scintillator strips depending on the distance and the solid angle between source and scintillators [Bo99c]. For the BPC, the signal from the scintillator directly in front of the source is less than 50% of the total signal. An additional 30% comes from the neighbouring scintillators. In order to determine the single scintillator response, the total $^{60}$Co signal response must be unfolded. The unfolding procedure for the 1997 $^{60}$Co scans is described in [Bo99]. The ratio of two unfolded $^{60}$Co results is expected to be 1 if no change in the setup or degradation of the scintillator material or photomultipliers has occurred in between. Since the BPC was not disassembled in 1997, and the data quality monitoring during data taking did not show any



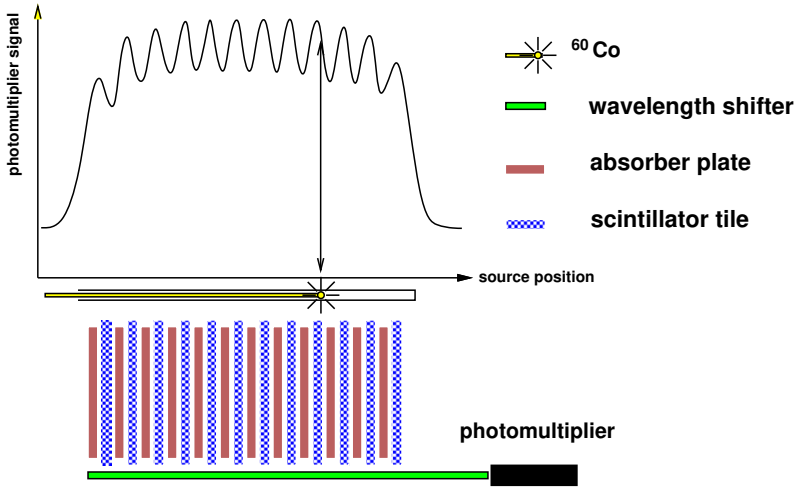


Figure 6.13: Schematics of $^{60}$Co scans of the BPC.

degradation of the test signals, the measured changes in the $^{60}$Co results from before and after the data taking are attributed to radiation damage of the scintillators.

After the exchange of the BPC scintillators in 1995, the response functions of single strips were measured using a $^{106}$Ru source. Since no scintillators were exchanged in 1997 this was not possible, and the response function of each scintillator had to be determined exclusively from the results of the $^{60}$Co measurements. This was done by using the 1995 measurements to relate the ratio of the unfolded results from the $^{60}$Co scans before and after the data taking to the non-uniform dose profile determined from $^{106}$Ru measurements. A linear relation was assumed, which for the expected radiation dose in 1997 results in an overestimate of the radiation damage [Bo99a].

The estimated radiation dose for each scintillator was used to calculate the attenuation curves of the BPC scintillators in 1997. The numerical simulation LIGHTSIM [Bo99] was used. This program simulates the light propagation throughout rectangular scintillator parallelepipeds with a non-uniform radiation damage. It integrates over the wavelength and fluorescence spectrum and all effective angles and takes into account the reduction of primary light yield and the change of the absorption coefficient. Light reflection effects at all sides of the sample are also included. The simulation was tuned using the $^{106}$Ru measurements of single damaged and undamaged scintillators from 1995. Measurement and simulation are in good agreement as shown in figure 6.14.

The response functions of all scintillator strips in the BPC were simulated based on the unfolded ratio of the $^{60}$Co scans before and after the 1997 data taking. These were incorporated into a MC simulation to determine the effects of irradiation on the linearity of the BPC of 1997. The simulation was done using the electron gamma simulation (EGS4) program [Bi94].

Figure 6.15 (left) shows the energy $E_{\mathrm{MEAS}}$ reconstructed in the simulated 1997 BPC for positron energies between 0.5 and 27.5 GeV normalized to the value at 27.5 GeV, which is in first approximation the mean energy used for calibration (see section 6.10.2) of the real BPC. The

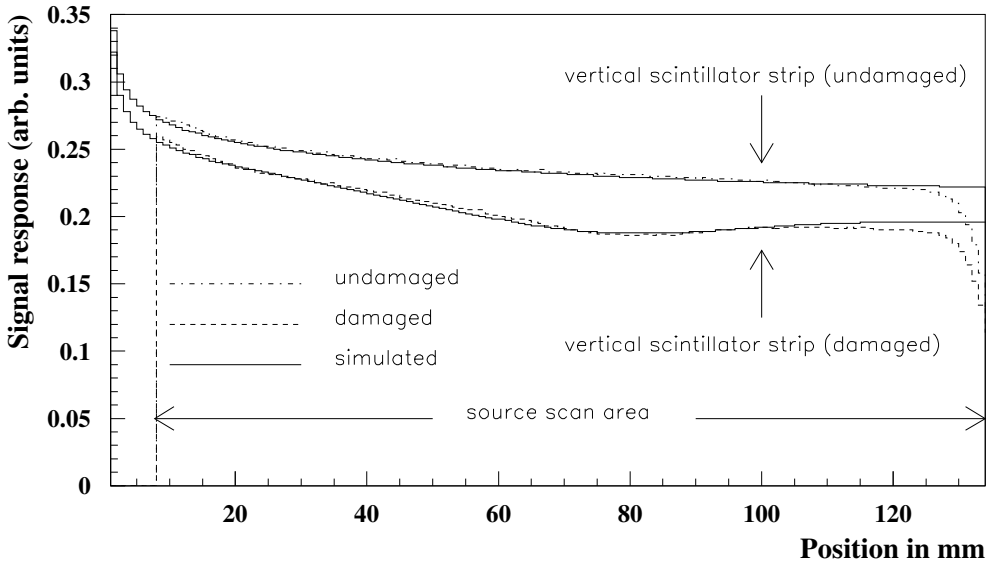


Figure 6.14: Comparison of measured and simulated attenuation curves of BPC scintillator fingers. The response function of scintillators from the 1995 BPC were measured using a $^{106}$Ru source.

right plot in figure 6.15 shows the non-linearity as a function of the positron energy. The measured energy for a certain positron energy is predicted by interpolating between the normalized response at 27.5 GeV (1) and 0 GeV (0). The non-linearity $E_{\rm NL}$ is defined as the deviation $E_{\rm NL} = 100 \cdot (E_{\rm MEAS} - E_{\rm PRED}))/E_{\rm PRED}$ of the reconstructed energy $E_{\rm MEAS}$ from the predicted energy $E_{\rm PRED}$. It is shown as a function of the positron energy $E_{\rm IN}$ in the right plot in figure 6.10.2. For all four displayed cases, the non-linearity can, to good approximation, be described by a function $E_{\rm NL} = a \cdot \ln(E_{\rm IN}/27.5\ {\rm GeV})$.
In the case of the reference BPC, the response functions of all horizontal and vertical scintillator strips respectively, were chosen to be identical and determined from $^{106}$Ru scans of undamaged scintillators. The results are in good agreement with results from test beam measurements of the BPC in 1994 [Mo98]. The open triangles indicate the results from the first analysis of the 1995 data, for which not the unfolded results of the $^{60}$Co scans but rather the simple ratio of the two scans were used. It is believed that this underestimates the radiation damage [Bo99a]. The non-linearity obtained from the unfolded $^{60}$Co results (black triangles) is worse than the one from the simple ansatz. As expected the non-linearity for 1997 is less than in 1995, but worse than the one of the reference BPC. It increases from zero at 27.5 GeV to about 1.25% at 3 GeV, which is the minimal energy used in the analysis presented here. The results are in good agreement with measurements using QED Compton events [Mo98a], which estimated the non-linearity at 16 GeV to be $(-0.26 \pm 0.19({\rm stat}) \pm 0.4({\rm sys}))\%$ and $(-0.38 \pm 0.30({\rm stat}) \pm 0.4({\rm sys}))\%$ for the two run ranges (run $< 27490$ and run $> 27490$) used here.



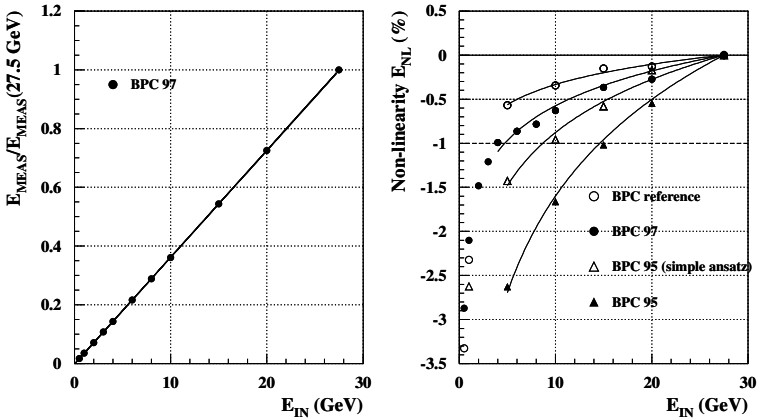


Figure 6.15: Reconstructed BPC energy normalized to the response at 27.5 GeV (left plot) and non-linearity (right plot) as a function of the positron energy.

In order to obtain an estimate of the systematic uncertainty in the unfolded values of $\sigma_{\rm tot}^{\gamma^* p}$ and $F_2$ due to the non-linearity, the BPC energy was corrected for an assumed non-linearity and $\sigma_{\rm tot}^{\gamma^* p}$ and $F_2$ were determined using the procedure described in section 10. The difference between the unfolded values and those without the correction for non-linearity is included in the total systematic error. In order to obtain an upper limit of the uncertainty in $\sigma_{\rm tot}^{\gamma^* p}$ and $F_2$, a non-linearity worse than the estimation from the simulation and the QED Compton events was used. It was parametrized as a linear function of the reconstructed BPC energy $E_{\rm BPC}$:

$$E_{\rm NL}(\%) = \frac{1}{19.6} \cdot \left( \pm \frac{E_{\rm BPC}}{\rm GeV} - 27.5 \right) \qquad (6.36)$$

## 6.11 BPC fiducial area

The area of the BPC usable for a precise measurement is, to first approximation, given by the projection of the beam pipe exit window (see section 5) on to the front face of the BPC. The upper left plot in figure 6.16 shows the reconstructed position $(X_{\rm BPC}, Y_{\rm BPC})$ in the BPC corrected for the mean vertex in X and Y and the positron beam tilt. It is expected that particles which do not pass through the exit window, but rather the beam pipe, pre-shower due to the larger amount of inactive material. In this case the energy reconstructed in the BPC is only a fraction of the initial energy of the particle. In order to limit the fraction of pre-showering particles, the fiducial area of the BPC used for an analysis is chosen to be smaller than the active area. In previous analyses the boundaries of the fiducial area were determined from geometrical and calibration studies ([Su98], [Mo98]). For this analysis the BPT was used. In the case of positrons which do not pre-shower, only a few hits per BPT plane are expected. In the case of particles, which pre-showered in the inactive material, more hits per BPT plane are expected. The upper right plot in figure 6.16 shows the mean number of hits in both BPT

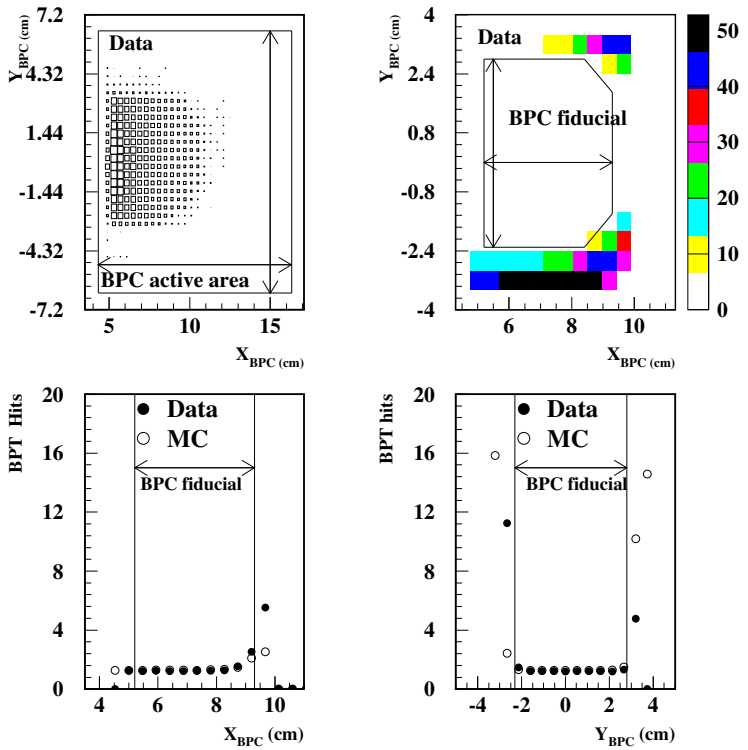


Figure 6.16: Determination of the BPC fiducial area. Shown are the reconstructed impact position on the BPC front face for data (upper left), the mean number of BPT hits per event (upper right) for data, and the mean number of BPT hits as a function of the reconstructed X- and Y-position for data and MC.

planes as a function of the reconstructed position $(X_{\mathrm{BPC}}, Y_{\mathrm{BPC}})$ in the BPC for data. The mean number of hits increases towards the edges of the active area, i.e. the boundaries of the exit window projected on to the BPC. The lower plots in figure 6.16 show the projection of the mean number of BPT hits on to the X- and Y-axis for data and MC. In both cases the number of hits is flat in the inner part of the plot. The mean number of hits is increasing towards higher values of $X_{\mathrm{BPC}}$ and towards lower and higher values of $Y_{\mathrm{BPC}}$. The small shifts between the distributions in data and MC are a result of the slightly different positions of the BPC and the BPT for both samples. The different positions are taken into account in the BPT track



reconstruction and in the reconstruction of the kinematic variables like $x$, $y$, $Q^2$, and $W$. The fiducial area was chosen to be the region in X and Y, where the mean number of BPT hits is flat for both data and MC as indicated in figure 6.16.

# Chapter 7

# MC generation

## 7.1 Signal events

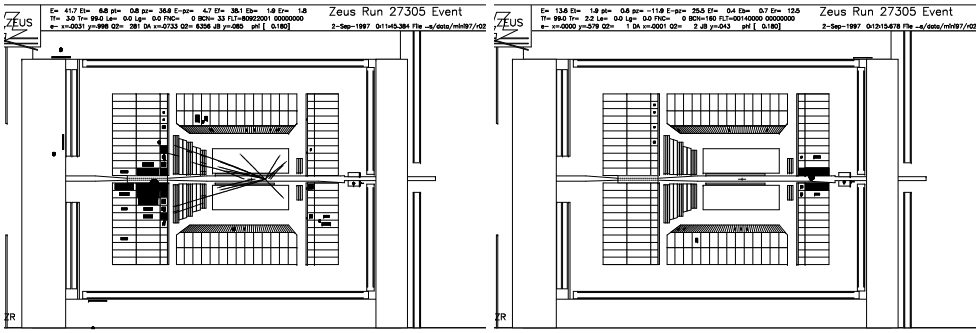


Figure 7.1: Non-diffractive (left) and diffractive (right) event pictures from the data sample used in the analysis. Both events pass all analysis cuts as described in chapter 9.

The hadronic final state in inclusive measurements such as the one presented here is a mixture of two classes of events. In figure 7.1 both types of events are shown. Non-diffractive events like the one to the left typically have a high particle multiplicity and the invariant mass reconstructed from all measured particles in the main detector excluding the scattered positron is high. For this event the positron was measured in the BPC, indicated by the energy deposit on the right hand outside the main calorimeter. Usually, several tracks are reconstructed and a significant amount of energy is deposited in the forward part of the calorimeter (left side in the plot). A diffractive event is shown in the right plot in figure 7.1. For these events the particle multiplicity and the invariant mass reconstructed from the measured hadronic final state is lower. Fewer or no tracks are reconstructed in the CTD and no significant energy is deposited in the forward direction. Two variables are generally used to separate the two different types of events: the invariant mass of the hadronic final state $M_X$ as defined in equation 7.1, and the pseudorapidity $\eta_{\max}$ defined by equation 7.2.

$$M_X = \sqrt{E_h^2 - P_h^2} \tag{7.1}$$

$$\eta_{\max} = -\ln(\tan(\frac{\theta_{\min}}{2})) \tag{7.2}$$





$E_h$ and $P_h$ are the total energy and momentum measured in the main detector, excluding the final state positron. $\eta_{\max}$ corresponds to the reconstructed calorimeter object, which is closest to the forward direction. This corresponds to the smallest value of $\theta$ as defined in chapter 4.
The aim of this analysis is to measure the inclusive $\gamma^* p$ cross section, which is a sum of the cross sections of diffractive and non-diffractive $\gamma^* p$ scattering. Therefore, the requirements on the generated MC events are less restrictive than they would be for example in an analysis such as [Ma98] which measures only the diffractive cross section. In both cases a precise description of the hadronic final state is necessary. In the later case the contributions from non-diffractive and diffractive events have to be separated in order to determine the diffractive cross section. This is not the case for inclusive measurements. A precise knowledge of the contributions from non-diffractive and diffractive events is not required provided that the hadronic final state is well described by the weighted sum of both MC samples. Separate MC samples were generated for non-diffractive and diffractive events. Both samples were mixed in order to describe the data. The determination of the mixing fraction is discussed in section 7.3.
the two MC generators used to generate the neutral current MC events were DJANGOH 1.1 [Sp99] and RAPGAP 2.06/51 [Ju99a]. In both cases the lepton vertex is generated by HERACLES [Sp99], which includes radiative corrections. Single photon emission from the positron or quarks, self energy corrections, and the complete set of one-loop weak corrections are taken into account. The hadronization is simulated by ARIADNE ([Lo92], [Bu92]) and JETSET ([Sj86], [Sj87], [Sj92]). The difference between DJANGOH 1.1 and RAPGAP 2.06/51 is the interaction between the virtual photon and the constituents of the proton. DJANGOH 1.1 is used to generate non-diffractive events and RAPGAP 2.06/51 to generate diffractive events. Vector meson production is included in RAPGAP. Both MC samples are mixed to give the best description of the hadronic final state. The following parameters were used to generate the events:

- $Q_e^2 > 0.03$ GeV$^2$
- W $> 3$ GeV
- $F_2 = F_{2,\mathrm{MRSA}}$
- $F_L$=0
- Energy of the final state positron $E_e' \geq 2$ GeV
  $\rightarrow y \leq 0.93$

The MRSA parametrization of $F_2$ was chosen because it is implemented in PDFLIB [Pl97] which is required by all generators and programs used for this analysis. This parametrization is valid at $Q^2$ above 0.625 GeV$^2$ and $x$ above $10^{-6}$. Below these values it is constant in the implementation of PDFLIB 7.09. More realistic parametrizations for the low $Q^2$ region such as ALLM97 [Ab97], which gives a good description of the previous measurements in the low $Q^2$ region, could not easily be interfaced to the MC generators. Therefore, MRSA was chosen and both MC samples are reweighted to the ALLM97 parametrization. The MRSA parametrization is constant in the generated $Q^2$ range. Therefore, relatively more events are generated in the lower $Q^2$ region compared to the ALLM97 parametrization and the statistical error from MC events is flat over the whole kinematic range covered in this analysis. Modifications to RAPGAP to make it use the same underlying structure function ($F_{2,\mathrm{MRSA}}$) as used in DJANGOH are discussed in section 7.2. The Z-vertex is taken from an unbiased estimate of the true vertex distribution [Qu98] for the BPT data taking period in 1997. The X- and Y-vertex are generated

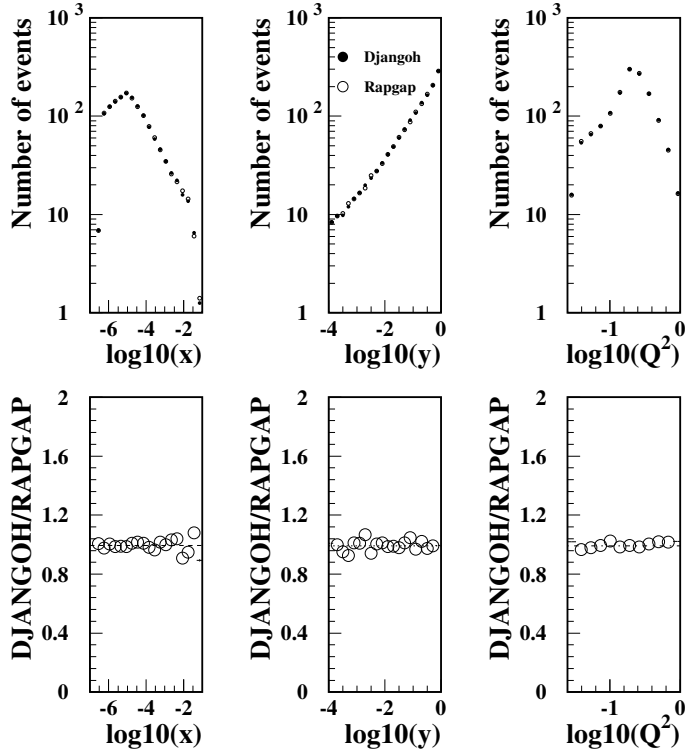


Figure 7.2: Generated $x$, $y$, and $Q^2$ distributions for both MC samples. The upper plots show the generated distribution of for the RAPGAP and DJANGOH MC sample. The lower plots show the ratios of the distributions of the two MC samples, which is compatible with 1.

using Gaussian distributions centered at –12.0 $\mu$m in X and at –360 $\mu$m in Y. The widths of the Gaussian distributions were $\sigma_X = 330$ $\mu$m and $\sigma_Y = 90$ $\mu$m. Only a preselected fraction of the generated events is used as input for the ZEUS detector simulation program MOZART (see section 4.5). The true event vertex and the four-momentum vector of the outgoing positron is used to predict its impact position on the BPC neglecting the effects of the magnetic field and multiple scattering. Events are preselected if the impact position ($X_{\rm IMPACT}$, $Y_{\rm IMPACT}$) on the BPC front face is within the following cuts:

$$4.4 \text{ cm} < X_{\rm IMPACT} < 10.8 \text{ cm}, \quad -3.3 \text{ cm} < Y_{\rm IMPACT} < 4.0 \text{ cm} \tag{7.3}$$



The applied cuts are looser than those used for the data selection described in chapter 9. A test sample of 15,000 MC events was used to check that none of the discarded events did pass the data selection. About two million events (2.5% of all generated events) remain after the preselection. The estimated luminosities of the diffractive and non-diffractive MC samples taking into account the efficiency of MOZART were 125.1 nb$^{-1}$ and 750.1 nb$^{-1}$ respectively. Figure 7.2 shows the distributions of $x$, $y$, and $Q^2$ for both MC samples normalized by the luminosity. A fit to the ratio of these distributions as shown in the lower plots, demonstrates that both MC samples are in good agreement.

## 7.2 Modifications to RAPGAP

It was necessary to modify the initial setup of RAPGAP to generate events with the same underlying structure function as in DJANGOH. In the default setting of RAPGAP the events are generated according to the given diffractive structure function $F_2^{D(4)}(x_{I\!P}, t, \beta, Q^2)$ and the corresponding $F_2(x, Q^2)$ is calculated by a numerical integration over $x_{I\!P}$, $\beta$, and $t$ and subsequent interpolation on a grid [Ju99a]:

$$F_2(x, Q^2) = \int F_2^{D(4)}(x_{I\!P}, t, \beta, Q^2)\delta(\beta \cdot x_{I\!P} - x)\mathrm{d}x_{I\!P}\mathrm{d}\beta\mathrm{d}t \tag{7.4}$$

$x_{I\!P}$ is interpreted as the fraction of the proton momentum carried by the colourless object (Pomeron) originating from the proton. $\beta$ is the fraction of $x_{I\!P}$, which takes part in the interaction. Thus, the fraction of the proton momentum taking part in the interaction is given by $x = \beta \cdot x_{I\!P}$. $t$ is the square of the difference of momenta between the initial proton and the hadronic final state $X$.
It was found that the integration (equation 7.4) and interpolation were not precise enough. Therefore, RAPGAP was used in the so-called 'mixed' mode, which is designed to generate diffractive and non-diffractive events. All events are generated according to a given $F_2(x, Q^2)$ and the probability of a single event to become a diffractive one is given by the ratio $F_2^{\rm diff}(x, Q^2)$ divided by $F_2(x, Q^2)$, where $F_2^{\rm diff}(x, Q^2)$ has to be provided by the user. In order to generate only diffractive events, RAPGAP was modified and the probability set to 1. The underlying structure function $F_2^{D(4)}(x_{I\!P}, t, \beta, Q^2)$ has to be given in form of parton distributions. Similar to the ones for DJANGOH, the parton distributions from $\mathrm{F}_{2,\mathrm{MRSA}}$ modified by a factor $e^{-g|t|}/x_{I\!P}^{1,3}$ were used. This approach, although only motivated to simulate the hadronic final state in this analysis, gives a reasonably good description of the diffractive structure function $x_{I\!P}F_2^{D(3)}$ as measured by ZEUS [Br98c] [Am99a].

## 7.3 Mixing of DJANGOH and RAPGAP events

Figure 7.3 shows the distributions of $\eta_{\rm max}$ for data in four selected ($y$–$Q^2$)-bins used in the extraction of $F_2$. The four upper plots indicate that the fraction of diffractive events, i.e. the fraction of events at low values of $\eta_{\rm max}$, changes significantly as a function of $y$ (and thus of $x$) and is almost constant as a function of $Q^2$. The four lower plots show the distribution for the non-diffractive (DJANGOH) and diffractive (RAPGAP) MC samples for two of the bins. In order to have a good simulation of the hadronic final state for the whole kinematic region covered by the analysis, the fraction of diffractive events $f(x, Q^2)$ ($0 \le f(x, Q^2) \le 1$) was fitted from the data using the following functional form:

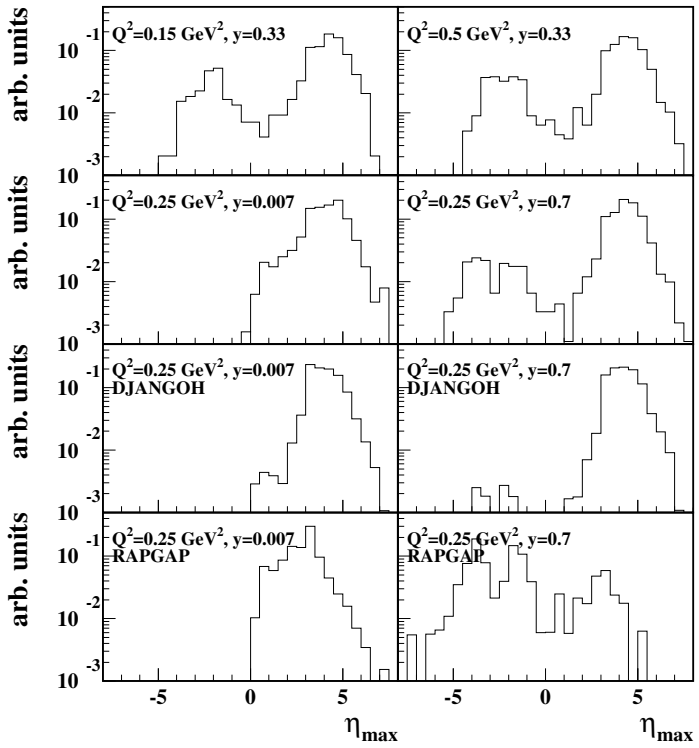


Figure 7.3: The four upper plots show the $\eta_{\max}$-distributions in selected bins used in the extraction of $F_2$ for data. The four lower plots show the $\eta_{\max}$-distributions of the DJANGOH and RAPGAP MC samples for two of the bins.

$$n_{\text{norm,bin}} \cdot n_{\text{Data,bin}}(x,Q^2) = n_{\text{RAPGAP,bin}}(x,Q^2) \cdot f(x,Q^2)_{\text{bin}} + n_{\text{DJANGOH,bin}}(x,Q^2) \cdot (1 - f(x,Q^2)_{\text{bin}}) \quad (7.5)$$

$f(x,Q^2)_{\text{bin}}$ was determined for each bin in the $(x-Q^2)$-plane used in the extraction of $F_2$ using distributions of different hadronic quantities as discussed below. $n_{\text{Data,bin}}$ is the number of events in the particular bin. $n_{\text{RAPGAP,bin}}$ and $n_{\text{DJANGOH,bin}}$ are the numbers of MC events in the particular bin, normalized to the luminosity of the data and reweighted to the measured structure function $F_2$. The normalization factor $n_{\text{norm,bin}}$ accounts for the fact that $F_2^{\text{MC}}$ differs



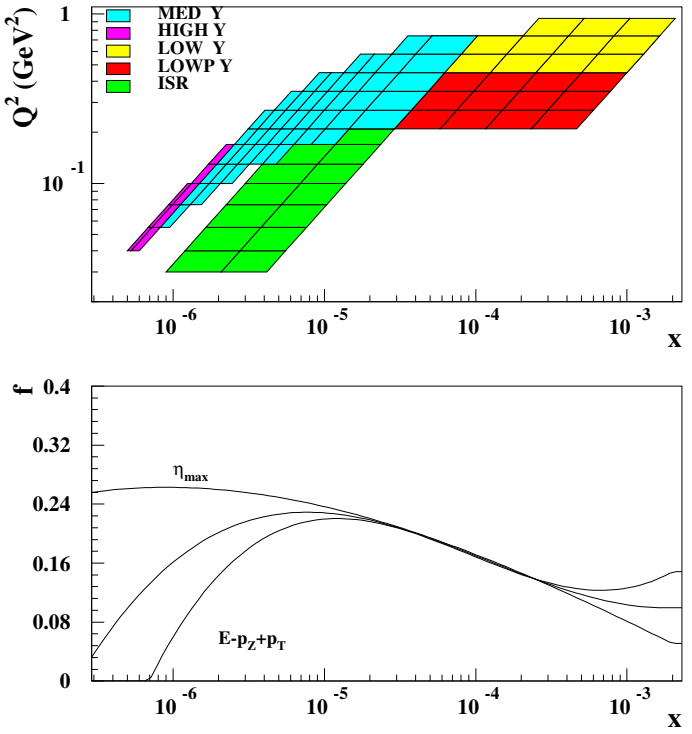


Figure 7.4: Parametrization of the diffractive fraction. The upper plot shows the $(x-Q^2)$-plane overlaid by the binning used for the extraction of $F_2$. The two parametrizations of the mixing fraction $f(x,Q^2)$ as a function of $x$ are shown in the lower plot [Am99]. The mean of the two parametrizations is also shown.

from $F_2^{\text{Data}}$ before the iterative unfolding of $F_2$ (see chapter 10.3.4) is finished. $n_{\text{norm,bin}}$ was found to be compatible with 1 after the unfolding. In the next step the fitted values of $f(x,Q^2)_i$ from all bins $i$ were fitted by a continuous function $f(x,Q^2)$. $f(x,Q^2)$ is a function of the generated MC quantities $x$ and $Q^2$. In order to determine $f(x,Q^2)$, the distributions which are available for both data and MC had to be used. In the case of MC these distributions differ from the true distributions in MC for example due to the reconstruction and detector simulation. To minimize the impact of these errors on the determined function $f(x,Q^2)$, the whole procedure described above is repeated several times. After reweighting the MC using the

result of the fit $n$, a correction of the previous results is determined with fit $n+1$. After a few iterations the procedure converges.
Two different approaches were used to determine the mixing fraction $f(x,Q^2)$. In the first approach the $\eta_{\max}$-distribution was used, because $\eta_{\max}$ is usually used to describe the fraction of non-diffractive and diffractive events. In the second approach, the hadronic quantities used in the data selection and reconstruction of the kinematic quantities were used in the fit. These are the difference of the energy and the longitudinal momentum $\delta_h = \sum_h (E_h - p_{Z,h})$ and the transverse momentum $p_{T,h}$ of the hadronic final state as defined in section 3.4. It was found that for both approaches $f(x,Q^2)$ could be parametrized as a function of one kinematic variable and that a parametrization as a function of $x$ resulted in the smallest $\chi^2$. $f(x)$ for both approaches is shown in figure 7.4. In the medium $y$ region $f(x)$ as determined from the $\eta_{\max}$ and the $\delta_h$- and $p_{T,h}$-distributions are in good agreement. The results of the two approaches in terms of $f(x)$ differ significantly at low and high $y$. It was chosen to use the average of the two parametrizations and to take into account their difference in the evaluation of the systematic uncertainties (see chapter 10.3.4).

## 7.4 Background MC events

The dominant source of background are events at values of $Q^2$ lower than the range covered in the analysis, which are reconstructed at higher values of $Q^2$ and pass all analysis cuts. The scattered positron leaves the detector through the rear beam pipe, and one or more photons originating from the hadronic final state fake a positron signal in the BPC. In most cases the photons are produced in $\pi^0$ decays. These events are referred to as photoproduction events.
Photoproduction events were generated using the PHYTHIA 5.724 generator. 109 K direct and 115 K resolved events were generated, which corresponds to a luminosity of 300 $\mathrm{nb}^{-1}$ and 30 $\mathrm{nb}^{-1}$ respectively. The following parameters were used to generate the events:

- $\mathrm{Q}_e^2 \geq 0.0$ GeV$^2$
- $F_2 = F_{2,\mathrm{ALLM97}}$
- $F_L$=0
- Energy of the final state positron $E_e^{'} \leq 17.64$ GeV
  $\rightarrow y \geq 0.36$

The distribution of the photoproduction MC events in the $(x-Q^2)$-plane overlaps with the signal MC for $Q_e^2 \geq 0.03$ GeV$^2$ and $0.36 \geq y \geq 0.93$. To avoid double counting of MC events, these photoproduction MC events were excluded from the sample. The events were generated using the ALLM97 parametrization of $F_2$, which gives a good description of 1995 BPC data [Br97] and the direct measurements of the photon-proton cross section at $Q^2 = 0$ GeV$^2$ from H1 and ZEUS (see chapter 11). Therefore, the photoproduction MC events were not reweighted.
Other sources of background events were found to be negligible (see section 9.7) and therefore not simulated.

# Chapter 8

# Efficiency and data quality studies

## 8.1 Introduction

An accurate reconstruction of the kinematic variables in the case of positrons scattered at angles close to $\pi$ requires a precise knowledge of the position of the interaction point and the positron beam tilt. In this analysis, positrons at scattering angles $\vartheta = \pi - \theta$ of $(15 - 40)$ mrad are detected using the BPC and BPT. Even a positron beam tilt of the order of 0.1 mrad has a significant impact on the reconstructed kinematic variables (see section 3.4). The same is true for the reconstructed vertex. A change in the reconstructed X-vertex of the order of the resolution of the CTD in X (1 mm) changes $\vartheta$ by 0.3 mrad. Therefore, it is necessary to take into account the positron beam tilt and the resolution of the reconstructed event vertex. This is discussed in section 8.2.
For a precise measurement it is required to estimate the efficiency of the triggers, detectors, and cuts applied. The selected number of events must also be corrected for the efficiency. BPC and BPT are used to select the signal events and to reduce the amount of background. Therefore, the efficiency of the BPC trigger and the BPT track finding has a significant impact on the selected number of events and has to be taken into account. Section 8.4 and 8.5 concentrate on the BPT and BPC efficiencies, respectively. The BPC timing, which is also used in the event selection, is discussed in section 8.3.

## 8.2 Vertex and beam tilt

The resolution of the X- and Y-vertex measured by the CTD amounts to 1 mm, which is considerably worse than the spread of the HERA beams of about 300 $\mu$m in X and 70 $\mu$m in Y. Instead of using the measured event-by-event X- and Y-vertex in the reconstruction of the kinematic quantities, the mean values for each run are calculated. They were determined by applying all trigger and analysis cuts used in the selection of the data sample for the extraction of $F_2$. Figure 8.1 shows the mean X- and Y-vertex as a function of the run number. The variations of the Z-vertex are considerably larger than the resolutions of both the CTD (4 mm) and the BPT (3 cm). Therefore, no averaging was done and the Z-vertex as determined on an event-by-event basis was used. The positron beam is tilted w.r.t. the ZEUS coordinate system. For large positron scattering angles, the effect of the beam tilt on the reconstruction of the kinematic variables $x$, $y$, and $Q^2$ is negligible. At small scattering angles w.r.t. the initial positron beam ($(15 - 40)$ mrad in this analysis) the beam tilt must be taken into account. The positron beam tilt with respect to the ZEUS coordinate system is determined by measuring the impact position of bremsstrahlung photons in the LUMIG detector. The beam tilt in X and Y





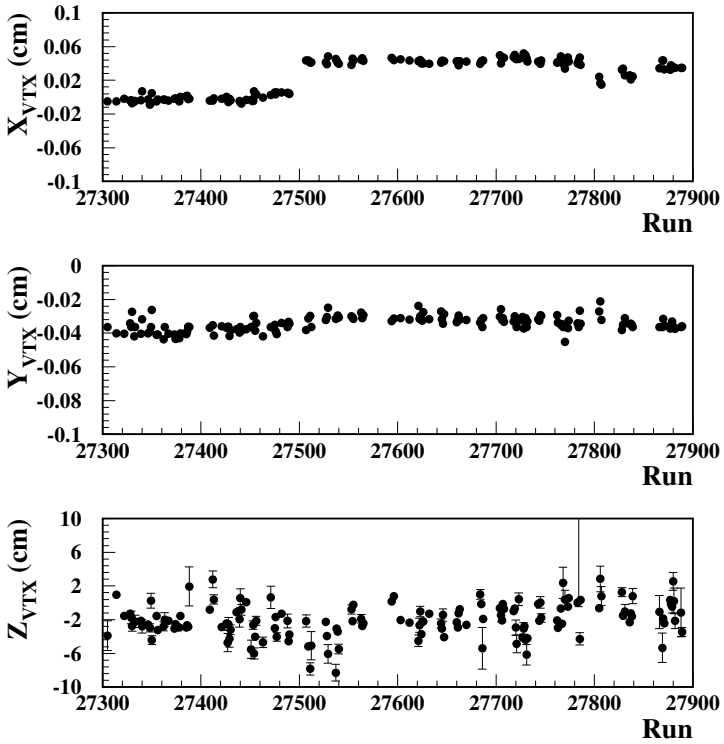


Figure 8.1: Mean X-, Y-, and Z-vertex in the data determined by the CTD as a function of the run number.

can be calculated using the reconstructed photon position in the LUMIG calorimeter and the Z-position of the detector (+107 m). The reconstructed position in the LUMIG calorimeter is given w.r.t. the nominal proton beam axis. Therefore, it has to be corrected for shifts between the ZEUS coordinate system and the nominal proton axis. The nominal proton orbit has been surveyed [We99] with respect to the mechanical axis of the CTD and therefore w.r.t. the ZEUS coordinate system. In the (X–Z)-plane the CTD axis is shifted by –0.405 mrad w.r.t. the nominal beam axis. In the (Y–Z)-plane the shift is 0.288 mrad. The upper plots in figure 8.2 shows the relationship of the ZEUS coordinate system (the mechanical coil axis of the CTD) and the nominal beam axis. The reconstructed X- and Y-positions in the LUMIG detector and the uncorrected and corrected beam tilts in X and Y are shown in the lower plots in figure 8.2 for one particular run. While the effect of the positron beam tilt in Y on the reconstructed

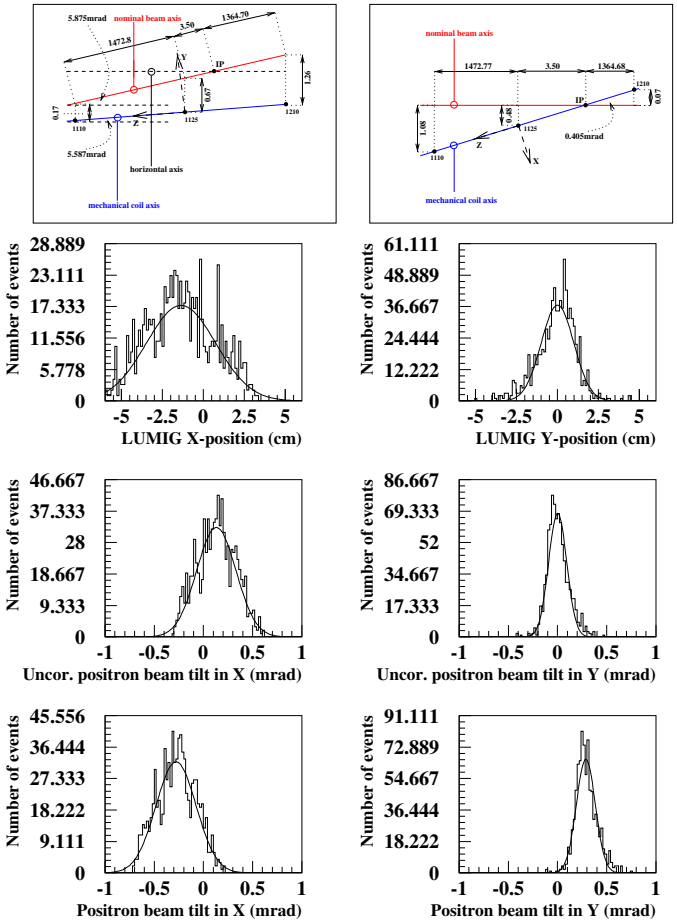


Figure 8.2: The two upper plots show the orientation of the mechanical axis of the ZEUS CTD w.r.t. the nominal beam axis [Su98]. In the X-Z-plane the CTD axis is shifted by –0.405 mrad w.r.t. the the nominal beam axis. In the Y-Z-plane the shift is 0.288 mrad. Since the position reconstructed in the LUMIG calorimeter is given w.r.t. the nominal beam axis the shifts have to be taken into account in the determination of the positron beam tilt. The six lower plots show the reconstructed X- and Y-position in the LUMIG detector, the uncorrected positron beam tilts in X and Y, and the beam tilts corrected for the tilt of the CTD axis w.r.t. the nominal proton orbit.

positron scattering angle is negligible small, the tilt in X does have to be taken into account. The variation of the beam tilt as a function of the run number has been checked. The results are shown in figure 8.3. Because of the variations of the beam tilt in X, the mean value of each



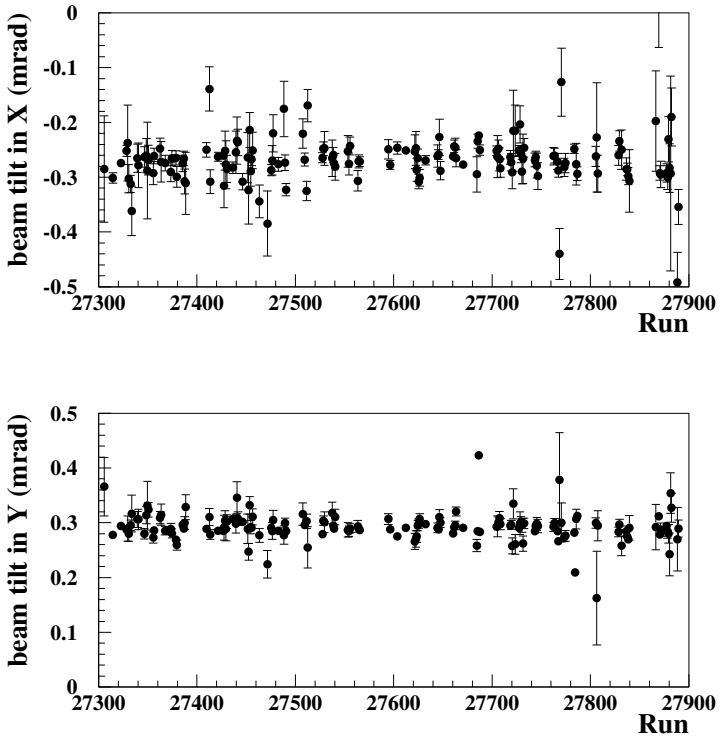


Figure 8.3: Positron beam tilt in X and Y corrected for the tilt of the CTD axis w.r.t. the proton orbit as a function of the run number.

run was used for the reconstruction of the kinematic variables.
The uncertainty of the measured run-dependent positron beam tilt was estimated from the average beam tilt for all runs. The error was estimated by adding conservative estimates of the uncertainties in the measurement in quadrature. These are the uncertainties of the X-vertex measured by the CTD (1 mm), the position of the LUMIG detector w.r.t. the nominal proton orbit in X (1 mm), the shifts between the nominal proton orbit and the ZEUS CTD X-axis at the Z-position of the LUMIG detector (1 mm), and the uncertainty of the reconstructed X-position in the LUMIG detector determined from a Gaussian fit (2.3 mm). The mean beam tilt was calculated as (–0.29 ±0.027) mrad.

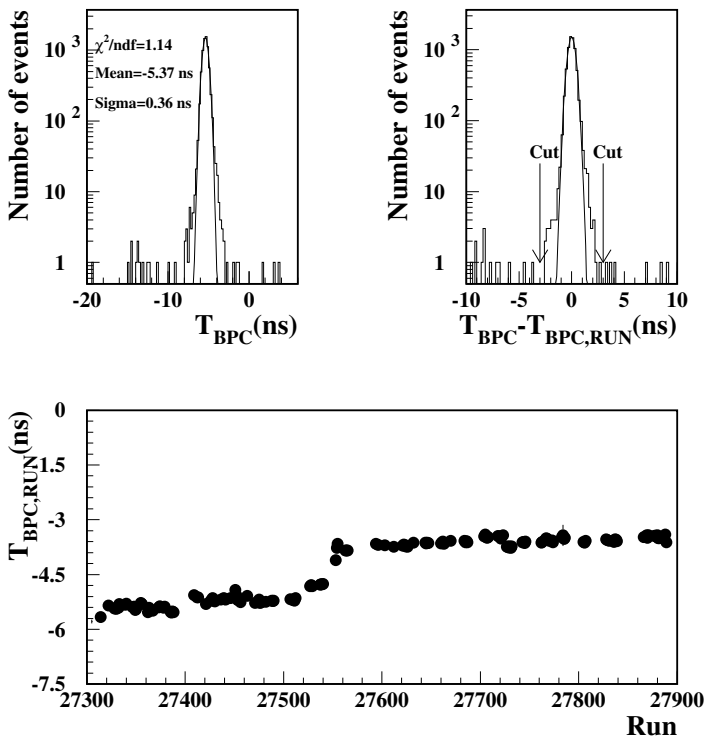


Figure 8.4: Reconstructed BPC time. The upper plots shows the reconstructed BPC time (left) fitted by a Gaussian and the deviation from the mean time (right) for one particular run. The lower plot shows the variations of the mean time as a function of the run number.

## 8.3 BPC timing

The BPC timing is calculated using the energy-weighted sum of the timing signals of all BPC readout channels as described in section 6.2. It is used to reject non $e^+p$ background in the event selection. Figure 8.4 shows the reconstructed BPC timing and the deviation from the mean BPC value for one particular run (upper plots) and the variations of the timing as a function of the run number (lower plot). The time distribution for one run is well described by the Gaussian. The width of the distribution is determined by the length of the HERA positron bunches of 0.8 mm and the resolution of the time reconstruction in the DSPs (see section 5.2). The width



of the time distribution expected due to the positron bunch size is given by $0.8\text{mm}/c = 0.003$ ns. Therefore, the dominant contribution to the measured distribution with a width of 0.5 ns is given by the time reconstruction in the DSPs.
The mean time has considerable variations from run to run. This is caused by run-to-run variations in the HERA $e^+p$ bunch crossing time which in turn is due to a shift in the relative phase of the proton and positron radio frequency. In order to select $e^+p$ events, the BPC timing was required to be within $\pm 3$ ns of the mean time of the respective run as indicated in figure 8.4.

## 8.4 BPT efficiency

The data taken with the BPC and BPT was checked using the online and offline DQM as described in section 5.6. Apart from some runs with the BPT high voltage turned off by mistake no problems were found for the runs used for the analysis presented here. Additional checks of the BPT data were conducted using the data sample used for the $F_2$ analysis. Figure 8.5 shows the efficiency of the two BPT planes as presented in section 6.8 as a function of the run number. No systematic changes of the efficiency of the two planes are visible, although there are variations from run to run. Runs with a lower efficiency typically suffer from low statistics. For these runs the efficiency is within errors compatible with the mean efficiency determined in section 6.8. Therefore, no run-dependent efficiency correction was applied in addition to the overall correction between data and MC.

## 8.5 BPC trigger efficicency

In the previous analyses of BPC data the efficiency of the used trigger slots was found to be 1 in the range of the selected offline energy ([Su98], [Mo98], [Ma98]). A detailed study of the efficiency of all trigger slots at FLT, SLT, and TLT level has been done. The results for the medium $y$ triggers, which have been used before are in agreement with the previous results. The low $y$ (LOW and LOWP), high $y$, and the ISR trigger slots have not been used in any previous analysis except for calibration purposes. Several of the analysis cuts for these regions have been designed to have a fully efficient trigger based on the results detailed below. An event sample independent of the BPC triggers was selected using the following FLT triggers and DSTBITs:

- FLT 18: LPS hit
- FLT 33: LUMIG signal
- FLT 40: CAL EMC
- FLT 41: CAL transverse momentum
- FLT 42: CAL and CTD
- FLT 44: BCAL and CTD
- DSTBIT 9: Positron found in CAL from at least one of four positron finders

None of these triggers uses information from the BPC or BPT. Most of the triggers select events based on information from the CAL and CTD. FLT 18 and FLT 33trigger on hits in the LPS and the LUMIG calorimeter respectively. The efficiency of all triggers (FLT, SLT,

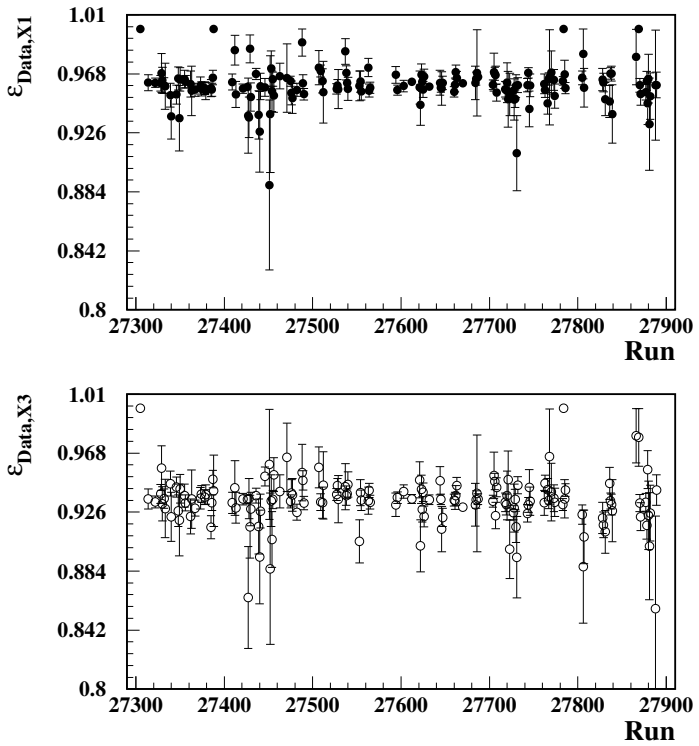


Figure 8.5: BPT efficiency as a function of the run number for plane X1 (upper plot) and plane X3 (lower plot).

TLT) was checked. To study the efficiency of the SLT and TLT triggers, subsets of the events selected by the seven triggers shown above were used. Each SLT (TLT) slot requires at least one fired FLT (FLT and SLT) slot to have fired as shown in figure 5.3. Each subset requires the corresponding FLT (FLT and SLT) trigger(s) to have accepted the events. To study the efficiency of one specific trigger as a function of one of its cut quantities, the analysis cut on this quantity was loosened and those on the other quantities kept at their nominal values.
The left plots in figure 8.6 show the efficiency of the three FLT slots 32, 50, and 52 as a function of the offline energy. For FLT 52 the efficiency is 1 at energies higher than the offline cut. FLT 50 is fully efficient at energies higher than 3.5 GeV. The analysis cut on the energies was chosen to be at 3.0 GeV to extend the kinematic region to higher values of $y$. The bins used for the



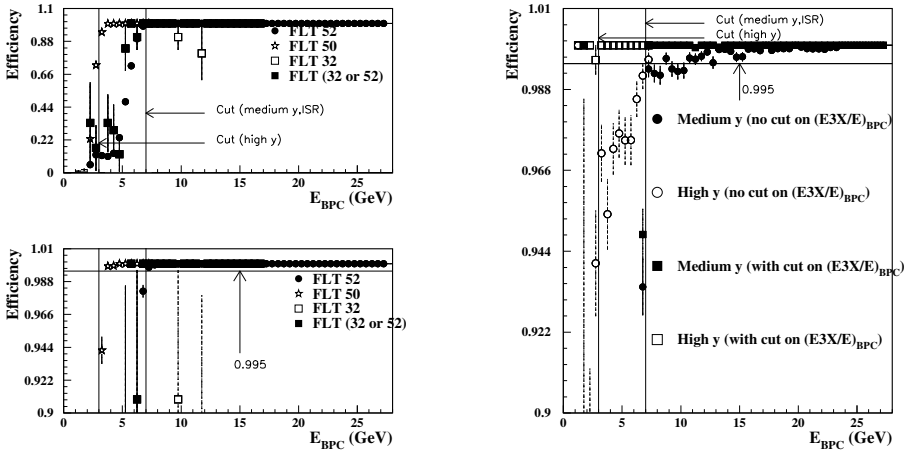


Figure 8.6: Efficiency of the FLT trigger slot 32, 50, and 52 (left plots) as a function of the offline BPC energy. The lower plot is a magnification of the upper one. The right plot shows the efficiency of the SLT trigger slot DIS 2 for the medium and high $y$ region as a function of the offline BPC energy. The plot includes the efficiencies with and without the offline cut $(E3X/E)_{\mathrm{BPC}} > 0.35$.

extraction of $F_2$ were chosen in such a way that only a few bins have an efficiency below 1. The inefficiency of these bins of up to 0.02 is taken into account in the extraction of $F_2$ and the uncertainty of the efficiency determination is included in the evaluation of the systematic errors. The lower plot shows that the efficiency for the ISR region is within errors compatible with 1 whether only FLT 32 or one of FLT 32 and FLT 52 is required.
The study of the efficiency of the SLT DIS 2 trigger showed that an analysis cut on the energy fraction $(E3X/E)_{\mathrm{BPC}} > 0.35$ had to be imposed offline to have a fully efficient trigger. $E3X$ is the energy deposited in the BPC X-finger with the most energy and the two neighbouring ones. A similar cut is made in SLT DIS 2 using the reconstructed energies at SLT level. The efficiency of SLT slot DIS 2 as a function of the offline energy is shown the right plot in figure 8.6 for the different analysis regions. Without the offline cut the efficiency drops at low energies for the medium and high $y$ region.
The efficiency of the TLT trigger slots was found to be 1 except for the low $y$ region. Due to the cuts on $y_{\mathrm{JB}}$ imposed by TLT DIS 17 ($y_{\mathrm{JB,TLT}} > 0.02$) and TLT DIS 23 ($y_{\mathrm{JB,TLT}} < 0.1$), both triggers are not fully efficient for the whole region. Figure 8.7 shows the efficiency of both triggers as a function of $y_{\mathrm{JB,TLT}}$. Also shown is the efficiency of an OR of the two triggers, which is fully efficient for the whole region. For the LOWP region the used trigger TLT DIS 18 was found to be fully efficient.

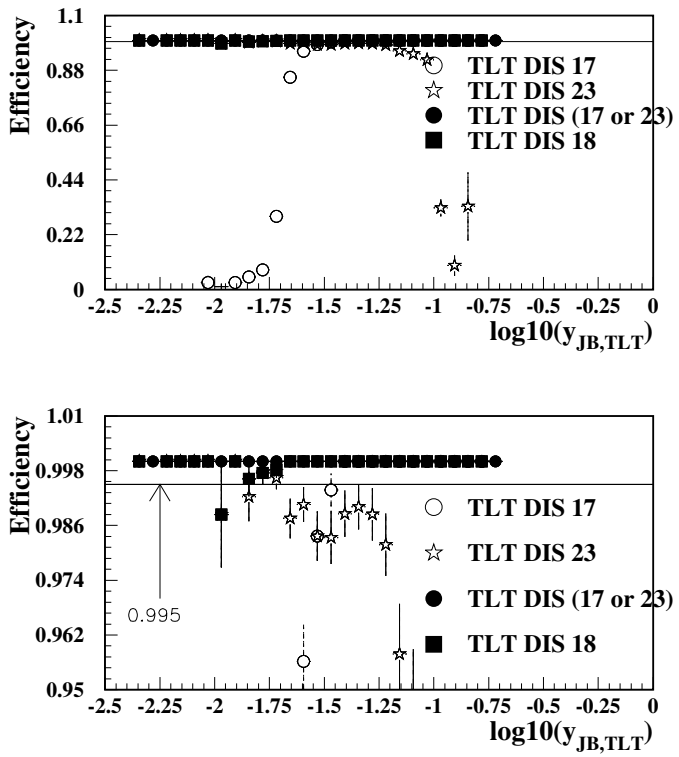


Figure 8.7: Efficiency of the TLT trigger slot 17, 18, and 23 in the low $y$ region (LOW and LOWP) as a function of the $y_{\rm JB}$ calculated at TLT level (upper plot). The lower plot is a magnification of the upper one.

# Chapter 9

# Event selection

The data used for the measurement of the total $\gamma^*$p cross section $\sigma_{tot}^{\gamma^* p}$ and the proton structure function $F_2(x, Q^2)$ at low $Q^2$ and very low $x$ using the ZEUS BPC and BPT was taken in 1997 after the BPT had been successfully installed and commissioned. The data taken from September 1997 until the end of the HERA running period in October 1997 corresponds to the ZEUS run range from 27305 to 27889. Only the runs for the low luminosity configuration were used because in the high luminosity configuration the BPC trigger slots were prescaled. Some special runs used for BPC calibration with lower prescale factors than in the low luminosity configuration were also included.

## 9.1 Trigger selection

The final state positron is detected in the BPC and BPT. For a precise measurement, energy and scattering angle of the final state positron have to be measured with high accuracy. The trigger and analysis cuts were chosen to provide a sample of identified final state positrons and to reduce background from beam gas and photoproduction events.
The BPC triggers were designed to measure $F_2$ in a broad kinematic range at low $Q^2$. In order to have better control of the trigger rate, several triggers rather than one for the whole region were designed (see section 4.4). To extend the kinematic region covered in the previous analysis [Su98], several of the BPC triggers were used. The data is selected by requiring one of the BPC third-level triggers TLT DIS 17, DIS 18, DIS 21, DIS 22 and 23. Figure 9.1 shows these triggers and their relationship to the BPC FLT and SLT triggers. Since all these TLT triggers, with the exception of DIS 18, require specific FLT and SLT slots, it is sufficient to select the events at TLT level. In the case of DIS 18, only events which originate from FLT 52 and SLT DIS 2 are selected in order to have a well-defined trigger chain. For the extraction of $F_2$ a binning in $y$ and $Q^2$ rather than in $x$ and $Q^2$ was used to make optimal use of the accessible phase space. The different trigger slots correspond to different regions in $y$ and $Q^2$. The regions correspond to the following ranges in $y$

- low $y$ (LOW): $0.005 < y < 0.08$
- low $y$ prescaled (LOWP): $0.005 < y < 0.16$
- medium $y$ (MED): $0.08 < y < 0.74$
- high $y$ (HIGH): $0.74 < y < 0.89$
- events with initial state radiation (ISR): $0.08 < y < 0.37$





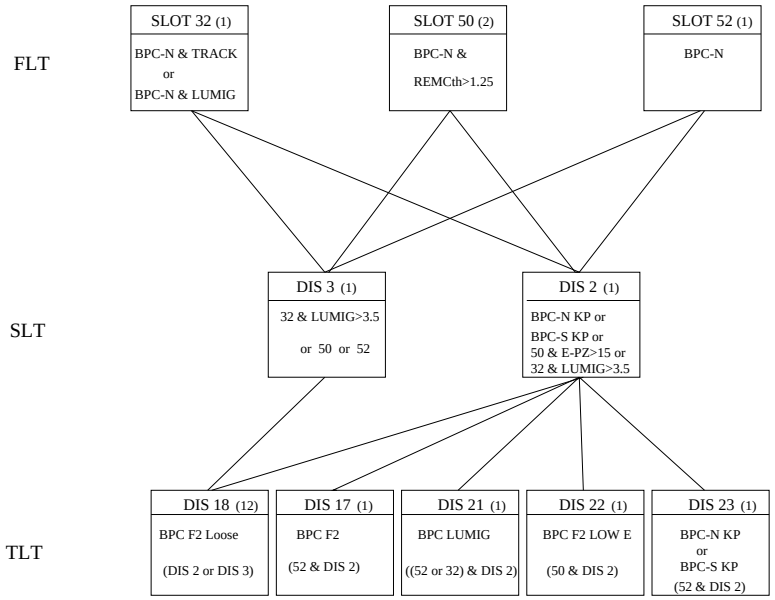


Figure 9.1: BPC trigger configuration used for the 1997 $F_2$ analysis. The FLT trigger slots are shown at the top, the SLT slots in the middle, and the TLT slots at the bottom. The lines indicate the relationship between the different trigger slots. The number in parenthesis after the slot name indicates the prescale factor used for the low luminosity runs in 1997. For the TLT slots a short description of the FLT and SLT triggers required is given in parenthesis.

The DIS 18 trigger used for the LOWP region can also be used to access the LOW region, but since it is prescaled by a factor of 12 compared to the other trigger statistics is low. The ISR region is not used to extract $F_2$, but to estimate the impact of radiative corrections as discussed in section 10.3.3. A list of the requirements at trigger level for the different regions is given in tables B.1 and B.2 in appendix B. In the case of the BPC, only BPC timing and energy cuts are applied at the FLT. Information from other components is also used. Usually the horizontal Y-strips are used because they are less affected by background events and radiation damage. The events for the MED and LOW regions are taken by the FLT slot 52. The BPC energy cut ($E^{\mathrm{FLT}}_{\mathrm{BPC,Y}} \geq 4$) rejects events with low energy positrons in the BPC, which corresponds to high values of $y$. To access this region FLT slot 50 with a lower BPC energy cut ($E^{\mathrm{FLT}}_{\mathrm{BPC,X}} \geq 1$) is used. At SLT level (SLT DIS 2) a cut on the position of the most energetic BPC X- and Y-strips ($2 < X^{\mathrm{SLT}}_{\mathrm{BPC,max}} < 12$, $5 < Y^{\mathrm{SLT}}_{\mathrm{BPC,max}} < 12$) is imposed on all events. The cuts reduce background, which peaks at $X^{\mathrm{SLT}}_{\mathrm{BPC,max}} = 1$, and events, where the scattered positron does not leave the beam pipe through the BPC exit window. The cut is in first approximation a cut on the fiducial area of the BPC as determined in section 6.11. Due to the cuts on $y^{\mathrm{TLT}}_{\mathrm{JB}}$ at TLT DIS 17 and DIS 23 each of these triggers were not fully efficient as shown in section 8.5. In order to have a fully efficient trigger for the low $y$ region an OR of these triggers was used.

## 9.2 Reconstruction

Several studies have been made to determine the best reconstruction methods for this analysis as detailed in chapter 6. It was found [Am99a] that the energy cuts used for noise suppression in the CAL are required to be higher than in the previous analysis [Su98]. The thresholds used for isolated EMC and HAC cells were $E_{\mathrm{EMC}} > 120$ MeV and $E_{\mathrm{HAC}} > 160$ MeV respectively. Only the low $y$ region is affected by the different cuts. The Z-vertex was reconstructed by the BPT, because the vertex reconstruction by the CTD was not fully efficient over the whole kinematic region. At low $y$ and for diffractive events the current jet is produced in the forward region, resulting in a reduced probability of reconstructing the event vertex. Since the BPT used only the scattered positron to reconstruct the Z-vertex it is efficient over the whole kinematic region independent of the event topology. Therefore, the Z-vertex as determined by the BPT was used.

### 9.2.1 Reconstruction of BPC and BPT quantities

The BPC and BPT quantities are reconstructed using the methods detailed in chapter 6. The X- and Y-position ($X_{\mathrm{BPC}}$ and $Y_{\mathrm{BPC}}$) at the shower center-of-gravity inside the BPC are calculated using the strip imbalance method. The BPC timing $T_{\mathrm{BPC}}$ and the shower size $\sigma_{\mathrm{BPC}}$ are calculated using the linear and logarithmically-weighted strip energies respectively. The BPT track is reconstructed as a straight line going through one hit in each silicon plane. The mean Z-vertex of the run and the reconstructed BPC position are included in the definition of $\chi^2$ to find the best track. $X_{\mathrm{BPT}}$ is calculated by extrapolating the BPT track to the shower center-of-gravity inside the BPC in Z, while $Y_{\mathrm{BPT}}$ is set to $Y_{\mathrm{BPC}}$ as the two BPT planes only measure in X. $Z_{\mathrm{VTX,BPT}}$ is the extrapolation of the BPT track to the mean X-vertex of the run. $X_{\mathrm{VTX,BPT}}$ and $Y_{\mathrm{VTX,BPT}}$ are set to the mean X- and Y-vertex of the run as measured by the CTD. The positron scattering angle $\theta_e$ is calculated from the BPT Z-vertex and $X_{\mathrm{BPT}}$ and $Y_{\mathrm{BPT}}$. It is corrected for the beamtilt as measured by the LUMIG detector on a run-by-run basis, which in turn has been calculated using the tilt of the nominal proton orbit w.r.t. the ZEUS coordinate system. The distance $X^{\mathrm{COR}}_{\mathrm{BPT}}$ and $Y^{\mathrm{COR}}_{\mathrm{BPT}}$ to the mean X- and Y-position of the positron beam are used for the BPC fiducial cut. They are calculated by projecting $X_{\mathrm{BPT}}$ and $Y_{\mathrm{BPT}}$ to the Z-position of the BPC front face, taking into account the Z-vertex and the beam tilt of the respective run.

### 9.2.2 Reconstruction of the hadronic final state

Three different methods to reconstruct the hadronic quantities were tested. In the previous analysis only the energy deposits in cells of the CAL were used. The CORANDCUT [Gr98] method, designed for the analysis of high $Q^2$ events, is also cell-based, but includes correction for backsplash of particles from one CAL segment to another. The so-called ZUFO [Br98] [Tu99] reconstruction uses combined objects of clusters of energy deposits in the CAL and the corresponding tracks from the CTD. The ZUFO method was found to have the best resolution and the best agreement between MC and data. Therefore, all hadronic quantities like $y_{\mathrm{JB}}$ and $\delta_h$ have been calculated using this method (see section 3.4).

### 9.2.3 Reconstruction of kinematic variables

Both BPC and BPT were designed to measure the energy, position, and scattering angle of the final state positron with high precision. In previous analyses ([Su98], [Ma98]) it was shown



that the electron method was superior to the others. Therefore, the same method has been used here whenever possible. This is the case for the medium and high $y$ regions. In the low $y$ and the ISR regions the $e\Sigma$ method is used, which calculates $Q^2$ from the scattered positron as the electron method, but $y$ from the $\delta_h$ of the hadronic final state and the positron scattering angle (see section 3.4). For the low $y$ region ($y < 0.08$) this is necessary as the resolution of the electron method diverges for low values of $y$ as shown in section 3.4. In the ISR region the same method was used to limit the migrations in $y$ dominated by the energy resolution of the LUMIG detector.

## 9.3 Background reduction

Background events, which survive the ZEUS trigger cuts, must either be rejected by the analysis cuts or be properly simulated in the MC. The background events originating from proton or positron beam gas interaction outside the detector are reduced by a cut on the reconstructed CAL timing $T_{\mathrm{CAL}}$. These events typically have a shifted reconstructed timing either in the RCAL or FCAL compared to events inside the detector with a nominal timing at 0 ns. A cut on the Z-vertex $Z_{\mathrm{VTX}}$ further reduces the number of these events, because they are characterized by a uniform Z-vertex distribution, contrary to the case of $e^+p$ events with a Gaussian-shaped Z-vertex distribution centered around the nominal interaction point, plus tails caused by $e^+p$ events in the proton satellite bunches. Another type of background is reduced by the vertex cut. Off-momentum positrons which have a reduced energy due to bremsstrahlung are transported by the HERA optics into the BPC. These positrons have a track in the BPT, but the vertex resolution of the BPT is sufficient to reject these events since the measured vertex is typically outside the ZEUS detector.
Events with positrons which have lost energy in inactive material due to pre-showering on the way to the BPC are expected to have a broader reconstructed shower size $\sigma_{\mathrm{BPC}}$. Most of these events are rejected by the BPC fiducial volume and the BPC shower width cut. Pre-showered positrons deposit less energy $E_{\mathrm{BPC}}$ in the BPC because a fraction of the produced particles leave the detector through the rear beam pipe. A cut on the total $(E - P_Z)$ of the event as defined below reduces the fraction of pre-showered positrons in the final event sample further. The main reason for a cut on the total $\delta = (E - P_Z)$ of the event defined as

$$\delta = (E - P_Z) = \delta_h + \delta_{\mathrm{BPC}} = \sum_h (E_h - p_{Z,h}) + 2 \cdot E_{\mathrm{BPC}} \tag{9.1}$$

is the reduction of background from initial state radiation, photoproduction, and proton beam gas events. The sum in equation 9.1 extends over all reconstructed CAL energy clusters. In the case of the BPC and other detector components located close to the beam pipe in the direction of the initial positron beam, $\delta_{\mathrm{BPC}}$ is, to good approximation, given by $2 \cdot E_{\mathrm{BPC}}$. Conservation of energy and momentum yields that the total $\delta$ of the event peaks at two times the positron beam energy of approximately 27.5 GeV. This ignores possible particle losses in the backward beam hole. In the case of pre-showered positrons the measured value $\delta_{\mathrm{meas}}$ is reduced by two times the energy, which is lost in the rear beam pipe. The same is also true for events with a radiated photon in the initial state, which is emitted close to the initial positron direction and lost in the rear beam pipe. A lower cut on $\delta_{\mathrm{meas}}$ of 30 GeV used in this analysis is equivalent to an upper cut on the energy of the radiated photon $E_\gamma$ of 12.5 GeV. The lower cut on $\delta_{\mathrm{meas}}$ provides a way to reduce the amount of ISR events with a hard photon in the initial state and therefore the amount of radiative corrections.

In the case of photoproduction events the initial positron emits an almost real photon with energy $E_\gamma^{\mathrm{PHP}}$, which causes the interaction while the final state positron leaves the main detector undetected through the rear beam hole. One or more photons originating from the hadronic final state fake a positron signal in the BPC. In most cases the photons are from $\pi^0$ decays. In the case of high energy $\pi^0$s it is expected that both photons hit the BPC and the event is rejected by the BPC shower cut. For photoproduction events, conservation of energy and momentum means that $\delta$ peaks at two times the energy $E_\gamma^{\mathrm{PHP}}$ of the quasi-real photon. The flux of quasi-real photons decreases with increasing values of $E_\gamma^{\mathrm{PHP}}$. This results in lower values of $\delta_{\mathrm{meas}}$ compared to signal events and most of the photoproduction background events are removed by imposing a lower cut on $\delta_{\mathrm{meas}}$.
Proton beam gas events with the event vertex inside the main detector result in energy depositions in the forward direction and thus are characterized by relatively small values of $\delta_{\mathrm{meas}}$. Proton beam gas events upstream of the main detector could lead to considerable energy depositions in the RCAL and BPC and thus values of $\delta_{\mathrm{meas}}$ greater than two times the positron beam energy. In addition to the CAL timing cut described above, an upper cut on $\delta_{\mathrm{meas}}$ further reduces the amount of proton beam gas events.
Events from $ep$ scattering at higher $Q^2$ than used in this analysis also contribute to the background. In this case the scattered positron is detected in the CAL and as in the case of photoproduction events photons fake a signal in the BPC. However, the contribution of events from higher $Q^2$ is expected to be negligible, because the $ep$ cross section increases towards lower values of $Q^2$. The amount of background events in the final sample is discussed in section 9.7.

## 9.4 Analysis cuts

Usually the quantities available at a certain trigger level (FLT, SLT, TLT) are slightly different, because the amount and accuracy of information available for the trigger decision increases from FLT to TLT. Since detailed calibration and noise studies can only be done after the trigger decision, the quantities available after reconstruction also differ from the ones at TLT level. Therefore, the cuts used at trigger level are usually looser than those used in the analysis. The BPC is not included in the MC trigger simulation ZGANA (see section 9.2). Therefore, the selection of MC events could not be done by the same triggers used for the data events. To make sure that data and MC events are selected by the same cuts, the analysis cuts used for both sets are tighter than those used at trigger level. If the hadronic quantities which are used at trigger level are also available offline, then the trigger cuts are repeated in the analysis cuts. The analysis cuts fall into two categories of requirements among the final state positron and the hadronic final state. The following section provides an overview of these two categories. The requirements on the final state positron except on its energy are essentially common to all five regions, whereas the cuts imposed on the hadronic final state differ due to the different event topologies and the requirements on the kinematic regions to be accessed. The following cuts are applied for the analysis. Unless stated otherwise, low $y$ applies to both the LOW and LOWP region and medium $y$ to both the MED and ISR region.

### 1. Identification of the final state positron

These cuts are used to identify the final state positron within the fiducial region of the BPC while reducing the number of background events.



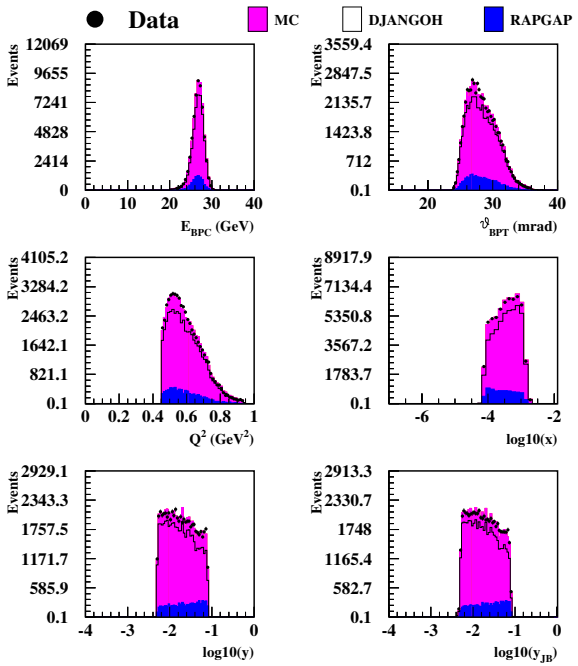


Figure 9.2: Comparison of MC and data: Low $y$ region (part one). Measured quantities from BPC and BPT and the reconstructed kinematic variables for the low $y$ region.

### 1a. BPC fiducial cut

The position of the final state positron $(X_{\mathrm{BPT}}, Y_{\mathrm{BPC}})$ is determined by extrapolating the best BPT track to the front face of the BPC and correcting for the different beamtilt and BPC position in data and MC. The Y-position $Y_{\mathrm{BPC}}$ is taken from the BPC position reconstruction as the two BPT planes installed in 1997 provide no means to measure this position. The fiducial region determined in section 6.11 is used. The tighter cut on $X_{\mathrm{BPT}}$ for the LOW region was necessary because of the cut on the X-position in the BPC done at the TLT DIS 23 ($X_{\mathrm{BPC}}^{\mathrm{TLT}} > 7.0$ cm).

- BPC fiducial cut:
  - 5.2cm (7.2cm for LOW) $< X_{\mathrm{BPT}} < 9.3$ cm
  - $-2.3$ cm $< Y_{\mathrm{BPC}} < 2.8$ cm
  - $X_{\mathrm{BPT}} - Y_{\mathrm{BPC}} < 10.7$ cm
  - $X_{\mathrm{BPT}} + Y_{\mathrm{BPC}} < 11.2$ cm

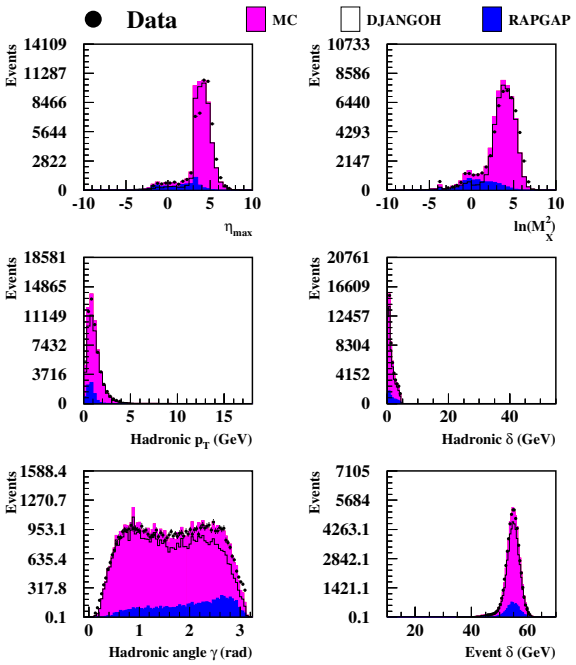


Figure 9.3: Comparison of MC and data: Low $y$ region (part two). Reconstructed quantities of the hadronic final state for data and MC.

### 1b. BPC shower cut

The reconstruction of the shower width was discussed in section 6.2. It provides a means of rejecting events of remaining pre-showered positrons after the fiducial cut or hadrons which have a larger reconstructed shower width compared to positrons.

- BPC shower size:
  - $\sigma_{\mathrm{BPC}} = \sqrt{\frac{1}{2}(\sigma^2_{X,\mathrm{BPC}} + \sigma^2_{Y,\mathrm{BPC}})} < 0.8$ cm

### 1c. BPC energy cut

The BPC energy reconstruction has been discussed in section 6.10. The trigger efficiency was checked in section 8.5. It was found that all used triggers were fully efficient above the used energy cuts, except the FLT slot 50 used to select low energetic positrons. The inefficiency which was below 2% affected only the bins at the highest $y$ and is taken into account in the evaluation of the systematic uncertainties.



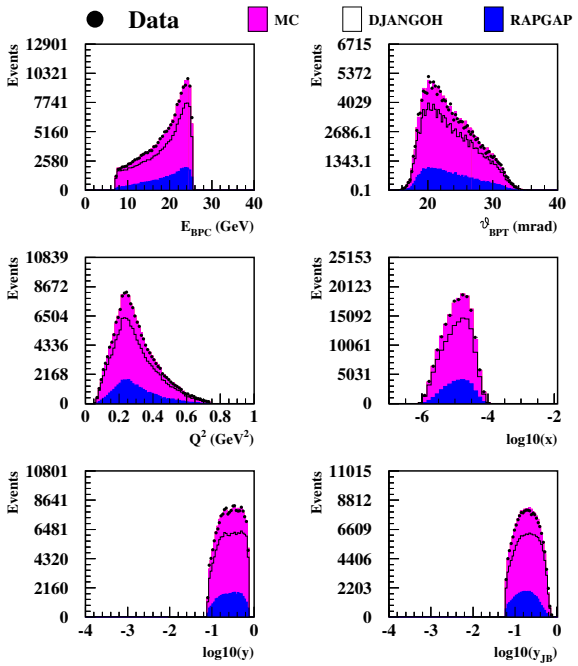


Figure 9.4: Comparison of MC and data: Medium $y$ region (part one). Measured quantities from BPC and BPT and the reconstructed kinematic variables for the medium $y$ region.

- BPC positron energy:
  - low $y$: $E_{\mathrm{BPC}} > 20$ GeV
  - medium $y$: $E_{\mathrm{BPC}} > 7$ GeV
  - high $y$: 3 GeV$< E_{\mathrm{BPC}} <$ 7.2 GeV

In order to have a fully efficient SLT (DIS 2) is was necessary to impose a similar cut on the energy fraction as applied at the SLT in the analysis cuts. At SLT the fraction of energy $E3X_{\mathrm{BPC}}/E_{\mathrm{BPC}}$ of the total energy contained in the vertical finger with the most energy and the two neighbouring strips was required to be greater than 35%. The required cut on the offline BPC energy was found to be the same.

- BPC energy fraction:
  - $E3X_{\mathrm{BPC}} > 0.35 \cdot E_{\mathrm{BPC}}$

### 1d. BPC timing

For a given event and run the BPC timing is required to be within 3 ns of the mean time $T^{\mathrm{RUN}}_{\mathrm{BPC}}$ for the $e^+p$ collision determined for this run. Since the BPC timing is not defined in the MC this cut is only applied to data events.

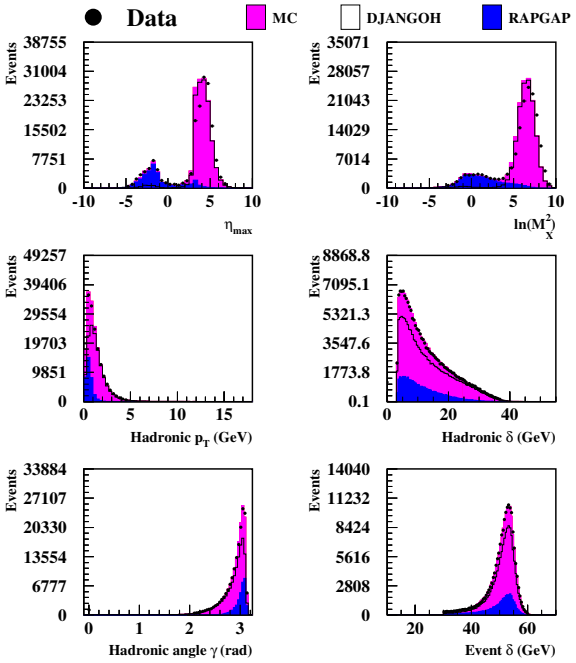


Figure 9.5: Comparison of MC and data: Medium $y$ region (part two). Reconstructed quantities of the hadronic final state and $\delta$ of the event for data and MC.

- BPC timing w.r.t. the mean timing of the run $T_{\mathrm{BPC}}^{\mathrm{RUN}}$:
  – $|T_{\mathrm{BPC}} - T_{\mathrm{BPC}}^{\mathrm{RUN}}| < 3$ ns

### 1e. BPT track requirement

The BPT track finding and fitting procedure has been described in section 6.5. To suppress photoproduction background and make use of the better position resolution of the BPT compared to the BPC at least one BPT track had to be found. Additionally, the X-positions on the BPC front face calculated from the BPC ($X_{\mathrm{BPC}}$) and the BPT track ($X_{\mathrm{BPT}}$) have to agree within $5\sigma$, where $\sigma$ is given by the position resolution of the BPC. The positron scattering angle w.r.t. the initial positron beam was required to be below 40 mrad.

- BPT track reconstruction:
  – at least one reconstructed BPT track

- BPC-BPT track matching:
  – $|X_{\mathrm{BPC}} - X_{\mathrm{BPT}}| < 5\sigma$, $\sigma = 0.22\ \mathrm{cm}/\sqrt{E_{\mathrm{BPC}}/\mathrm{GeV}}$



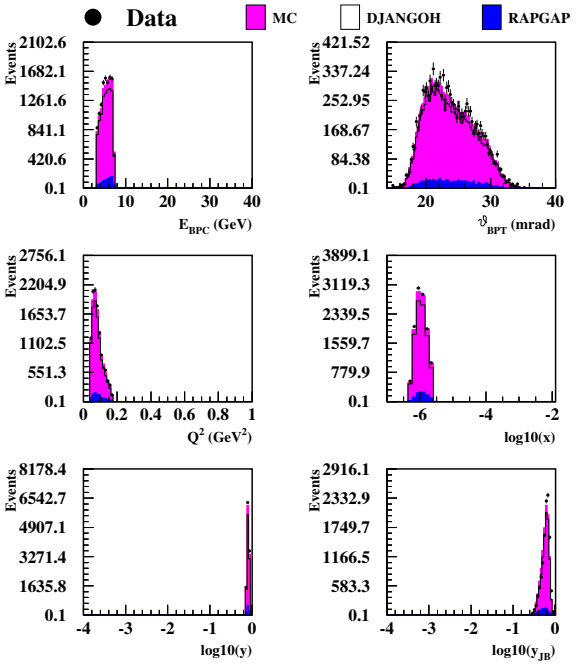


Figure 9.6: Comparison of MC and data: High $y$ region (part one). Measured quantities from BPC and BPT and the reconstructed kinematic variables for the high $y$ region.

- Positron scattering angle w.r.t. the initial positron beam as reconstructed from the BPT track:
  – 0.0 mrad $\leq \theta_e \leq$ 40 mrad

### 1f. Vertex

The Z-position of the vertex $Z_{\mathrm{VTX}}$ was reconstructed by extrapolation of the BPT track to the mean X-position of the vertex for a given run as described in section 6.5. Because the MC sample was generated with a Z-vertex distribution up to $\pm$100 cm the reconstructed vertex was required to be within $\pm$90 cm.

- Vertex:
  – $-90$ cm $< Z_{\mathrm{VTX}} <$ 90 cm

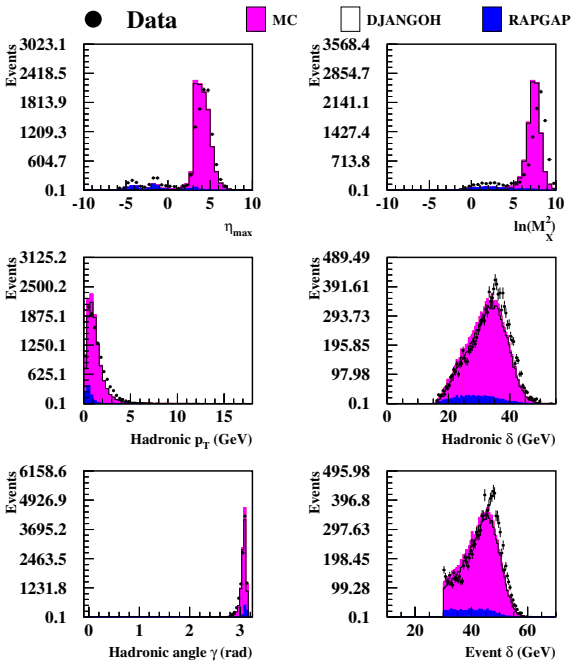


Figure 9.7: Comparison of MC and data: High $y$ region (part two). Reconstructed quantities of the hadronic final state and $\delta$ of the event for data and MC.

### 2. Cuts on the hadronic final state

#### 2a CAL timing

The CAL timing $T_{\mathrm{CAL}}$ was required to be within 10 ns of the nominal value at 0 ns. Since the CAL timing is not defined in the case of MC this cut is only applied to data events.

- CAL timing:
  $-|T_{\mathrm{CAL}}| < 10$ ns

#### 2b. Cut on $y_{\mathrm{JB}}$ using the CAL

The reconstruction of the kinematic variable $y$ using the Jacquet-Blondel method has been discussed in detail in section 3.4. At low $y$ the Jacquet-Blondel method is more accurate in reconstructing the kinematical variable $y$ than the estimate of $y$ using the electron method. At high and medium $y$ a cut $y_{\mathrm{JB}} > 0.06$ was used to reduce the amount of migration from lower values of $y$. For the same reason a lower cut is required at low $y$. The cut was set to $y_{\mathrm{JB}} > 0.004$ because the version of HERACLES used to generate the MC events was known to produce reasonable results only for $y \cdot (1-x)^2 \geq 0.004$ [Sp96]. The upper cut of $y_{\mathrm{JB}} < 0.1$ in the low $y$ region is used to reduce migrations in the other direction.



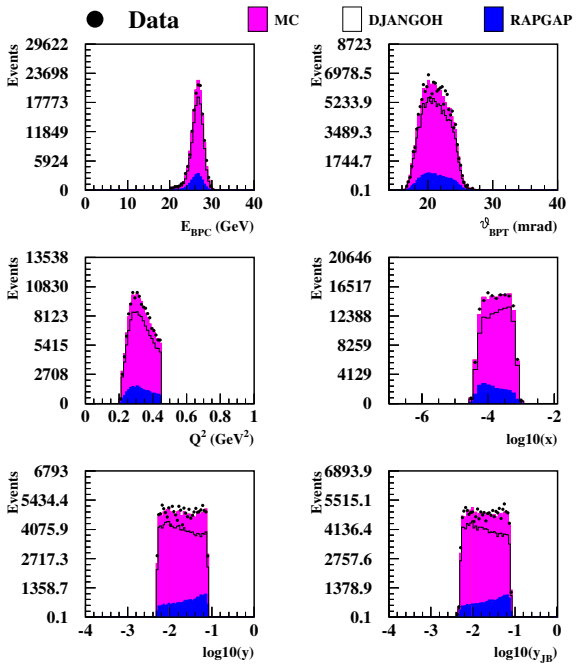


Figure 9.8: Comparison of MC and data: Low $y$ (prescaled) region (part one). Measured quantities from BPC and BPT and the reconstructed kinematic variables for the low $y$ (prescaled) region.

- $y_{\mathrm{JB}}$:
  - medium and high $y$: $y_{\mathrm{JB}} > 0.06$
  - low $y$: $0.004 < y_{\mathrm{JB}} < 0.1$

#### 2c. Cut on the total $(E - P_Z)$ of the event

A lower cut on $\delta_{\mathrm{meas}}$ of 30 GeV rather than 35 GeV as done in the previous analysis [Su98] was used. This was done to be less sensitive to the simulation of the hadronic final state in the MC, especially at low values of $x$ (see section 7.3). In the case of the ISR region, where the initial state photon is detected in the LUMIG detector, the cuts on $\delta_{\mathrm{meas}}$ are tightened and the LUMIG detector is included in the calculation.

- $\delta_{\mathrm{meas}} = \delta_h + 2 \cdot E_{\mathrm{BPC}}$:
  - all excecpt ISR: 30 GeV $< \delta_{\mathrm{meas}} <$ 65GeV
  - ISR: 40 GeV $< \delta_{\mathrm{meas}} + 2 \cdot E_{\mathrm{LUMIG}} <$ 60 GeV

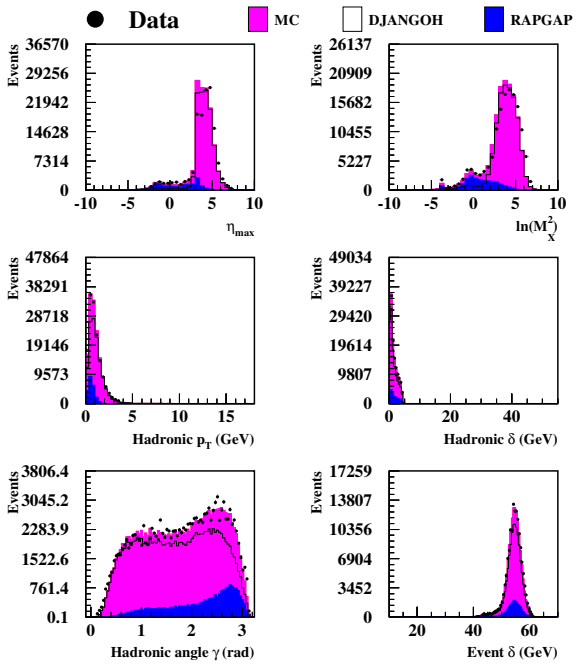


Figure 9.9: Comparison of MC and data: Low $y$ (prescaled) region (part two). Reconstructed quantities of the hadronic final state and $\delta$ of the event for data and MC.

### 3. Cuts to simulate the FLT and TLT cuts for MC

The following cuts are applied to simulate the FLT and TLT cuts for MC, because the BPC is not included in the MC trigger simulation. They were applied to both data and MC. The hadronic quantities are the same as used in the trigger. For BPC and LUMIG the offline energy was used. It was checked that the use of offline energies did impose tighter cuts than the ones used at trigger level.

- $y_{\rm JB}$ reconstructed from the hadronic variables at TLT:
  – only medium $y$ (TLT DIS 17): $y_{\rm JB}^{\rm TLT} > 0.02$
  – only ISR (TLT DIS 21): $y_{\rm JB}^{\rm TLT} > 0.04$

- $\delta_{\rm meas}^{\rm TLT} = \delta_h^{\rm TLT} + 2 \cdot E_{\rm BPC}$ reconstructed from the hadronic $\delta^{h,{\rm TLT}}$ at TLT and the BPC and LUMIG offline energy:
  – only medium $y$ (TLT DIS 17): 25 GeV$\leq \delta_{\rm meas}^{\rm TLT} = \delta_h^{\rm TLT} + 2 \cdot E_{\rm BPC} \leq$ 65 GeV
  – only high $y$ (TLT DIS 22): 20 GeV$\leq \delta_{\rm meas}^{\rm TLT} + 2 \cdot E_{\rm LUMIG}$
  – only ISR (TLT DIS 21): 30 GeV$\leq \delta_{\rm meas}^{\rm TLT} + 2 \cdot E_{\rm LUMIG} \leq$ 65 GeV



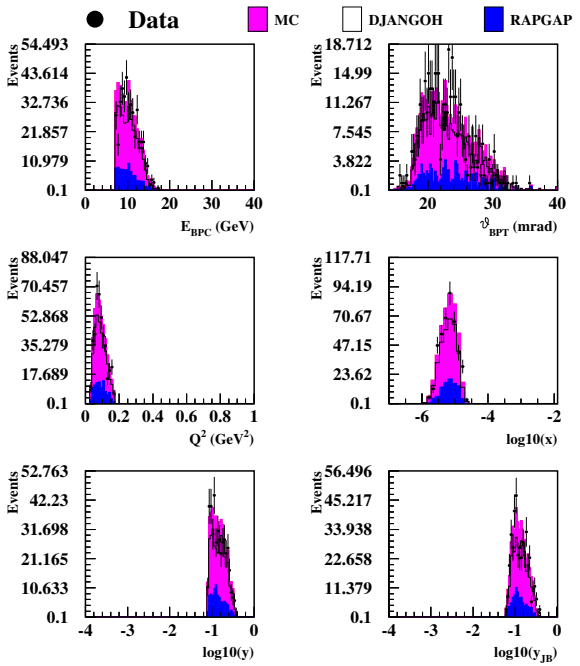


Figure 9.10: Comparison of MC and data: ISR region (part one). Measured quantities from BPC and BPT and the reconstructed kinematic variables for the ISR region.

- RCAL FLT energy cut:
  – only high $y$ (FLT 50): RCAL$_{\rm EMCE} > 464$ or RCAL$_{\rm EMCTH} > 1250$

### 4. Additional cuts used for the ISR region

In order to select events with initial state radiation with the ISR photon tagged in the LUMIG detector, additional cuts were used. The most important source of background for the ISR region is a normal DIS events with an additional bremsstrahlung ($ep \to e\gamma p$) event. To reduce this background, only events with a signal of (9–18) GeV in the LUMIG detector were selected. In this energy range the LUMIE detector is highly efficient in tagging a potential bremsstrahlung positron. Events with more than 3 GeV energy deposited in the LUMIE detector were rejected in order to reduce this background. Further background reduction is done by limiting the sum of BPC and LUMIG energy to be less than 35 GeV. For ISR events $y_{\rm JB}$ was corrected for initial state radiation by taking into account the photon energy $E_{\rm LUMIG}$ as measured in the LUMIG detector.

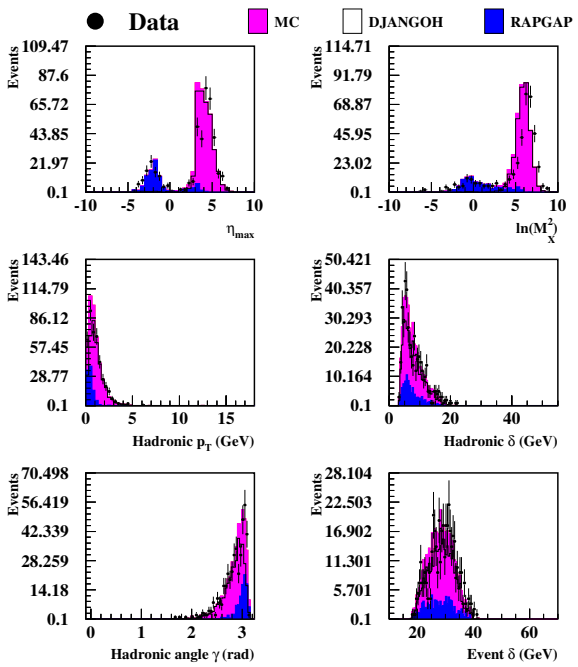


Figure 9.11: Comparison of MC and data: ISR region (part two). Reconstructed quantities of the hadronic final state and $\delta$ of the event for data and MC.

$$y_{\mathrm{JB}}^{\mathrm{cor}} = y_{\mathrm{JB}} \cdot \frac{E_e}{E_e - E_{\mathrm{LUMIG}}} \tag{9.2}$$

$E_e$ is the positron beam energy. A lower cut on $y_{\mathrm{JB}}^{\mathrm{cor}}$ was imposed to ensure a minimal hadronic activity in the CAL. The following additional cuts were used:

- LUMIG energy:
  – 9 GeV$< E_{\mathrm{LUMIG}} <$ 18 GeV
- LUMIE energy:
  – $E_{\mathrm{LUMIE}} <$ 3 GeV
- BPC and LUMIG energy:
  – $E_{\mathrm{BPC}} + E_{\mathrm{LUMIG}} <$ 35 GeV
- $y_{\mathrm{JB}}^{\mathrm{cor}}$ corrected for initial state radiation:
  – $y_{\mathrm{JB}}^{\mathrm{cor}} > 0.01$



| Region | LOW Y | MEDIUM Y | HIGH Y | LOWP Y | ISR |
|---|---|---|---|---|---|
| Cut | Rejected events | | | | |
| Events before selection | 1283253 | | | | |
| TLT | 244443 | 535757 | 1111011 | 993219 | 1265856 |
| BPC energy | 426324 | 96637 | 1199470 | 426324 | 96637 |
| BPC fiducial | 757757 | 293636 | 293636 | 293636 | 293636 |
| $y_{JB}$ | 803230 | 614612 | 614612 | 803230 | 614612 |
| $y_{JB}^{\mathrm{TLT}}$ | 0 | 481506 | 60881 | 0 | 796983 |
| $E3X_{\mathrm{BPC}}$ | 36708 | | | | |
| $\mathrm{T}_{\mathrm{BPC}}$ | 23586 | | | | |
| $\sigma_{\mathrm{BPC}}$ | 57680 | | | | |
| BPT track | 249100 | | | | |
| $\vartheta_{\mathrm{BPT}}$ | 12343 | | | | |
| $X_{\mathrm{BPC}} - X_{\mathrm{BPT}}$ | 104171 | | | | |
| $Z_{\mathrm{VTX}}$ | 67335 | | | | |
| $\delta$ | 165296 | | | | |
| $\mathrm{T}_{\mathrm{CAL}}$ | 7256 | | | | |
| Events before cuts on $y$ and $Q^2$ | 79121 | 202982 | 6423 | 30115 | 565 |
| Events after all cuts | 58847 | 171516 | 6132 | 26835 | 449 |

Table 9.1: Number of rejected events in data for the different cuts.

## 9.5 Effects of the selection cuts

The number of events rejected by the different selection cuts for data and MC are given in tables 9.1 and 9.2 respectively. Note, that an event might have been rejected by more than one cut. Most of the events are rejected by the the cut on the BPC fiducial area and energy, the requirement of at least one reconstructed BPT track, the track matching between BPC and BPT, the cut on $y_{\mathrm{JB}}$, and the cut on the total $\delta$ of the event. It was checked that the trigger selection in the case of data was fully efficient w.r.t. the offline selection cuts. The inefficiency of the FLT used for the high $y$ region in taken into account in the extraction of $\sigma_{\mathrm{tot}}^{\gamma^* p}$ and $F_2$ and a correction is applied for the different BPT efficiency in data and MC. Different efficiencies in data and MC related to the specific choice of the cut value were estimated and the results taken into account in the uncertainties of the extracted results of $\sigma_{\mathrm{tot}}^{\gamma^* p}$ and $F_2$ (see section 10.4). The cuts on the BPC and CAL timing could only be applied to data as the timing is not defined in the case of MC events. It was checked that the cuts did not significantly influence the event selection by rejecting signal events. The data selection was redone without these two cuts. The BPC timing had the most effect in the high $y$ region, where 0.7% of the events are rejected. In the other regions the effect was less than 0.1%. The CAL timing cut rejected 0.3% of the events in the low $y$ (LOW and LOWP) region. In the other regions the effect was less than 0.1%.

## 9.6 Comparison of data and MC

MC events were generated with the underlying structure function $F_2$ from the MRSA parton distribution function. All events were initially reweighted to the ALLM97 Parametrization of

| Region | LOW Y | MEDIUM Y | HIGH Y | LOWP Y | ISR |
|---|---|---|---|---|---|
| Cut | Rejected events | | | | |
| Events before selection | 2160490 | | | | |
| TLT | not used | | | | |
| BPC energy | 1201446 | 473680 | 1801827 | 1201446 | 473680 |
| BPC fiducial | 1491748 | 822558 | 822558 | 822558 | 822558 |
| $y_{JB}$ | 1359025 | 1000747 | 1000747 | 1359025 | 1000747 |
| $y_{JB}^{\mathrm{TLT}}$ | 0 | 823271 | 183118 | 0 | 1039104 |
| $E3X_{\mathrm{BPC}}$ | 45409 | | | | |
| $\mathrm{T}_{\mathrm{BPC}}$ | not used | | | | |
| $\sigma_{\mathrm{BPC}}$ | 82302 | | | | |
| BPT track | 449105 | | | | |
| $\vartheta_{\mathrm{BPT}}$ | 21629 | | | | |
| $X_{\mathrm{BPC}} - X_{\mathrm{BPT}}$ | 98118 | | | | |
| $Z_{\mathrm{VTX}}$ | 54249 | | | | |
| $\delta$ | 461208 | | | | |
| $\mathrm{T}_{\mathrm{CAL}}$ | not used | | | | |
| Events before cuts on $y$ and $Q^2$ | 46217 | 329019 | 58108 | 219035 | 3043 |
| Events after all cuts | 32456 | 301985 | 55915 | 202707 | 2509 |

Table 9.2: Number of rejected events in MC for the different cuts.

$F_2$ as discussed in chapter 7. The resulting MC distribution are in good agreement with the data. For each iteration during the iterative unfolding procedure (see section 10.3.4) the MC events were reweighted to the structure function $F_2$ as extracted from the previous iteration.
The Z-vertex as reconstructed from the CTD and BPT has been shown in figure 6.4. As expected the distributions are in good agreement, because the Z-vertex used in the MC was taken from an unbiased estimate of the true vertex distribution [Qu98] for the BPT data taking period in 1997. Usually, almost all of the protons of one bunch are confined in a region in phase space called a *bucket*, which is defined by the HERA RF system used for the acceleration. If the two systems, operating at 52 and 208 Mhz respectively, are not synchronized protons may also populate two smaller buckets which are shifted w.r.t. the nominal one by $\pm 4.8$ ns. If these satellite bunches contribute a significant fraction to the total number of interaction, additional peaks in the Z-vertex distribution at approximately $\pm 70$ cm are measured. For the previous analysis the agreement between data and MC was worse, mainly because the proton satellite bunches had not been taken into account in the Z-vertex distribution in the MC. Therefore, the Z-vertex in MC had to be reweighted [Su98]. In 1997 the problem was significantly reduced due to better tuning of the HERA proton accelerator [Ho99] and no additional peaks in the Z-vertex are visible in figure 6.4. In order to quantify the uncertainty of the results of this analysis related to the simulation of the satellite bunches, the regions dominated by these bunches are excluded in the data selection as a systematic check and the results compared to the nominal one (see section 10.4).
The distributions of measured and reconstructed quantities for MC and data are shown in figures 9.2 to 9.11 after the extraction of the final $F_2$ results. No background subtraction was done. In general the agreement between MC and data is good. The quantities reconstructed from the scattered positron using the BPC and BPT and the kinematic variables are in good



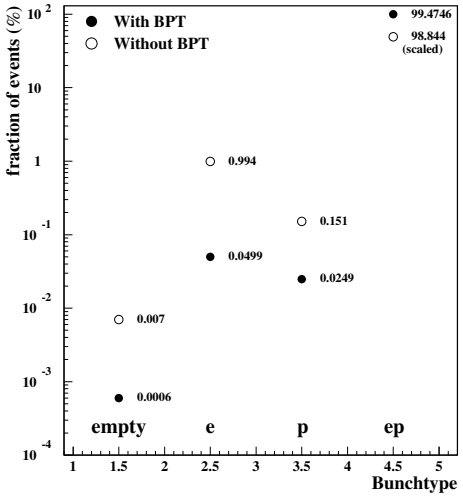


Figure 9.12: Bunch crossing number of all data events surviving the analysis cuts. The events from the unpaired bunches are scaled by the ratio of the current in the colliding and unpaired bunches. The amount of events from empty and unpaired bunches is less than 1.5% without the requirement of a BPT track and 0.5% after the cut is applied.

agreement for all regions. In the medium $y$ region the hadronic final state is well simulated. At low and high $y$ the agreement is not so good. This is related to the uncertainty of the fraction of diffractive events. The disagreement between the two parametrizations of the diffractive events is most pronounced in the high $y$ region (see figure 9.7): The $\eta_{\mathrm{max}}$-distribution would be in better agreement with the data with a higher fraction of diffractive events, while the $\delta$-distribution looks reasonable at low values of $\delta$, where most of the diffractive events are concentrated. Although the statistics is low for the ISR region the agreement between data and MC is still reasonable.

## 9.7 Background estimation

The analysis cuts described in section 9.4 are designed to reduce the background events in the data sample. Especially the photoproduction background, which was the dominant background in the previous analysis, was significantly reduced. Several methods were used to estimate the amount of background in the selected data sample.
The background from non $ep$ interactions can be estimated from the fraction of events, which survive the analysis cuts but originate from unpaired or empty bunches. Figure 9.12 shows the distribution of selected events in empty, unpaired positron and proton and colliding bunches.

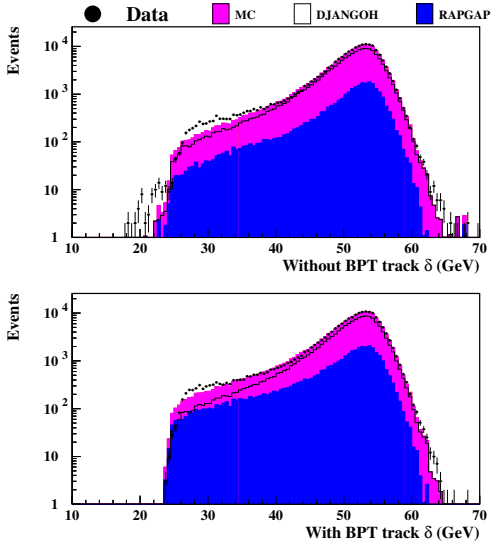


Figure 9.13: The reduction of the photoproduction background by the BPT track cut is illustrated as a function of the event $\delta$ for the medium $y$ region. Photoproduction background is expected predominantly at low values of $\delta$. Without the BPT track cut there is a significant discrepancy between data and MC at low values of $\delta$. By including the BPT track, the amount of background is reduced and the agreement between MC and data is much better. For this analysis $\delta$ is restricted to be within 30 and 65 GeV.

The events from the unpaired bunches are scaled by the ratio of the current in the colliding and unpaired bunches. Without the BPT track cut less than 1.5% of all selected events were found to have originated from unpaired or empty bunches. By including the cut the background was found to be less than 0.5% and has been neglected.
The dominant source of background is photoproduction. The BPT track cut did significantly reduce the photoproduction background as shown in figure 9.13. Without the BPT track cut there is a significant discrepancy between data and MC at low values of $\delta$. By including the BPT track, the amount of background is reduced and the agreement between MC and data is much better.
Three different methods have been used to quantify the amount of background remaining in the final data sample. The first two methods make use of the photoproduction MC, while the third one uses only the final data and signal MC samples.
In the first method the photoproduction MC is used to estimate the background. The photoproduction MC events which pass all analysis cuts are weighted by the ratio of the luminosity of the data sample to the background MC of 3925/300, and 3925/30 for the direct and resolved sample respectively. Only 18 pass all the selection cuts. Most of the events (14) concentrate in



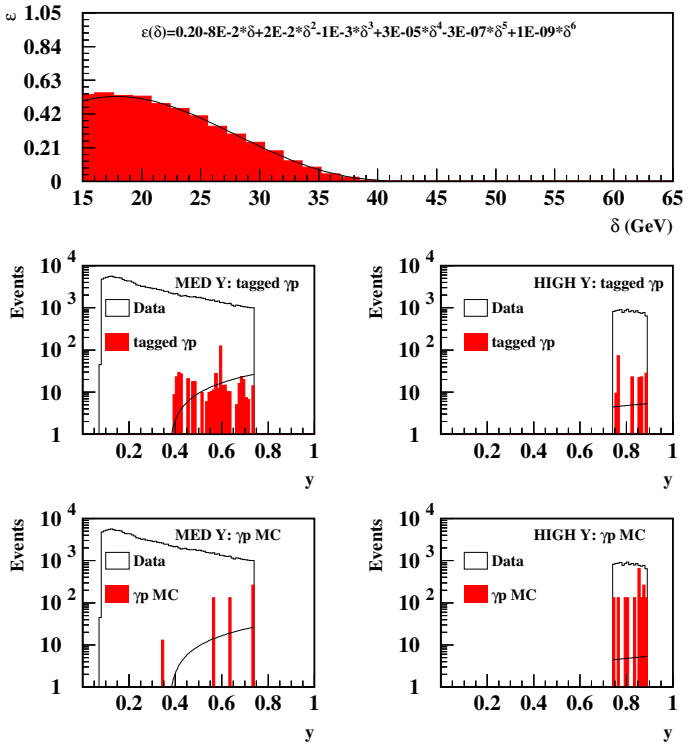


Figure 9.14: Estimation of the photoproduction background. The upper plot shows the positron tagging efficiency of the LUMIE detector as a function of the event $\delta$. The two plots in the middle show the distributions of the tagged photoproduction events as a function of $y$ and the lower ones the distributions of photoproduction MC events as a function of $y$. The smoothed curve in the lower four lower plots was derived from the tagged photoproduction events.

the high $y$ region.
The second method uses the LUMIE detector to identify photoproduction events in the final data sample. The photoproduction MC is only used to estimate the positron tagging efficiency as a function $\delta$ of the event. The LUMIE detector is designed to tag positrons with $Q^2 < 0.01$ GeV$^2$ scattered at very low angles. The acceptance of the detector is limited to positrons of (7–20) GeV. Therefore, it can only tag events up to $\delta < 55 - 2 \cdot 7$ GeV$= 41$ GeV, which is

the region of interest for this analysis (see figure 9.13). This efficiency was parametrized as a polynomial function of $\delta$ as shown in the upper plot in figure 9.14. Events were selected with 7-20 GeV energy in the LUMIE detector. The tagged photoproduction sample is itself contaminated by overlay events originating from a Bethe-Heitler process $ep \to ep\gamma$. For these events, the positron from the Bethe-Heitler process is misidentified in the LUMIE detector at the final state positron, while the photon is measured in the LUMIG detector. The background is effectively suppressed by additional cuts on the energy measured in the LUMIG detector (less than 3 GeV) and the total $\delta$ of the event including the LUMIG detector ($35 \leq \delta + 2 \cdot E_{\mathrm{LUMIG}} \leq 65$ GeV). The tagged photoproduction events in data are corrected for the tagging efficiency to estimate the amount of background. A total of 55 tagged photoproduction events are found. As expected only the medium (44 events) and high $y$ (11 events)regions are affected by background. The number of estimated background events are shown in the second row of plots in figure 9.14 as a function of $y$.

The two methods discussed above are in good agreement in the medium $y$ region, but differ in the high $y$ region. For $y = 0.80$ the photoproduction MC predicts a background of $(7.7 \pm 3.5)\%$, while the tagged photoproduction events estimate it at $(1.2^{+1.4}_{-0.6})\%$. Both methods suffer from low statistics. Because the statistical accuracy is too low to subtract the background statistically in each bin, a parametrization of the distribution of the background events was used to estimate the number of photoproduction events per bin. The background estimation derived from the tagged photoproduction events was used for background subtraction. First, this method only depends on the simulation of the tagging efficiency of the LUMIE detector and not of the hadronic final state, and second, the statistical precision is slightly better than in the other method (55 compared to 18 events).

The distribution of the tagged photoproduction events is smoothed and parametrized as a linear function $p(y)$ of $y$. No photoproduction event was tagged for $y < 0.37$. Therefore, $p(y)$ was fixed at zero for $y = 0.37$. $p(y)$ was normalized such that the integral of $p(y)$ over the $y$-range of the medium and high $y$ regions was equal to the number of tagged photoproduction events corrected for the tagging efficiency. This was done separately for the two regions to take into account the different selection cuts. The estimated amount of photoproduction background events per bin is less than $(1.3^{+0.8}_{-0.6})\%$ in the medium $y$ region and less than $(2.6^{+2.2}_{-1.9})\%$ in the high $y$ region. This estimation of the background is used to correct the measured $F_2$ for contamination from photoproduction. In order to take into account the uncertainty based on the results of the two methods described above, the amount of photoproduction background subtracted was changed by $-100\%$ and $+200\%$.

A third method to estimate the amount of background events in the final event sample is based on the hit multiplicity in the BPT. In order to pass the selection cuts, each event has to have at least one reconstructed BPT track, i.e. one or more hits in each BPT plane. In the efficiency studies described in section 6.8 $\epsilon$, the amount of noise hits per plane per bunch-crossing, was estimated to be 0.14 (0.19) for plane X1 (X3) for data and 0.13 (0.15) for plane X1 (X3) for MC. The selection cuts where chosen to minimize the amount of background in the sample. For several sources of background the number of hits in the BPT planes is expected to be more than the expected number of $1.0 + \epsilon$ hits per plane and bunch-crossing. This includes photoproduction events where $e^+e^-$–pairs from photon conversion in the beampipe exit window fake a positron signal in the BPC and BPT. However, with a opening angle in the order of $m_e/k$, where $k$ is the photon energy, even the angular resolution of the BPT is not sufficient to separate the two tracks. Other sources of background which might cause additional hits in the BPT are off-peak positrons and particles of the hadronic final state. The latter one is expected to increase with $y$ as the current jet shifts towards the rear beam hole and thus towards the



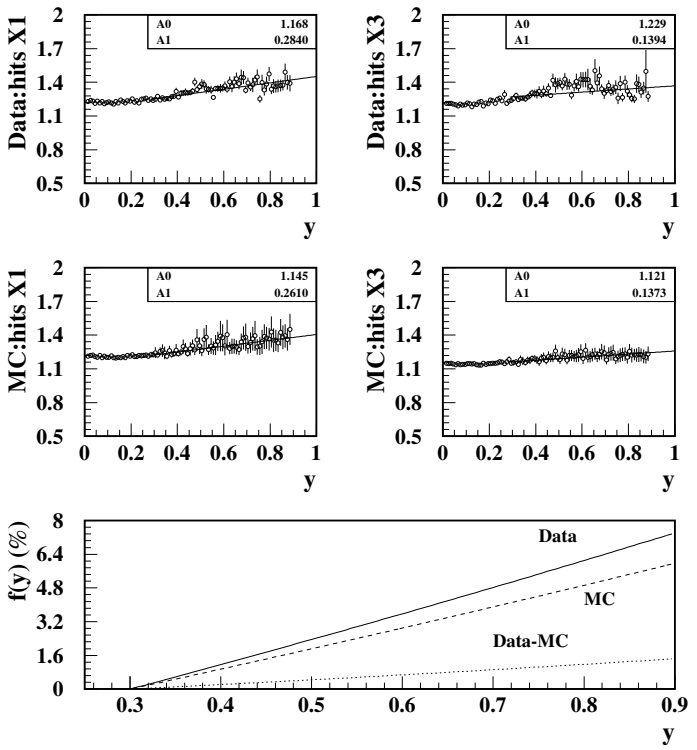


Figure 9.15: The upper four plots show the mean number of hits per event in the two BPT planes after the masking of dead and noisy channels and the simulation of noise in the MC. The lower plot shows the amount of background estimated from the BPT hit multiplicity using equation 9.4 for data and MC and the difference of both fractions.

BPC and BPT. A (although somewhat crude) estimation of the background in the final sample was derived from the mean number of BPT hits. Figure 9.15 shows the mean number of BPT hits for both planes after the masking of noisy and dead channels and the noise simulation in the case of the MC. For both data and MC the mean number of hits is increasing with $y$. The distributions are fitted by a linear function $f(y) = p_0 + p_1 \cdot (y - y_0)$ with $y_0 = 0.3$. It has been shown in section 9.6, that the distribution of the selected events as a function of $y$ is in good agreement between data and MC. Therefore, the slope $p_1$ can be related to the amount of events with more than the expected $1.0 + 0.15$ hits per plane and bunch-crossing. For both

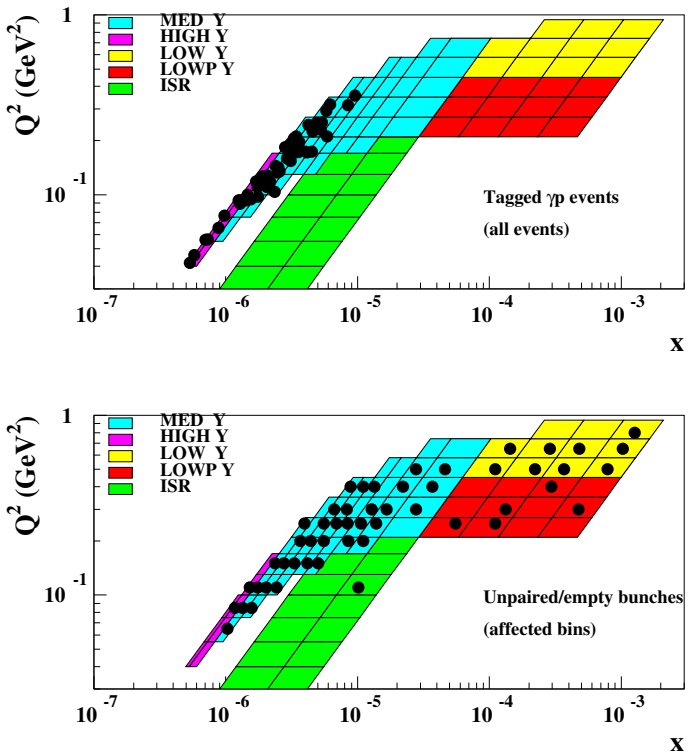


Figure 9.16: The upper plot shows the distribution of the tagged photoproduction events. The bins, for which events originating from empty or unpaired HERA bunches pass all selection cuts, are marked in the lower plot.

BPT planes the slope is smaller for the MC sample. For a given sample of events $n = \sum_i n_i$ with $n_i$ being the number of events with $i$ hits per BPT plane the mean number of hits is approximately given by:

$$\bar{n} = \frac{\sum_i i \cdot n_i + \sum_i n_i \epsilon}{\sum_i n_i} \tag{9.3}$$

$$\approx \frac{1+\epsilon}{1+n_2/n_1} + \frac{2+\epsilon}{1+n_1/n_2} \approx (1+\epsilon) + \frac{2+\epsilon}{1+n_1/n_2} \tag{9.4}$$

$\epsilon$ is the expected number of noise hits per plane and bunch-crossing (0.15). Equation 9.4 is only valid if $n_1 >> n_2 >> n_3 ....$ As shown in figure 6.3 this is the case. Fitting $\bar{n}$ by a



linear function $f(y)$ allows to extract the fraction $n_2/n_1$. This fraction is an estimate of the amount of events in the final sample which are either signal events with additional hits due to background or background events with higher multiplicity than signal events. The lower plot in figure 9.15 shows the extracted fraction $n_2/n_1$ for both data and MC and the difference between the two fractions. All curves were averaged over the slopes obtained from both planes. The method only allows a crude estimation of the total fraction of background and overlay events, but not the identification of the source of the events. In that sense the only meaningful result is the difference between data and MC which indicates that a small fraction of background events is either not included or badly simulated in the MC. The estimated fraction rises, to good approximation, linear from 0% at $y = 0.30$ to $(1.4 \pm 0.05)\%$ at $y = 0.89$. The result is close to the prediction obtained from the tagged photoproduction events and indicates that the method using the whole photoproduction MC overestimates the background at high $y$. All three methods confirm that the background is reduced significantly compared to the previous BPC analysis [Br97].

The distribution of the tagged photoproduction events and the events from empty and unpaired HERA bunches in the $(x - Q^2)$-plane are shown in figure 9.16. As expected, the events from unpaired or empty HERA bunches have a uniform distribution, while the photoproduction events concentrate at high values of $y$.

Background from DIS events at higher $Q^2$ was checked by comparing the rate, position, and energy of positron candidates in the CAL found by the positron finder SINISTRA [Si95]. Data and MC are in reasonable agreement. Since the MC by construction contains no events with the scattered positron in the CAL ($Q^2 < 1.0$ GeV$^2$), it was concluded that this background is negligible [Am99b].

The dominant background in the case of the ISR analysis are overlays of a normal DIS event and a bremsstrahlung event. The energy measured in the LUMIG was required to be within (9–18) GeV. In the case of bremsstrahlung events, for this energy range, the LUMIE efficiency of tagging the bremsstrahlung positron is high [Ke98]. A veto on the LUMIE energy strongly suppresses this background ($E_{\mathrm{LUMIE}} < 3$ GeV, see section 9.4).

# Chapter 10

# Extraction of $\sigma_{\rm tot}^{\gamma^* p}(W^2, Q^2)$ and $F_2(x, Q^2)$

## 10.1 Introduction

In this chapter a detailed description of the extraction of the total $\gamma^* p$ cross section $\sigma_{\rm tot}^{\gamma^* p}(W^2, Q^2)$ and the proton structure function $F_2(x, Q^2)$ at low $Q^2$ and very low $x$ is given. $F_2(x, Q^2)$ and $\sigma_{\rm tot}^{\gamma^* p}$ were extracted for $0.045\ \text{GeV}^2 \leq Q^2 \leq 0.80\ \text{GeV}^2$ and $3.0 \cdot 10^{-7} \leq x \leq 10^{-3}$ using the ZEUS detector with the Beam Pipe Calorimeter (BPC) and the Beam Pipe Tracker (BPT) described in section 5. The analysis is based on $3.9\,\text{pb}^{-1}$ of data taken during September and October 1997 after the BPT detector was installed and commissioned. Several triggers were used to select events at low, medium, and high values of $y$ as described in section 9.1. In the low $y$ region the kinematic variables were reconstructed with the $e\Sigma$ method, while at medium and high $y$ the electron method was used (see section 9.2.3). Various efficiencies and systematic effects were taken into account (see chapter 9). This included the BPC trigger efficiency, the determination of the event vertex using the BPT, the dependence of the acceptance on the underlying physics process introduced by various requirements on the hadronic final state, and the determination of the run-dependent beam tilt and BPC timing. Online and offline selection cuts were outlined in chapter 9 as was the amount of background events remaining after applying all selection cuts.
The following section will discuss in detail the resolution in the kinematic variables and the binning used to extract $\sigma_{\rm tot}^{\gamma^* p}$ and $F_2$. Section 10.3 will present the procedure used to extract $\sigma_{\rm tot}^{\gamma^* p}$ and $F_2$. The treatment of the longitudinal structure function $F_L$ and $\sigma_L^{\gamma^* p}$, is the topic of section 10.3.2. The effect of radiative corrections is discussed in section 10.3.3. Section 10.3.4 gives a description of the unfolding procedure used to obtain an estimation of the true distribution of kinematic variables from the corresponding measured distributions. The evaluation of the systematic uncertainties is discussed in section 10.4, followed by a presentation of the final results on the proton structure function $F_2(x, Q^2)$ and the total $\gamma^* p$ cross section $\sigma_{\rm tot}^{\gamma^* p}$ in section 10.5.

## 10.2 Binning of the data

The geometrical acceptance of the BPC and the various selection cuts restrict the accessible kinematic region and therefore the region over which $\sigma_{\rm tot}^{\gamma^* p}$ and $F_2$ can be extracted. $\sigma_{\rm tot}^{\gamma^* p}$ and $F_2$ are extracted by subdividing the kinematic plane into bins. $(y - Q^2)$-bins were chosen rather than $(x - Q^2)$-bins to make optimal use of the available phase space, taking into account the cuts on $y_{\rm JB}$, the lower positron energy cuts in the BPC, which correspond to upper limits





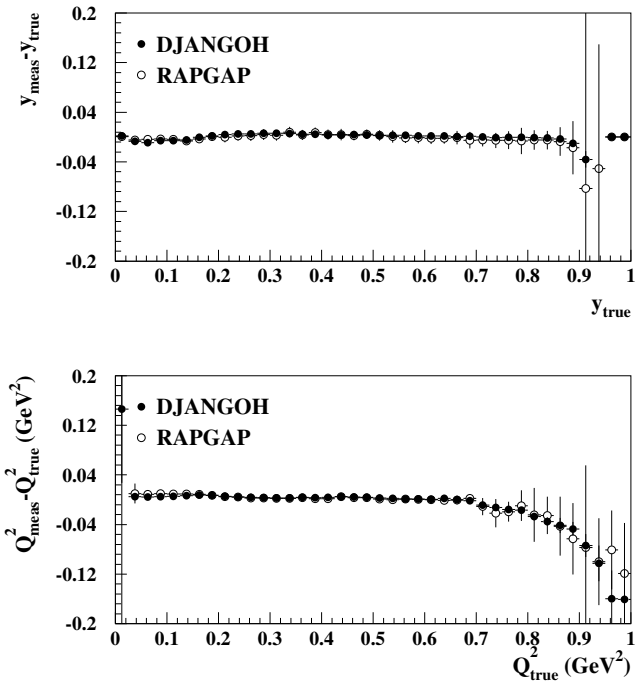


Figure 10.1: Resolution and bias for the kinematic variables $y$ and $Q^2$ as a function of the respective true variables from MC events. The term 'true' denotes the true variables at the hadronic vertex. 'meas' refers to the respective measured variables.

in $y$, and the reconstructed angle of the final state positron. The choice of the binning in the accessible kinematic region represents a compromise between various requirements and experimental constraints. In order to study in detail the behaviour of $\sigma_{\rm tot}^{\gamma^* p}$ and $F_2$ in the transition region between deep-inelastic scattering (DIS) and photoproduction, small bins in the kinematic plane are desirable. In order to keep statistical fluctuations, correlations, and systematic effects between bins, due to the finite resolution in the kinematic variables, at an acceptable level, a minimal bin size is necessary. Figure 10.1 shows the systematic shift and resolution in $y$ and $Q^2$ as a function of the respective true values using the two MC samples. The size of the error bars denotes the of the RMS resolution. The size of the systematic shift is typically smaller than the resolution for a particular bin and is mainly due to events with a photon radiated in the initial state. At high $y$ and $Q^2$ the resolution decreases. At high $y$ the BPC energy resolution is the main reason for the decreasing resolution. Only events with

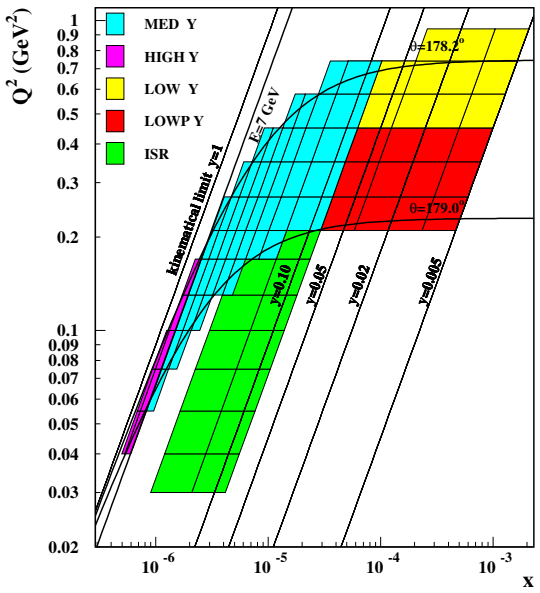


Figure 10.2: Selected bins in the $(x - Q^2)$-plane.

$y \leq 0.89$ are used in this analysis to minimize the impact of the decreasing resolution. The bad resolution in high $Q^2$ (which corresponds to low $y$) is caused by the limited statistics in this region, because only the tails of the vertex distribution allow to access $Q^2 > 0.74$ GeV$^2$.
The widths $\Delta y$ and $\Delta Q^2$ of each bin were chosen to be larger than the corresponding resolutions $\sigma_y$ and $\sigma_{Q^2}$ of the bin, i.e.:

$$\Delta y > \sigma_y \quad (10.1)$$
$$\Delta Q^2 > \sigma_{Q^2} \quad (10.2)$$

The bins in the medium $y$ region were chosen identical to the ones used for the previous analysis [Br97]. The lowest bin boundary in $Q^2$ is chosen to be at 0.040 GeV$^2$. The lowest $Q^2$-bin has a width of approximately $1.5\,\sigma_{Q^2}$. A constant bin width in $\ln Q^2$ was chosen for higher $Q^2$-bins to accommodate the rapidly falling event statistics due to the $1/Q^4$ dependence of the double-differential cross section. The chosen $Q^2$-bin sizes yield an approximately constant number of events in each $Q^2$ interval. The highest bin boundary in $Q^2$ was chosen at 0.94 GeV$^2$. The lowest bin boundary in $y$ is chosen to be at 0.005 and the highest one at 0.89. The size of the lowest $y$-bin is chosen to be $2\sigma_y$. For $y$ values above 0.37, bins of approximately constant width are used to take into account the decrease in the number of events due to the $1/y$ dependence of the double-differential cross section. The bins above $y = 0.84$ have only half



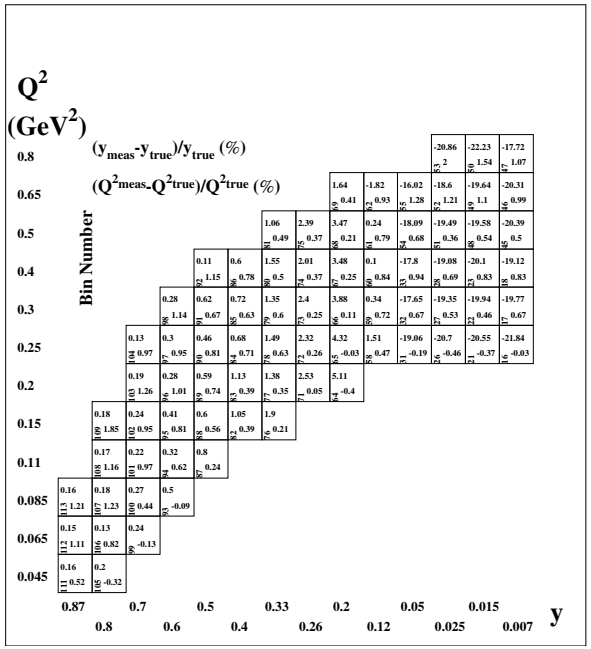


Figure 10.3: Fractional $y$ and $Q^2$ resolution in the chosen $(y - Q^2)$-bins. The resolution values (in %) from Gaussian fits to the distributions of $(y_{\text{meas}} - y_{\text{true}})/y_{\text{true}}$ and $(Q^2_{\text{meas}} - Q^2_{\text{true}})/Q^2_{\text{true}}$ are given for each bin. The vertical number denotes the bin identifier.

the size of the other ones. This is due to the lower energy cut of 3 GeV. In contrast to the bins at lower $y$ the trigger efficiency for these bins is slightly lower than 1. This is taken into account in the extraction of $\sigma_{tot}^{\gamma^* p}$ and $F_2$ and the evaluation of the systematic errors. The bin boundaries are given in table A.2 and A.3 in appendix A. The bins in the ISR region, which are used to estimate the uncertainty of the results due to radiative corrections, are given in table A.1 in the same appendix.
Figure 10.2 shows the chosen bins in the $(x - Q^2)$-plane. The shading indicates the different analysis regions (LOW, MED, HIGH, LOW, ISR) as defined in section 9.1.
The fractional resolutions $(Q^2_{\text{meas}} - Q^2_{\text{true}})/Q^2_{\text{true}}$ and $(y_{\text{meas}} - y_{\text{true}})/y_{\text{true}}$ for each bin are given in figure 10.3. These are typically in the order of a few per cent, with the exception of the low $y$ region, where the fractional resolution in $y$ is approximately –20%. This is caused by the reconstruction. It was chosen not to correct for this shift since the $y$-distributions for both data and MC are in good agreement as shown in the last chapter.
The migration of events in the $(x - Q^2)$-plane was studied using the MC sample. Comparing the average reconstructed and true values for $y$ and $Q^2$ gives an estimate of the size and direction of the migrations. Figure 10.4 shows the migrations for the chosen bins. The head of each arrow denotes the average reconstructed $y$ and $Q^2$ after all selection cuts for a particular bin.

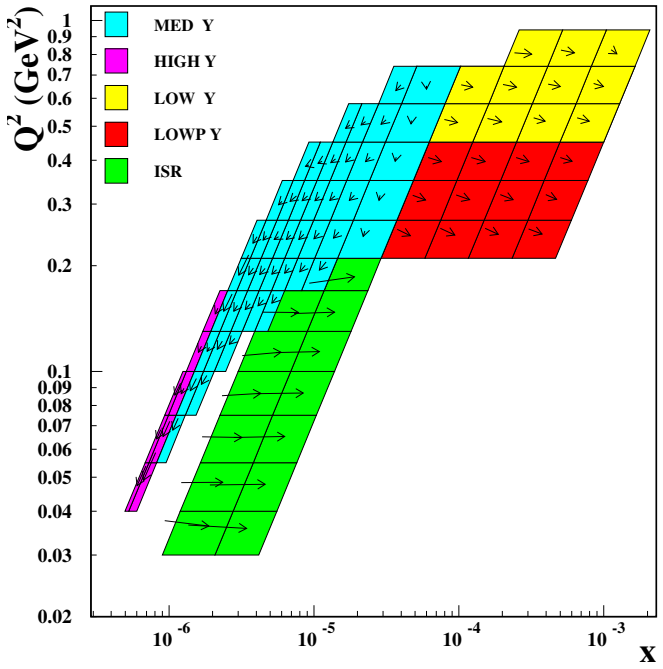


Figure 10.4: Migration of the kinematic variables $y$ and $Q^2$ in the $(x-Q^2)$-plane.

The base of the arrow is at the average generated $y$ and $Q^2$ for the same events. The size of the systematic shift is typically smaller than the resolution for a particular bin. The effect is most pronounced in the low $y$ regions and in the ISR bins. In both regions the $e\Sigma$ method is used in the reconstruction. In the case of the ISR bins the effect is bigger due to the radiated ISR photon.

Table 10.1 provides a summary of various bin variables that are used throughout the following discussion. The index $i$ denotes a particular $(y-Q^2)$-bin. The quality of each bin is quantified using the bin quality factors *purity* $p(i)$, *acceptance* $a(i)$, and *geometrical acceptance* $g(i)$, defined as follows:

$$a(i) = \frac{M_{\rm in}^{\rm MC}(i)}{N^{\rm MC}(i)} \tag{10.3}$$

$$p(i) = \frac{M_{\rm in}^{\rm MC}(i)}{M^{\rm MC}(i)} \tag{10.4}$$



| Quantity | Definition |
|---|---|
| $N^{\rm MC}(i)$ | Number of MC events generated in bin $(i)$ |
| $M^{\rm MC}(i)$ | Number of MC events reconstructed in bin $(i)$ |
| $M_{\rm in}^{\rm MC}(i)$ | Number of MC events generated and reconstructed in bin $(i)$ |
| $G^{\rm MC}(i)$ | Number of MC events generated in bin $(i)$ before any selection |
| $G_{\rm in}^{\rm MC}(i)$ | Number of MC events generated in bin $(i)$ before any selection and reconstructed in the fiducial area of the BPC |
| $N{\rm Data}_{\rm obs}(i)$ | Number of measured data events in bin $(i)$ before correction for prescale factors and background selection |
| $N^{\rm Data}(i)$ | Estimated true number of data events in bin $(i)$ after correction for prescale factors and background selection |
| $M^{\rm Data}(i)$ | Number of measured data events in bin $(i)$ including background |

Table 10.1: Summary of bin quantities.

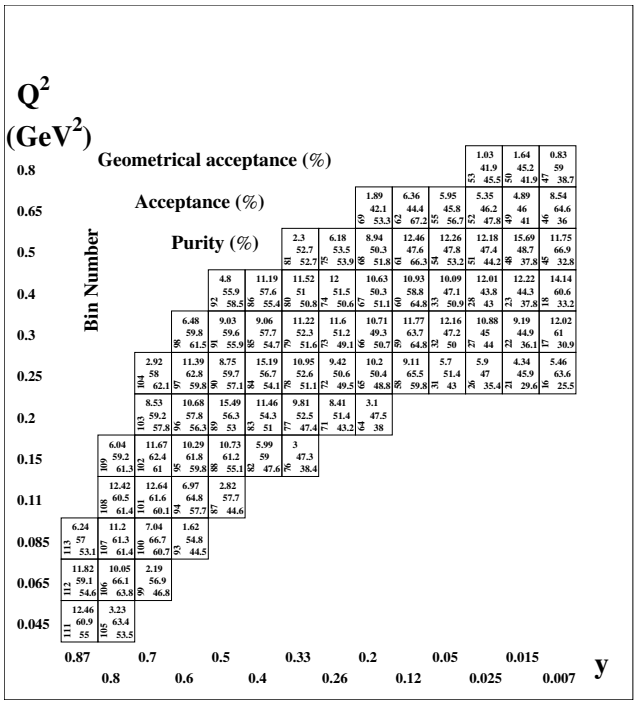


Figure 10.5: Quality factors (geometrical acceptance, acceptance, and purity) for each bin. The vertical number denotes the bin identifier.

$$g(i) \;=\; \frac{G_{\rm in}^{\rm MC}(i)}{G^{\rm MC}(i)} \tag{10.5}$$

The bin quality factors as determined from the MC sample are shown in figure 10.5. The geometrical acceptance $g(i)$ is typically between 4% and 15% for most bins, but drops to $(1-4)\%$ for the outermost bins. As expected, a maximum acceptance is achieved for the central bins whereas the edge bins have a significantly lower acceptance due to the limited azimuthal angle acceptance of the BPC. A low geometrical acceptance typically corresponds to a high statistical error. This leads to higher uncertainties in the extracted values of $\sigma_{\rm tot}^{\gamma^* p}$ and $F_2$.
The acceptance $a(i)$ measures the amount of event migration from a bin and was found to be $(40-70)\%$. The purity $p(i)$ measures the amount of event migration into a bin and is typically around $(40-65)\%$, decreasing to 25% for low $y$.

## 10.3 Determination of $\sigma_{\rm tot}^{\gamma^* p}$ and $F_2$

The $e^+p \to e^+X$ inclusive double-differential cross section $({\rm d}^2\sigma/{\rm d}y{\rm d}Q^2)$ can be expressed in terms of the total cross sections $\sigma_T^{\gamma^* p}$ and $\sigma_L^{\gamma^* p}$ of transverse and longitudinal polarized photon-proton scattering or equivalently in terms of the structure functions $F_2$ and $F_L$ as shown in detail in chapter 2:

$$\left(\frac{{\rm d}^2\sigma}{{\rm d}y{\rm d}Q^2}\right) \;=\; \frac{2\pi\alpha^2 Y_+}{yQ^4}(F_2 - \frac{y^2}{Y_+}F_L)\cdot[1+\delta_r] = \frac{2\pi\alpha^2 Y_+}{yQ^4}(F_2)_{\rm eff}\cdot[1+\delta_r] \tag{10.6}$$

$$\;=\; \Gamma\cdot(\sigma_T^{\gamma^* p} + \epsilon\sigma_L^{\gamma^* p})\cdot[1+\delta_r] = \Gamma\cdot(\sigma_{\rm tot}^{\gamma^* p})_{\rm eff}\cdot[1+\delta_r] \tag{10.7}$$

$$Y_+ \;=\; 1+(1-y)^2$$

$$\Gamma \;=\; \alpha(1+(1-y)^2)/(2\pi Q^2 y) \;\text{ Photon Flux}$$

$$\epsilon \;=\; 2(1-y)/(1+(1-y)^2) \;\text{ Photon Polarization}$$

$\delta_r$ is the electromagnetic radiative correction. Since the photon polarization $\epsilon(y)$ is not 1, but varies between 0.31 and 0.99, only the effective cross section $(\sigma_{\rm tot}^{\gamma^* p})_{\rm eff}$ and structure function $(F_2)_{\rm eff}$ can be determined experimentally for a given positron and proton beam energy. The double-differential cross section $({\rm d}^2\sigma/{\rm d}y{\rm d}Q^2)$ integrated over a bin of size $(\Delta y,\ \Delta Q^2)$ is determined from the estimated true event distribution $N^{\rm Data}(i)$ in a given bin in the kinematic plane and the luminosity $\mathcal{L}^{\rm Data}$ as discussed in the preceding sections:

$$< \sigma >_{\rm bin\ (i)} = \int\int_{\rm bin\ (i)} \left(\frac{{\rm d}^2\sigma}{{\rm d}y{\rm d}Q^2}\right){\rm d}y{\rm d}Q^2 = \frac{N^{\rm Data}(i)}{\mathcal{L}^{\rm Data}} \tag{10.8}$$

$< \sigma >_{\rm bin\ (i)}$ is the double-differential cross section $({\rm d}^2\sigma/{\rm d}y{\rm d}Q^2)$ averaged over the bin (i) of size $(\Delta y,\ \Delta Q^2)$. In principle $< \sigma >_{\rm bin\ (i)}$ can be quoted at any point in the bin if a correction is applied, which takes into account the shape of $({\rm d}^2\sigma/{\rm d}y{\rm d}Q^2)$. According to the mean value theorem, for any function $f(x)$ continuous in the interval $[a,b]$ there exists $\xi \in [a,b]$ with

$$f(\xi)\cdot(b-a) = \int_a^b f(x){\rm d}x \tag{10.9}$$

Thus, for every $(y-Q^2)$-bin, there exists one point $(y_a, Q_a^2)$ for which the cross section $\sigma$ is equal to the measured average one:

$$\sigma(y_a,Q_a^2) = < \sigma >_{\rm bin\ (i)} = \int\int_{\rm bin\ (i)} \left(\frac{{\rm d}^2\sigma}{{\rm d}y{\rm d}Q^2}\right){\rm d}y{\rm d}Q^2 \tag{10.10}$$



In order to quote the extracted values for $\sigma$ at any other point than $(y_a, Q_a^2)$ within a particular $(y-Q^2)$-bin, a bin-centering correction has to be applied:

$$\sigma(y,Q^2) \;=\; \sigma(y_a,Q_a^2)\cdot f(y_a,Q_a^2,y,Q^2) \tag{10.11}$$

$$\;=\; < \sigma >_{\rm bin\ (i)} \cdot f(y_a,Q_a^2,y,Q^2) \tag{10.12}$$

This can be done for example by using an explicit parametrization of the extracted values of $\sigma^{\gamma^* p}$. For this analysis it was chosen to quote $\sigma^{\gamma^* p}$ and $F_2$ at the centers-of-gravity of the true MC $y$ and $Q^2$ distributions for a particular $(y-Q^2)$-bin. The applied unfolding procedure, described in section 10.3.4, extracts $(\sigma_{\rm tot}^{\gamma^* p})^{\rm Data}$ from the known values $(\sigma_{\rm tot}^{\gamma^* p})^{\rm MC}$ in the MC by a iterative procedure. For each bin $(\sigma_{\rm tot}^{\gamma^* p})^{\rm Data}$ is related to $(\sigma_{\rm tot}^{\gamma^* p})^{\rm MC}$ at the same quoted $(y-Q^2)$-point. Providing the MC describes the data, which is the case after the unfolding, i.e. after a few iterations, the bin-centering corrections in data and MC are equal and cancel. Therefore, no bin-centering correction had to be applied.
Note that for the following discussion cross sections like $(\sigma_{\rm tot}^{\gamma^* p})_{\rm eff}$ and structure functions $F_2(y,Q^2)$ refer to the extracted values for a particular bin quoted at the centers-of-gravity of the kinematic variables as discussed above.
An iterative procedure is used to reweight the MC input structure function to ensure that the $y$ and $Q^2$ dependence in MC match those in the data. This is discussed in section 10.3.4. The effective cross section $(\sigma_{\rm tot}^{\gamma^* p})_{\rm eff}$, or equivalently the effective proton structure function $(F_2)_{\rm eff}$, for a particular bin in data and MC can be related to the respective event distributions:

$$\frac{N^{\rm Data}(i)/\mathcal{L}^{\rm Data}}{N^{\rm MC}(i)/\mathcal{L}^{\rm MC}} \;=\; \frac{\int\int_{\rm bin\ (i)}\left(\frac{{\rm d}^2\sigma}{{\rm d}y{\rm d}Q^2}\right)^{\rm Data}{\rm d}y{\rm d}Q^2}{\int\int_{\rm bin\ (i)}\left(\frac{{\rm d}^2\sigma}{{\rm d}y{\rm d}Q^2}\right)^{\rm MC}{\rm d}y{\rm d}Q^2}$$

$$\;=\; \frac{(\sigma_{\rm tot}^{\gamma^* p})_{\rm eff}^{\rm Data}(y,Q^2)}{(\sigma_{\rm tot}^{\gamma^* p})_{\rm eff}^{\rm MC}(y,Q^2)}\frac{\Gamma}{\Gamma}\frac{[1+\delta_r^{\rm Data}(y,Q^2)]}{[1+\delta_r^{\rm MC}(y,Q^2)]}\frac{[1+\delta_R^{\rm Data}(y,Q^2)]}{[1+\delta_R^{\rm MC}(y,Q^2)]} \tag{10.13}$$

$$\;=\; \frac{(F_2)_{\rm eff}^{\rm Data}(y,Q^2)}{(F_2)_{\rm eff}^{\rm MC}(y,Q^2)}\frac{[\frac{2\pi\alpha^2 Y_+}{yQ^4}]}{[\frac{2\pi\alpha^2 Y_+}{yQ^4}]}\frac{[1+\delta_r^{\rm Data}(y,Q^2)]}{[1+\delta_r^{\rm MC}(y,Q^2)]}\frac{[1+\delta_R^{\rm Data}(y,Q^2)]}{[1+\delta_R^{\rm MC}(y,Q^2)]} \tag{10.14}$$

$\delta_R^{\rm Data}$ and $\delta_R^{\rm MC}$ describe the treatment of $\epsilon$ $[F_L]$ for data and MC. $\delta_r^{\rm Data}$ and $\delta_r^{\rm MC}$ describe the electromagnetic radiative corrections in both cases. Assuming that the MC simulation provides a correct description of the radiative corrections in the data the last equation can be simplified using $\delta_r^{\rm Data}(y,Q^2) = \delta_r^{\rm MC}(y,Q^2)$. In this case $(\sigma_{\rm tot}^{\gamma^* p})_{\rm eff}^{\rm Data}$ $[(F_2)_{\rm eff}^{\rm Data}(y,Q^2)]$ is given as follows:

$$(\sigma_{\rm tot}^{\gamma^* p})_{\rm eff}^{\rm Data}\ \left[(F_2)_{\rm eff}^{\rm Data}\right]\ (y,Q^2) \;=\; \frac{N^{\rm Data}(i)/\mathcal{L}^{\rm Data}}{N^{\rm MC}(i)/\mathcal{L}^{\rm MC}}\frac{[1+\delta_R^{\rm Data}(y,Q^2)]}{[1+\delta_R^{\rm MC}(y,Q^2)]}\,(\sigma_{\rm tot}^{\gamma^* p})_{\rm eff}^{\rm MC}\ \left[(F_2)_{\rm eff}^{\rm MC}\right]\ (y,Q^2) \tag{10.15}$$

In order to obtain the total photon-proton cross section $\sigma_{\rm tot}^{\gamma^* p}$ $[F_2]$ from the extracted values of $(\sigma_{\rm tot}^{\gamma^* p})_{\rm eff}^{\rm Data}$ $[(F_2)_{\rm eff}]$, the contribution of $\sigma_L^{\gamma^* p}$ $[F_L]$ has to be separated. The factor $\delta_R^{\rm MC}(y,Q^2)$ is zero, since the contribution from $F_L$ has not been included in the generation of the used MC sample (see section 7). In this case, $(\sigma_{\rm tot}^{\gamma^* p})^{\rm MC} = (\sigma_{\rm tot}^{\gamma^* p})_{\rm eff}^{\rm MC}$ $[F_2^{\rm MC} = (F_2)_{\rm eff}^{\rm MC}]$ and $\sigma_{\rm tot}^{\gamma^* p}$ is obtained as follows:

$$(\sigma_{\rm tot}^{\gamma^* p})^{\rm Data} = (\sigma_{\rm tot}^{\gamma^* p})_{\rm eff}^{\rm Data}[1+\delta_R^{\rm Data}(y,Q^2)] \tag{10.16}$$

where $\delta_R = \sigma^{\epsilon=1}(i)/\sigma^{\epsilon\neq 1}(i) - 1$. The treatment of $\epsilon$ $[F_L]$ for the data is subject of the section 10.3.2. The structure function $F_2$ is determined from the total $\gamma^* p$ cross section $\sigma_{\rm tot}^{\gamma^* p}$ according to:

$$F_2(y,Q^2) \;=\; \frac{Q^2}{4\pi^2\alpha}\cdot\sigma_{\rm tot}^{\gamma^* p}(W^2,Q^2) \tag{10.17}$$

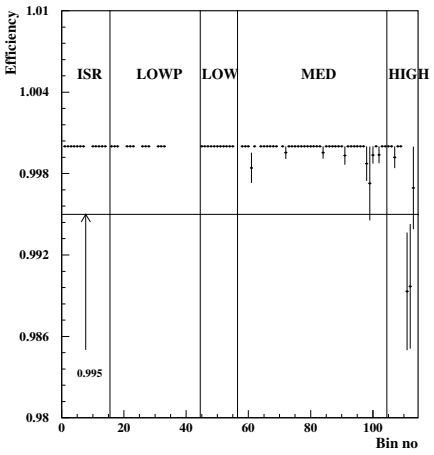


Figure 10.6: BPC overall trigger efficiency (FLT·SLT·TLT) for all $(y-Q^2)$-bins used in the extraction of $(\sigma_{tot}^{\gamma^* p})_{eff}^{Data}$ $[(F_2)_{eff}^{Data}]$.

$$W = \sqrt{|m_p^2 + \frac{Q^2(1-x)}{x}|} \simeq \sqrt{ys}$$

The estimation of the radiative corrections is discussed in section 10.3.3. The bin-by-bin unfolding procedure used in the extraction of $\sigma_{tot}^{\gamma^* p}$ $[F_2]$ is discussed in detail in section 10.3.4.

### 10.3.1 Treatment of BPC and BPT efficiency

The extraction of $(\sigma_{tot}^{\gamma^* p})_{eff}^{Data}$ $[(F_2)_{eff}^{Data}]$ using equation 10.15 assumes that both BPC and BPT are fully efficient. In the case of different efficiencies in data and MC the extracted value of $(\sigma_{tot}^{\gamma^* p})_{eff}^{Data}$ $[(F_2)_{eff}^{Data}]$ has to be corrected. The BPT efficiency was determined in section 8.4. $(\sigma_{tot}^{\gamma^* p})_{eff}^{Data}$ $[(F_2)_{eff}^{Data}]$ is corrected for the difference in the efficiency (the efficiency for data is 95.8% of the efficiency for MC). The efficiency ratio between data and MC is stable within $\pm 1.5\%$. This uncertainty is taken into account in the evaluation of the systematic uncertainties.
The BPC trigger efficiency was determined in section 8.5. The same data sample used to determine the overall trigger efficiency was used to estimate the efficiency for each bin. The results are shown in figure 10.6. Except for the bins at the highest $y > 0.84$ the efficiency is above 0.995. The bins at high $y$ correspond to low positron energies. The inefficiency in these bins was traced back to the FLT slot 50 used to select the events at high $y$. FLT slot 50 was found to be fully efficient at energies above 3.5 GeV in section 8.5. The bin boundaries at high $y$ were chosen in such a way that only those bins at the highest $y > 0.84$ are not fully efficient. For each of these bins the calculated values of $(\sigma_{tot}^{\gamma^* p})_{eff}^{Data}$ $[(F_2)_{eff}^{Data}]$ were divided by the efficiency of the particular bin. The uncertainty in the efficiency is taken into account in the evaluation of the systematic uncertainties of $(\sigma_{tot}^{\gamma^* p})_{eff}^{Data}$ $[(F_2)_{eff}^{Data}]$.



### 10.3.2 Treatment of $\epsilon$ $(F_L)$

The effective cross section $(\sigma_{tot}^{\gamma^* p})_{eff}^{Data}$ $[(F_2)_{eff}^{Data}]$ is corrected by a factor $(1 + \delta_R^{Data}(y, Q^2))$ to extract the total cross section $(\sigma_{tot}^{\gamma^* p})^{Data}$ $[(F_2)^{Data}]$. $(1 + \delta_R^{Data})$ is parametrized as a function of the ratio $R$ of the longitudinal and transverse cross section for virtual photon-proton scattering:

$$R(y, Q^2) = \frac{\sigma_L^{\gamma^* p}(W^2, Q^2)}{\sigma_T^{\gamma^* p}(W^2, Q^2)} = \frac{F_L(y, Q^2)}{F_2(y, Q^2) - F_L(y, Q^2)} \quad (10.18)$$

$(\sigma_{tot}^{\gamma^* p})^{Data}$ $[(F_2)^{Data}]$ is extracted from $(\sigma_{tot}^{\gamma^* p})_{eff}^{Data}$ $[(F_2)_{eff}^{Data}]$ using the definition of $R$ (10.18) and equation 10.16:

$$(\sigma_{tot}^{\gamma^* p})^{Data}\,[(F_2)^{Data}] = (\sigma_{tot}^{\gamma^* p})_{eff}^{Data}\,[(F_2)_{eff}^{Data}] \cdot \left(\frac{1+R}{1+\epsilon \cdot R}\right) \quad (10.19)$$

The ratio $R$ of the cross section of transversely and longitudinally polarized photon-proton scattering $\sigma_T^{\gamma^* p}$ and $\sigma_L^{\gamma^* p}$, has been measured using vector meson production at HERA [Br98b]. In the low $Q^2$ region, $R$ was found to be independent of $W$ within $2\sigma$ and was parametrized as a function of $Q^2$ by:

$$R = \kappa \cdot Q^2, \quad \kappa = 0.81 \pm 0.05\ (\text{stat}) \pm 0.06\ (\text{sys}) \quad (10.20)$$

At higher values of $Q^2$ the results are also in good agreement with the predictions given in [Ma97]. The value of $R$ is in good agreement with the parametrization $R = 0.5 \cdot Q^2/m_{\rho^0}^2$ used in the BPC 1995 analysis [Br97]. It is higher by roughly a factor of 3 than the value from the BKS model, which, to good approximation, is given at low $Q^2$ by $R_{BKS} = 0.165 \cdot Q^2/m_{\rho^0}^2$. Both models include the required limit of $\sigma_L^{\gamma^* p} \propto Q^2$ as $Q^2 \to 0$.
In the second approach, an attempt is made to separate the contribution of $\sigma_T^{\gamma^* p}$ and $\sigma_L^{\gamma^* p}$ from the extracted values of $(\sigma_{tot}^{\gamma^* p})_{eff} = \sigma_T + \epsilon\sigma_L$ and thus obtain a value for $R$ constrained by the data itself. This is done by using the same GVDM parametrization of $\sigma_T^{\gamma^* p}$ and $\sigma_L^{\gamma^* p}$ as used in the unfolding (see section 11.2.1). The extracted values of $R$ are referred to as $R_{BPT}$.
For this analysis $R_{BKS}$ was used, which is in good agreement with $R_{BPT}$ (see section 11.2.1). This allows easy comparison to the results from H1. For comparison the results obtained by using $R$ as determined from the vector meson production at HERA ($R_{GVDM}$) and the BPT data ($R_{BPT}$) are also shown.
The correction factor $(1 + \delta_R^{Data})$ increases for $y \to 1$ but the effect is still small. Using $R_{BKS}$ it reaches 3% in some bins at medium and high $y$, while it is negligible for all other bins. This is due to the very low $Q^2$ in this analysis and the required limit of $\sigma_L^{\gamma^* p} \propto Q^2$ for $Q^2 \to 0$. Using $R_{BPT}$ changes the results by less than 0.8%, while the use of $R_{GVDM}$ changes the results by up to 5%. The changes in $F_2$ and $\sigma_{tot}^{\gamma^* p}$ of both approaches for $R$ compared to the use of $R_{BKS}$ are given in section 10.5.

### 10.3.3 Treatment of the radiative correction

Assuming that the MC provides a correct simulation of the radiative corrections, the effective cross section $(\sigma_{tot}^{\gamma^* p})_{eff}^{Data}$ $[(F_2)_{eff}^{Data}]$ can be calculated using equation 10.15. The program HERACLES [Sp99] used to generate the lepton vertex in the MC simulation (see section 7), takes into account one-photon radiative corrections. These are photon emission from the incoming positron (**I**nitial **S**tate **R**adiation), the outgoing positron (**F**inal **S**tate **R**adiation), self-energy corrections, and the complete set of one-loop weak corrections. The two latter ones are calculable in QED and are therefore properly simulated in the MC. An FSR photon which carries

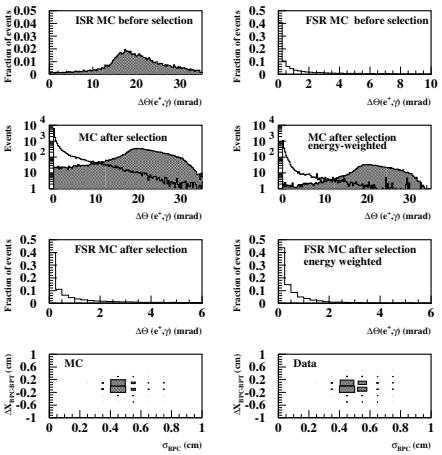


Figure 10.7: Angular distribution of ISR and FSR photons.

a significant fraction of the positron energy and is emitted at a large angle might cause an additional peak in the BPC energy distribution. This affects the BPC position reconstruction and the calculation of the BPC shower width $\sigma_{\rm BPC}$. Since both quantities are used in the event selection, an incorrect simulation of FSR in MC would in this case influence the extracted values of $\sigma_{\rm tot}^{\gamma^* p}$ and $F_2(x,Q^2)$. It was checked that FSR is negligible in this analysis. The results are shown in figure 10.7. The upper plots show the angle $\Theta$ between positron and photon for ISR and FSR events before the event selection. The angle is large for ISR events, but for the majority (40%) of FSR events it is less than 0.25 mrad. This corresponds to a distance of roughly 0.8 mm at the BPC front face assuming that the FSR is emitted close to the nominal interaction point at Z = 0 cm. The shape of the distribution is not changed after the event selection as shown in the left plot in the second row. The left plot shows the same distribution weighted by the ratio $E_\gamma/E_{e^+}$ of photon and positron energy. The number of FSR events is reduced by a factor of 10. This indicates that most of the FSR photons do not carry a significant fraction of the positron energy. The plots in the third row show the distributions of MC FSR events as a function of $\Theta$. The energy-weighted distribution (right) indicates that 90% of the FSR photons are emitted at less than 2 mrad w.r.t. the final state positron. The original distribution (left) indicates 90% of the photons being emitted at less than 2.5 mrad. In both cases this corresponds to a distance at the BPC front face of less than 16 mm (2 times the BPC strip width). The last row of plots show the correlations between $\sigma_{\rm BPC}$ and the difference $\Delta_{\rm BPC-BPT}$ between the reconstructed BPC and BPT X-positions. If there were a significant influence of the FSR photons on the BPC reconstruction, the distributions would be expected to have a tail towards higher values of $\sigma_{\rm BPC}$ and $|\Delta_{\rm BPC-BPT}|$. Neither the data nor the MC show this feature and both distributions are in good agreement. Therefore, the FSR events are properly simulated in the MC and FSR photons do not significantly influence the BPC



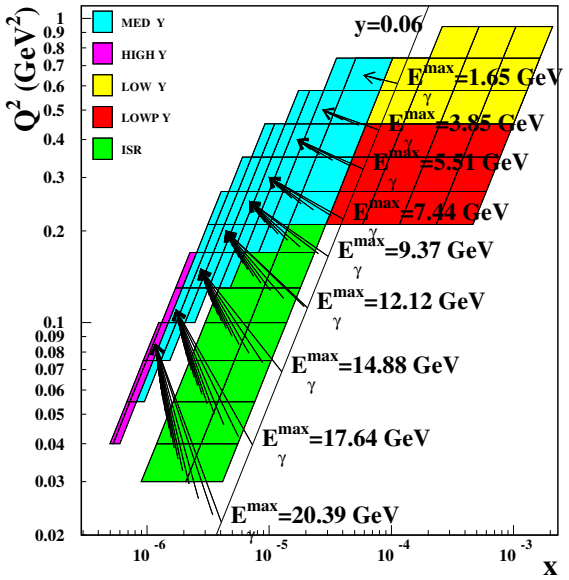


Figure 10.8: Migration of events due to ISR if the ISR photon is not taken into account in the reconstruction of the kinematic variables using the electron method. The arrows point from the true $x$ and $Q^2$ to the reconstructed values in steps of 1 GeV in $E_\gamma$. The number at the longest arrow for one reconstructed point in $x$ and $Q^2$ indicates the highest possible photon energy $E_\gamma^{\rm max}$, for which $y_{\rm JB}^{\rm true} > 0.06$. Each group of arrows is representative for the whole set of bins at the same apparent $y$.

reconstruction.

Contrary to events with FSR, photons from ISR are not detected in the BPC together with the final state positron. Unrecognized ISR events are reconstructed at lower values of $x$ and higher values of $Q^2$. How far they migrate in the $(x-Q^2)$-plane is correlated to the radiated photon energy as illustrated in figure 10.8. The lower cuts on $y_{\rm JB}$ and $\delta$ (see section 9.4) suppress events where the ISR photon disappears through the rear beam hole. Since the radiative cross section falls steeply with increasing energy of the ISR photon, the migration in the $(x-Q^2)$-plane is limited. Therefore, the uncertainty in the description of the radiative corrections for a certain bin in the $(x-Q^2)$-plane is caused by events migrating from a region close to the bin. The bins at high and medium $Q^2$ are therefore expected to be only very weakly affected because $(\sigma_{\rm tot}^{\gamma^* p})^{\rm Data}$ $[(F_2)^{\rm Data}]$ is at the same time also measured in the region where the migrating events originate and the MC events are reweighted accordingly. At lower $Q^2$ the effect is expected to be bigger since $(\sigma_{\rm tot}^{\gamma^* p})^{\rm Data}$ $[(F_2)^{\rm Data}]$ is not measured at lower $Q^2$ and higher $x$, where the events

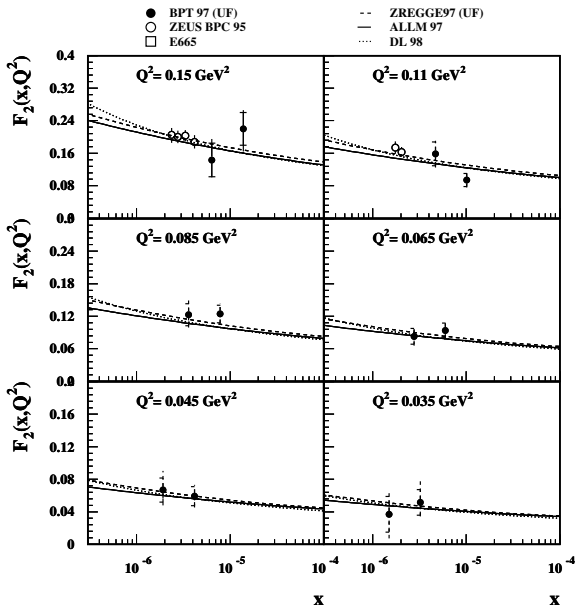


Figure 10.9: $F_2$ as estimated in the ISR bins. The ISR bins were not included in the iterative unfolding procedure. The resulting fit of $F_2$ obtained from the nominal analysis region was also used to reweight the MC events for the ISR bins. The agreement of the extracted $F_2$ compared to the fit result is reasonable although the statistical error is large.

originate. The maximal energy $E_\gamma^{\rm max}$ of the ISR photon is related to the lower cut $y_{\rm JB}^{\rm min}$ on $y_{\rm JB}$ for a given reconstructed energy $E_e$ and $y_e$:

$$E_\gamma^{\rm max} = E_e \cdot (y_e - y_{\rm JB}^{\rm min}) \tag{10.21}$$

For the medium and high $y$ region $y_{\rm JB}^{\rm min} = 0.06$ was used. Figure 10.8 shows the size and direction of the migrations due to undetected ISR in the $(x - Q^2)$-plane. The arrows indicate the direction of the migration of events into the analysis region. In order to quantify the effect of ISR on this analysis, the events selected for the ISR region (see section 9) are used to estimate $(\sigma_{\rm tot}^{\gamma^* p})^{\rm Data}$ $[(F_2)^{\rm Data}]$ at lower $Q^2$ than the nominal analysis.
The GVDM- and Regge-inspired fit used to extract $(\sigma_{\rm tot}^{\gamma^* p})^{\rm Data}$ $[(F_2)^{\rm Data}]$ (see chapter 11) is repeated for the ISR region keeping all parameters except the normalization $A_{I\!P}$ fixed at the values of the nominal fit. Using only the ISR bins $A_{I\!P}$ was determined to be $(52.522 \pm 2.863)$ $\mu$b. The uncertainty of the magnitude of $(\sigma_{\rm tot}^{\gamma^* p})^{\rm Data}$ $[(F_2)^{\rm Data}]$ given by the statistical error of the normalization was 6%. Figure 10.9 shows the extracted values of $F_2$ for the ISR bins



| $Q^2$ (GeV$^2$) | $y$ | $F_2$ | $\delta_{\rm stat}$ | $\delta_{\rm sys}^-$ | $\delta_{\rm sys}^+$ | $\sigma_{\rm tot}^{\gamma^* p}$ ($\mu$b) | $\delta_{R_{\rm GVDM}}$ (%) | $\delta_{R_{\rm BPT}}$ (%) |
|---|---|---|---|---|---|---|---|---|
| 0.1500 | 0.260 | 0.143346 | 0.041151 | 0.030659 | 0.010353 | 107.23 | 0.3 | 0.1 |
| 0.1500 | 0.120 | 0.219947 | 0.039974 | 0.022882 | 0.038622 | 164.53 | 0.1 | 0.0 |
| 0.1100 | 0.260 | 0.158778 | 0.029286 | 0.012175 | 0.016559 | 161.96 | 0.2 | 0.0 |
| 0.1100 | 0.120 | 0.093989 | 0.015983 | 0.014042 | 0.009015 | 95.87 | 0.0 | 0.0 |
| 0.0850 | 0.260 | 0.122912 | 0.020239 | 0.016167 | 0.012643 | 162.25 | 0.2 | 0.0 |
| 0.0850 | 0.120 | 0.124301 | 0.016129 | 0.011418 | 0.008504 | 164.09 | 0.0 | 0.0 |
| 0.0650 | 0.260 | 0.082828 | 0.014545 | 0.008698 | 0.009316 | 142.98 | 0.1 | 0.0 |
| 0.0650 | 0.120 | 0.093945 | 0.013482 | 0.008012 | 0.006339 | 162.17 | 0.0 | 0.0 |
| 0.0450 | 0.260 | 0.066778 | 0.014815 | 0.018058 | 0.011934 | 166.51 | 0.1 | 0.0 |
| 0.0450 | 0.120 | 0.059202 | 0.011619 | 0.007542 | 0.007598 | 147.62 | 0.0 | 0.0 |
| 0.0350 | 0.260 | 0.036859 | 0.021980 | 0.019789 | 0.019834 | 118.17 | 0.1 | 0.0 |
| 0.0350 | 0.120 | 0.051608 | 0.015675 | 0.022292 | 0.007107 | 165.45 | 0.0 | 0.0 |

Table 10.2: Table of the estimated $F_2$ values for the ISR region. The quoted values of $y$ and $Q^2$ are given in the first two columns. The extracted value of $F_2$ using $R_{\rm BKS}$ including statistical and systematic errors are given in the next four columns. The difference in $F_2$ if $R_{\rm GVDM}$ or $R_{\rm BPT}$ is used are given in the last two columns.

compared to the $F_2$ fit obtained from the nominal analysis bins. As a systematic check of the uncertainty of the radiative corrections, the MC events at $Q^2$ below the region covered by the nominal analysis were reweighted to values of $(\sigma_{\rm tot}^{\gamma^* p})^{\rm Data}$ $[(F_2)^{\rm Data}]$, which were shifted up and down by 6%. The reweighting of the MC events in the region of the nominal measurement was not changed. $(\sigma_{\rm tot}^{\gamma^* p})^{\rm Data}$ $[(F_2)^{\rm Data}]$ was then unfolded ignoring the partial reweighting of the MC. The result was compared to the nominal values of $(\sigma_{\rm tot}^{\gamma^* p})^{\rm Data}$ $[(F_2)^{\rm Data}]$ to give the result of the check. The effect on $F_2$ was found to be less than 4%.

### 10.3.4 Unfolding of $\sigma_{\rm tot}^{\gamma^* p}$ and $F_2$

The measured number of events $M^{\rm Data}(i)$ differs from the true number of events $N^{\rm Data}(i)$ due to smearing and efficiency effects, background events surviving all selection cuts, and the limited detector acceptance. Smearing effects arise from the finite detector resolution, the chosen reconstruction method, and from the presence of radiative corrections. Efficiency effects are due to online and offline selection cuts and to the inefficiencies of the used detectors. The goal of the *unfolding procedure* is to extract an estimate of the true distribution in $y$ and $Q^2$ from the corresponding measured distribution, i.e. to extract $N^{\rm Data}(i)$ from $M^{\rm Data}(i)$.
In mathematical terms, the $n$-dimensional measured distribution $M(x_1, \ldots, x_n)$ is related to the $n$-dimensional true distribution $N(y_1, \ldots, y_n)$ through the transfer function $f(x_i, y_i)(i = 1 \ldots n)$. Knowing the transfer function permits the estimation of the true distribution from the measured distribution. In our case the unfolding problem is two-dimensional with two discrete variables, i.e. the measured $M_{(i)}^{\rm MC}$ and the true $N_{(i)}^{\rm MC}$ number of events for a particular $(y - Q^2)$-bin $i$. The effect of the transfer function can be described by a *transfer matrix*, and the problem is formulated as follows:

$$M_k^{\rm MC} = \sum_{l=1}^{n} T_{kl}^{\rm MC} N_l^{\rm MC} \tag{10.22}$$

$n$ is the number of bins covering the whole $(y-Q^2)$-phase space, including regions outside the region covered by the particular analysis. $M_k^{\rm MC}$ and $N_l^{\rm MC}$ are both $n$-dimensional vectors, representing the measured and true number of events in each bin $k$ and $l$, respectively. $T_{kl}^{\rm MC}$ describes the probability that an event which originated in bin $l$ is reconstructed in bin $k$. Several approaches have been taken in the past to determine the transfer matrix $T_{kl}^{\rm MC}$. In this analysis the *bin-by-bin unfolding method* is used. It was used in various measurements of the proton structure function $F_2$ at ZEUS [De96], including the previous low $x$ and low $Q^2$ measurement [Br97], and was shown to give stable results. A detailed discussion on the *Bayes unfolding method* [Ag94] and the *Matrix unfolding method* can be found in [Qu96]. For the bin-by-bin unfolding to work, it is required that the MC simulation correctly describes the data distributions in all phase space regions from which the measured events originate and that migration effects among bins are small, i.e. the purity of the bins is large. This is achieved by an iterative procedure. Each MC event is reweighted to the structure function $(F_2)_{\rm eff}^{\rm Data(n)}$ obtained from the *nth* iteration. The result of this iteration, $(F_2)_{\rm eff}^{\rm Data(n+1)}$, is then used for the next iteration. In the bin-by-bin unfolding, a first estimate of the true data distribution for each bin $k$ is given by:

$$N_k^{\rm Data(n=0)} = \left(\frac{N_k^{\rm MC(n=0)}}{M_k^{\rm MC(n=0)}}\right) M_k^{\rm Data} \tag{10.23}$$

If $(F_2)_{\rm eff}^{\rm MC(n)}$, $M_k^{\rm Data}$, and $M_k^{\rm MC}$ are given for iteration $n$, the corresponding $(F_2)_{\rm eff}^{\rm Data(n+1)}$ for iteration $(n+1)$ is then given by the following equation derived from equation 10.15 and 10.23:

$$(F_2)_{\rm eff}^{\rm Data(n+1)} = \left(\frac{N^{\rm Data(n)}/\mathcal{L}^{\rm Data}}{N^{\rm MC(n)}/\mathcal{L}^{\rm MC}}\right)(F_2)_{\rm eff}^{\rm MC(n)} = \left(\frac{M^{\rm Data}/\mathcal{L}^{\rm Data}}{M^{\rm MC(n)}/\mathcal{L}^{\rm MC}}\right)(F_2)_{\rm eff}^{\rm MC(n)} \tag{10.24}$$

The effective structure function in the case of MC $(F_2)_{\rm eff}^{\rm MC(n)}$ is taken to be ALLM97 for iteration $n=0$ as this parametrization provided a good description of the previous BPC data. Starting from the second iteration the parametrization of $F_2$ as determined from a GVDM- and Regge-inspired fit as described in the next chapter is used. The measured number of events in MC, $M^{\rm MC(n)}(i)$, for a particular bin is given by:

$$M^{\rm MC(n)}(i) = \sum_{s=1}^{n_{\rm bin}(i)} w^s = \sum_{s=1}^{n_{\rm bin}(i)} w^s_{\rm gen}\cdot w^s_{\rm diff}\cdot w^s_{\mathcal{L}}\cdot w^s_{\rm vtx} \tag{10.25}$$

where $n_{\rm bin}(i)$ is the number of entries in MC in bin $i$. The MC weight factors $w^s_{\rm gen}$, $w^s_{\rm diff}$, $w^s_{\mathcal{L}}$, and $w^s_{\rm vtx}$ are used to reweight the MC events to the data. They depend on the true MC quantities $x$, $y$, $Q^2$, and the Z-position of the interaction vertex. $w^s_{\rm gen}(x_{\rm true}, Q^2_{\rm true})$ takes into account that the MC events were generated with the MRSA parametrization for $F_2$. It is defined as $w^s_{\rm gen} = (F_2)_{\rm eff}^{\rm MC(n)}/F_2^{\rm MRSA}$. The weigh $w^s_{\rm diff}(x_{\rm true}, Q^2_{\rm true})$ accounts for the mixing of the two MC samples as discussed in section 7.3. The weight $w^s_{\mathcal{L}}$ takes care of the different luminosities of the two MC samples and is defined as $w^s_{\mathcal{L}} = \mathcal{L}_{\rm DJANGOH}/\mathcal{L}_{\rm RAPGAP}$ for the RAPGAP sample and 1 in the case of the DJANGOH sample. Therefore, $\mathcal{L}^{\rm MC}$ is defined to be that of the DJANGOH sample. $w^s_{\rm vtx}$ describes any reweighting of the Z-vertex distribution in MC. Since the MC Z-vertex is taken from an unbiased estimate of the true vertex distribution for the time the data was collected, it is set to 1. The above bin-by-bin unfolding procedure excludes the determination of the covariance matrix. Therefore, the statistical error $\delta(F_2)_{\rm eff}/(F_2)_{\rm eff}$ of the obtained results for $(F_2)_{\rm eff}$ was estimated from the statistical uncertainties of the data and MC samples assuming a statistical independence of the two samples and ignoring any correlation



between bins. The contribution of background events in the data was found to be less than 2.6% for all bins (see section 9.7). It was therefore neglected in the calculation of $\delta(F_2)_{\rm eff}/(F_2)_{\rm eff}$.

$$\frac{\delta(F_2)_{\rm eff}}{(F_2)_{\rm eff}} = \sqrt{\left(\frac{\delta N_{\rm obs}^{\rm Data}}{N_{\rm obs}^{\rm Data}}\right)^2 + \left(\frac{\delta M^{\rm MC}}{M^{\rm MC}}\right)^2} \tag{10.26}$$

$$= \sqrt{\frac{1}{N_{\rm obs}^{\rm Data}} + \frac{\sum_{s=1}^{n_{\rm bin}}(w^s)^2}{(\sum_{s=1}^{n_{\rm bin}} w^s)^2}} \tag{10.27}$$

## 10.4 Evaluation of the systematic uncertainties

Systematic uncertainties in the measurement of $F_2$ arise from uncertainties in the detector understanding, the MC simulation and the conditions under which $F_2$ is being extracted. In order to estimate the systematic error of $F_2$ assigned to each bin several systematic checks were performed. For each check a certain aspect of the analysis cuts, the reconstruction of kinematic variables or the determination of $F_2$ itself was changed. The obtained $F_2$ values were compared to the $F_2$ values extracted under nominal conditions and the differences recorded as a systematic error for a particular systematic check. The total systematic error for $F_2$ for a particular bin is then determined by adding the final systematic errors for a particular systematic check in quadrature. The following part will discuss in detail all systematic checks.

### 10.4.1 Systematic errors related to the positron identification

The final state positron is identified by several requirements on the reconstructed BPC quantities and BPT tracks as described in section 9.4. The alignment of BPC and BPT w.r.t. the ZEUS coordinate system, the BPC energy linearity and uniformity, and the efficiency of both detectors are crucial for the extraction of $F_2$ . In addition to these sources of uncertainties, the effect of changing the cut on the fiducial area of the BPC, the BPC shower width and the track matching between BPT track and reconstructed BPC position were studied. The effect of the cut on the Z-position of the interaction point was also taken into account.

**1. BPC and BPT alignment**

The uncertainty of the BPC and BPT alignment was found to be 200 $\mu$m (see section 6.4). As a systematic check the alignment of both detectors was changed by $\pm$200 $\mu$m for data only. The BPC and BPT reconstruction was repeated using the modified alignment.

**2. BPC energy uniformity**

In section 6.10 the BPC energy was found to be stable within $\pm$0.3% after calibration. The energy scale of the BPC was therefore systematically changed by $\pm$0.3% for data events only.

**3. BPC energy linearity**

An upper limit for a non-linear behaviour of the BPC due to radiation damage was estimated in section 6.10.3. In order to have an upper limit of the influence of non-linearity on $F_2$, the BPC energy was corrected for an estimated non-linearity worse than that determined in section 6.10.3. A linear behaviour of the non-linearity as a function of the measured BPC energy was used with zero non-linearity at the calibration energy at the kinematic peak and $\pm$1.25% at 3 GeV.

**4. BPC fiducial cut**

To estimate the impact of the uncertainty in the definition of the BPC fiducial volume, the fiducial volume boundaries defined in section 6.11 were systematically varied separately by ±1 mm in X and Y for both data and MC.

**5. BPC shower width cut**

To estimate the uncertainty in the positron finding efficiency, the shower width cut ($\sigma_{\rm BPC} <$ 0.8 cm) was changed by ±0.1 cm in data and MC.

**6. BPT efficiency**

The BPT efficiency for both planes in data and MC was determined in section 6.8. It was used to correct the measured value of $(F_2)_{\rm eff}$ by the ratio of the efficiency in MC divided by the efficiency in data. As a systematic check the efficiency in data was changed by ±1.5% which directly results in a change in $F_2$ by the same percentage for all bins.

**7. BPC-BPT track matching cut**

In order to estimate the uncertainty in the track matching cut ($\Delta X < 5\sigma$) between the X-position reconstructed with the BPC and the BPT, the cut was changed by ±1 $\sigma$.

**8. BPC trigger efficiency**

The overall BPC trigger efficiency (FLT·SLT·TLT) was calculated for all bins used to extract $F_2$ and the amount of events in data corrected in the case of an efficiency below 1. As a consequence the correction was changed by the estimated uncertainty for each bin.

**9. Cut on the Z-vertex**

The range of the cut on the Z-vertex position as determined by the BPT was changed from ±90 cm to ±50 cm in data and MC in order to estimate the uncertainty on the satellite luminosity and acceptance.

### 10.4.2 Systematic errors related to the main ZEUS detector

The systematic errors related to the main ZEUS detector include the uncertainty of the energy scale of the main calorimeter and the impact of changing the cuts on $y_{\rm JB}$ and $\delta$.

**10. Energy scale of the main calorimeter**

The uncertainty of the energy scale of the main calorimeter of approximately 3% influences the reconstruction of the hadronic variables $\delta_h$ and $y_{\rm JB}$. The energy measured in the main calorimeter was systematically varied by ±3% for data events prior to the determination of $\delta_h$ and $y_{\rm JB}$.

**11. Change of the cut on $y_{\rm JB}$**

The effect on the cut of $y_{\rm JB} > 0.06$ ($y_{\rm JB} > 0.004$ at low $y$) due to a possible mismatch in the $y_{\rm JB}$ resolution between data and MC and the simulation of the hadronic final state or the noise description of the ZEUS uranium calorimeter, was taken into account by changing the cut on $y_{\rm JB}$ by ±0.01 (±0.001 at low $y$) for both data and MC events.

**12. Change of the cut on $\delta$**

The impact of changing the lower cut on $\delta$ of $\delta > 30\,{\rm GeV}$ to account for the photoproduction background contamination, a possible mismatch in the $\delta$ resolution between data and MC and the simulation of the hadronic final state was included in the evaluation of the systematic errors by changing the cut by ±2 GeV for both data and MC events.



### 10.4.3 Systematic errors related to the MC event simulation

Systematic uncertainties related to the MC event simulation are due to the amount of photoproduction background, the fraction of diffractive events, the description of the hadronic final state, and the simulation of radiative corrections.

**13. Number of photoproduction background events**

The amount of photoproduction background was determined in section 9.7 to be up to $(1.3^{+0.8}_{-0.6})\%$ in the medium $y$ region and up to $(2.6^{+2.2}_{-1.9})\%$ in the high $y$ region. A smoothed distribution of these events in $y$ rising linearly with $y$ (0% at $y = 0.37$ to 2.6% at $y = 0.87$) was used to correct the measured $F_2$. To account for the difference of the photoproduction background as determined by the different methods, the amount of the photoproduction background was changed by +200% and −100%.

**15. Fraction of diffractive events**

The fraction of diffractive events was determined in section 7.3. The mean values of diffractive events as determined from the two different methods were used. In order to take into account the uncertainty on the number of diffractive events between the two parametrizations, the amount of diffractive events was changed by ±15%.

**14. Simulation of radiative corrections**

The uncertainty in the radiative corrections in MC and data was determined using the ISR analysis as described in section 10.3.3. As a systematic check of the uncertainty of the radiative corrections, the MC events at $x$ and $Q^2$ below the region covered by the nominal analysis are reweighted to an $F_2$ which is shifted by 6%.

### 10.4.4 Other sources of systematic uncertainties

**15. Uncertainty in the luminosity measurement**

The total luminosity of the data used in this analysis is known to a precision of ±1.8%. As a consequence in addition to the overall systematic error, a normalization uncertainty of ±1.8% exists. Since this uncertainty is 100 %-correlated between all bins it is not included in the total bin-by-bin systematic error but is given as an overall uncertainty.

**Total systematic error**

The results of the systematic checks for each bin are shown in figures 10.10 and 10.11. Also shown are the total positive and negative systematic errors together with the statistical errors. The total positive and negative systematic errors for a particular $(y-Q^2)$-bin are determined by adding the positive and negative systematic errors for all systematic checks in quadrature. The bin numbers correspond to those given in figure 10.5 and are increasing with $y$. For each $y$-bin, the bin number is increasing with $Q^2$. The average statistical error is 2.6% and the average systematic error 3.3%. In most bins the systematic and statistical errors are very similar. The systematic error is usually composed of several small ones of the order of $(1.0-1.5)\%$. Only the bins at high $y$ and the bins at lower $y$ in the medium $y$ region are dominated by single systematic uncertainties. In the case of the bins at high values of $y$ the uncertainty in the diffractive fraction is the dominating contribution. At medium $y$ the uncertainty of the CAL energy scale is dominating the systematic error. Apart from this, the largest overall contribution to the

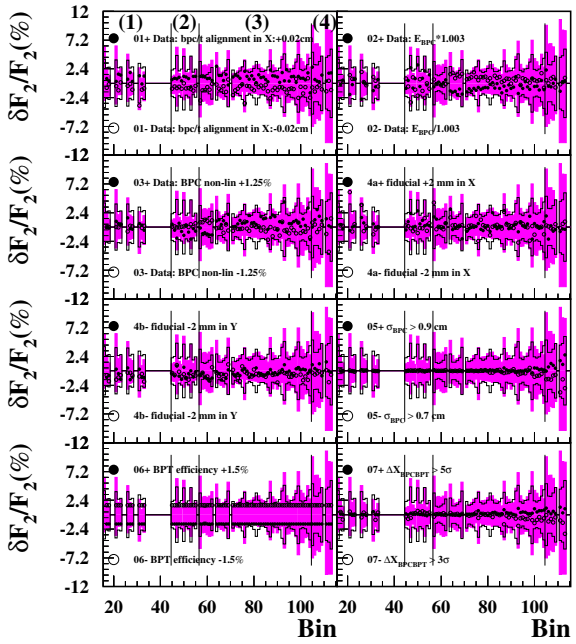


Figure 10.10: Individual systematic errors, $\delta F_2/F_2$ (in %) as a function of the bin number (part one). The bin numbers correspond to those given in figure 10.5 and are increasing with $y$. For each $y$-bin the bin number is increasing with $Q^2$. The numbers in the upper left plot denote the analysis region: LOWP (1), LOW (2), MED (3), HIGH (4). The shaded area denotes the total systematic error. In addition, there is a 1.8% normalization uncertainty. The total statistical error is given as the black line.

systematic error is the uncertainty of $\pm 1.5\%$ in the BPT efficiency.
Compared to the previous measurement at low $x$ and low $Q^2$ [Br97] the total systematic error was reduced by a factor of roughly 2–3. The main improvement is due to the better understanding of the detectors used to identify the scattered positron at low scattering angles (BPC and BPT), the estimated knowledge of the radiative corrections, and the reduced uncertainty of photoproduction background. The detector understanding improved in terms of alignment accuracy (500 $\mu$m $\rightarrow$ 200 $\mu$m), energy uniformity (uncertainty 0.5% $\rightarrow$ 0.3%) and energy non-linearity (1.5% $\rightarrow$ 0.5% at 7 GeV). The error due to the uncertainty of the radiative corrections was reduced from being $(3-4)\%$ to $(0-1)\%$ with the exception of a few bins where it is about 3%. The significantly improved background reduction due to the BPT track requirement



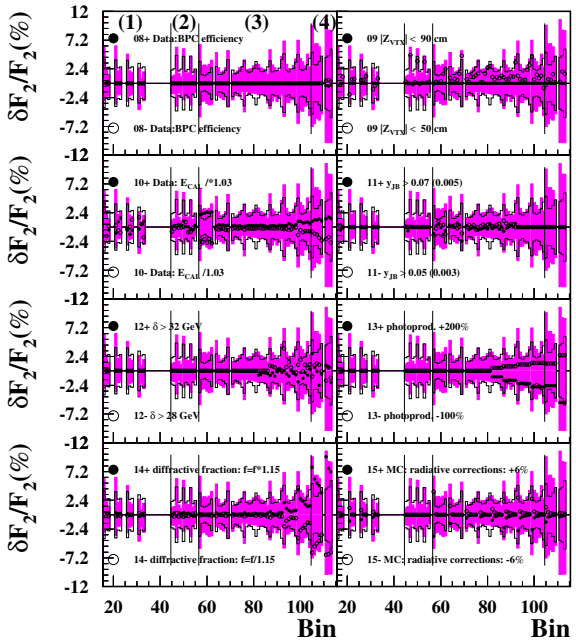


Figure 10.11: Individual systematic errors, $\delta F_2/F_2$ (in %) as a function of the bin number (part two). See figure 10.10 for description.

resulted in a decrease of the error on $F_2$ related to the amount of remaining photoproduction background events in the final data sample. It was reduced from up to 10% down to 1.5% in those bins at the highest $y$ in the medium $y$ region, which were also used in the previous analysis. At the new bins at higher $y$ the uncertainty is still small (up to 2.6%). The uncertainties in the luminosity measurement leads to a normalization error of 1.8% (not included in the total bin-by-bin systematic error).

## 10.5 Results on $\sigma_{\rm tot}^{\gamma^* p}$ and $F_2$

The final values for $\sigma_{\rm tot}^{\gamma^* p}$ and $F_2$ were determined using the $(y-Q^2)$-bins as discussed in detail in section 10.2. The mean values for $\sigma_{\rm tot}^{\gamma^* p}$ and $F_2$ for each bin, including their statistical uncertainties, were then evaluated using an iterative bin-by-bin unfolding procedure. The estimation of systematic uncertainties was presented in the last section.
The final values for $F_2$, assuming $R = R_{\rm BKS}$, together with their statistical and systematic errors are given in the tables 10.3 and 10.4. As discussed in section 10.3.2, assuming $R$ to be

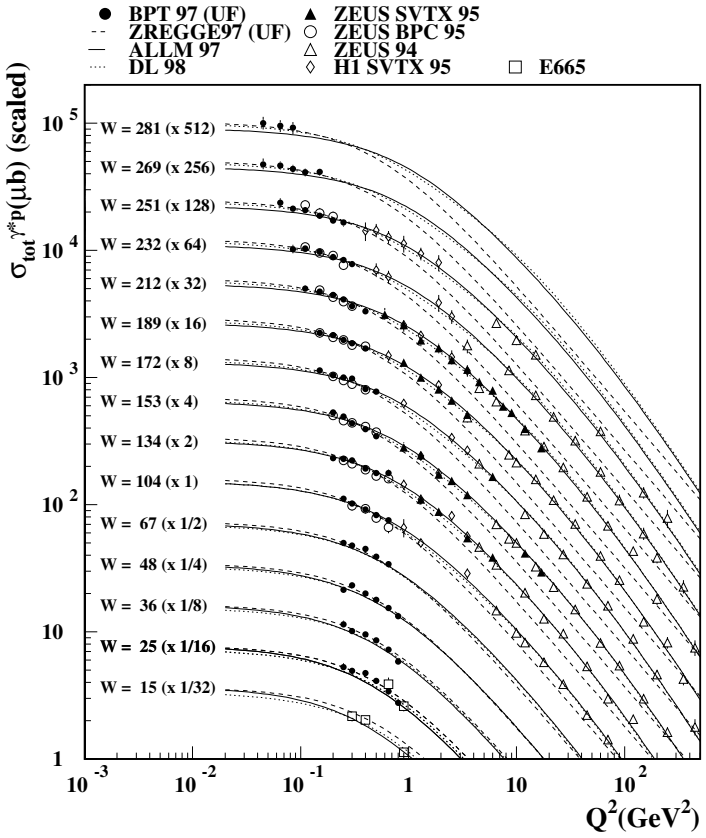


Figure 10.12: The total virtual photon-proton cross section $\sigma_{tot}^{\gamma^* p}$ as a function of $Q^2$ for fixed values of $W$ [GeV]. The data from this analysis ('BPT 97 (UF)'), previous ZEUS analyses, H1, and E665 are shown. The parametrization labeled 'ZREGGE97 (UF)' is the result of the fit used to extract $F_2$ as described in chapter 11. The predictions of the DL98 and the ALLM97 parametrization are also shown.

zero, decreases the extracted $F_2$ values compared to the case of $R_{BKS}$ by at most 3% for the highest $y$-bins used in this analysis. Using $R_{BPT}$ changes the results by less than 0.8%, while the use of $R_{GVDM}$ by up to 5%. The changes in $F_2$ and $\sigma_{tot}^{\gamma^* p}$ of both approaches for $R$ are also given in the tables. The results from the ISR analysis were used only to estimate the uncertainty on the radiative correction as discussed in section 10.3.3 and are given in table 10.2.
The results of this analysis labeled 'BPT 1997 (UF)' in terms of $\sigma_{tot}^{\gamma^* p}$ are presented in the figures 10.12 and 10.13. Figure 10.12 displays $\sigma_{tot}^{\gamma^* p}$ as a function of $Q^2$ in bins of $W$, figure 10.13



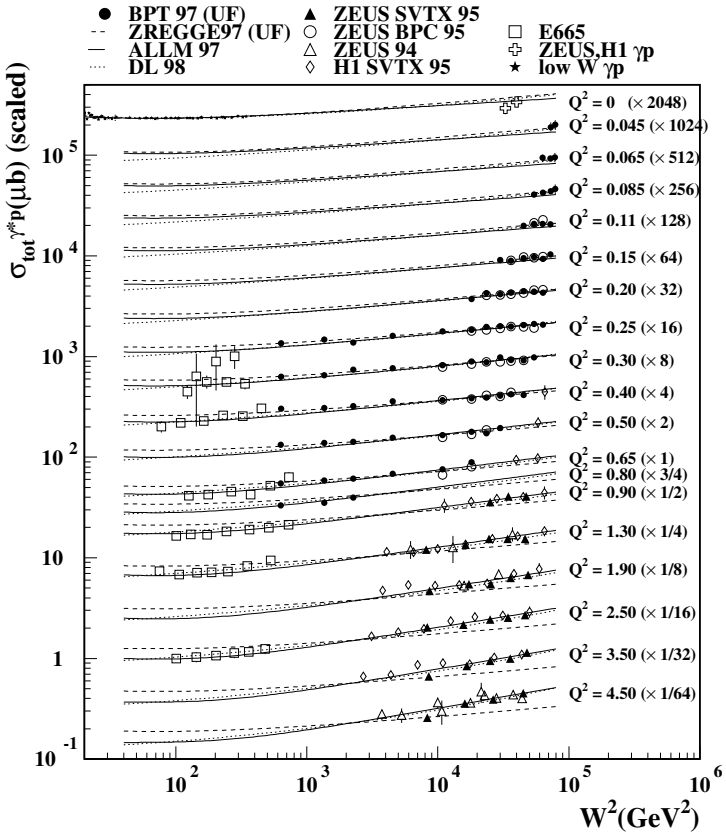


Figure 10.13: The total virtual photon-proton cross section $\sigma_{tot}^{\gamma^* p}$ as a function of $W^2$ for fixed values of $Q^2$ [GeV$^2$]. The total cross section for real photon-proton scattering from ZEUS, H1, and photoproduction experiments at low $W$ are also shown. See figure 10.12 for the description.

as a function of $W^2$ in bins of $Q^2$. The results in terms of $F_2$ as a function of $x$ for different $Q^2$-bins are shown in figure 10.14 and 10.15. The value of $R$ was taken from the BKS model, as discussed in section 10.3.2. For comparison, the results from other measurements including the previous ZEUS BPC [Br97] and the E665 [Ad96a] data at low $Q^2$ and low $x$ are also shown. The predicted behaviour of $\sigma_{tot}^{\gamma^* p}$ and $F_2$ as given by the ALLM97 and DL98 parametrizations are also shown. Two other independent analyses of the data sets presented here were done by Vincenzo Monaco [Mo98a] and Christoph Amelung [Am99]. All three results are in agreement with each other and for most bins with the ZEUS BPC results. Due to the extension of the

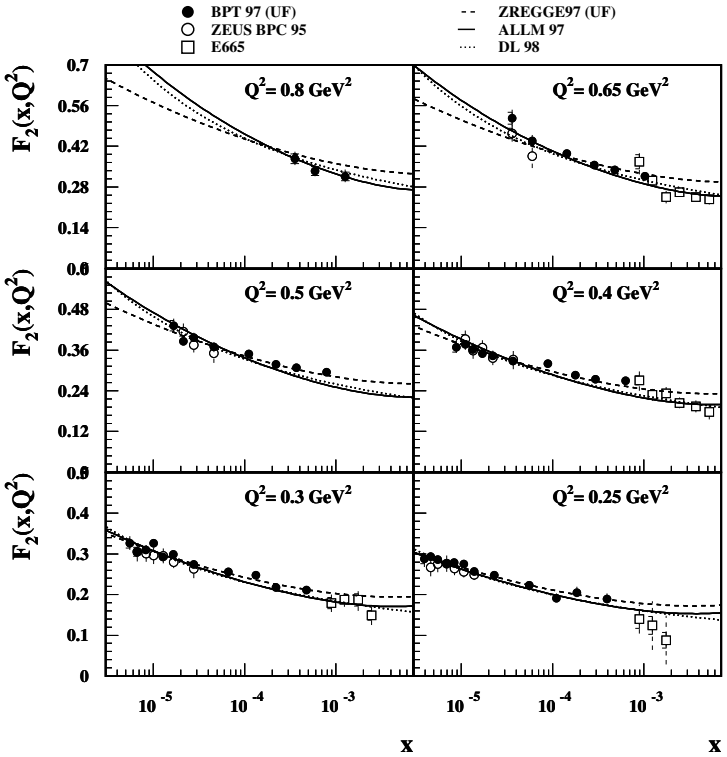


Figure 10.14: $F_2(x, Q^2)$ as a function of $x$ for fixed values of $Q^2$ ($Q^2 > 0.20$ GeV$^2$). The data from this analysis ('BPT 97 (UF)'), the previous ZEUS BPC analysis, and E665 are shown. The parametrization labeled 'ZREGGE97 (UF)' is the result of the fit used to extract $F_2$ as described in chapter 11. The predictions of the DL98 and the ALLM97 parametrization are also shown.

kinematic region towards higher values of $x$, for the first time overlap with the E665 data at low $Q^2$ was possible. To compare the E665 measurements to those presented here, they were extrapolated to the same $Q^2$ values using the ALLM97 parametrization [Ab97]. The agreement is reasonable except for the bins at $Q^2 = 0.25$ GeV$^2$ and the E665 data points at lowest $x$ for $Q^2 = 0.40$ GeV$^2$ and $Q^2 = 0.65$ GeV$^2$. In all cases the E665 points have significantly larger errors.

A QCD analysis of the 1995 BPC and shifted vertex data showed that pQCD calculations were



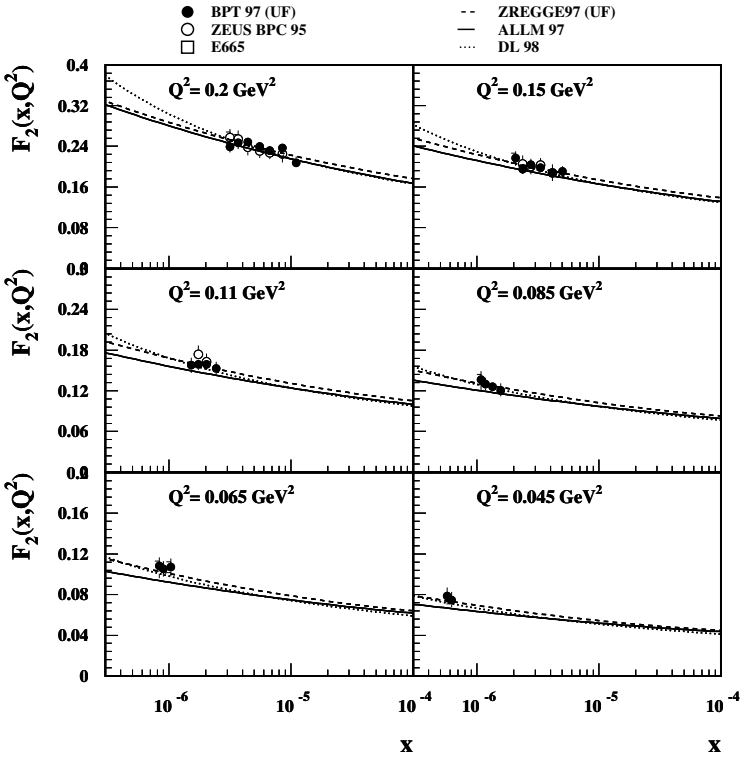


Figure 10.15: $F_2(x, Q^2)$ as a function of $x$ for fixed values of $Q^2$ ($Q^2 \leq 0.20$ GeV$^2$). See figure 10.14 for the description.

no longer valid below $Q^2 = 1.0$ GeV$^2$ [Su98]. The results presented here are in good agreement with the previous BPC measurements [Br97]. Therefore, the QCD analysis was not repeated with the new data. A comparison of the new results to various models of the behaviour of $\sigma_{tot}^{\gamma^* p}$ and $F_2$ is presented in the next chapter.

| $Q^2$ (GeV$^2$) | $y$ | $F_2$ | $\delta_{\rm stat}$ | $\delta^-_{\rm sys}$ | $\delta^+_{\rm sys}$ | $\sigma_{\rm tot}^{\gamma^* p}$ ($\mu$b) | $\delta_{R_{\rm GVDM}}$ (%) | $\delta_{R_{\rm BPT}}$ (%) |
|---|---|---|---|---|---|---|---|---|
| 0.8000 | 0.025 | 0.377102 | 0.017132 | 0.016684 | 0.013582 | 52.89 | 0.0 | 0.0 |
| 0.8000 | 0.015 | 0.334770 | 0.015028 | 0.019331 | 0.009215 | 46.95 | 0.0 | 0.0 |
| 0.8000 | 0.007 | 0.315877 | 0.014609 | 0.018953 | 0.012126 | 44.30 | 0.0 | 0.0 |
| 0.6500 | 0.200 | 0.516572 | 0.020472 | 0.028155 | 0.019531 | 89.17 | 0.5 | 0.0 |
| 0.6500 | 0.120 | 0.437997 | 0.011615 | 0.016945 | 0.015393 | 75.61 | 0.2 | 0.0 |
| 0.6500 | 0.050 | 0.395357 | 0.009263 | 0.008385 | 0.005896 | 68.25 | 0.0 | 0.0 |
| 0.6500 | 0.025 | 0.355513 | 0.008236 | 0.006053 | 0.008843 | 61.37 | 0.0 | 0.0 |
| 0.6500 | 0.015 | 0.338758 | 0.007973 | 0.003562 | 0.007968 | 58.48 | 0.0 | 0.0 |
| 0.6500 | 0.007 | 0.316427 | 0.007667 | 0.004332 | 0.005567 | 54.62 | 0.0 | 0.0 |
| 0.5000 | 0.330 | 0.432188 | 0.015683 | 0.013421 | 0.007404 | 96.99 | 1.3 | 0.1 |
| 0.5000 | 0.260 | 0.385824 | 0.010558 | 0.010536 | 0.005252 | 86.58 | 0.7 | 0.0 |
| 0.5000 | 0.200 | 0.397302 | 0.008620 | 0.010280 | 0.009205 | 89.16 | 0.4 | 0.0 |
| 0.5000 | 0.120 | 0.369081 | 0.006508 | 0.011566 | 0.013404 | 82.83 | 0.1 | 0.0 |
| 0.5000 | 0.050 | 0.348690 | 0.006362 | 0.004314 | 0.006843 | 78.25 | 0.0 | 0.0 |
| 0.5000 | 0.025 | 0.317556 | 0.006246 | 0.005418 | 0.006211 | 71.26 | 0.0 | 0.0 |
| 0.5000 | 0.015 | 0.308134 | 0.006375 | 0.005021 | 0.004788 | 69.15 | 0.0 | 0.0 |
| 0.5000 | 0.007 | 0.294649 | 0.006481 | 0.003428 | 0.004975 | 66.12 | 0.0 | 0.0 |
| 0.4000 | 0.500 | 0.368261 | 0.014480 | 0.016413 | 0.007072 | 103.30 | 3.0 | 0.2 |
| 0.4000 | 0.400 | 0.377057 | 0.010386 | 0.005443 | 0.012404 | 105.77 | 1.7 | 0.1 |
| 0.4000 | 0.330 | 0.362085 | 0.008854 | 0.010383 | 0.006104 | 101.57 | 1.1 | 0.1 |
| 0.4000 | 0.260 | 0.349349 | 0.007169 | 0.008946 | 0.007613 | 98.00 | 0.6 | 0.1 |
| 0.4000 | 0.200 | 0.343175 | 0.005916 | 0.007069 | 0.009346 | 96.27 | 0.4 | 0.0 |
| 0.4000 | 0.120 | 0.327392 | 0.004783 | 0.009301 | 0.010948 | 91.84 | 0.1 | 0.0 |
| 0.4000 | 0.050 | 0.319652 | 0.008727 | 0.006018 | 0.009359 | 89.67 | 0.0 | 0.0 |
| 0.4000 | 0.025 | 0.285694 | 0.007879 | 0.004966 | 0.005413 | 80.14 | 0.0 | 0.0 |
| 0.4000 | 0.015 | 0.274364 | 0.007474 | 0.006917 | 0.005085 | 76.96 | 0.0 | 0.0 |
| 0.4000 | 0.007 | 0.270093 | 0.007303 | 0.003631 | 0.005803 | 75.76 | 0.0 | 0.0 |
| 0.3000 | 0.600 | 0.326184 | 0.011446 | 0.013192 | 0.011960 | 122.00 | 3.9 | 0.4 |
| 0.3000 | 0.500 | 0.304622 | 0.007645 | 0.006155 | 0.007322 | 113.93 | 2.5 | 0.3 |
| 0.3000 | 0.400 | 0.309649 | 0.006602 | 0.006898 | 0.006305 | 115.81 | 1.4 | 0.2 |
| 0.3000 | 0.330 | 0.326512 | 0.006406 | 0.007891 | 0.005465 | 122.12 | 0.9 | 0.1 |
| 0.3000 | 0.260 | 0.292230 | 0.004994 | 0.005917 | 0.006104 | 109.30 | 0.5 | 0.1 |
| 0.3000 | 0.200 | 0.299086 | 0.004334 | 0.005480 | 0.007307 | 111.86 | 0.3 | 0.0 |
| 0.3000 | 0.120 | 0.273895 | 0.003398 | 0.008413 | 0.008003 | 102.44 | 0.1 | 0.0 |
| 0.3000 | 0.050 | 0.256263 | 0.006485 | 0.002165 | 0.005189 | 95.85 | 0.0 | 0.0 |
| 0.3000 | 0.025 | 0.247304 | 0.006237 | 0.005009 | 0.005149 | 92.50 | 0.0 | 0.0 |
| 0.3000 | 0.015 | 0.217720 | 0.005602 | 0.004510 | 0.004222 | 81.43 | 0.0 | 0.0 |
| 0.3000 | 0.007 | 0.210886 | 0.005394 | 0.005592 | 0.004616 | 78.88 | 0.0 | 0.0 |

Table 10.3: Results on the measurement of $F_2$ and $\sigma_{\rm tot}^{\gamma^* p}$ (part one, $Q^2 > 0.25$ GeV$^2$). The quoted values of $y$ and $Q^2$ are given in the first two columns. The extracted value of $F_2$ using $R_{\rm BKS}$ including statistical and systematic errors are given in the next four columns. The difference in $F_2$ if $R_{\rm GVDM}$ or $R_{\rm BPT}$ is used are given in the last two columns.



| $Q^2$ (GeV$^2$) | $y$ | $F_2$ | $\delta_{\rm stat}$ | $\delta^-_{\rm sys}$ | $\delta^+_{\rm sys}$ | $\sigma_{\rm tot}^{\gamma^* p}$ ($\mu$b) | $\delta_{R_{\rm GVDM}}$ (%) | $\delta_{R_{\rm BPT}}$ (%) |
|---|---|---|---|---|---|---|---|---|
| 0.2500 | 0.700 | 0.287877 | 0.012050 | 0.007643 | 0.015676 | 129.21 | 5.0 | 0.7 |
| 0.2500 | 0.600 | 0.293196 | 0.007230 | 0.008746 | 0.008194 | 131.59 | 3.4 | 0.4 |
| 0.2500 | 0.500 | 0.286290 | 0.005983 | 0.005331 | 0.008673 | 128.49 | 2.1 | 0.3 |
| 0.2500 | 0.400 | 0.275779 | 0.005281 | 0.006518 | 0.004894 | 123.78 | 1.2 | 0.2 |
| 0.2500 | 0.330 | 0.279079 | 0.004920 | 0.006615 | 0.005099 | 125.26 | 0.8 | 0.1 |
| 0.2500 | 0.260 | 0.274805 | 0.004334 | 0.004548 | 0.005390 | 123.34 | 0.5 | 0.1 |
| 0.2500 | 0.200 | 0.256481 | 0.003731 | 0.006555 | 0.005475 | 115.11 | 0.3 | 0.0 |
| 0.2500 | 0.120 | 0.247737 | 0.003518 | 0.007334 | 0.007533 | 111.19 | 0.1 | 0.0 |
| 0.2500 | 0.050 | 0.222715 | 0.007390 | 0.005742 | 0.009804 | 99.96 | 0.0 | 0.0 |
| 0.2500 | 0.025 | 0.191059 | 0.007351 | 0.009300 | 0.005797 | 85.75 | 0.0 | 0.0 |
| 0.2500 | 0.015 | 0.204657 | 0.007927 | 0.012732 | 0.007122 | 91.85 | 0.0 | 0.0 |
| 0.2500 | 0.007 | 0.189126 | 0.007610 | 0.011521 | 0.005449 | 84.88 | 0.0 | 0.0 |
| 0.2000 | 0.700 | 0.239085 | 0.007400 | 0.011636 | 0.008821 | 134.13 | 4.1 | 0.6 |
| 0.2000 | 0.600 | 0.246631 | 0.005840 | 0.005166 | 0.006847 | 138.37 | 2.8 | 0.4 |
| 0.2000 | 0.500 | 0.248456 | 0.005120 | 0.006408 | 0.005476 | 139.39 | 1.8 | 0.3 |
| 0.2000 | 0.400 | 0.239810 | 0.004656 | 0.006170 | 0.004416 | 134.54 | 1.0 | 0.2 |
| 0.2000 | 0.330 | 0.231372 | 0.004750 | 0.005223 | 0.003225 | 129.81 | 0.7 | 0.1 |
| 0.2000 | 0.260 | 0.236819 | 0.005253 | 0.003710 | 0.006618 | 132.86 | 0.4 | 0.1 |
| 0.2000 | 0.200 | 0.207703 | 0.005828 | 0.010641 | 0.004215 | 116.53 | 0.2 | 0.0 |
| 0.1500 | 0.800 | 0.216604 | 0.009869 | 0.009617 | 0.011052 | 162.03 | 4.5 | 0.8 |
| 0.1500 | 0.700 | 0.195043 | 0.004602 | 0.005642 | 0.007460 | 145.90 | 3.2 | 0.6 |
| 0.1500 | 0.600 | 0.203591 | 0.003834 | 0.005021 | 0.006514 | 152.29 | 2.2 | 0.4 |
| 0.1500 | 0.500 | 0.198135 | 0.003743 | 0.005999 | 0.005966 | 148.21 | 1.4 | 0.2 |
| 0.1500 | 0.400 | 0.187459 | 0.004564 | 0.005915 | 0.003657 | 140.23 | 0.8 | 0.1 |
| 0.1500 | 0.330 | 0.190435 | 0.007170 | 0.007401 | 0.009153 | 142.45 | 0.5 | 0.1 |
| 0.1100 | 0.800 | 0.157663 | 0.005705 | 0.009600 | 0.009688 | 160.82 | 3.4 | 0.7 |
| 0.1100 | 0.700 | 0.158858 | 0.003372 | 0.005678 | 0.007458 | 162.04 | 2.4 | 0.5 |
| 0.1100 | 0.600 | 0.158842 | 0.003434 | 0.004982 | 0.005160 | 162.03 | 1.7 | 0.3 |
| 0.1100 | 0.500 | 0.152714 | 0.005716 | 0.008528 | 0.006425 | 155.78 | 1.1 | 0.2 |
| 0.0850 | 0.870 | 0.136544 | 0.007802 | 0.011990 | 0.013573 | 180.25 | 3.2 | 0.7 |
| 0.0850 | 0.800 | 0.129687 | 0.003982 | 0.008544 | 0.007655 | 171.20 | 2.6 | 0.5 |
| 0.0850 | 0.700 | 0.125972 | 0.002925 | 0.005146 | 0.005793 | 166.29 | 1.9 | 0.4 |
| 0.0850 | 0.600 | 0.120778 | 0.005921 | 0.008502 | 0.006703 | 159.43 | 1.3 | 0.3 |
| 0.0650 | 0.870 | 0.108089 | 0.004948 | 0.009581 | 0.010743 | 186.59 | 2.5 | 0.5 |
| 0.0650 | 0.800 | 0.105286 | 0.003262 | 0.006919 | 0.007097 | 181.75 | 2.0 | 0.4 |
| 0.0650 | 0.700 | 0.106954 | 0.005159 | 0.007686 | 0.007151 | 184.63 | 1.5 | 0.3 |
| 0.0450 | 0.870 | 0.078556 | 0.003376 | 0.008336 | 0.007812 | 195.88 | 1.7 | 0.4 |
| 0.0450 | 0.800 | 0.074404 | 0.003837 | 0.007214 | 0.005363 | 185.52 | 1.4 | 0.3 |

Table 10.4: Results on the measurement of $F_2$ and $\sigma_{\rm tot}^{\gamma^* p}$ (part two, $Q^2 \leq 0.25$ GeV$^2$). See table 10.4 for the description.

# Chapter 11

# Results

## 11.1 Introduction

The analysis of the new data in the low $Q^2$-region from ZEUS [Br98a] and H1 [Ad97], especially the ZEUS BPC data [Br97] at $Q^2$ as low as 0.11 GeV$^2$ generated a lot of interest. Several models used to describe $\sigma_{\rm tot}^{\gamma^* p}$ and $F_2$ at low $x$ and low $Q^2$ were updated and new ones developed. In most cases the new data sets were used in the determination of the parameters of these models. The models are based on Regge theory (see section 2.8.2), the GVDM (see section 2.8.1), pQCD, or a combination of one or more of these. The first part of this chapter concentrates on the functional form of $\sigma_{\rm tot}^{\gamma^* p}$ and $F_2$ used in the unfolding. The extrapolation of the data points to $Q^2 = 0$ GeV$^2$ including a comparison with direct measurements of $\sigma_{\rm tot}^{\gamma p}$ are discussed in detail. An estimation of the ratio $R = \sigma_L^{\gamma^* p}/\sigma_T^{\gamma^* p}$ is made based on the data of this analysis and compared to the result obtained from vector meson production at HERA and THE BKS prediction. In the second part of the chapter, the extracted values of $F_2$ are compared to the predictions from various models of the low $x$ and low $Q^2$ region. The last part of the chapter will discuss the slope $\frac{{\rm d}\ln(F_2)}{{\rm d}\ln(1/x)}$ of $F_2$.

## 11.2 The functional form of $\sigma_{\rm tot}^{\gamma^* p}$ used in the unfolding

The functional form of $\sigma_{\rm tot}^{\gamma^* p}$, which was used in the iterative bin-by-bin unfolding discussed in section 10.3.4 is based on the GVDM and Regge theory. The $Q^2$-dependence of $\sigma_{\rm tot}^{\gamma^* p}$ is based on the GVDM, while the $W$-dependence was chosen based on Regge theory. Several different models of the $Q^2$- and $W$-dependence have been examined as discussed in the next two sections. The chosen functional form of $\sigma_{\rm tot}^{\gamma^* p}$ is given by:

$$\sigma_{\rm tot}^{\gamma^* p}(Q^2, W^2) = \frac{1}{(1+Q^2/m_0^2)} \cdot \left( A_{I\!R}\,(W^2)^{\alpha_{I\!R}-1} + A_{I\!P}\,(W^2)^{\alpha_{I\!P}-1} \right) \tag{11.1}$$

The parameters $m_0^2$, $A_{I\!R}$, $\alpha_{I\!R}$, $A_{I\!P}$, and $\alpha_{I\!P}$ were determined using a fit of the extracted values of $\sigma_{\rm tot}^{\gamma^* p}$ and fixed-target data at $Q^2 = 0$ GeV$^2$ after each iteration of the bin-by-bin unfolding. This fit is referred to as fit 0. The final values of the parameters including statistical and systematic errors are given in table 11.1. In contrast to the 1995 analysis of BPC data [Br97] $\alpha_{I\!R}$ was not fixed to 0.5 but determined in the same fit as the other parameters. In order to estimate the systematic errors of the parameters, the fit was repeated for each systematic check discussed in section 10.4 and the difference of the parameters w.r.t. the nominal values added in quadrature.





| Parameter (fit 0) | Value | $\delta_{\rm stat}$ | $\delta_{\rm sys}^-$ | $\delta_{\rm sys}^+$ |
|---|---|---|---|---|
| $A_{I\!R}$ ($\mu$b) | 141.316 | 1.843 | 1.8217 | 1.9062 |
| $\alpha_{I\!R}$ | 0.594 | 0.020 | 0.0215 | 0.0232 |
| $A_{I\!P}$ ($\mu$b) | 54.119 | 1.805 | 3.6735 | 3.3767 |
| $\alpha_{I\!P}$ | 1.115 | 0.003 | 0.0082 | 0.0088 |
| $m_0^2$ (GeV$^2$) | 0.535 | 0.005 | 0.0239 | 0.0237 |
| $\chi^2/ndf$ | 1.32 | | | |

Table 11.1: Parameters of the functional form of $\sigma_{\rm tot}^{\gamma^* p}$ used in the unfolding.

### 11.2.1 The $Q^2$-dependence of $\sigma_{\rm tot}^{\gamma^* p}$

The $Q^2$-dependence of $\sigma_{\rm tot}^{\gamma^* p} = \sigma_T^{\gamma^* p} + \sigma_L^{\gamma^* p}$ is based on the GVDM as discussed in section 2.8.1. For each $W$-bin the measured cross section $\sigma_{\rm tot}^{\gamma^* p}$ is extrapolated to $Q^2 = 0$ GeV$^2$. A certain ansatz for the cross sections of transversely and longitudinally polarized photon-proton scattering, $\sigma_T^{\gamma^* p}$ and $\sigma_L^{\gamma^* p}$, is made based on equations 11.2–11.5. The formulas are the same as those given in section 2.8.1 and are repeated here for convenience. The parameters of the adopted ansatz were determined from a fit of the extracted values of $\sigma_{\rm tot}^{\gamma^* p}$ using MINUIT. $\sigma_0^{\gamma p}(W)$, the extrapolated cross sections at $Q^2 = 0$ GeV$^2$ for each $W$-bin, were included as free parameters in the fit.

$$\sigma_T^{\gamma^* p}(W, Q^2) = \left( \sum_{V=\rho^0,\omega,\phi} \frac{4\pi\alpha \cdot r_V}{(1+Q^2/m_V^2)^2} + \sigma_{T,C}^{\gamma^* p} \right) \cdot \sigma_0^{\gamma p}(W) \tag{11.2}$$

$$\sigma_L^{\gamma^* p}(W, Q^2) = \left( \sum_{V=\rho^0,\omega,\phi} \frac{4\pi\alpha \cdot r_V}{(1+Q^2/m_V^2)^2} \cdot \xi_V \cdot \frac{Q^2}{m_V^2} + \sigma_{L,C}^{\gamma^* p} \right) \cdot \sigma_0^{\gamma p}(W) \tag{11.3}$$

$$\sigma_{T,C}^{\gamma^* p} = \frac{4\pi\alpha \cdot r_C}{(1+Q^2/m_0^2)} \tag{11.4}$$

$$\sigma_{L,C}^{\gamma^* p} = 4\pi\alpha \cdot r_C \cdot \xi_C \cdot \left[ \frac{m_0^2}{Q^2} \cdot \ln\left(1 + \frac{Q^2}{m_0^2}\right) - \frac{1}{(1+Q^2/m_0^2)} \right] \tag{11.5}$$

The maximal number of parameters in addition to the extrapolated cross sections at $Q^2 = 0$ GeV$^2$ is nine based on equations 11.2–11.5. Six parameters describe the contribution of the three lightest vector mesons $r_{\rho^0}$, $r_\omega$, $r_\phi$, $\xi_{\rho^0}$, $\xi_\omega$, and $\xi_\phi$. The other three parameters describe the contribution from the continuum: $r_C$, $\xi_C$, and $m_0^2$. Several different approaches have been compared to the data. The results are summarized in table 11.2. A reasonable fit was possible with only the continuum term and $m_0^2$ as an additional free parameter. This fit is referred to as fit 1. The same parametrization for the $Q^2$-dependence of $\sigma_{\rm tot}^{\gamma^* p}$ was used in the unfolding. The contributions from $\rho^0$, $\omega$, and $\phi$ were neglected ($r_{\rho^0} = r_\omega = r_\phi = 0$), as was that from $\sigma_L^{\gamma^* p}$ ($\xi_C = 0$). In order to estimate the systematic errors of the parameters, the fit was redone for each systematic check discussed in section 10.4 and the difference of the parameters w.r.t. the nominal values added in quadrature.
The result of the extrapolation is shown in figure 11.1. The fitted $Q^2$-dependence is in good agreement with the measured points with the exception of the data points at $Q^2 = 0.8$ GeV$^2$. Even at low values of $W$ the agreement is good, although the extrapolation is over the largest

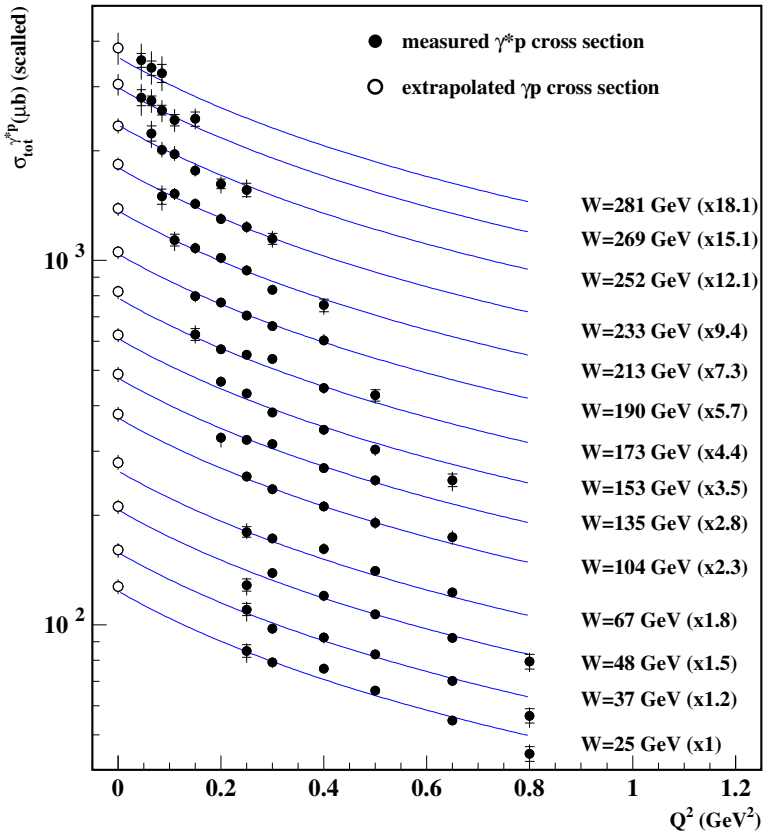


Figure 11.1: Extrapolation of $\sigma_{tot}^{\gamma^* p}$ to $Q^2 = 0$ GeV$^2$.

range in $Q^2$. The transition to $Q^2 = 0$ GeV$^2$ appears to be smooth. However, a comparison of the extrapolated cross sections $\sigma_0^{\gamma p}(W)$ with direct measurements from ZEUS [De94] and H1 [Ai95] shows that the extrapolated values overshoot the direct measurements, as shown in figure 11.2. Unpublished results from ZEUS from 1995 [Ma95] are slightly above the extrapolated values. In order to check whether the simplification made for fit 1 was the reason for the disagreement, more detailed fits based on equations 11.2–11.5 were performed.

Fit 2 included the contribution of $\sigma_L^{\gamma^* p}$ from the continuum term, which was also used in the



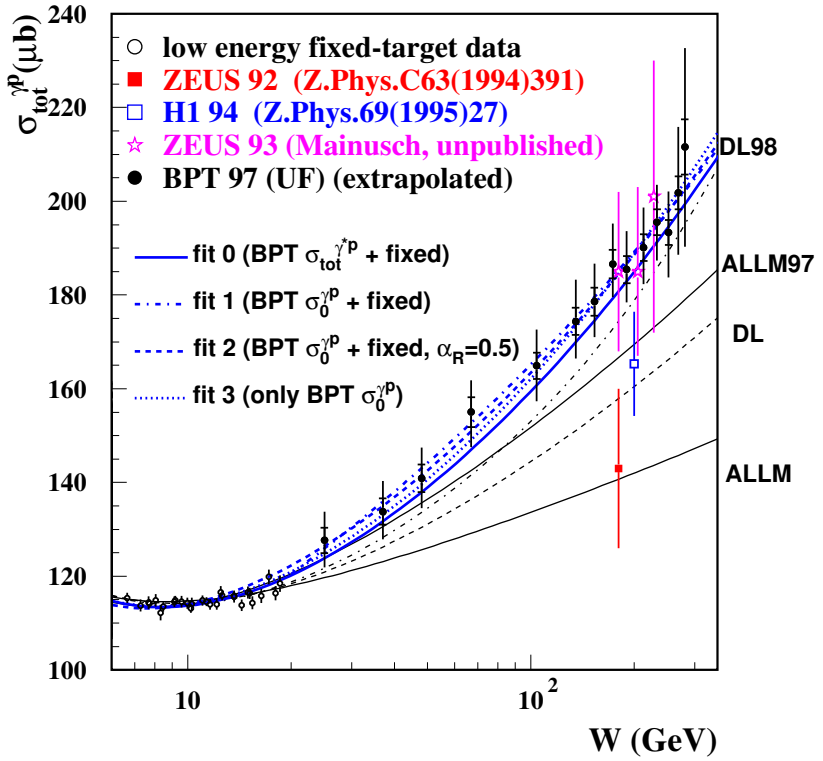


Figure 11.2: Comparison of $\sigma_0^{\gamma p}$ to direct measurements at $Q^2 = 0$ GeV$^2$. Also shown are the results of the fits of the $W$-dependence of $\sigma_0^{\gamma p}$ as discussed in section 11.2.2.

previous analysis [Br98a] ($\xi_C = 0.2$). Fit 3 included $\xi_C$ as a free parameter. If $\xi_C$ is limited between zero and one the result of the fit is zero. Without lower bound $\xi_C$ was determined as $-0.15 \pm 0.27$, which is compatible with zero. The results for this fit are given in table 11.2. The resulting values of the extrapolated cross sections from both versions of fit 2 are identical within statistical errors. As shown in table 11.2, the extrapolated cross sections at $Q^2 = 0$ GeV$^2$ for all fits are, within 1.5 times the statistical errors, in agreement with those obtained from fit 1, although in the case of fit 2 the value of $m_0^2$ is significantly smaller.

In order to estimate the impact of the contribution from $\rho^0$, $\omega$, and $\phi$, two fits similar to those described in [Sa72] were conducted. In fit 4 the contributions from the three vector mesons

| | fit 1 | | | | fit 2 | fit 3 | fit 4 | fit 5 |
|---|---|---|---|---|---|---|---|---|
| $W$ (GeV) | $\sigma_0^{\gamma p}$ ($\mu$b) | $\delta_{\rm stat}$ ($\mu$b) | $\delta_{\rm sys}^-$ ($\mu$b) | $\delta_{\rm sys}^+$ ($\mu$b) | $\sigma_0^{\gamma p}$ ($\mu$b) | $\sigma_0^{\gamma p}$ ($\mu$b) | $\sigma_0^{\gamma p}$ ($\mu$b) | $\sigma_0^{\gamma p}$ ($\mu$b) |
| 25 | 127.64 | 2.72 | 5.53 | 5.06 | 130.43 | 125.72 | 133.85 | 133.84 |
| 36 | 133.81 | 2.84 | 5.82 | 5.23 | 136.75 | 131.79 | 140.34 | 140.34 |
| 47 | 140.87 | 2.96 | 5.91 | 5.64 | 143.98 | 138.73 | 147.78 | 147.77 |
| 67 | 155.02 | 3.18 | 6.02 | 6.81 | 158.56 | 152.58 | 162.81 | 162.80 |
| 104 | 164.89 | 2.81 | 7.24 | 7.01 | 168.85 | 162.17 | 173.27 | 173.25 |
| 134 | 174.35 | 2.89 | 8.42 | 7.33 | 178.55 | 171.49 | 183.06 | 183.04 |
| 153 | 178.58 | 2.99 | 7.53 | 6.95 | 182.89 | 175.64 | 187.46 | 187.43 |
| 172 | 186.64 | 3.04 | 8.00 | 6.43 | 191.06 | 183.65 | 195.56 | 195.53 |
| 189 | 185.44 | 2.91 | 7.63 | 6.37 | 189.74 | 182.53 | 193.95 | 193.93 |
| 212 | 190.10 | 2.85 | 8.04 | 7.24 | 194.32 | 187.25 | 198.30 | 198.28 |
| 232 | 195.55 | 2.75 | 7.49 | 7.73 | 199.52 | 192.89 | 203.01 | 202.98 |
| 251 | 193.36 | 2.65 | 8.32 | 9.28 | 196.78 | 191.09 | 199.55 | 199.53 |
| 270 | 201.81 | 3.50 | 13.60 | 12.76 | 204.58 | 200.00 | 206.57 | 206.56 |
| 281 | 211.62 | 5.88 | 20.27 | 20.53 | 213.86 | 210.17 | 215.34 | 215.33 |
| $m_0^2$ | 0.507 | 0.020 | 0.039 | 0.034 | 0.411 | 0.585 | 3.0100 | 3.488 |
| $r_C$ | 1 | - | - | - | 1 | 1 | 0.22 | 0.22 |
| $\xi_C$ | 0 | - | - | - | 0.2 | -0.15±0.27 | 0.25 | 0 |
| $r_{\rho^0}$ | 0 | - | - | - | 0 | 0 | 0.65 | 0.65 |
| $r_\omega$ | 0 | - | - | - | 0 | 0 | 0.08 | 0.08 |
| $r_\phi$ | 0 | - | - | - | 0 | 0 | 0.05 | 0.05 |
| $\xi_{\rho^0}$ | 0 | - | - | - | 0 | 0 | 0.25 | 0.25 |
| $\xi_\omega$ | 0 | - | - | - | 0 | 0 | 0.25 | 0.25 |
| $\xi_\phi$ | 0 | - | - | - | 0 | 0 | 0.25 | 0.25 |
| $\chi^2/ndf$ | 1.68 | | | | 1.71 | 1.71 | 1.78 | 1.78 |

Table 11.2: Extrapolated cross section at $Q^2 = 0$ GeV$^2$.

were fixed according to the ratios determined from experiments at Orsay [Wo71] ($r_{\rho^0} = 0.65$, $r_\omega = 0.08$, $r_\phi = 0.05$) and the missing part contributed to the continuum ($r_C = 1 - 0.78 = 0.22$). The contribution of $\sigma_L^{\gamma^* p}$ was in all four cases fixed at 0.25. Fit 5 uses the same set of parameters except that no contribution of $\sigma_L^{\gamma^* p}$ for the continuum contribution is taken into account ($\xi_C = 0$). The results are also given in table 11.2. They are, within errors, in agreement with those obtained from fit 1, but systematically higher. Therefore, disagreement between the extrapolated BPT points and the direct measurement cannot be attributed to the used parametrization. Recent analyses of the total $\gamma p$ cross section from ZEUS [Gi99] at $W = 209$ GeV$^2$ are more precise than the old measurement [De94]. The results are also in better agreement with the H1 data [Ai95]. Therefore, the unpublished ZEUS results from 1995 [Ma95] are believed to be high. It has been suggested [H199] to lower the energy of the HERA positron beam for special runs in the year 2000 to gain access to lower values of $Q^2$. This would enable H1 and ZEUS to further investigate the disagreement before the HERA luminosity upgrade, after which the low $Q^2$ region will no longer be accessible due to modifications of the detectors.



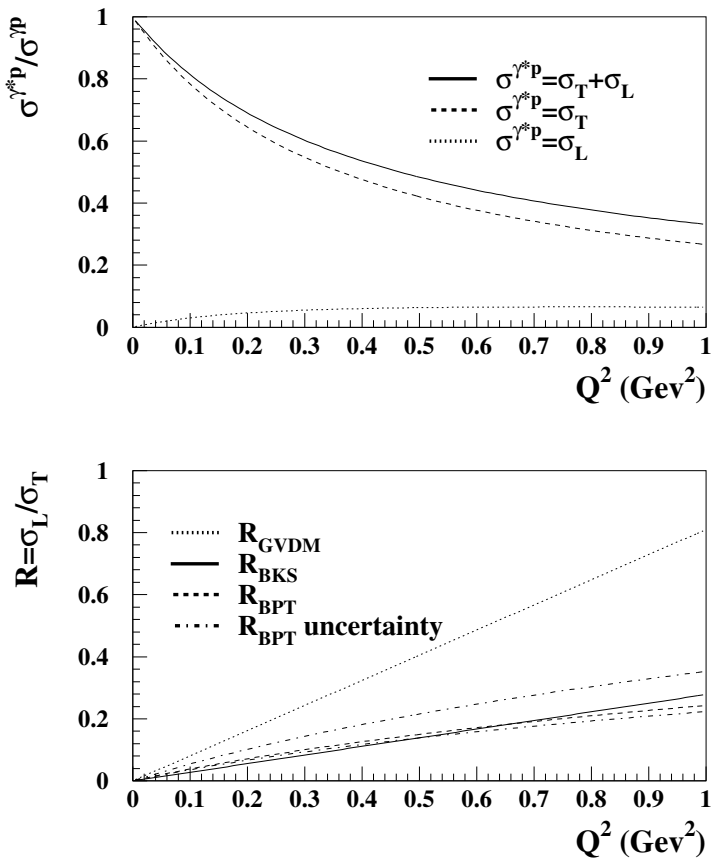


Figure 11.3: The upper plot shows the contribution of $\sigma_L^{\gamma^* p}$ and $\sigma_T^{\gamma^* p}$ to $\sigma_{\rm tot}^{\gamma^* p}$ normalized to the extrapolated cross section at $Q^2 = 0$ GeV$^2$ as determined from a fit of $\sigma_{\rm eff}^{\gamma^* p}$. The lower plot shows $R = \sigma_L^{\gamma^* p}/\sigma_T^{\gamma^* p}$ as determined from this analysis ($R_{\rm BPT}$) compared with the BKS parametrization ($R_{\rm BKS}$) and the results from vector meson production at HERA ($R_{\rm GVDM}$) as a function of $Q^2$.

**Estimation of the ratio $R = \sigma_L^{\gamma^* p}/\sigma_T^{\gamma^* p}$**

The ratio $R = \sigma_L^{\gamma^* p}/\sigma_T^{\gamma^* p}$ has recently been measured using vector meson production at HERA [Br98b]. In the low $Q^2$ region, $R$ was found to be independent of $W$ within $2\sigma$ and was

parametrized as a function of $Q^2$ given by equation 10.20. The value of $R_{\rm GVDM}$ is in good agreement with the parametrization $R = 0.5 \cdot Q^2/m_{\rho^0}^2$ used in the BPC 1995 analysis [Br97]. It is higher by roughly a factor of three than the value from the BKS model, which in good approximation at low $Q^2$ is given by $R = 0.165 \cdot Q^2/m_{\rho^0}^2$. The results from [Su98] obtained from the 1995 BPC analysis with a fit similar to fit 2 indicate an even smaller value. $R$ was extracted from the fitted functional forms of $\sigma_T^{\gamma^* p}$ and $\sigma_L^{\gamma^* p}$ as determined from a fit of type 3. The same iterative bin-by-bin unfolding as for the extraction of $\sigma_{\rm tot}^{\gamma^* p}$ and $F_2$ was used. In order to estimate the behaviour of $R$ from the data, no correction for $\epsilon(y) \neq 1$ was applied and the effective cross section $\sigma_{eff}^{\gamma^* p} = \sigma_T^{\gamma^* p} + \epsilon(y) \cdot \sigma_L^{\gamma^* p}$ was fitted. The agreement between the fitted function and the data points is not particularly good ($\chi^2/ndf = 1.72$). The resulting values were $m_0^2 = (0.363 \pm 0.03(\text{stat}))$ GeV$^2$ and $\xi_C = (0.303 \pm 0.07\ (\text{stat}))$. The results are shown in figure 11.3 together with the approximation of the BKS prediction ($R_{\rm BKS}$) and the parametrization measured from vector meson production at HERA ($R_{\rm GVDM}$). The error band indicates the change of $\xi_C$ and $m_0^2$ by $1\sigma$. The data is clearly in favour of the BKS parametrization of $R$. Therefore, this parametrization has been used in the extraction of $\sigma_{\rm tot}^{\gamma^* p}$ and $F_2$.

### 11.2.2 The $W$-dependence of $\sigma_{\rm tot}^{\gamma^* p}$

The $W$-dependence of the extrapolated cross sections $\sigma_0^{\gamma p}$ at $Q^2 = 0$ GeV$^2$ is parametrized with the following functional form based on Regge theory (see section 2.8.2):

$$\sigma_{\rm tot}^{\gamma p}(W^2) = A_{I\!R}\,(W^2)^{\alpha_{I\!R}-1} + A_{I\!P}\,(W^2)^{\alpha_{I\!P}-1} \tag{11.6}$$

The approach is similar to the initial one approach by Donnachie and Landshoff (see section 11.3.7). $A_{I\!R}$, $\alpha_{I\!R}$, $A_{I\!P}$, and $\alpha_{I\!P}$ are parameters and are determined from fits using MINUIT. The different fits described below take into account the extrapolated cross sections $\sigma_0^{\gamma p}$ of this analysis, fixed-target data at lower values of $W$, and measurements of $\sigma_{\rm tot}^{\gamma p}$ made by H1 and ZEUS using quasi-real photons. $A_{I\!R}$ and $\alpha_{I\!R}$ describe the fall of $\sigma_{\rm tot}^{\gamma p}$ at low values of $W$ (Reggeon trajectory), while $A_{I\!P}$ and $\alpha_{I\!P}$ describe the rise at higher values of $W$ (Pomeron trajectory).
Three different classes of fits were made. The results of all fits are shown in figure 11.2 and table 11.3. Fit 1 includes only the Pomeron term ($A_{I\!R} = 0$) of equation 11.6 and only the extrapolated BPT data points are used. The fit gives a good description of the BPT data, but overshoots the $\sigma_{\rm tot}^{\gamma p}$ measurements of H1 and ZEUS and the fixed-target data at high $W$. Fit 2 includes both the fixed-target and the extrapolated BPT data points. All parameters except

| | fit 3 | | | | fit 2 | fit 1 | fit 3a | fit 2a | fit 1a |
|---|---|---|---|---|---|---|---|---|---|
| Parameter | Value | $\delta_{\rm stat}$ | $\delta_{\rm sys}^-$ | $\delta_{\rm sys}^+$ | Value | Value | Value | Value | Value |
| $A_{I\!R}$ ($\mu$b) | 142.90 | 1.91 | 1.57 | 4.94 | 150.95 | 0.0 | 141.21 | 147.57 | 0.0 |
| $\alpha_{I\!R}$ | 0.591 | 0.021 | 0.060 | 0.010 | 0.500 | 0.0 | 0.571 | 0.500 | 0.0 |
| $A_{I\!P}$ ($\mu$b) | 53.58 | 1.96 | 2.53 | 7.23 | 60.45 | 66.98 | 56.97 | 62.12 | 70.61 |
| $\alpha_{I\!P}$ | 1.118 | 0.003 | 0.0156 | 0.008 | 1.107 | 1.098 | 1.110 | 1.101 | 1.090 |
| $\chi^2/ndf$ | 1.20 | | | | 1.27 | 0.78 | 1.92 | 1.95 | 13.25 |

Table 11.3: $W$-dependence of $\sigma_{\rm tot}^{\gamma^* p}$ extrapolated to $Q^2 = 0$ GeV$^2$.



$\alpha_{I\!R}$ are fitted. $\alpha_{I\!R}$ is fixed at 0.5, which is compatible with the original value of Donnachie and Landshoff (0.5475) and with recent estimates [Cu99]. The fit gives a good description of both data sets. In the third fit, $\alpha_{I\!R}$ is also fitted from the data with a resulting value compatible with that of Donnachie and Landshoff. The results from fit 2 and 3 are very similar, as shown in figure 11.2. All three fits are repeated including also the $\sigma_{\rm tot}^{\gamma p}$ measurements of H1 and ZEUS. The results (fit 1a, fit 2a, fit 3a) are compatible with the original fits within statistical errors and are given in table 11.3.

## 11.3 Models for $\sigma_{\rm tot}^{\gamma^* p}$ and $F_2$ and in the low $Q^2$ and very low $x$ region

The results of this analysis are compared to several models, which are briefly discussed in this section. The data presented here has so far not been used in the determination of the parameters of these models. Therefore, it is expected that the agreement between the new data and the models will increase after this is done.

### 11.3.1 Abramowicz, Levin, Levy, Maor (ALLM, ALLM97)

The parametrization proposed by Abramowicz, Levin, Levy, and Maor is based on a Regge motivated ansatz including pQCD expectations at high $Q^2$. It permits the parametrization of $F_2$ over the whole phase space in $Q^2$ and $x$ by a 23 parameter fit to experimental data [Ab90]. $F_2$ is parametrized as the sum of a Pomeron and a Reggeon term.

$$F_2 = \frac{Q^2}{Q^2 + m_0^2}\left(F_2^R + F_2^P\right) \tag{11.7}$$

Each term $F_2^i$, $(i = R, P)$ is represented by

$$F_2^i = \frac{Q^2}{Q^2 + m_0^2} \cdot C_i(t) \cdot x_i^{a_i(t)}(1-x)^{b_i(t)}, \quad \frac{1}{x_i} = 1 + \left(\frac{W^2 - m_p^2}{Q^2 + m_i^2}\right), \quad t = \ln\left(\frac{\ln\frac{Q^2+Q_0^2}{\Lambda^2}}{\ln\frac{Q_0^2}{\Lambda^2}}\right)$$

$\Lambda$ is the QCD scale and $m_p$ the proton mass. The four parameters $C_R$, $b_R$, $a_R$, and $b_P$ are assumed to be of the form $f(t) = f_1 + f_2 \cdot t^{f_3}$ and the two parameters $C_P$, $a_P$ of the form $g(t) = g_1 + (g_1 - g_2)\left(\frac{1}{1+t^{g_3}} - 1\right)$. The most recent version of this parametrization (*ALLM97*) was obtained by including the HERA data at low $x$ and $Q^2$ from 1994 and 1995 in the fit. The Pomeron intercept at $Q^2 = 0$ was fixed to the value of Donnachie and Landshoff (1.0808) since the total photoproduction measurements at HERA do not allow a precise determination of this value. The biggest change compared to the old fit is the change in the scale parameter of the Pomeron $m_P$. This parameter changed by about a factor of 5, which results in an earlier start of the transition region from the soft to the hard regime compared to the older ALLM parametrizations [Ab97].

### 11.3.2 Adel, Barreiro, Ynduráin (ABY)

A parametrization for $F_2$ at low $x$ is presented extending a high $Q^2$ QCD-inspired ansatz into the low $Q^2$ region [Ad96]. The assumption is made that at low values of $Q^2$ $F_2$ can be written in terms of a soft and a hard component. The evolution of $\alpha_s$ is modified such that it saturates

at a finite value when going to low values of $Q^2$. The proposed description of $F_2$ is given as follows:

$$F_2(x,Q^2) = \langle e_q^2 \rangle \left[ B_{ns} \widetilde{\alpha_s}(Q^2)^{-(1-\rho_0)} x^{\rho_0} + B_s \widetilde{\alpha_s}(Q^2)^{-(1+\lambda_0)} x^{-\lambda_0} + C \frac{Q^2}{Q^2+\Lambda^2_{\rm eff}} \right] \qquad (11.8)$$

### 11.3.3 Badelek, Kwiecinski (BK)

The ansatz for $F_2$ of Badelek and Kwiecinski is based on the generalized vector dominance model [Ba90]. Only the three lightest vector mesons are summed explicitly. The contribution of all higher mass vector meson states with $m_V^2 > Q_0^2$ are described by the structure function $F_2^{\rm AS}$ in the high $Q^2$ region and is assumed to be given. $F_2(x,Q^2)$ is then given as the sum of a vector meson part and a partonic part:

$$\begin{aligned} F_2(x,Q^2) &= F_2^V(x,Q^2) + F_2^{\rm par}(x,Q^2) \\ &= \frac{Q^2}{4\pi} \sum_{V=\rho^0,\omega,\phi} \left( \frac{m_V^4 \sigma_V(W^2)}{\gamma_V^2 (Q^2+m_V^2)^2} \right) + \left( \frac{Q^2}{Q^2+Q_0^2} \right) F_2^{\rm AS}(\bar{x}, Q^2+Q_0^2) \end{aligned} \qquad (11.9)$$

where $\bar{x} = (Q^2+Q_0^2)/(s+Q^2-m_p^2+Q_0^2)$. $Q_0^2 = 1.2$ GeV$^2$ is chosen to be greater than the mass of the heaviest vector meson explicitly used. The authors stress that apart from $Q_0^2$ which is constrained by physical requirements, the proposed representation of $F_2$ does not contain any free parameters apart from those included in $F_2^{AS}$.

### 11.3.4 Capella, Kaidalov, Merino, Tran-Than-Van (CKMT, CKMT98)

Capella et al. presented a common description of $\sigma_{\rm tot}^{\gamma p}$ and $F_2$ for $0 \le Q^2 \le 5\,{\rm GeV}^2$ within the framework of conventional Regge theory [Ca94]. They use in their Regge theory motivated ansatz one bare Pomeron with an intercept $1+\Delta(Q^2)$ which interpolates between the effective soft Pomeron and the effective hard Pomeron. The authors provide the following simple parametrization of $F_2$ for $0 \le Q^2 \le 5\,{\rm GeV}^2$:

$$\begin{aligned} F_2(x,Q^2) &= A x^{-\Delta(Q^2)} (1-x)^{n(Q^2)+4} \left( \frac{Q^2}{Q^2+a} \right)^{1+\Delta(Q^2)} + B x^{1-\alpha_R} (1-x)^{n(Q^2)} \left( \frac{Q^2}{Q^2+b} \right)^{\alpha_R} \qquad (11.10) \\ \Delta(Q^2) &= \Delta_0 \left( 1 + \frac{Q^2}{Q^2+d} \right), \qquad n(Q^2) = \frac{3}{2} \left( 1 + \frac{Q^2}{Q^2+c} \right) \end{aligned}$$

The first term accounts for the Pomeron contribution with the $Q^2$ dependent intercept given by $\Delta(Q^2)$. The second term corresponds to the Reggeon contribution at $x \to 0$. The behaviour of $F_2$ for $x \to 1$ is given by the factor $n(Q^2)$ in each term. The most recent parametrization is denoted *CKMT98*. It was derived by including the HERA data at low $x$ and $Q^2$ from 1994 and 1995 ([Br97], [Ad97]). A modified version of the model which includes a logarithmic dependence on $Q^2$ resulted in a less accurate description of the data [Ka98].

### 11.3.5 D'Alesio, Metz, Pirner (DMP)

The model developed by D'Alesio, Metz, and Pirner [Da99] to describe $\sigma_{\rm tot}^{\gamma^* p}$ and $F_2$ at low $x$ and low $Q^2$ consists of two components, a soft Pomeron and a hard Pomeron. This is similar to the ansatz discussed in section 11.3.2, but the treatment of the soft and hard contribution



is different. The soft Pomeron contribution $F_2^{\rm soft}$ is calculated using the Stochastic Vacuum Model [Do87] [Do88] and has only one free parameter, which regulates the scale. The hard Pomeron contribution $F_2^{\rm hard}$ was modeled using a power-law behaviour $F_2 \propto x^{-\lambda}$ with three free parameters. The treatment of $\alpha_s$ is different compared to ABY, and a phenomenological factor was added in order to get a finite cross section in the case of photoproduction. The complete ansatz for $F_2$ is given by:

$$\begin{aligned} F_2 &= F_2^{\rm soft} + F_2^{\rm hard} = F_2^{\rm soft} + C_2 \cdot \tilde{\alpha}_s(Q^2)^{-d_+(1+\lambda)} \cdot x^{-\lambda} \cdot \left( \frac{Q^2}{Q^2+M^2} \right) \qquad (11.11) \\ \tilde{\alpha}_s(Q^2) &= \frac{4\pi}{\beta_0 \ln((Q^2+M^2)/\Delta_{\rm QCD})}, \qquad d_+(1+\lambda) = \frac{108-101\lambda}{9\beta_0\lambda}, \qquad \beta_0 = 9 \end{aligned}$$

### 11.3.6 Desgrolard, Lengyel, Martynov (DLM)

The model described by Desgrolard, Lengyel, and Martynov was developed in the framework of traditional Regge theory. It is based on a single soft Pomeron independent of $Q^2$ with an intercept close or equal to 1. The $Q^2$ dependence of $\sigma_{\rm tot}^{\gamma^* p}$ is given by the residue function. The two models discussed in [De99] differ in the description of the Pomeron. In the so-called *Dipole Pomeron* model, the intercept of the Pomeron is fixed at 1. The *supercritical Pomeron* model uses a Pomeron intercept fixed at 1.0808. Both models give identical results in the range of the fitted experimental data ($W > 3$ GeV), but differ at lower $W$ and higher $Q^2$.

### 11.3.7 Donnachie, Landshoff (DL, DL98)

Donnachie and Landshoff fitted all total cross sections for $pp$, $p\bar{p}$, $\pi^{\pm}p$, $K^{\pm}p$, and $\gamma\, p$ scattering [Do92]. The fits were based on Regge theory. The total cross sections were fitted by the sum of two terms:

$$\sigma_{\rm tot} = X s^{\epsilon} + Y s^{-\eta} \qquad (11.12)$$

where $s$ is the square of the center-of-mass energy of the relevant process, i.e. $s \equiv W^2_{\gamma^* p}$ in the case of $\gamma^* p$ collisions. The first term accounts for the Pomeron exchange and the second one for the exchange of a conventional trajectory $(\rho, \omega, ...)$, i.e. a Reggeon. In the case of the total $\gamma\, p$ cross section the above parametrization together with $X = 0.0677$ mb, $\epsilon = 0.0808$, $Y = 0.129$ mb, and $\eta = 0.4525$ provides a good description of $\sigma_{\rm tot}^{\gamma p}$ measured at HERA [De94] [Ai95]. Cudell et al. [Cu99] presented a similar analysis with the Pomeron intercept at $(1.093 \pm 0.003)$. Donnachie and Landshoff extended their ansatz to $\gamma^* p$ cross sections. The proton structure function $F_2$ is parametrized as the sum of powers of $x^{\epsilon_i}$ multiplied by functions $f_i(Q^2)$ [Do94].

$$\begin{aligned} F_2 &= \sum_{i=1,2} f_i(Q^2) x^{\epsilon_i}, \quad f_i = A_i \cdot \left( \frac{Q^2}{Q^2+a_i} \right)^{1+\epsilon_i} \cdot g_i, \quad g_i = 1.0 \qquad (11.13) \\ \epsilon_1 &= 0.0808, \quad \epsilon_2 = -0.4525, \quad A_1 = 0.324, \quad A_2 = 0.098, \quad a_1 = 0.562, \quad a_2 = 0.01113 \end{aligned}$$

The first term in equation 11.13, the valence quark term, accounts for the Pomeron contribution whereas the second one, the sea quark term, accounts for the Reggeon contribution. The parameters in the fit are constrained such that for $Q^2 \to 0$ one retrieves the value for the $\sigma_{\rm tot}^{\gamma p}$ measurement. Recently [DL98] Donnachie and Landshoff repeated their fit using the latest data sets from HERA. They explain the rapid rise of $F_2$ at small $x$ by two Pomerons. Another term $f_0 \epsilon_0$ is added in equation 11.13 to account for the second (*hard*) Pomeron. The best fit of

the data was achieved by the following functions $f_i$ keeping $\epsilon_1$ and $\epsilon_2$ fixed at the same value as before. This new fit is referred to as *DL98*.

$$g_0 = \left[1 + X \cdot \log\left(1 + \frac{Q^2}{Q_0^2}\right)\right], \quad g_1 = \left(\frac{1}{1+\sqrt{\frac{Q^2}{Q_1^2}}}\right), \quad g_2 = 1.0 \tag{11.14}$$

$$A_0 = 0.0410 \quad A_1 = 0.387 \quad A_2 = 0.0504 \quad Q_0^2 = 10.600 \quad Q_1^2 = 48.00$$

$$a_0 = 7.1300 \quad a_1 = 0.684 \quad a_2 = 0.00291 \quad \epsilon_0 = 0.41800 \quad X = 0.485$$

### 11.3.8 Golec-Biernat, Wüsthoff (GBW)

Golec-Biernat and Wüsthoff developed a model for the low $x$ and low $Q^2$ region based on saturation (see section 2.7.5). They make use of the fact that at low $Q^2$ the photon-proton scattering process is dominated by one-photon exchange. They assume that the photon fluctuates into a quark-antiquark pair, which then scatters off the proton. The photon dissociation and the scattering is factorized into the photon wave function convoluted with a cross section $\hat{\sigma}(x, r^2) = \sigma_0 \cdot g(\hat{r}^2)$ describing the quark-antiquark scattering off the proton [Gb98]. The quark-antiquark separation $r$ is scaled by an $x$-dependent saturation radius $R_0(x) = 1/Q_0 \cdot (x/x_0)^{\lambda/2}$. The effective radius $\hat{r}$ is given by:

$$\hat{r} = \frac{r}{2 \cdot R_0(x)} = \frac{r}{2 \cdot \frac{1}{Q_0}\left(\frac{x}{x_0}\right)^{\lambda/2}} \tag{11.15}$$

where $x_0$, $\lambda$, and $\sigma_0$ are parameter, which were determined from a fit of DIS data below $x = 0.01$ including the BPC 95 data. $Q_0$ is a scale factor and was set to 1 GeV. Using $g(\hat{r}^2) = 1 - e^{-\hat{r}^2}$ resulted in a good description. The following functional form for $\sigma_{tot}^{\gamma^* p}$ is found:

$$\sigma_{tot}^{\gamma^* p}(x, Q^2) = \sigma_0 \cdot \left(\ln\left[k+1\right] + k \cdot \ln\left[\frac{1}{k} + 1\right]\right), \quad k = \left(\frac{x_0}{x}\right)^{\lambda} \cdot \frac{Q_0^2}{Q^2} \tag{11.16}$$

The authors stress that equation 11.16 is a simplification of the initial approach that reproduces all features but requires a refit of the parameters $x_0$, $\lambda$, and $\sigma_0$.

### 11.3.9 Haidt (HAIDT)

The parametrization proposed by Haidt [Ha99] is based on the experimental results, that in the low $x$ region the structure function $F_2$ is linear in terms of the empirical variable $\xi = \log(1 + \frac{Q^2}{Q_0^2}) \cdot \log(\frac{x_0}{x})$. A fit to the available data at low $x$ including the HERA data at low $x$ and $Q^2$ from 1994 and 1995 ([Br97], [Ad97]) resulted in the following parametrization for $F_2$:

$$F_2 = 0.41 \cdot \log(1 + \frac{Q^2}{0.5}) \cdot \log(\frac{0.04}{x}) \tag{11.17}$$

### 11.3.10 Martin, Ryskin, Stasto (MRS)

The description of $F_2$ developed by Martin, Ryskin, and Stasto is based on an extension of the ansatz of the BK (see section 11.3.3). $F_2$ is given as the sum of three parts [Ma98a]. The scale $Q_0^2$ and a boundary in the quark transverse momentum $k_0$ are defined to separate the three different regions. In the non-perturbative region $F_2$ is parametrized as the sum of two



parts. A pure VDM-based description is used in the region of $m_V^2 < Q_0^2$ (see $F_2^V(x, Q^2)$ in section 11.3.3). For $m_V^2 > Q_0^2$ the additive quark model is used to account for the contribution from large distances (quark transverse momentum $k_t < k_0$). The contribution to $F_2$ from the region of pQCD ($m_V^2 > Q_0^2$, $k_t > k_0$) is calculated by solving a coupled pair of integral equations for the gluon and sea quark contributions. The starting scale for the gluon distribution was chosen as $xg = Nx^{-\lambda} \cdot (1-x)^{\beta}$ with the parameters $N$, $\lambda$, and $\beta$.

### 11.3.11 Schildknecht, Spiesberger (SCSP)

Schildknecht and Spiesberger formulated explicit expressions for $\sigma_T^{\gamma^* p}$ and $\sigma_L^{\gamma^* p}$ in the framework of the generalized vector dominance model [Sc97]. Using $F_2 = \frac{Q^2}{4\pi^2\alpha}(\sigma_T^{\gamma^* p} + \sigma_L^{\gamma^* p})$, H1 and ZEUS data in the range of $Q^2 < 350\,\mathrm{GeV}^2$ were fitted by the following expression for $F_2$:

$$F_2(W^2, Q^2 \gg m_0^2) = \frac{N}{4\pi^2\alpha}\left(\ln\frac{1}{ax}\right)\left[1 + \xi\left(\ln\frac{Q^2}{m_0^2} - 1 - \frac{1}{6}\frac{3\ln^2(\frac{Q^2}{m_0^2}) + \pi^2}{\ln(\frac{1}{ax})}\right)\right] \tag{11.18}$$

The resulting values of the parameters were $N = 1.48$, $m_0^2 = 0.89$ GeV$^2$, $\xi = 0.171$, and $a = 15.1$. The authors remark that refinements to their GVDM ansatz following an old idea [Sa72] are necessary such as the treatment of the charm contribution to $F_2$ and the low energy behaviour of photoproduction.

## 11.4 Comparison of $F_2$ to various models

The results of this analysis are compared to the models described in the last section. Figure 11.4 shows $F_2$ as a function of $x$ for three $Q^2$-bins together with the predictions from the models. In general the predictions from the models are differ significantly, although the DLM, GBW, and DL98 model are in reasonably good agreement. In order to obtain a more quantitative comparison between data and prediction, the following definition of $\chi^2$ is used to compare the data points to the predictions:

$$\chi^2 = \sum_{\text{bins}} \left(\frac{F_2^{\text{Data}} - F_2^{\text{pred}}}{\delta F_2^{\text{Data}}}\right)^2 \tag{11.19}$$

$F_2^{\text{Data}}$ and $F_2^{\text{pred}}$ are the extracted and predicted values of $F_2$ for a given bin respectively. $\delta F_2^{\text{Data}}$ is calculated by adding the statistical and the mean of the upper and lower systematic errors of each bin in quadrature.
$\chi^2$ was determined for all bins used in this analysis. The results are shown in figure 11.5. Also given are the $\chi^2$ per bin, calculated separately for the low, medium, and high $y$ regions and for all bins in total. Table 11.4 summarizes the results.
As expected, the results from the Regge- and GVDM-inspired fit used in the unfolding are in best agreement with the final data points The results of the 1995 BPC measurement [Br97] for the medium $y$ region have been taken into account in the determination of the parameters of all models except for ALLM, CKMT, DL, ABY, and SS. Since the results of this analysis are in good agreement with the 1995 measurement, it is expected that the models except for those specifically mentioned above give a reasonably good description of the data. The new data in the low and high $y$ regions has so far not been used in any model. This is clearly visible in figure 11.5 and table 11.4.

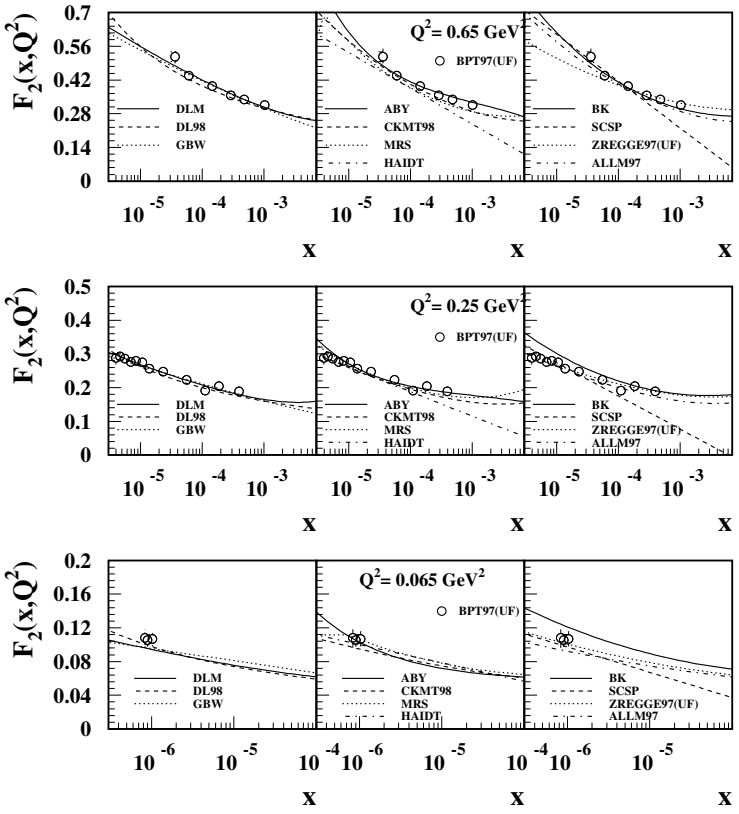


Figure 11.4: Comparison of $F_2$ with the models described in section 11.3. The ALLM, DL and CKMT models are omitted. Instead the updated models ALLM97, DL98 and CKMT98 are shown. The DMP model is not shown because for this model only predictions for the quoted $(y-Q^2)$-points of this analysis were available.

The best description of the data is given by the GBW, DLM, and DL98 models. GBW has the best overall description with a $\chi^2$/bin = 1.4, although the description of the low $y$ region is considerably worse, with a $\chi^2$/bin = 2.2. The model used only three parameters and one constant not fitted from the data to describe both the low $x$ and low $Q^2$ region behaviour of $F_2$ and the fraction of diffractive events in the total cross section. However, from the BPC and BPT data alone it cannot be concluded that there is indeed saturation at low $x$.
The second best description in terms of overall $\chi^2$/bin is given by DLM (1.5). The model gives an almost equally good description of the low $y$, medium $y$, and high $y$ region. This confirms



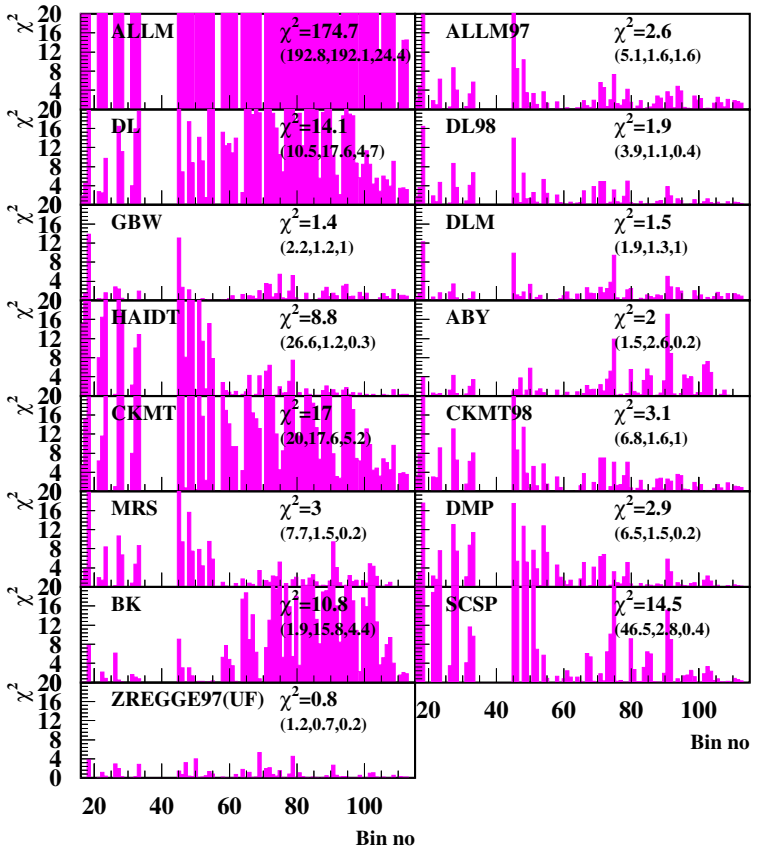


Figure 11.5: Contribution of all bins used in the analysis to the overall $\chi^2$/bin for the different models. The total $\chi^2$/bin and the separate values for the low, medium, and high $y$ regions are also given.

the results of the Regge-inspired fit used in the unfolding that the $W$-dependence at low $x$ and $Q^2$ is well described by a Pomeron with an intercept close to 1. Although GBW and DLM give the best overall description of the data, the low and medium $y$ regions are separately better described by the ABY ($\chi^2$/bin = 1.5) and DL98 ($\chi^2$/bin = 1.1) model respectively. In the ABY model a QCD-inspired ansatz is extended to lower values of $Q^2$. The analysis of the 1995

| Region | low $y$ | medium $y$ | high $y$ | total |
|---|---|---|---|---|
| Bins | 23 | 45 | 8 | 76 |
| Model | $\chi^2$/bin | | | |
| ZEUSREGGE (UF) | 1.2 | 0.7 | 0.2 | 0.8 |
| GBW | 2.2 | 1.2 | 1.0 | 1.4 |
| DLM | 1.9 | 1.3 | 1.0 | 1.5 |
| DL98 | 3.9 | 1.1 | 0.4 | 1.9 |
| ABY | 1.5 | 2.6 | 0.2 | 2.0 |
| ALLM97 | 5.1 | 1.6 | 1.6 | 2.6 |
| DMP | 6.5 | 1.5 | 0.2 | 2.9 |
| MRS | 7.7 | 1.5 | 0.2 | 3.0 |
| CKMT98 | 6.8 | 1.6 | 1.0 | 3.1 |
| HAIDT | 26.6 | 1.2 | 0.3 | 8.8 |
| BK | 1.9 | 15.8 | 4.4 | 10.8 |
| DL | 10.5 | 17.6 | 4.7 | 14.1 |
| SCSP | 46.5 | 2.8 | 0.4 | 14.5 |
| CKMT | 20.0 | 17.6 | 5.2 | 17.0 |
| ALLM | 192.8 | 192.1 | 24.4 | 174.7 |

Table 11.4: Comparison of $F_2$ in terms of $\chi^2$/bin to various models.

shifted vertex and BPC data [Br98a] has shown that the data is well described by pQCD down to $Q^2 = 1$ GeV$^2$. In that sense it is not surprising that the ABY model provides a good description of the new data at low $y$, which corresponds to the region of the highest $Q^2$ as shown in figure 10.2. On the other hand, the HAIDT model describes the data almost as good as the DL98 model ($\chi^2$/bin = 1.2 compared to 1.1), which is somewhat surprising. This model uses the simple phenomenological ansatz, that $F_2$ is linear in terms of an empirical variable $\xi$ with only three parameters. Since H1 and ZEUS data with $Q^2 < 2$ GeV$^2$ have also been used to fit the parameters, it seems reasonable to also expect agreement in the low $y$ (high $Q^2$) region to be improved once the new BPT data is included in the fit.

## 11.5 Slope of $F_2$

The slope $\frac{\mathrm{d}\ln(F_2)}{\mathrm{d}\ln(1/x)} = \lambda_{\mathrm{eff}}$ can be used to estimate the region in $Q^2$, where a single Regge trajectory dominates. At small $x$ and $Q^2$ the behaviour of $F_2$ at fixed $Q^2$ is characterized by $F_2 \propto x^{-\lambda_{\mathrm{eff}}}$. If a single Regge trajectory dominates, $\lambda_{\mathrm{eff}}$ is expected to be independent of $Q^2$ and equal to $\alpha_{I\!P} - 1$, whereas in the region of pQCD it is in LO BFKL expected to rise with $Q^2$. $F_2$ is fitted in bins of $Q^2$ to the functional form $F_2(x) = C(Q^2) \cdot x^{-\lambda_{\mathrm{eff}}}$. The data sets used are the BPT points of this analysis, the E665 data [Ad96a] extrapolated to the same values of $Q^2$ using the ALLM97 parametrization and unpublished points from an ongoing $F_2$ analysis of ZEUS 1996 and 1997 data [Wo99]. Only the data points with $x < 0.01$ are included, and $Q^2$-bins with less than three points are excluded from the fit. The fit is done using statistical errors only. The systematic errors of the results are estimated by repeating the fit using the results of each systematic check of the BPT data. For the other data sets the points are not



| $Q^2$ (GeV$^2$) | points used | $\lambda_{\mathrm{eff}}$ | $\delta^-_{\mathrm{sys}}$ | $\delta^+_{\mathrm{sys}}$ | $\delta_{\mathrm{stat}}$ |
|---|---|---|---|---|---|
| 0.065 | 3 | 0.032 | 0.264 | 0.325 | 0.360 |
| 0.085 | 4 | 0.278 | 0.195 | 0.194 | 0.209 |
| 0.110 | 4 | 0.056 | 0.115 | 0.151 | 0.121 |
| 0.150 | 7 | 0.068 | 0.018 | 0.022 | 0.026 |
| 0.200 | 8 | 0.059 | 0.011 | 0.013 | 0.014 |
| 0.250 | 15 | 0.100 | 0.005 | 0.009 | 0.006 |
| 0.300 | 14 | 0.104 | 0.004 | 0.004 | 0.004 |
| 0.400 | 16 | 0.101 | 0.004 | 0.004 | 0.004 |
| 0.500 | 8 | 0.089 | 0.006 | 0.003 | 0.006 |
| 0.650 | 11 | 0.131 | 0.007 | 0.006 | 0.006 |
| 0.800 | 15 | 0.113 | 0.018 | 0.012 | 0.012 |

Table 11.5: $\lambda_{\mathrm{eff}}$ as obtained from a fit to the BPT and E665 data.

changed. The results for the whole range in $x$ for each $Q^2$ interval are given shown in figure 11.6 and are given in table 11.5. Also shown are the predictions from the DL98, ALLM97, GBW, DLM, and ABY models. In the case of the predictions the fitted values of $F_2$ were taken from the models and the errors from the measured data points.
The BPT data is consistent with a constant value of $\lambda_{\mathrm{eff}} = 0.10$ for $Q^2 \leq 0.50$ GeV$^2$. Above $Q^2 = 2$ GeV$^2$ the rise of $\lambda_{\mathrm{eff}}$ with $Q^2$ is clearly visible and confirms the results of the 1995 analysis [Br98a]. At $Q^2 \geq 0.65$ GeV$^2$ there is indication that $\lambda_{\mathrm{eff}}$ is starting to deviate from the Regge-type behaviour although the significance of this is still small given the size of the errors. It is, however, consistent with the fact that the $F_2$ points at $Q^2 = 0.80$ GeV$^2$ are not described by the parametrization used in the unfolding, and that the $F_2$ points at the lowest values of $x$ for $Q^2 = 0.65$ GeV$^2$ and to a lower extend also for $Q^2 = 0.50$ GeV$^2$ overshoot the prediction of the parametrization used in the unfolding (see plot 10.15). None of the modes provides are good description over the whole $Q^2$-range. The GBW model is in good agreement with the BPT data points and reproduces the behaviour of the data points down to $Q^2 = 0.11$ GeV$^2$, but fails completely in the description of the data above $Q^2 = 1.0$ GeV$^2$. The other models have the tendency to overshoot the BPT data points especially at $Q^2 \leq 0.2$ GeV$^2$, where also the difference between the predictions is large. With the exception of the GBW model the data points at higher values of $Q^2$ are reasonably well described by the models, although the ALLM97 and ABY predictions tend to be low compared to the data at higher $Q^2$.

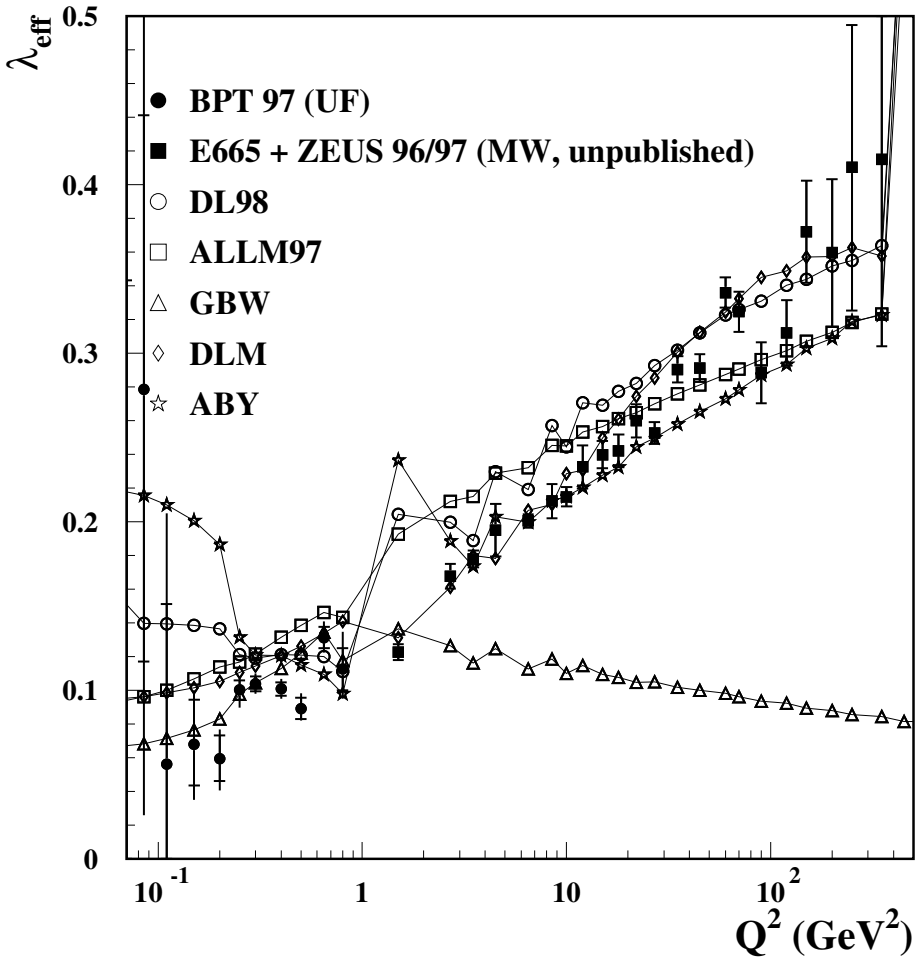


Figure 11.6: $\lambda_{\text{eff}}$ as a function of $Q^2$. In the case of the models the measured values of $F_2$ were replaced by the predictions and the fit was repeated. The errors of the data points were used.

# Chapter 12

# Conclusions

The total virtual photon-proton ($\gamma^* p$) cross section $\sigma_{\rm tot}^{\gamma^* p}$ and the proton structure function $F_2$ have been measured in the transition region between photoproduction ($Q^2 \approx 0$ GeV$^2$) and the regime of perturbative QCD in inelastic neutral current scattering, $e^+ p \to e^+ X$, using the ZEUS detector at HERA. The analysis covers the kinematic region $0.045 \leq Q^2 \leq 0.80$ GeV$^2$ and $3 \cdot 10^{-7} \leq x \leq 10^{-3}$. This corresponds to a range in the $\gamma^* p$ center-of-mass energy of $25 \leq W \leq 281$ GeV.

The analysis is based on a data sample of $3.9\,\mathrm{pb}^{-1}$ collected with the ZEUS detector during the last months of the HERA data taking in 1997. Events with positrons scattered at (15-40) mrad w.r.t. the direction of the HERA positron beam were selected with two special components of the ZEUS detector, the Beam Pipe Calorimeter (BPC) and the Beam Pipe Tracker (BPT). The BPC, a small segmented tungsten-scintillator calorimeter located close to the HERA beam pipe approximately 3 m from the interaction point, was installed in 1995 and has been used to access the kinematic region of $0.11 \leq Q^2 \leq 0.65$ GeV$^2$ and $0.08 \leq y \leq 0.74$ [Br97]. The BPT, installed in 1997 in front of the BPC, consisted in 1997 of two silicon microstrip detectors oriented orthogonal to the HERA beams. It was used for the measurement of the X-position of the scattered positron with an accuracy of about 40 $\mu$m and the horizontal positron scattering angle with an accuracy of about 0.04 mrad.

Using the combination of BPC and BPT, the kinematic acceptance was extended significantly compared to the 1995 analysis, for which only the BPC was used. At the same time the precision of the measurement was increased by a factor of 2–3. This was achieved through a reduction of detector-related uncertainties and through a reduction of the background in the final event sample.

Detector-related uncertainties include alignment, reconstruction, resolution, the energy scale and uniformity of the BPC, and the vertex finding efficiency. A new algorithm for the position reconstruction in the BPC was developed. Resolution and bias were determined by comparison with the position reconstructed with the BPT. The BPC position resolution was improved from $0.33\ \mathrm{cm}/\sqrt{E_{\rm BPC}/\mathrm{GeV}}$ to $0.22\ \mathrm{cm}/\sqrt{E_{\rm BPC}/\mathrm{GeV}}$. The bias was found to be of the order of 300 $\mu$m. The BPC energy calibration was improved by using the position reconstructed from the BPT if available, the new BPC position reconstruction algorithm, and an improved calibration procedure based on a global fit with all relevant parameters. The final uncertainty in the absolute energy scale of the BPC and uniformity of the energy response as a function of the shower position were reduced from $\pm 0.5\%$ to $\pm 0.3\%$. The alignment accuracy in X of both detectors was improved from $\pm 500$ $\mu$m to $\pm 200$ $\mu$m. This was achieved by comparing reconstructed BPT tracks with the reconstructed impact position in the BPC and with the vertex measured by the ZEUS central tracking chamber (CTD). One of the limiting uncertainties of the 1995 BPC





analysis was the inefficiency of the CTD to reconstruct the event vertex for events at low $y$ and for diffractive events. This was not the case for this analysis because the BPT track of the final state positron were used to reconstruct the Z-position of the event vertex. For events with a positron identified in the BPC and BPT, the reconstructed BPT tracks were extrapolated to the mean X-vertex measured with high precision with the CTD. The resolution of the Z-vertex reconstructed with the BPT was 3 cm.

The dominating source of background was photoproduction. For these events the final state positron is lost in the rear beam hole and particles from the hadronic final state fake a positron signal in the BPC. This background was reduced by requiring at least one reconstructed BPT track and a match between the reconstructed BPC X-position and the X-position obtained by extrapolating the BPT track to the BPC. Compared to the 1995 BPC analysis, the amount of this background in the final event sample was reduced from 10% to less than 1.5% in the kinematic region where both analyses overlap. In the kinematic region at higher values of $y$, previously not covered, the background was estimated to be less than 2.6%. A cut on the Z-position of the event vertex reconstructed by the BPT reduced the amount of beam-related background such as off-peak positrons and positron-beam gas interactions. This type of background was found to be less than 0.5%.

Due to the improvement in the background reduction, it was possible to extend the measurement into previously unexplored kinematic regions towards higher values of $y$ ($y_{\rm max}$: $0.74 \to 0.89$) and lower values of $Q^2$ ($Q^2_{\rm min}$: $0.11 \to 0.045$ GeV$^2$). An extension of the kinematic acceptance towards lower values of $y$ was made possible by the use of the BPT in the vertex determination and by the reconstruction of the kinematic variables with the $e\Sigma$ method instead of the electron method. The lower limit in $y$ was lowered from 0.08 to 0.005. This allowed for the first time a direct comparison of the HERA measurements of $F_2$ at low $Q^2$ with the results from the fixed-target experiment E665 [Ad96a].

The extracted values of $\sigma_{\rm tot}^{\gamma^* p}$ and $F_2$ were found to be in good agreement with the results of the 1995 BPC data in the region where both measurements overlap. They are compatible with the results from the E665 measurements although the E665 points at the lowest values of $x$ have the tendency to overshoot the BPT results. For $Q^2 \leq 0.65$ GeV$^2$ the data is well described by a phenomenological ansatz based on the GVDM for the $Q^2$-dependence and Regge theory for the $W$-dependence of $\sigma_{\rm tot}^{\gamma^* p}$. The $W$-dependence was parametrized as the sum of a Reggeon and Pomeron term. The Pomeron intercept $\alpha_{I\!P}$ was found to be $1.115 \pm 0.003^{+0.008}_{-0.008}$, which is slightly above the values of Donnachie and Landshoff [DL98] and Cudell et al. [Cu99]. The data points at $Q^2 = 0.8$ GeV$^2$ are poorly described by the phenomenological fit used in the unfolding, but are in agreement with the ALLM97 parametrization. This might be an indication that the simple ansatz is not valid at such values of $Q^2$. However, the data points are on the edge of the acceptance of the BPC and BPT and therefore have large errors. The $F_2$ points at the lowest values of $x$ for $Q^2 \geq 0.50$ GeV$^2$ start to overshoot the prediction from this GVDM- and Regge-inspired fit, indicating that the effects of the transition towards the regime of perturbative QCD (pQCD) are already present at these values of $Q^2$. The same indication was found in the logarithmic slope $\lambda_{\rm eff} = \mathrm{d}\ln(F_2)/\mathrm{d}\ln(1/x)$. For $Q^2 \leq 0.50$ GeV$^2$, $\lambda_{\rm eff}$ is compatible with a constant of 0.10, while it starts to rise with $Q^2$ for $Q^2 \geq 0.65$ GeV$^2$.

The results are compared to various models for the behaviour of $\sigma_{\rm tot}^{\gamma^* p}$ and $F_2$ in the region of low $x$ and low $Q^2$, based on the GVDM, Regge theory, pQCD, or a combination of these. The agreement is best in the medium $y$ region also covered in the 1995 BPC analysis ($0.08 \leq y \leq 0.74$). However, one has to keep in mind that for most models the results from the BPC measurements have been used in the determination or updating of the parameters of the models. The agreement in the high $y$ region ($y \geq 0.74$) is generally better, taking into account the relative

large errors for these bins. In the low $y$ region ($y \leq 0.08$) the agreement is worse in general than for the medium $y$ region. The best agreement for this region is found with the model of Adel, Barreiro, and Ynduráin (ABY). Since the low $y$ region corresponds to the highest values of $Q^2$, the good agreement with the ABY model in this region can be taken as another hint for the effects of pQCD already being present at $Q^2$ as low as 0.5 GeV$^2$. In the medium and high $y$ regions the best agreement between data and predictions was found for the model of Golec-Biernat and Wüsthoff (GBW), which is based on saturation, and the model of Desgrolard, Lengyel, and Martynov (DLM), which is based on traditional Regge theory with a single soft Pomeron.

The measured $\sigma_{\rm tot}^{\gamma^* p}$ cross sections were extrapolated to $Q^2 = 0$ GeV$^2$ and compared to the direct measurements of the total photon-proton cross section using quasi-real photons by H1 and ZEUS at HERA. As already observed in the 1995 BPC analysis, the extrapolated cross sections overshoot the results of the direct measurements. This effect is now even more pronounced due to the smaller errors of the extrapolated cross sections. It was checked that this was not an effect of the simple ansatz for the $Q^2$-dependence used in the extrapolation. Including the contributions from the three lightest vector mesons explicitly does not change the extrapolated cross sections by more than 1.5 times the statistical error. The extrapolated cross sections were even less affected by changes in the assumption for the relative strength of the cross section for longitudinal polarized photons ($\sigma_L^{\gamma^* p}$) compared to the one for transverse polarized photons ($\sigma_T^{\gamma^* p}$). It has been proposed that the HERA positron beam energy be lowered for a limited time in early 2000 to extend the kinematic acceptance of the ZEUS BPC and BPT and the corresponding components of the H1 detector to even lower values of $Q^2$, in order to study the discrepancy between the direct measurements and the extrapolated cross sections.

$\sigma_{\rm tot}^{\gamma^* p}$ and $F_2$ have been measured in the transition region between photoproduction and the regime of perturbative QCD with a significantly extended kinematic acceptance and an accuracy improved by a factor of two to three compared to previous measurements. The data points constrain the behaviour of any model used to describe the transition region and indicate that the effects of perturbative QCD are already present at $Q^2$ as low as 0.5 GeV$^2$.

# Appendix A

# Bin definitions

| $Q^2$-range (GeV$^2$) | $y$-range | $Q^2$ (GeV$^2$) | $y$ | $x$ | $W$ (GeV) |
|---|---|---|---|---|---|
| 0.1300 – 0.1700 | 0.1600 – 0.3700 | 0.1500 | 0.2600 | 0.0000064 | 153.0 |
| 0.1300 – 0.1700 | 0.0800 – 0.1600 | 0.1500 | 0.1200 | 0.0000138 | 104.0 |
| 0.1000 – 0.1300 | 0.1600 – 0.3700 | 0.1100 | 0.2600 | 0.0000047 | 153.0 |
| 0.1000 – 0.1300 | 0.0800 – 0.1600 | 0.1100 | 0.1200 | 0.0000101 | 104.0 |
| 0.0750 – 0.1000 | 0.1600 – 0.3700 | 0.0850 | 0.2600 | 0.0000036 | 153.0 |
| 0.0750 – 0.1000 | 0.0800 – 0.1600 | 0.0850 | 0.1200 | 0.0000078 | 104.0 |
| 0.0550 – 0.0750 | 0.1600 – 0.3700 | 0.0650 | 0.2600 | 0.0000028 | 153.0 |
| 0.0550 – 0.0750 | 0.0800 – 0.1600 | 0.0650 | 0.1200 | 0.0000060 | 104.0 |
| 0.0400 – 0.0550 | 0.1600 – 0.3700 | 0.0450 | 0.2600 | 0.0000019 | 153.0 |
| 0.0400 – 0.0550 | 0.0800 – 0.1600 | 0.0450 | 0.1200 | 0.0000041 | 104.0 |
| 0.0300 – 0.0400 | 0.1600 – 0.3700 | 0.0350 | 0.2600 | 0.0000015 | 153.0 |
| 0.0300 – 0.0400 | 0.0800 – 0.1600 | 0.0350 | 0.1200 | 0.0000032 | 104.0 |

Table A.1: Bins of the ISR region in the $(y - Q^2)$-plane used to estimate the uncertainty due to radiative corrections.





| $Q^2$-range (GeV$^2$) | $y$-range | $Q^2$ (GeV$^2$) | $y$ | $x$ | $W$ (GeV) |
|---|---|---|---|---|---|
| 0.7400 – 0.9400 | 0.0200 – 0.0400 | 0.8000 | 0.0250 | 0.0003537 | 48.0 |
| 0.7400 – 0.9400 | 0.0100 – 0.0200 | 0.8000 | 0.0150 | 0.0005895 | 37.0 |
| 0.7400 – 0.9400 | 0.0050 – 0.0100 | 0.8000 | 0.0070 | 0.0012633 | 25.0 |
| 0.5800 – 0.7400 | 0.1600 – 0.2300 | 0.6500 | 0.2000 | 0.0000359 | 135.0 |
| 0.5800 – 0.7400 | 0.0800 – 0.1600 | 0.6500 | 0.1200 | 0.0000599 | 104.0 |
| 0.5800 – 0.7400 | 0.0400 – 0.0800 | 0.6500 | 0.0500 | 0.0001437 | 67.0 |
| 0.5800 – 0.7400 | 0.0200 – 0.0400 | 0.6500 | 0.0250 | 0.0002874 | 48.0 |
| 0.5800 – 0.7400 | 0.0100 – 0.0200 | 0.6500 | 0.0150 | 0.0004790 | 37.0 |
| 0.5800 – 0.7400 | 0.0050 – 0.0100 | 0.6500 | 0.0070 | 0.0010264 | 25.0 |
| 0.4500 – 0.5800 | 0.3000 – 0.3700 | 0.5000 | 0.3300 | 0.0000167 | 173.0 |
| 0.4500 – 0.5800 | 0.2300 – 0.3000 | 0.5000 | 0.2600 | 0.0000213 | 153.0 |
| 0.4500 – 0.5800 | 0.1600 – 0.2300 | 0.5000 | 0.2000 | 0.0000276 | 135.0 |
| 0.4500 – 0.5800 | 0.0800 – 0.1600 | 0.5000 | 0.1200 | 0.0000461 | 104.0 |
| 0.4500 – 0.5800 | 0.0400 – 0.0800 | 0.5000 | 0.0500 | 0.0001105 | 67.0 |
| 0.4500 – 0.5800 | 0.0200 – 0.0400 | 0.5000 | 0.0250 | 0.0002211 | 48.0 |
| 0.4500 – 0.5800 | 0.0100 – 0.0200 | 0.5000 | 0.0150 | 0.0003685 | 37.0 |
| 0.4500 – 0.5800 | 0.0050 – 0.0100 | 0.5000 | 0.0070 | 0.0007896 | 25.0 |
| 0.3500 – 0.4500 | 0.4500 – 0.5400 | 0.4000 | 0.5000 | 0.0000088 | 213.0 |
| 0.3500 – 0.4500 | 0.3700 – 0.4500 | 0.4000 | 0.4000 | 0.0000111 | 190.0 |
| 0.3500 – 0.4500 | 0.3000 – 0.3700 | 0.4000 | 0.3300 | 0.0000134 | 173.0 |
| 0.3500 – 0.4500 | 0.2300 – 0.3000 | 0.4000 | 0.2600 | 0.0000170 | 153.0 |
| 0.3500 – 0.4500 | 0.1600 – 0.2300 | 0.4000 | 0.2000 | 0.0000221 | 135.0 |
| 0.3500 – 0.4500 | 0.0800 – 0.1600 | 0.4000 | 0.1200 | 0.0000368 | 104.0 |
| 0.3500 – 0.4500 | 0.0400 – 0.0800 | 0.4000 | 0.0500 | 0.0000884 | 67.0 |
| 0.3500 – 0.4500 | 0.0200 – 0.0400 | 0.4000 | 0.0250 | 0.0001769 | 48.0 |
| 0.3500 – 0.4500 | 0.0100 – 0.0200 | 0.4000 | 0.0150 | 0.0002948 | 37.0 |
| 0.3500 – 0.4500 | 0.0050 – 0.0100 | 0.4000 | 0.0070 | 0.0006317 | 25.0 |
| 0.2700 – 0.3500 | 0.5400 – 0.6400 | 0.3000 | 0.6000 | 0.0000055 | 233.0 |
| 0.2700 – 0.3500 | 0.4500 – 0.5400 | 0.3000 | 0.5000 | 0.0000066 | 213.0 |
| 0.2700 – 0.3500 | 0.3700 – 0.4500 | 0.3000 | 0.4000 | 0.0000083 | 190.0 |
| 0.2700 – 0.3500 | 0.3000 – 0.3700 | 0.3000 | 0.3300 | 0.0000100 | 173.0 |
| 0.2700 – 0.3500 | 0.2300 – 0.3000 | 0.3000 | 0.2600 | 0.0000128 | 153.0 |
| 0.2700 – 0.3500 | 0.1600 – 0.2300 | 0.3000 | 0.2000 | 0.0000166 | 135.0 |
| 0.2700 – 0.3500 | 0.0800 – 0.1600 | 0.3000 | 0.1200 | 0.0000276 | 104.0 |
| 0.2700 – 0.3500 | 0.0400 – 0.0800 | 0.3000 | 0.0500 | 0.0000663 | 67.0 |
| 0.2700 – 0.3500 | 0.0200 – 0.0400 | 0.3000 | 0.0250 | 0.0001326 | 48.0 |
| 0.2700 – 0.3500 | 0.0100 – 0.0200 | 0.3000 | 0.0150 | 0.0002211 | 37.0 |
| 0.2700 – 0.3500 | 0.0050 – 0.0100 | 0.3000 | 0.0070 | 0.0004737 | 25.0 |

Table A.2: Bins in the $(y - Q^2)$-plane used to extract $F_2$ and $\sigma_{\rm tot}^{\gamma^* p}$ (part one, $Q^2 > 0.25$ GeV$^2$).

| $Q^2$-range (GeV$^2$) | $y$-range | $Q^2$ (GeV$^2$) | $y$ | $x$ | $W$ (GeV) |
|---|---|---|---|---|---|
| 0.2100 – 0.2700 | 0.6400 – 0.7400 | 0.2500 | 0.7000 | 0.0000039 | 252.0 |
| 0.2100 – 0.2700 | 0.5400 – 0.6400 | 0.2500 | 0.6000 | 0.0000046 | 233.0 |
| 0.2100 – 0.2700 | 0.4500 – 0.5400 | 0.2500 | 0.5000 | 0.0000055 | 213.0 |
| 0.2100 – 0.2700 | 0.3700 – 0.4500 | 0.2500 | 0.4000 | 0.0000069 | 190.0 |
| 0.2100 – 0.2700 | 0.3000 – 0.3700 | 0.2500 | 0.3300 | 0.0000084 | 173.0 |
| 0.2100 – 0.2700 | 0.2300 – 0.3000 | 0.2500 | 0.2600 | 0.0000106 | 153.0 |
| 0.2100 – 0.2700 | 0.1600 – 0.2300 | 0.2500 | 0.2000 | 0.0000138 | 135.0 |
| 0.2100 – 0.2700 | 0.0800 – 0.1600 | 0.2500 | 0.1200 | 0.0000230 | 104.0 |
| 0.2100 – 0.2700 | 0.0400 – 0.0800 | 0.2500 | 0.0500 | 0.0000553 | 67.0 |
| 0.2100 – 0.2700 | 0.0200 – 0.0400 | 0.2500 | 0.0250 | 0.0001105 | 48.0 |
| 0.2100 – 0.2700 | 0.0100 – 0.0200 | 0.2500 | 0.0150 | 0.0001842 | 37.0 |
| 0.2100 – 0.2700 | 0.0050 – 0.0100 | 0.2500 | 0.0070 | 0.0003948 | 25.0 |
| 0.1700 – 0.2100 | 0.6400 – 0.7400 | 0.2000 | 0.7000 | 0.0000032 | 252.0 |
| 0.1700 – 0.2100 | 0.5400 – 0.6400 | 0.2000 | 0.6000 | 0.0000037 | 233.0 |
| 0.1700 – 0.2100 | 0.4500 – 0.5400 | 0.2000 | 0.5000 | 0.0000044 | 213.0 |
| 0.1700 – 0.2100 | 0.3700 – 0.4500 | 0.2000 | 0.4000 | 0.0000055 | 190.0 |
| 0.1700 – 0.2100 | 0.3000 – 0.3700 | 0.2000 | 0.3300 | 0.0000067 | 173.0 |
| 0.1700 – 0.2100 | 0.2300 – 0.3000 | 0.2000 | 0.2600 | 0.0000085 | 153.0 |
| 0.1700 – 0.2100 | 0.1600 – 0.2300 | 0.2000 | 0.2000 | 0.0000111 | 135.0 |
| 0.1300 – 0.1700 | 0.7400 – 0.8400 | 0.1500 | 0.8000 | 0.0000021 | 269.0 |
| 0.1300 – 0.1700 | 0.6400 – 0.7400 | 0.1500 | 0.7000 | 0.0000024 | 252.0 |
| 0.1300 – 0.1700 | 0.5400 – 0.6400 | 0.1500 | 0.6000 | 0.0000028 | 233.0 |
| 0.1300 – 0.1700 | 0.4500 – 0.5400 | 0.1500 | 0.5000 | 0.0000033 | 213.0 |
| 0.1300 – 0.1700 | 0.3700 – 0.4500 | 0.1500 | 0.4000 | 0.0000041 | 190.0 |
| 0.1300 – 0.1700 | 0.3000 – 0.3700 | 0.1500 | 0.3300 | 0.0000050 | 173.0 |
| 0.1000 – 0.1300 | 0.7400 – 0.8400 | 0.1100 | 0.8000 | 0.0000015 | 269.0 |
| 0.1000 – 0.1300 | 0.6400 – 0.7400 | 0.1100 | 0.7000 | 0.0000017 | 252.0 |
| 0.1000 – 0.1300 | 0.5400 – 0.6400 | 0.1100 | 0.6000 | 0.0000020 | 233.0 |
| 0.1000 – 0.1300 | 0.4500 – 0.5400 | 0.1100 | 0.5000 | 0.0000024 | 213.0 |
| 0.0750 – 0.1000 | 0.8400 – 0.8900 | 0.0850 | 0.8700 | 0.0000011 | 281.0 |
| 0.0750 – 0.1000 | 0.7400 – 0.8400 | 0.0850 | 0.8000 | 0.0000012 | 269.0 |
| 0.0750 – 0.1000 | 0.6400 – 0.7400 | 0.0850 | 0.7000 | 0.0000013 | 252.0 |
| 0.0750 – 0.1000 | 0.5400 – 0.6400 | 0.0850 | 0.6000 | 0.0000016 | 233.0 |
| 0.0550 – 0.0750 | 0.8400 – 0.8900 | 0.0650 | 0.8700 | 0.0000008 | 281.0 |
| 0.0550 – 0.0750 | 0.7400 – 0.8400 | 0.0650 | 0.8000 | 0.0000009 | 269.0 |
| 0.0550 – 0.0750 | 0.6400 – 0.7400 | 0.0650 | 0.7000 | 0.0000010 | 252.0 |
| 0.0400 – 0.0550 | 0.8400 – 0.8900 | 0.0450 | 0.8700 | 0.0000006 | 281.0 |
| 0.0400 – 0.0550 | 0.7400 – 0.8400 | 0.0450 | 0.8000 | 0.0000006 | 269.0 |

Table A.3: Bins in the $(y - Q^2)$-plane used to extract $F_2$ and $\sigma_{tot}^{\gamma^* p}$ (part two, $Q^2 \leq 0.25$ GeV$^2$).

# Appendix B

# BPC trigger cuts

| Region | Trigger | Requirements/Cuts/Comments |
|---|---|---|
| ISR | FLT 32 | (CTD tracks or $E^{\rm FLT}_{\rm LUMIG}$) $+ 1 \leq T^{\rm FLT}_{\rm BPC,Y} < 8 + E^{\rm FLT}_{\rm BPC,Y} \geq 4$ |
| HIGH | FLT 50 | RCAl energy cut: (RCAL$_{\rm EMCE} > 464$ or RCAL$_{\rm EMCTH} > 1250$) $+ 1 \leq T^{\rm FLT}_{\rm BPC,Y} < 8 + E^{\rm FLT}_{\rm BPC,X} \geq 1$ |
| LOW LOWP MED | FLT 52 | $1 \leq T^{\rm FLT}_{\rm BPC,Y} < 8 + E^{\rm FLT}_{\rm BPC,Y} \geq 4$ or BPC SOUTH: $((1 \leq T^{\rm FLT}_{\rm BPC,X} < 8 + E^{\rm FLT}_{\rm BPC,X} \geq 2)$ or $(1 \leq T^{\rm FLT}_{\rm BPC,Y} < 8 + E^{\rm FLT}_{\rm BPC,Y} \geq 2))$ |
| All | SLT DIS 2 | $(2 < X^{\rm SLT}_{\rm BPC,max} < 12 + 5 < Y^{\rm SLT}_{\rm BPC,max} < 12$ $(E3X/E)^{\rm SLT}_{\rm BPC} > 0.35)$ and ((FLT 52 and $E^{\rm SLT}_{\rm BPC} > 6$ GeV) or (FLT 50 and $(E - P_Z)^{\rm SLT}_{\rm h+BPC+LUMIG} > 15$ GeV) or (FLt 32 and $E^{\rm SLT}_{\rm LUMIG} > 3.5$ GeV ) |
| NONE | SLT DIS 3 | (FLT 32 and $E^{\rm SLT}_{\rm LUMIG} > 3.5$ GeV) or (FLT 50) or (FLT 52)) |

Table B.1: 1997 BPC FLT and SLT trigger cuts. The indices of the quantities refer to the trigger level at which they are calculated. CTD, LUMIG, and LUMIE refer to the ZEUS components as described in chapter 4. All BPC quantities refer to the BPC North module unless noted otherwise. $X^{\rm SLT}_{\rm BPC,max}$ and $Y^{\rm SLT}_{\rm BPC,max}$ refer to the BPC X- and Y-finger with most energy at SLT level. $(E3X/E)^{\rm SLT}_{\rm BPC}$ is the fraction of energy deposited in $X^{\rm SLT}_{\rm BPC,max}$ and the two neighbouring fingers of the total BPC energy at SLT level. Energy and timing information at FLT level are in ADC counts as provided by the ADCs and TDCs (see section 5.2). The vetos applied at all FLT slots to reject background events have been omitted.

| Region | Trigger | Requirements/Cuts/Comments |
|---|---|---|
| LOW | FLT 52 + SLT DIS 2 + ((TLT DIS 17) or (TLT DIS 23)) | see table B.1<br>see MED $y$ for DIS 17 cuts<br>FLT 52 and SLT DIS 3<br>$-10$ ns $< T^{\mathrm{TLT}}_{\mathrm{BPC}} < -5$ ns<br>17 GeV $< E^{\mathrm{TLT}}_{\mathrm{BPC}} < 35$ GeV<br>$X^{\mathrm{TLT}}_{\mathrm{BPC}} > 7.0$ cm<br>$Y^{\mathrm{TLT}}_{\mathrm{JB}} < 0.1$ |
| LOWP | FLT 52 + SLT DIS 2 + TLT DIS 18 | see table B.1<br>SLT DIS 2 or SLT DIS 3 (no cuts) |
| MED | FLT 52 + SLT DIS 2 + TLT DIS 17 | see table B.1<br>FLT 52 and SLT DIS 2<br>$-10$ ns $< T^{\mathrm{TLT}}_{\mathrm{BPC}} < -5$ ns<br>$E^{\mathrm{TLT}}_{\mathrm{BPC}} > 6$ GeV<br>$25 < (E - P_Z)^{\mathrm{TLT}}_{\mathrm{h+BPC}} < 65$ GeV<br>$Y^{\mathrm{TLT}}_{\mathrm{JB}} > 0.02$ |
| HIGH | FLT 50 + SLT DIS 2 + TLT DIS 22 | see table B.1<br>FLT 50 and SLT DIS 22<br>$-10$ ns $< T^{\mathrm{TLT}}_{\mathrm{BPC}} < -5$ ns<br>20 GeV $< (E - P_Z)^{\mathrm{TLT}}_{\mathrm{h+BPC+LUMIG}}$ |
| ISR | FLT (32 or 52) + SLT DIS 2 + TLT DIS 21 | see table B.1<br>FLT (32 or 52) and SLT DIS 2<br>$30 < (E - P_Z)^{\mathrm{TLT}}_{\mathrm{h+BPC+LUMIG}} < 65$ GeV<br>$E^{\mathrm{TLT}}_{\mathrm{LUMIG}} > 3.5$ GeV<br>$E^{\mathrm{TLT}}_{\mathrm{LUMIE}} < 4.0$ GeV<br>$Y^{\mathrm{TLT}}_{\mathrm{JB}} > 0.04$ |

Table B.2: 1997 BPC TLT trigger cuts. The indices of the quantities refer to the trigger level at which they are calculated. CTD, LUMIG, and LUMIE refer to the ZEUS components as described in chapter 4. All BPC quantities refer to the BPC North module unless noted otherwise.

# Bibliography


[Ab83] CDHS Collaboration, H. Abramowicz et al., *Z. Phys.* **C 17** (1983) 283.

[Ab90] H. Abramowicz et al., *Phys. Lett.* **B 269** (1991) 465.

[Ab93] H1 Collaboration, I. Abt et al., *Nucl. Phys.* **B 407** (1993) 515.

[Ab95] H. Abramowicz et al., *DESY 95-047* (1995).

[Ab96] H. Abramowicz et al., in *Proceedings of the Workshop on Future Physics at HERA*, edited by G. Ingelman et al. (Hamburg, Germany, 1995).

[Ab97] H. Abramowicz and A. Levy, *DESY 97-251* (1997).

[Ad96] K. Adel et al., *FTUAM 96-39* (1996).

[Ad96a] M. Adams et al., *Phys. Rev.* **D 54** (1996) 3006.

[Ad97] H1 Collaboration, C. Adloff et al., 'A Measurement of the Proton Structure Function F2(x,Q2) at low x and low Q2 at HERA', *Nucl. Phys.* **B 497** (1997) 3.

[Ag94] G. D'Agostini, *DESY 94-099* (1994).

[Ai95] H1 Collaboration, S. Aid et al., *Z. Phys.* **C 69** (1995) 27.

[Ai96] H1 Collaboration, S. Aid et al., *Nucl. Phys.* **B 470** (1996) 3.

[Al77] G. Altarelli and G. Parisi, *Nucl. Phys.* **B 126** (1977) 298.

[Am99] C. Amelung, Ph.D. thesis (in preparation), Univ. of Bonn (1999).

[Am99a] C. Amelung, 'Measurement of $F_2$ at Very Low $Q^2$ Using 1997 ZEUS BPC and BPT Data', *ZEUS-note 99-056* (1999).

[Am99b] C. Amelung, private communications.

[An91] A. Andresen et al., *Nucl. Instr. and Meth.* **A 309** (1991) 101.

[An92] J. Andruskow et al., *DESY 92-066* (1992).

[Ar95] ARMCO EISEN GmbH, *Technical information*, (Köln, Germany, 1990).

[As94] A.J. Askew et al., *Phys. Rev.* **D 49** (1994) 4402.

[As94a] A.J. Askew et al., *Phys. Lett.* **B 325** (1994) 212.

[Ba78] Y. Balitzki and L.N. Lipatov, *Phys. Rev. Lett.* **28** (1978) 822;
E.A. Kuraev et al., *Phys. Rev. Lett.* **44** (1976) 443;
E.A. Kuraev et al., *Phys. Rev. Lett.* **45** (1977) 199.







[Ba90] B. Badelek and J. Kwiecinski, *Phys. Lett.* **B 295** (1992) 263.

[Ba92] T.H. Bauer et al., *Rev. Mod. Phys.* **50** (1978) 261.

[Ba95] L.A.T. Bauerdick et al., *DESY-95-236* (1995).

[Ba96] Particle Data Group, R.M. Barnett et al., *Phys. Rev.* **D 54** (1996) 1.

[Ba97] B. Badelek, *Z. Phys.* **C 74** (1997) 297.

[Ba97a] U. Bassler, G. Bernardi, *DESY 97-137* (1997).

[Be34] H. Bethe and W. Heitler, *Proc. Roy. Soc.* **A 146** (1934) 83.

[Be91] S. Bentvelsen et al., in *Proceedings of the Workshop on Physics at HERA*, edited by W. Buchmüller and G. Ingelman (Hamburg, Germany, 1991).

[Be93] B. Bernstein et al., *Nucl. Instr. and Meth.* **A 336** (1993) 23.

[Bi94] A.F. Bielajew et al., *SLAC-PUB-6499* (1994);
R. L. Ford and W. R. Nelson, *SLAC-PUB-210* (1978);
W. R. Nelson et al., *SLAC-PUB-265* (1985).

[Bl69] E.D. Bloom et al., *Phys. Rev. Lett.* **23** (1969) 930.

[Bo96] I. Bohnet and B. Surrow, 'Studies on radiation damage effects in the Beam Pipe Calorimeter at ZEUS in 1995', *ZEUS-note 98-026* (1998).

[Bo99] I. Bohnet, 'Investigations on Uniformity, Radiation Resistance and Calibration of ZEUS Calorimeter Components at HERA', Ph.D. thesis, Univ. of Hamburg.

[Bo99a] I. Bohnet, U. Fricke, 'Studies of radiation damage effects in the Beam Pipe Calorimeter at ZEUS in 1997', *ZEUS-note 99-057* (1999).

[Bo99b] I. Bohnet, U. Fricke, B. Surrow, K. Wick, 'Radiation Damage Effects in the Beam Pipe Calorimeter at ZEUS', Proceedings of the 6.International Conference on Advanced Technology and Particle Physics Villa Olmo, Italy October 1998, *Nucl. Phys.* **B 78** (Proc. Suppl.) (1999) 713.

[Bo99c] I. Bohnet, N. Gedner, F. Goebel, T. Neumann, K. Wick, 'Radiation Hardness of different calorimeters studied with a movable $^{60}$Co source at the ZEUS detector', Proceedings of the 8.International Conference on Calorimetry in High Energy Physics, Lisbon, Portugal 1999, to be published in World Scintific Publishing Co.Pte.Ltd.

[Bo99d] I. Bohnet, A. Meyer-Larsen, U. Fricke, private communications.

[Bo99e] A. Bornheim, 'Measurement of the Proton Structure Function $F_2$ using ISR events', Ph.D. thesis, Univ. of Bonn (1999).

[Br89] R. Brun et al., *GEANT3, CERN DD/EE/81-1* (1989).

[Br97] ZEUS Collaboration, J.Breitweg et al., 'Measurement of the Proton Structure Function $F_2$ and $\sigma_{\rm tot}^{\gamma^* p}$ at Low $Q^2$ and Very Low $x$ at HERA' *DESY 97-135* (1997).

[Br98] G. Briskin, 'Diffractive Dissociation in $ep$ Deep Inelastic Scattering', Ph.D. thesis, University of Tel Aviv (1998), DESY-THESIS-1998-036.

[Br98a] ZEUS Collaboration, J. Breitweg et al., 'ZEUS Results on the Measurement and Phenomenology of $F_2$ at Low $x$ and low $Q^2$', *DESY 98-121* (1998).

[Br98b] ZEUS Collaboration, J. Breitweg et al., 'Exclusive Electroproduction of $\rho^0$ and $J/\psi$ Mesons at HERA' , *DESY 98-107* (1998).

[Br98c] ZEUS Collaboration, J. Breitweg et al., 'Measurement of the Diffractive Cross Section in Deep Inelastic Scattering using ZEUS 1994 Data',*DESY 98-084* (1998).

[Bu92] W. Buchmueller, Proceedings of the Workshop on Physics at HERA, Vol 3, 1440, 1992.

[Ca69] C.G. Callan and D. Gross, *Phys. Rev. Lett.* **22** (1969) 156.

[Ca90] S. Catani, et al., *Phys. Lett.* **B 234** (1990) 339;
S. Catani, et al., *Nucl. Phys.* **B 336** (1990) 18.

[Ca93] A. Caldwell et al., *Nucl. Instr. and Meth.* **A 321** (1992) 356.

[Ca94] A. Capella et al., *Phys. Lett.* **B 337** (1994) 358.

[Ca96] A. Caldwell et al., *ZEUS-note 96-044* (1996).

[Cl86] F. Close, M. Marten and C. Sutton, *The Particle Explosion*,
(Oxford University Press Inc., New York, 1986).

[Co70] R.D.B. Collins, *An Introduction into Regge Theory and High Energy Physics*,
(Cambrige University Press, Cambrige, 1977).

[Co92] A. Courau and P. Kessler, *Phys. Rev.* **D 46** (1992) 117.

[Co96] M. Costa, D. Williams, *ZEUS-note 96-039* (1996).

[Cu96] J. Cudell et al., *BROWN-HET-1060* (1997).

[Cu99] J. Cudell et al., *BROWN-HET-1184* (1999).

[DESY94] DESY, *Annual report* (1994).

[Da99] U.D. 'Alesio, A. Metz, H.J. Pirner, 'Soft amd hard Pomeron in the structure function of the proton at low $x$ and low $Q^2$', Eur. Phys. Journal **C 9** 601-609 (1999).

[De75] Deden at al., *Nucl. Phys.* **B 85** (1975) 269.

[De91] M. Derrick et al., *Nucl. Instr. and Meth.* **A 309** (1991) 77.

[De93] ZEUS Collaboration, M.Derrick et al., *Phys. Lett.* **B 316** (1993) 412.

[De94] ZEUS Collaboration, M.Derrick et al., *Z. Phy.* **C63** (1994) 391.

[De96] ZEUS Collaboration, M. Derrick et al., *Z. Phys.* **C 69** (1996) 607.

[De99] P. Desgrolard, A. Lengyel, E. Martynov, 'New possibilities of old soft pomeron in DIS', Eur. Phys. Journal **C 7** 665-667 (1999).

[Do87] H.G. Dosch, *Phys. Lett.* **B 190** (1987) 177.

[Do88] H.G. Dosch, Yu.A.Simonov, *Phys. Lett.* **B 205** (1988) 339.

[Do92] A. Donnachie and P.V. Landshoff, *Phys. Lett.* **B 296** (1992) 227.

[Do94] A. Donnachie and P.V. Landshoff, *Z. Phys.* **C 61** (1994) 139.

[DL98] A. Donnachie and P.V. Landshoff, *hep-ph/9806344* (1998).





[Dr64] S.D. Drell and J.D. Walecka, *Amn. Phys. (N.Y.)* **28** (1964) 18.

[Es99] K.J.Eskola, V.J.Kolhinen, P.V. Ruuskanen, 'Nuclear Parton Distributions - a DGLAP Analysis', hep-ph/9906484 (1999).

[Fe69] R.P. Feynman, *Phys. Rev. Lett.* **23** (1969) 1415.

[Fo74] D.J. Fox et al., *Phys. Rev. Lett.* **33** (1975) 898.

[Fo93] B. Foster et al., *Nucl. Instr. and Meth.* **A 338** (1993) 254.

[Fr61] M. Froissart, *Phys. Rev.* **123** (1961) 1053.

[Fr73] H. Fritzsch et al., *Phys. Lett.* **B 47** (1973) 365.

[Fr98] U. Fricke, 'BPCRECON: User's Guide and Reference', *ZEUS-note 98-081* (1998).

[Fu82] W. Furmanski and R. Petronzio, *Phys. Lett.* **B 97** (1980) 437.

[Gb98] K. Golec-Biernat, 'Saturation effects in deep inelastic scattering at low $Q^2$ and its implications on diffraction', *Phys. Rev.* **D 59** (1998) 3006.

[Ge64] M. Gell-Mann, *Phys. Lett.* **8** (1964) 214.

[Ge99] N. Gendner, Ph.D. thesis, Univ. of Hamburg, in preparation.

[Gi72] F.J. Gilman, *Phys. Rev.* **129** (1968) 1365.

[Gi99] C. Ginsburg, private communications.

[Gr64] O.W. Greenberg, *Phys. Rev. Lett.* **13** (1964) 598.

[Gr72] V.N. Gribov and L.N. Lipatov, *Sov. J. Nucl Phys.* **15** (1972) 438;
L.N. Lipatov, *Sov. J. Nucl. Phys.* **20** (1975) 96;
Y.L. Dokshitzer, *Sov. Phys. JETP.* **46** (1977) 641.

[Gr73] D.J. Gross and F. Wilczek, *Phys. Rev.* **D 8** (1973) 3633.

[Gr89] M.G. Green, *RNBNC 89-01* (1989).

[Gr98] J. Grosse-Knetter, *ZEUS-note 98-031* (1998).

[Gu80] G. Gurci et al., *Nucl. Phys.* **B175** (1980) 27.

[H199] Suggested by H1 in the HERA coordination meeting in October 1999

[HB94] HERA-B Collaboration, *Technical Design Report*, DESY-PRC 95/01 (1995).

[HE93] HERMES Collaboration, *Technical Design Report* (1993).

[Ha63] L.N. Hand, *Phys. Lett.* **B 129** (1963) 1834.

[Ha84] F. Halzen and A.D. Martin, *Quarks and Leptons*,
(John Wiley Sons Inc., New York, 1984).

[Ha94] Hamamatsu, *Technical information*, (Tokyo, Japan, 1994).

[Ha99] D. Haidt, 'Log-Log behaviour of $F_2$ at low $x$ in the $Q^2$ range from 0.1 to 35 GeV$^2$', Proccedings of the DIS99 Workshop (1999).

[He44] W. Heisenberg, *Physikalische Prinzipien der Quantentheorie*, (S. Hirzel Verlag, Stuttgart, 1958).

[Ho53] R. Hofstadter et al., *Phys. Rev.* **91** (1953) 422.

[Ho55] R. Hofstadter and R.W. McAllister, *Phys. Rev.* **98** (1955) 217.

[Ho57] R. Hofstadter, *Ann. Rev. Nucl. Part. Sci.* **7** (1957) 458.

[Ho93] ZEUS Collaboration, *The ZEUS Detector*, Status Report 1993, edited by U. Holm, (1993).

[Ho99] B. Holzer and A.Mesek, private communications.

[In87] G. Ingelman and R. Rückl, *Phys. Lett.* **201** (1988) 369.

[Io69] B.L. Ioffe, *Phys. Lett.* **B 30** (1969) 123.

[Ja75] F. James, M.Roos, Comp. Phys. Comm. **D 10** (1975) 343.

[Ja79] F. Jacquet and A. Blondel, in *Proceedings of the study of an ep facility for Europe*, edited by U. Amaldi, (Hamburg, Germany, 1979).

[Ju99] H. Jung, 'CCGM prediction for $F^2$ and forward jets at HERA', hep-ph/9905554 v2 (1999).

[Ju99a] H. Jung, 'THE RAPGAP Monte Carlo for Deep Inelastic Scattering, Version 2.06/26'.

[Ka83] T. Kamon et al., *Nucl. Instr. and Meth.* **213** (1983) 261.

[Ka98] A.B. Kaidalow, C. Merino, 'Theoretical Description of the HERA Data on $F_2$ at Low $Q^2$', hep-ph/9806367 (1998).

[Ke98] R. Kerger, A. Bornheim, E. Hilger, 'Measurement of the Proton Structure Function $F_2(x,Q^2)$ using ISR events from 1995 data', *ZEUS-note 98-034* (1998).

[Kw94] J. Kwiecinski et al., *Phys. Rev.* **D 50** (1994) 217.

[Kw97] J. Kwiecinski et al., in *Proceedings of the Workshop on Deep Inelastic Scattering and QCD (DIS 97)*, edited by J. Repond (AIP, Chicago, 1997).

[La93] H. Larsen et al., 'The LPS readout system', CERN/LAA/LP/93-17.

[Le87] W.R. Leo, *Techniques for Nuclear and Particle Physics Experiments*, (Springer, New York, 1987).

[Le97] A. Levy, *DESY 97-013* (1997).

[Lo92] L. Loennblad, Comp. Phys. Comm. **71** (1992) 15.

[Ma95] J. Mainusch, 'Measurement of the total photon-proton cross-section at HERA energies', Ph.D. thesis., Univ. of Hamburg (1995), *DESY F35D-95-14* (1995).

[Ma97] A.D. Martin, M.G. Ryskin, T. Teubner, Phys. Rev. **D 55** (1997) 4329.

[Ma98] M. Inuzuka, 'Measurement of the Diffractive Cross Section in Low $Q^2$ in $ep$ Scattering at HERA', Ph.D. thesis, Univ. of Tokio (1999).

[Ma98a] A.D. Martin, M.G. Ryskin, A.M. Stasto, 'The description of $F_2$ at low $Q^2$', hep-ph/9806212 (1998).



[Me99] A. M.-Larsen, 'Konstruktion, Aufbau und Kalibration eines strahlrohrnahen Kalorimeters zur Verwendung im ZEUS-Experiment', Ph.D. thesis, Univ. of Hamburg.

[Mo29] N.F. Mott, *Proc. Roy. Soc.* **124** (1929) 425.

[Mo98] T. Monteiro, 'Study of Exclusive Electroproduction of Mesons at Low $Q^2$ Using the ZEUS Beam Pipe Calorimeter at HERA', Ph.D. thesis, Univ. of Hamburg (1998), DESY-THESIS-1998-027.

[Mo98a] V. Monaco, 'Measurement of the proton structure function $F_2$ at low $Q^2$ and low $x$ with the Beam Pipe Tracker and Beam Pipe Calorimeter of ZEUS at HERA', Ph.D. thesis, Univ. of Turin (1998).

[Mo99] V. Monaco, private communications.

[Mu90] A.H. Mueller, *Nucl. Phys. B (Proc. Suppl.)* **18 C** (1990) 125.

[Pa68] W. Panofski, in *Proceedings of the International Conference in High Energy Physics*, (Vienna, Austria, 1968).

[Pe99] A. Pellegrino, private communications.

[Pi93] K. Piotrzkowski, *DESY F35D-93-06* (1993).

[Pl94] Metallwerk Plansee GmbH, *Technical information*, (Lechbruck, Austria, 1994).

[Pl97] H. Plothow-Besch, 'PDFLIB: User's Manual', Version 7.09, 1997.

[Pr93] K. Prytz, *Phys. Lett.* **B 311** (1993) 286.

[Qu96] A. Quadt, 'Measurement and QCD analysis of the Proton Structure Function $F_2$ from the 1994 HERA Data using the ZEUS Detector', Ph.D. thesis., Univ. of Oxford (1996).

[Qu98] A. Quadt, O. Ruske, 'A new Method to Measure Vertex Distributions', *ZEUS-note 98-036* (1998).

[Ro50] M.N. Rosenbluth, *Phys. Rev.* **79** (1950) 615.

[Sa60] J.J. Sakurai, *Ann. Phys.* **11** (1960) 1.

[Sa72] J.J. Sakurai and D. Schildknecht, *Phys. Lett.* **B 40** (1972) 121.

[Sc97] D. Schildknecht and H. Spiesberger, *BI-TP 97/25* (1997).

[Si95] R. Sinkus, H. Abramowicz, A. Caldwell, 'Neural network based electron identification in the ZEUS calorimeter' *DESY 95-054* (1995).

[Sj86] T. Sjoestrand, Comp. Phys. Comm **39** (1986) 347.

[Sj87] T. Sjoestrand, M.Bengtsson, Comp. Phys. Comm **43** (1987) 367.

[Sj92] T. Sjoestrand, CERN-TH 6488/92.

[Sp96] H. Spiesberger, 'HERACLES. An Event Generator for ep Interactions at HERA Including Radiative Processes'.

[Sp99] H. Spiesberger, 'HERACLES and DJANGOH: Event Generation for ep Interactions at HERA Including Radiative Processes'.

[St95] G. Sterman et al., *Rev. Mod. Phys.* **67** (1995) 157.

[Su97] B. Surrow and B. Holzer, private communications.

[Su98] B. Surrow, 'Measurement of the Proton Structure Function $F_2$ at Low $Q^2$ and Very Low $x$ with the ZEUS Beam Pipe Calorimeter at HERA', Ph.D. thesis, Univ. of Hamburg (1998), DESY-THESIS-1998-004.

[Ti97] J. Tickner, 'Proton Structure Functions at low $Q^2$', Ph.D. thesis., Univ. of Oxford (1997).

[Tu99] `http://www-zeus.desy.de/~ntuning/ZEUS_ONLY/zufos_new.html`

[Ui92] H. Uijterwaal, 'The Global Second Level Trigger for ZEUS', Ph.D. thesis., Univ. of Amsterdam (1992).

[We73] S. Weinberg, *Phys. Rev. Lett.* **31** (1973) 494.

[We98] A. Weber, 'Der Silizium-Spurdetector BPT für kleinste Elektron-Streuwinkel in ZEUS: Alignment mit Teilchenspuren', Diploma thesis., Univ. of Bonn (1998).

[We99] E. Weiss, private communications.

[Wi98] D.C. Williams, 'BPRECON: User's Guide and Reference', *ZEUS-note 98-038* (1998).

[Wo71] G. Wolf, Lefrancois, Proc. 5th Intern. Symp. on Electron and photon interactions at high energies, Cornell University (1971).

[Wo99] M. Wodarczyk, private communications.

[Wu84] S.L. Wu, *Phys. Rep.* **107** (1984) 1.

[Wu94] B. Wulkop, K.Wick, W.Busjan, A.Dannemann, U.Holm, 'Investigation of the Radiation Damage Process in Scintillators During Irradiation', Symposium on Radiation Effects on Polymers, Washington D. C. (USA), 23.-25.8.94, and Polymer Preprints **35** (1994) 924.

[Zw64] G. Zweig, *CERN-8182/TH 401* (1964);
G. Zweig, *CERN-8419/TH 402* (1964).

# Acknowledgments

I am writing the acknowledgments now, so I guess I am (almost) through with my Ph.D.! Wow, the end is near.
I would like to thank all the people from DESY, ZEUS, and Hamburg University for their continuing support during my work here. Special thanks to Prof. Robert Klanner and Prof. Erich Lohrmann for offering me the opportunity work on my Ph.D. at the ZEUS BPC. Additional thanks to Prof. Robert Klanner for his patience during the last months of the work.
Working with the BPC/BPT group and the BPT-$F_2$-club was a great experience. I enjoyed work and chats with Bernd Surrow, Teresa Monteiro, Dorian Kçira, Antonio Pellegrino, Marco Costa, Marta Ruspa, Vincenzo Monaco, Christoph Amelung, Arnulf Quadt, Ilja Bohnet, Nils Gendner, Armin Meyer-Larsen, and our volunteer for hardware work Niel Mcdonald.
But of course there was more fun beyond BPC and $F_2$. Ulrike Wollmer, Atoosa Meseck, Michael Sievers, Margherita Milite, Kirstin Hebbel, Matthias Moritz, Stefan Stonjek, Florian Göbel, Olaf Deppe, Guido Nellen, Astrid Nagel, Kai Dessler, Amaya Lopez-Duran-Viani, and Enrico Tassi contributed quite a lot to the life-apart-from-physics. Keep the cake coming!
Thanks to Adrian Fox-Murphy and Ursula Rehder for their corrections which made my thesis much more readable and understandable.
Finally, there are Michaela Töde and Edith Fricke, who supported me the whole time of my work, especially the last few months in which I was hardly seen outside of DESY.